

Thorsten Schnabel

Molecular Modeling and
Simulation of Hydrogen Bonding
Pure Fluids and Mixtures



λογος



Molecular Modeling and Simulation of Hydrogen Bonding Pure Fluids and Mixtures

Von der Fakultät Energie-, Verfahrens- und Biotechnik
der Universität Stuttgart zur Erlangung der Würde eines
Doktor-Ingenieur (Dr.-Ing.)

genehmigte Dissertation

Vorgelegt von
Dipl.-Ing. Thorsten Schnabel
aus Stuttgart

Hauptberichter:
Mitberichter:

Prof. Dr.-Ing. habil. Hans Hasse
Prof. Dr. Florian Müller-Plathe
Dr.-Ing. habil. Jadran Vrabec

Tag der mündlichen Prüfung: 6. Mai 2008

Institut für Technische Thermodynamik
und Thermische Verfahrenstechnik
der Universität Stuttgart

2008

Bibliografische Information der Deutschen Nationalbibliothek

Die Deutsche Nationalbibliothek verzeichnet diese Publikation in der Deutschen Nationalbibliografie; detaillierte bibliografische Daten sind im Internet über <http://dnb.d-nb.de> abrufbar.

D93 (Dissertation Universität Stuttgart)

©Copyright Logos Verlag Berlin GmbH 2008

Alle Rechte vorbehalten.

ISBN 978-3-8325-1945-2

Logos Verlag Berlin GmbH
Dominiushof, Gubener Str. 47,
10243 Berlin
Tel.: +49 030 42 85 10 90
Fax: +49 030 42 85 10 92
INTERNET: <http://www.logos-verlag.de>

Vorwort

Die vorliegende Arbeit entstand in der Zeit von Januar 2003 bis September 2007 während meiner Tätigkeit als wissenschaftlicher Mitarbeiter von Prof. Dr.-Ing. habil. H. Hasse am Institut für Technische Thermodynamik und Thermische Verfahrenstechnik der Universität Stuttgart. Herr Prof. Dr.-Ing. habil. H. Hasse hat die Arbeit angeregt und gemeinsam mit Herrn Dr.-Ing. habil. J. Vrabec betreut. Herr Prof. Dr.-Ing. habil. H. Hasse hat mit seinem wertvollen fachlichen Rat in zahlreichen Diskussionen über wissenschaftliche Fragestellungen und seiner engagierten Förderung in allen Phasen dieser Arbeit entscheidend zu deren Gelingen beigetragen, wofür ich ihm herzlich danke. Herr Dr.-Ing. habil. J. Vrabec leitete mit großem Engagement die Arbeitsgruppe Molekulare Simulation am Institut. Mein aufrichtiger Dank gilt ihm für seine tägliche Diskussionsbereitschaft, die den Austausch von Fachwissen ermöglichte, der für das Gelingen der vorliegenden Arbeit unverzichtbar war.

Herrn Prof. Dr. F. Müller-Plathe danke ich für die freundliche Übernahme des Koferats und die Durchsicht dieser Dissertation.

Der Deutschen Forschungsgemeinschaft danke ich für die finanzielle Förderung dieser Arbeit. Weiterhin danke ich dem Höchstleistungsrechenzentrum der Universität Stuttgart für die gute Zusammenarbeit und für die Möglichkeit, die Rechnerressourcen im Rahmen des Bundesrechenprojekts MMHBF zu benutzen.

Bei allen Kolleginnen und Kollegen am Institut bedanke ich mich für die freundliche Atmosphäre und den guten Zusammenhalt. Namentlich möchte ich Bernhard Eckl aus der molekularen Simulationsgruppe nennen, mit dem eine unkomplizierte und offene Zusammenarbeit sowie reger Gedankenaustausch leicht möglich war. Des Weiteren möchte ich mich bei Oliver Steinhof, Thomas Grützner und Michael Maiwald für die angenehme Abwechslung neben der Arbeit in Stuttgart bedanken. Das Gleiche gilt ebenso für die Vereinsmitglieder der Stuttgarter Rudergesellschaft.

Darüber hinaus bedanke ich mich bei allen Studentinnen und Studenten, die mit ihrer Begeisterung und ihrem Engagement als Diplom- und Studienarbeiter, als wissenschaftliche Hilfskräfte, als indische, spanische oder griechische Austauschstudenten bzw. Austauschstudentinnen zu der vorliegenden Arbeit beitrugen. Im Speziellen möchte ich namentlich Thorsten Merker aufführen, der durch seine Studienarbeit und langjährige wissenschaftliche Hilfstätigkeit bei mir zum Gelingen vieler Projekte beigetragen hat.

Mein besonderer Dank gilt meinen Eltern und meiner Lebenspartnerin Stephanie Holz, die gerade in Zeiten mit gesundheitlichen Rückschlägen zu mir hielten.

Brig-GLIS, im Juni 2008

Thorsten Schnabel

Abstract

A simple molecular modeling approach for hydrogen bonding fluids was applied in the present work to yield quantitative thermophysical and structural properties of pure fluids and mixtures. The approach is based on Lennard-Jones potentials (LJ) to account for the dispersive interactions between the molecules and on point charges to describe the polarity and hydrogen bonding.

Using this approach, molecular models for methanol, ethanol, monomethylamine, dimethylamine, methanethiol, formic acid and water were developed. The parameters of the molecular models were adjusted to experimental vapor pressures and bubble densities. With this modeling strategy, an accurate description of vapor-liquid equilibria for the pure components over wide temperature ranges was obtained. Only for water, the simple modeling approach turned out to be inefficient. The vapor-liquid equilibrium could not be described with the same accuracy over a wide range of states as for the other substances.

The molecular simulation of mixtures is not straightforward since unlike dispersive interactions can presently not be obtained by simple physical laws as this is the case for other types of interactions like, e.g., electrostatic interactions. Combining rules, which use solely pure component quantities, are often used in the literature to determine unlike LJ parameters. Such combining rules were investigated here regarding their capability to quantitatively yield binary vapor-liquid equilibria. The findings show that it is necessary to adjust one binary interaction parameter to quantitatively describe those properties.

Following this, state-independent binary interaction parameters were adjusted for mixtures consisting of one hydrogen bonding and one non-hydrogen bonding component. The excellent agreement of the simulation results for vapor-liquid equilibria and Henry's law constants with experimental data shows that the new models for hydrogen bonding fluids give favorable description of thermophysical mixture properties.

The capability of the new models to yield structural properties were exemplarily investigated for methanol. Site-site radial distribution functions were evaluated and their prediction with simulation compare favorably to experimental data. NMR chemical shift experiments were carried out that yield information on hydrogen bonding in mixtures of methanol and carbon dioxide. Hydrogen bonding statistics of methanol species from molecular simulation were assessed with a physico-chemical classification of the species and their relation to NMR chemical shifts. The excellent prediction of NMR chemical shifts with the hydrogen bonding statistics from simulation show that with the simple molecular modeling approach for hydrogen bonding investigated here quantitatively correct results can be obtained not only for thermophysical properties but also for structural properties.

Zusammenfassung

Die Wasserstoffbrücke als eine der stärksten intermolekularen Wechselwirkungen ist in der Thermodynamik Grund für außergewöhnliche Stoffeigenschaften. Wegen dieser starken, gerichteten Wechselwirkung kommt es in Wasserstoffbrücken bildenden Fluiden zur Formation von Assoziaten und dreidimensionale Netzwerken, welche die Basis für die außergewöhnlichen thermodynamischen Stoffeigenschaften wie hohe kritische Temperaturen und hohe Verdampfungsenthalpien bilden. Die Wasserstoffbrücke spielt aber nicht nur in der Thermodynamik eine besondere Rolle. In der Biologie werden viele Vorgänge durch die Wasserstoffbrücke dominiert wie das Zusammenhalten von Faltstrukturen in Proteinen durch mehrere nebeneinander liegenden Wasserstoff verbrückten Polypeptidketten.

Die thermodynamische Modellierung von Wasserstoffbrücken bildenden Fluiden stellt eine besondere Herausforderung dar. Bei der Modellierung der Wasserstoffbrücke muss das Wechselspiel zwischen Energie und Struktur richtig abgebildet werden, um quantitative Daten erlangen zu können. Um die Ausbildung solcher Strukturen auf molekularer Ebene und deren energetischen Beiträge zu thermodynamischen Stoffeigenschaften richtig zu erfassen, muss ein Modell in der Lage sein, die energetischen und strukturellen Eigenschaften der Wasserstoffbrücke wiederzugeben. Die molekulare Modellierung und Simulation stellt einen solchen Ansatz dar.

In dieser Arbeit wurde ein einfacher, rechenzeiteffizienter molekularer Modellierungsansatz auf seine Vorhersagekraft von thermodynamischen und strukturellen Stoffeigenschaften von Wasserstoffbrücken bildenden Fluiden in Reinstoffen und Mischungen untersucht. Rechenzeiteffizienz ist wichtig, da sich noch immer die langen Simulationszeiten trotz der Fortschritte in Software- und Hardwarearchitekturen limitierend auf den heutigen Einsatz von molekularen Simulationen auswirkt.

Die molekulare Modellierung und Simulation beruht auf der Beschreibung der Wechselwirkungen zwischen den Molekülen und die sich daraus ergebenden Anordnungen. Es sind verschiedene Wechselwirkungsarten zwischen Molekülen von einander zu unterscheiden: die Repulsion aufgrund sich überlagernden Elektronenhüllen bei kurzen intermolekularen Abständen, die Dispersion wegen temporär induzierten Dipolen in der Elektronenhülle durch die Bewegung der Elektronen, permanent auftretende elektrostatische Ladungsverteilungen wie Dipole oder Quadrupole, und die Wasserstoffbrücke als eine quasischemische Bindung. Modellierungsphilosophie bei molekularen Simulationen ist es, diese verschiedenen Wechselwirkungsarten durch eigene Potentialtypen wieder zu geben. In dieser Arbeit wurde jedoch ein Modellierungsansatz aus Gründen der Rechenzeiteffizienz gewählt, bei dem die Dispersion, die Polarität und die Wasserstoffbrückenbildung des Moleküls durch Kombination nur zweier Potentialtypen abgebildet werden. Dieser Ansatz benutzt eine geeignete Überlagerung des Lennard-Jones 12-6 Potentials für die Dispersion und Punktladungen für die Polarität und Wasserstoffbrückenbildung. Bevor diese Potentialtypen näher erläutert werden, sollen noch grundlegende Informationen zu molekularen Simulationen gegeben werden.

In einer molekularen Simulation werden die Anordnungen nur weniger tausend Moleküle ausgewertet. Diese Anordnungen der Moleküle werden auch Konfigurationen genannt. Die Konfigurationen sind durch die intermolekularen Wechselwirkungen und den thermodynamischen Zustandspunkt eindeutig festgelegt. Die geringe Anzahl an Molekülen reicht jedoch aus, um makroskopische thermodynamische Stoffeigenschaften über die Gesetze der statistischen Thermodynamik zu bestimmen. Es gibt zwei grundlegende Typen von Simulationen zur Erzeugung der Konfigurationen: die Molekulardynamik und die Monte Carlo Simulation. Bei der Molekulardynamik werden aus den verschiedenen Potentialen zwischen den Molekülen die Gesamtkraft und das Drehmoment auf das Einzelteilchen bestimmt, so dass die Newtonschen Bewegungsgleichungen integriert werden können. Daraus ergibt sich eine zeitliche Abfolge von Konfigurationen, aus denen durch Zeitmittelung sich die makroskopischen Stoffdaten bestimmen lassen. In Monte Carlo Simulationen werden die Konfigurationen durch zufällige Verschiebungen und Drehungen der Moleküle erzeugt. Solche zufällig erzeugten Konfigurationen werden über eine Auswertung der Ab- bzw. Zunahme der potentiellen Gesamtenergie des Systems akzeptiert bzw. abgelehnt. Die aus energetischen Gründen erzeugten Konfigurationen werden statistisch gemittelt und dadurch die makroskopischen Stoffeigenschaften bestimmt.

Molekulare Simulationen sind aber nicht nur auf die Berechnung von Stoffeigenschaften begrenzt. Es können Strömungsvorgänge von Molekülen durch Nanokanäle, die Diffusion von Molekülen durch Poren, die Anlagerung von Molekülen an Oberflächen oder Nukleationsvorgänge wie Verdampfung und Kondensation mit molekularen Simulationen abgebildet werden. Aus solchen Simulationen können Informationen wie Strömungsprofile in Nanokanälen, die Diffusionsgeschwindigkeit in Poren, die bevorzugte Anlagerung von Molekülen an Oberflächensegmenten und Nukleationsraten abgeleitet werden.

Die molekulare Modellierung und Simulation zeigt wegen ihrer physikalischen Betrachtungsweise bei geeigneter Parametrierung der zugrunde liegenden Potentiale eine bessere Vorhersagekraft von Stoffdaten als phänomenologische Modelle. Ein weiterer Vorteil der Verwendung von molekularen Simulationen ist, dass bei Vorlage eines guten molekularen Modells die Vorhersage praktisch aller Stoffeigenschaften und die Beschreibung von Vorgängen im nanoskaligen Bereich hochgenau möglich ist.

Der in der vorliegenden Arbeit verwendete rechenzeiteffiziente molekulare Modellierungsansatz benutzt zur Beschreibung der Repulsion, Dispersion, Polarität und Wasserstoffbrückenbildung anisotropisch united-atom Lennard-Jones 12-6 Potentiale und Punktladungen. Im Folgenden soll dieser Ansatz näher erläutert werden. Das Gesamtpotential u zwischen zwei gleichen Wasserstoffbrücken bildenden Molekülen, modelliert durch n Wechselwirkungszentren, ist gegeben durch

$$u = \sum_{a=1}^n \sum_{b=1}^n 4\epsilon_{ab} \left[\left(\frac{\sigma_{ab}}{r_{ab}} \right)^{12} - \left(\frac{\sigma_{ab}}{r_{ab}} \right)^6 \right] + \frac{q_a q_b}{4\pi\epsilon_0 r_{ab}},$$

wobei a und b der Index der Wechselwirkungszentren des jeweiligen Moleküls, r_{ab} der Abstand zwischen den Wechselwirkungszentren, σ_{ab} und ϵ_{ab} die Lennard-Jones Längen- und Energieparameter, q_a und q_b die Punktladungen auf den Wechselwirkungszentren a und b , und ϵ_0 die Permittivität des Vakuums ist.

Das Lennard-Jones 12-6 Potential wird in dieser Arbeit verwendet, um die Wechselwirkungsarten Repulsion und Dispersion zwischen Molekülen abzubilden. Dieses radialsymmetrische Potential wurde von Jones [109, 110] vorgeschlagen, um thermischen Zustandsgleichungen und Stoffdaten von Gasen einen physikalischeren Hintergrund zu geben. Der Zusatz 12-6 bedeutet, dass die Repulsion proportional zur 12. Potenz und die Dispersion proportional zur 6. Potenz des inversen Abstands zwischen zwei Lennard-Jones Wechselwirkungszentren ist, wie in dem linken Term der obigen Formel zu sehen ist. Der Term proportional zur 6. Potenz beschreibt die Dispersion und geht auf Untersuchungen von London [144, 145] zurück. Diese Proportionalität der Dispersion ist durch quantenchemische Reihenentwicklungen physikalisch begründet. Die Repulsion nimmt ebenfalls aus quantenchemischen Argumenten exponentiell zum Abstand ab. Der exponentielle Verlauf der Repulsion wird aber im Lennard-Jones 12-6 Potential durch das Abstandsverhalten mit der 12. Potenz aus numerischen Gründen angenähert. Im Folgenden wird der Zusatz 12-6 weggelassen. Der rechte Term in obiger Gleichung ist das Coulombsche Gesetz, über welches das Potential zwischen zwei Punktladungen berechnet wird.

Die Beiträge der kleinen H-Atome zur Dispersion in funktionalen Gruppen wie der Methyl- (CH_3) und Methylengruppe (CH_2) werden im Modellierungsansatz dieser Arbeit zu einem Wechselwirkungszentrum zusammengefasst. Die Reduktion der Dispersion auf ein Wechselwirkungszentrum ist in der molekularen Simulationsgemeinschaft als united-atom Ansatz bekannt [73].

Die Beschreibung der Dispersion durch united-atom Potentiale wurde erheblich durch Toxvaerd [241] verbessert durch die Einführung einer Verschiebung des Wechselwirkungszentrums in Richtung des größeren Atoms, an welches die H-Atome gebunden sind. Die Position des Wechselwirkungszentrums ist bei Methyl- und Methylengruppen typischer Weise in der Nähe des geometrischen Mittels der funktionalen Gruppe [244].

Der Potentialansatz, beschrieben durch obige Gleichung, wurde in der vorliegenden Arbeit verwendet, um hochgenaue molekulare Modelle für Methanol [206], Ethanol [202], Monomethylamin [207], Dimethylamin [207], Methanthiol, Ameisensäure [204] und Wasser zu entwickeln. Die Geometrie dieser Modelle außer von Methanol und Wasser wurde aus quantenchemischen Berechnungen unter Verwendung der Hartree-Fock Methode und des Basissatz 6-31G berechnet. Für die kleinen Moleküle in dieser Arbeit wurde der Einfluss der inneren Freiheitsgrade vernachlässigt. Bei mehreren möglichen Konformationen eines Moleküls wurde die energetisch wahrscheinlichste Anordnung gewählt wie bei Ethanol die *cis*-Konformation. Die Vernachlässigung der inneren Freiheitsgrade hat den Vorteil von kürzeren Simulationszeiten und einer geringeren zu bestimmenden Anzahl von Modellpa-

rametern.

Da für Methanol als Ausgangsmodell der Parametrierung das Modell von Stoll [228] diente, ist die Geometrie des vorliegenden Methanolmodells äquivalent zu diesem. Die Geometrie des ursprünglichen Methanolmodells wurde bestimmt aus Gasphasenexperimenten [248] zu Bindungslängen und Winkeln. Bei Wasser wurde die Orientierung des Moleküls zwar aus quantenchemischen Rechnungen übernommen, die Bindungslängen waren jedoch Bestandteil der Optimierung.

Für die Lennard-Jones Potentialparameter der Methyl- und Methylengruppe wurden die Parameter von Ungerer et al. [244] für die neuen Modelle übernommen. Die restlichen Potentialparameter wurden an Korrelationen von experimentellen Siededichten und Dampfdrücken [50, 55] über praktisch den gesamten Temperaturbereich der Dampf-Flüssigkeit Koexistenz angepasst. Die Anpassung der Modellparameter erfolgte über eine Sensitivitätsstudie und einem Anpassungsverfahren, welches von Stoll [228] bereits in früheren Arbeiten angewandt wurde. Zur simulativen Bestimmung des Dampf-Flüssigkeit Gleichgewichts wurde die NpT +Testteilchenmethode [162, 163, 165] verwendet.

Bei der Anpassung der Modellparameter wurden Abweichungen zu den Korrelationen der experimentellen Daten typischerweise für Siededichte kleiner als 1 % und für Dampfdruck kleiner als 5 % erreicht. Die Vorhersage von Verdampfungsenthalpien ergab Abweichungen zu Korrelationen von experimentellen Werten [50, 55] typischer Weise um die 5 %. In Tabelle 1 sind die mittleren Abweichungen der neuen Reinstoffmodelle für Siededichte, Dampfdruck und Verdampfungsenthalpie über praktisch den gesamten Temperaturbereich der Dampf-Flüssigkeit Koexistenz gegeben.

Tabelle 1: Mittlere Abweichung von Siededichte, Dampfdruck und Verdampfungsenthalpie der neuen molekularen Modelle für Alkohole, Amine, Thiole und organische Säuren.

Component	$\bar{\delta}\rho$ %	$\bar{\delta}p$ %	$\bar{\delta}\Delta\bar{h}_v$ %
Methanol	0.6	1.1	5.5
Ethanol	0.3	3.7	0.9
Monomethylamin	0.6	6.5	0.7
Dimethylamin	0.4	6.2	4.9
Methanthiol	0.6	7.4	7.4
Ameisensäure	0.8	5.1	19.6

Für die stark assoziierende Komponente Ameisensäure, die in der Gasphase zur Ausbildung von Dimeren neigt [199, 243], gelang die Anpassung an Siededichte und Dampfdruck ähnlich gut wie bei den anderen Substanzen aufgelistet in der Tabelle 1. Allerdings konnte die Verdampfungsenthalpie nicht mit der gleichen Genauigkeit vorhergesagt werden wie durch die anderen Reinstoffmodelle. Ein möglicher Grund ist die unzureichende

Beschreibung der Gasphase, da die Taudichte durch das neue Ameisensäuremodell nur mit Abweichungen zu experimentellen Werten von über 25 % vorhergesagt werden konnte. Ein anderer Grund kann sein, dass bei Verwendung des einfachen, rechenzeiteffizienten Modellierungsansatzes die gleichzeitige Beschreibung der Polarität und der Wasserstoffbrücke durch Punktladungen nicht ausreichend genug möglich ist. Diese mögliche Unzulänglichkeit des Modellierungsansatzes bei extrem stark assoziierenden Komponenten führte zu einer Pilotstudie über molekulare Modelle für Wasser, da diese Substanz als eine stark dipolare Komponente mit gleichzeitiger Ausbildung von dreidimensionalen Netzwerken gilt.

In der Pilotstudie zu Wasser wurden die Modellklassen TIP4P [112] und TIP5P [153] untersucht. Diese Modellklassen wurden verwendet, um neue Lennard-Jones basierende Wassermoleküle zu entwickeln mit dem Ziel, genaue Beschreibungen des Dampf-Flüssigkeit Gleichgewichts über den gesamten Temperaturbereich zu erlangen. Es stellte sich heraus, dass selbst mit den physikalischeren angeordneten Punktladungen in der Modellklasse TIP5P dies nicht möglich ist. Die Einführung von Lennard-Jones Wechselwirkungszentren auf den Positionen der positiven Punktladungen, was hier als all-atom Modellklasse bezeichnet werden soll, verbesserte sich die gleichzeitige Wiedergabe von Siededichte und Dampfdruck. Die mittleren Abweichungen des all-atom Modells zu experimentellen Werten sind aber immer noch ungenügend. Tabelle 2 gibt die mittleren Abweichungen für Siededichte, Dampfdruck und Verdampfungsenthalpie für die neuen Parametrierungen der Modellklassen TIP4P, TIP5P und all-atom. Bei dem Modell TIP4P/D wurde das Augenmerk darauf gelegt, die Siededichte genauer wiederzugeben, bei dem Modell TIP4P/P den Dampfdruck, da eine gleichzeitige Anpassung mit dem Modellierungsansatz nicht möglich war. Trotzdem gehören die neuen molekularen Modelle für Wasser zu den besten Lennard-Jones basierenden Wassermolekülen in der Literatur zur Beschreibung des Dampf-Flüssigkeit Gleichgewichts.

Tabelle 2: Mittlere Abweichung von Siededichte, Dampfdruck und Verdampfungsenthalpie der neuen molekularen Modelle für Wasser.

Modell	$\bar{\delta\rho}$ %	$\bar{\delta p}$ %	$\bar{\delta\Delta h_v}$ %
TIP4P/D	1.1	52.6	15.4
TIP4P/P	2.9	20.7	8.3
TIP5P/DP	2.1	46.6	8.1
all-atom	1.6	21.9	2.4

Die neuen molekularen Modelle aus Tabelle 1 mit ausreichend genauer Beschreibung des Dampf-Flüssigkeit Gleichgewichts wurden in der vorliegenden Arbeit für Simulationen von binären Mischungen verwendet [207]. Die Vorgehensweise zur molekularen Modellierung von Mischungen ist nicht eindeutig. Deshalb wurde im Vorfeld eine umfassende

Studie [205] dazu durchgeführt, die im Folgenden beschrieben werden soll.

In einer binären Mischung aus den Komponenten A und B sind drei Wechselwirkungsarten zu unterscheiden: die beiden zwischen den gleichen Komponenten A-A und B-B, und die zwischen den ungleichen Komponenten A-B. Die Wechselwirkungen zwischen den gleichen Komponenten sind über das Reinstoffmodell eindeutig definiert. Die elektrostatischen Wechselwirkungen zwischen den ungleichen Komponenten sind ebenfalls eindeutig durch die physikalischen Gesetze der Elektrostatik gegeben. Zur Bestimmung der ungleichen dispersiven Wechselwirkungen gibt es keine physikalischen Gesetze. Bei der Verwendung des Lennard-Jones Potentials zur Modellierung der dispersiven Wechselwirkungen zwischen ungleichen Komponenten müssen die ungleichen Lennard-Jones Längen- und Energieparameter σ_{ab} und ϵ_{ab} definiert werden.

Es gibt zwei Möglichkeiten die ungleichen Lennard-Jones Parameter zu bestimmen: über Kombinationsregeln oder über Anpassung an experimentelle Mischungsdaten. Kombinationsregeln verwenden Reinstoffdaten zur Bestimmung der ungleichen Lennard-Jones Parameter. Somit bleibt die Berechnung von Mischungsdaten mit molekularen Simulationen eine strenge Vorhersage. Bei der Anpassung der ungleichen Lennard-Jones Parameter an binäre Mischungsdaten ist die Vorhersage der binären Systeme nicht mehr streng gegeben. Da aber die intermolekularen Wechselwirkungen in dieser Arbeit über Paarpotentiale modelliert sind, bleibt zumindest die Vorhersage von polynären Mischungen bei der Anpassung der ungleichen Lennard-Jones Parameter an binäre Randsysteme voll gegeben.

Um feststellen zu können, ob Kombinationsregeln ausreichend sind für eine hochgenaue Modellierung von Mischungen oder ob eine Anpassung notwendig ist, wurde der Einfluss der ungleichen Längen- und Energieparameter auf Dampf-Flüssigkeit Gleichgewichtsdaten untersucht. Grundlage dafür bildeten Untersuchungen von 44 binären Mischungen aus früheren Arbeiten [226, 228, 258]. Die Reinstoffe dieser 44 Mischungen bestehen aus Edelgasen, homonuklearen und heteronuklearen zweiatomigen Molekülen wie Sauerstoff und Kohlenmonoxid, kleineren Kohlenwasserstoffen und halogenierten Kohlenwasserstoffen wie Kühlmittel. Das thermodynamische Verhalten dieser Reinstoffe können durch die Modellklassen unpolar sphärisch Ein-Zentren-Lennard-Jones Potential (1CLJ) [255], symmetrisch Zwei-Zentren-Lennard-Jones mit Quadrupol [255] oder Dipol [227] Potential (2CLJQ oder 2CLJD) mit nur geringen Abweichungen zu experimentellen Werten wiedergegeben werden. Bei den binären Kombinationen dieser Modellklassen existiert nur ein Paar an ungleichen Lennard-Jones Parametern σ_{ab} und ϵ_{ab} wegen der symmetrischen Modellierung der dispersiven Reinstoffpotentiale. Aus diesem Grund kann direkt der Einfluss der ungleichen Lennard-Jones Parameter auf die binären Dampf-Flüssigkeit Gleichgewichtsdaten abgeleitet werden.

Dazu wurde exemplarisch für die Mischungen Kohlenmonoxid + Ethan und Stickstoff + Propylen die Sensitivität von Dampfdruck, Siededichte und Dampfzusammensetzung auf die ungleichen Lennard-Jones Längen- und Energieparameter ermittelt. Für die

Bestimmung des Dampf-Flüssigkeit Gleichgewichts durch molekulare Simulationen wurde die Grand Equilibrium Methode [256] verwendet. Diese Studie zeigte, dass der Dampfdruck stark sensitiv auf Änderungen von beiden ungleichen Lennard-Jones Parametern, die Siededichte praktisch nur auf den ungleichen Lennard-Jones Längenparameter, und die Dampfzusammensetzung nur schwach sensitiv auf beide ungleichen Lennard-Jones Parameter reagiert. In dieser Studie wurden Konfidenzintervalle für diese drei Stoffgrößen eingeführt, um Simulationsunsicherheiten und Messungenauigkeiten zu berücksichtigen.

Durch die Einführung der Konfidenzintervalle wird ein Bereich für die ungleichen Lennard-Jones Parameter definiert, in dem Parameterpaarungen für die gleichzeitig ausreichend genaue Beschreibung alle drei Größen Dampfdruck, Siededichte und Dampfzusammensetzung gefunden werden kann. Dieser Bereich wird von ungleichen Lennard-Jones Längenparametern σ_{ab} geschnitten, die über das arithmetische Mittel gebildet werden, d.h. die Verwendung der Lorentz-Kombinationsregel [147]. Durch eine Anpassung des ungleichen Lennard-Jones Energieparameters ϵ_{ab} an den experimentellen Dampfdruck unter gleichzeitiger Verwendung des arithmetischen Mittels für σ_{ab} kann eine optimale Paarung der ungleichen Lennard-Jones Parameter gefunden werden. Dieses Ergebnis untermauert Mischungsstudien auf früheren Arbeiten von Stoll et al. [226, 228] und Vrabec et al. [254, 258]. Die Anpassung des ungleichen Lennard-Jones Energieparameters kann durch einen binären Wechselwirkungsparameter ξ ausgedrückt werden. Dieser Parameter ξ ist das Verhältnis des angepassten ungleichen Lennard-Jones Energieparameters bezogen auf das geometrische Mittel der Reinstoff Lennard-Jones Energieparameter. Das geometrische Mittel der Reinstoff Lennard-Jones Energieparameter ist auch als die Berthelot-Kombinationsregel [18] bekannt.

Ein weiterer Aspekt der Untersuchung des Einfluss von ungleichen Lennard-Jones Parametern auf binäre Dampf-Flüssigkeit Gleichgewichte war die Untersuchung der Vorhersagekraft von 11 Kombinationsregeln. Tabelle 3 gibt eine Übersicht der untersuchten 11 Kombinationsregeln, die anhand von physikalischen, mathematischen und semi-empirischen Überlegungen entwickelt wurden.

Die Beurteilung dieser 11 Kombinationsregeln erfolgte im Detail mit Hilfe der Sensitivitätsanalyse der zwei Mischungen Kohlenmonoxid + Ethan und Stickstoff + Propylen. Es zeigte sich, dass keine der Kombinationsregeln in der Lage ist, den Dampfdruck generell genau wiederzugeben. Alle Kombinationsregeln beschreiben aber die Siededichte noch mit akzeptablen Abweichungen. Da für die 44 Mischungen aus früheren Arbeiten [226, 228, 258] ein optimaler ungleicher Lennard-Jones Energieparameter durch Anpassungen an einen zuverlässigen experimentellen Dampfdruck vorlag, konnten die 11 Kombinationsregeln umfassend beurteilt werden. Dazu wurden die Standardabweichungen des ungleichen Lennard-Jones Energieparameters aus der Kombinationsregel bezogen auf den optimalen angepassten Lennard-Jones Energieparameter gebildet. Diese Studie ergab, dass die Kombinationsregeln HMC, M2, SK, S und LB zu den Besseren gehören, dass aber bei der Verwendung dieser Kombinationsregeln mit Abweichungen über 25 % im

Tabelle 3: 11 Kombinationsregeln zusammen mit ihren Akronymen. Die letzte Spalte gibt an, ob der ungleiche Lennard-Jones Längenparameter über die Lorentz-Kombinationsregel [147] bestimmt wird.

Name	Akronym	Referenz	Lorentz
Lorentz-Berthelot	LB	[18, 147]	ja
Kohler	K	[121]	
Hudson-McCoubrey	HMC	[94]	
Fender-Halsey	FH	[63]	
Hiza	H	[91, 92, 93]	nein
Sikora	S	[216]	
Smith-Kong	SK	[123, 218]	
Halgren	HHG	[87]	
Waldman-Hagler	WH	[261]	
Al-Matar-Rockstraw-1	M1	[5]	
Al-Matar-Rockstraw-2	M2	[5]	

Dampfdruck zu rechnen ist.

Da sich gezeigt hatte, dass die Verwendung von Kombinationsregeln keine quantitative Beschreibung von Mischungsdaten garantiert, wurde das bewährte Modellierungskonzept für ungleiche Lennard-Jones Parameter auf 32 binäre Mischungen mit einer Wasserstoffbrücken bildenden Komponente aus dieser Arbeit und einer nicht Wasserstoffbrücken bildenden Komponente [227, 255] angewandt. Solche Mischungen können als eine Messlatte in der thermodynamischen Modellierung betrachtet werden, da gleichzeitig starke und schwache Wechselwirkungen vom Modell richtig wiedergegeben werden müssen.

Für die nicht Wasserstoffbrücken bildende Komponente wurden Modelle vom Potentialtyp 1CLJ [255], 2CLJQ [255] und 2CLQD [227] verwendet. Aufgrund der unsymmetrischen Modellierung der Wasserstoffbrücken bildenden Komponente liegen bei solchen binären Mischungen mehrere ungleiche Lennard-Jones Paarungen vor. Die Anpassung des ungleichen Lennard-Jones Energieparameters erfolgte aber nur durch einen binären Wechselwirkungsparameter ξ , um den Polarisationsseffekten in Mischungen Rechnung zu tragen. Es hätte auch für jeden Lennard-Jones Energieparameter jeweils ein eigenes ξ verwendet werden können, was aber hier nicht untersucht wurde.

Ein weiterer Aspekt dieser Mischungsstudie war, ob der binäre Wechselwirkungsparameter ξ nicht nur an einen experimentellen Dampfdruck, sondern auch an eine experimentelle Henrykonstante angepasst werden kann. Ergebnis dieser Mischungsstudie war, dass die Anpassung an Dampfdruck oder Henrykonstante gegeneinander austauschbar ist, solange die experimentellen Daten zuverlässig sind. Es zeigte sich, dass eine in sich thermodynamisch konsistente Vorhersage von Dampfdrücken bei verschiedenen Flüssigkeitszusammensetzungen und Isothermen, von Dampfzusammensetzungen und von Hen-

rykonstanten bei verschiedenen Temperaturen mit nur einem angepassten Zustandspunkt unabhängigen binären Wechselwirkungsparameter ξ möglich ist.

Da sich in Reinstoffen und Mischungen durch die Wasserstoffbrücken bildende Komponente charakteristische Strukturen ausbilden, war zu klären, ob mit dem einfachen, rechenzeiteffizienten molekularen Modellierungsansatz die Struktur in Fluiden abgebildet werden kann. Die Untersuchungen zur Struktur in Fluiden mit molekularen Simulationen wurden in der vorliegenden Arbeit exemplarisch für Methanol durchgeführt.

Radiale Paarverteilungsfunktionen geben das Verhältnis der lokalen Dichte zweier Atomkerne im Verhältnis zur makroskopischen Dichte abhängig von Nukleiarabstand an. Radiale Paarverteilungsfunktionen sind also eine Schlüsselgröße bei der Charakterisierung der Struktur in Materie. Für reines Methanol wurden radiale Paarverteilungsfunktionen aus Neutronenbeugungsexperimenten von Yamaguchi et al. [277, 278] bei 193.15 K und 298.15 K bestimmt. Da das neue Methanolmodell wegen der Verwendung des united-atom Ansatzes aus drei Wechselwirkungszentren besteht, konnten 6 radiale Paarverteilungsfunktionen aus Simulation [206] und Experiment [277, 278] miteinander verglichen werden. Die guten Übereinstimmungen zeigen, dass mit dem molekularen Modellierungsansatz für die Wasserstoffbrücke die Struktur in Reinstoffen abgebildet werden kann.

In der Literatur konnte für die relevanten Mischungen von dieser Arbeit keine radialen Paarverteilungsfunktionen gefunden werden. Aus spektroskopischen Daten kann jedoch die Menge der Wasserstoffverbrückungen quantifiziert werden. Allerdings sind die in der Literatur verfügbaren Daten nicht ausreichend genug, um umfassende Studien der Wasserstoffverbrückung über weite Zustandsbereiche im Vergleich zu molekularen Simulationen anzustellen. Deshalb wurden eigene Nuklear magnetische Resonanz (NMR) Spektroskopien von Methanol in nah- und überkritischen Kohlendioxid durchgeführt, die mit Simulationsdaten [206] verglichen wurden. Der experimentelle Aufbau von den Messungen verwendet in dieser Arbeit ist von Maiwald et al. [156] beschrieben.

Um magnetischen Bulksuszeptibilitäten und Dichteeffekte zu kompensieren [97, 262, 263], wurden relative chemische Verschiebungen verwendet, d.h. die chemische Verschiebung der Hydroxylgruppe minus die chemische Verschiebung der Methylgruppe. Von den experimentellen relativen chemischen Verschiebungen kann direkt der Einfluss der Zustandsgrößen abgelesen werden. Mit steigender Temperatur nimmt die Anzahl an Wasserstoff verbrückten Methanolmolekülen ab. Das Gleiche gilt für abnehmende Methanolkonzentrationen. Es konnte kein Einfluss des Drucks auf die Wasserstoffverbrückung im untersuchten Druckbereich festgestellt werden. Durch Extrapolation der experimentellen Werte zu unendlich verdünnten Methanolzusammensetzungen konnte die relative chemische Verschiebung von Methanolmonomeren bestimmt werden: -3.356 ppm. Dieser Wert ist in guter Übereinstimmung zu NMR Untersuchungen von Methanol durch Asahi und Nakamura [6] sowie durch Hoffmann und Conradi [97].

Um feststellen zu können, wann eine Wasserstoffbrücke in der Simulation vorliegt, wurde das geometrische Kriterium von Haughney et al. [89] in den Simulationscode imple-

mentiert. Mit dieser Implementierung wurden Wasserstoffbrückenstatistiken von Methanol in der Simulation über praktisch den kompletten Zusammensetzungsbereich, einen weiten Temperatur- und Druckbereich berechnet. Damit mindestens 50 Methanolkoleküle in der Simulation vorliegen, mussten bei hohen Verdünnungen große Teilchenzahlen simuliert werden. In den Wasserstoffbrückenstatistiken wurde unterschieden, ob Methanolkoleküle als Protonendonator oder Protonenakzeptor fungieren. Durch einen Fit von nur zwei Zustandspunkt unabhängigen Parametern für die Wasserstoff verbrückten Spezies Protonendonator und Protonenakzeptor wurde mit der Gewichtung der verschiedenen Speziesanteilen aus den Wasserstoffbrückenstatistiken die gesamte relative chemische Verschiebung vorhergesagt. Dazu wurde auch die aus den Experimenten direkt abgeleitete relative chemische Verschiebung der Spezies Methanolmonomer verwendet.

Die exzellente Übereinstimmung mit den experimentellen relativen chemischen Verschiebungen rundet ab, dass nicht nur thermodynamische sondern auch strukturelle Stoffeigenschaften von fluiden Reinstoffen und Mischungen mit dem einfachen, rechenzeiteffizienten molekularen Modellierungsansatz für die Wasserstoffbrücke hochgenau vorhergesagt werden können.

Contents

List of Symbols	XVII
1 Introduction	1
2 Fundamentals	3
2.1 Molecular Modeling and Simulation	3
2.1.1 Reduced Quantities	3
2.1.2 Modeling of Hydrogen Bonding Components	3
2.2 Determination of Vapor-Liquid Equilibria with Molecular Simulation	8
2.2.1 Vapor-Liquid Coexistence Curves	8
2.2.2 Henry's Law Constants	10
2.3 Implementation of Electrostatic Interactions	10
2.3.1 Approximation of a Point Dipole by Point Charges	11
2.3.2 Approximation of a Linear Elongated Point Quadrupole by Point Charges	11
2.3.3 Electrostatic Long-Range Corrections	12
3 Development of Molecular Models for Pure Hydrogen Bonding Fluids	14
3.1 Parameterization Strategy	14
3.2 Methanol	16
3.3 Ethanol	21
3.4 Monomethylamine	24
3.5 Dimethylamine	29
3.6 Methanethiol	32
3.7 Formic Acid	37
3.8 Summary of Molecular Models for Pure Hydrogen Bonding Fluids	43
3.9 Pilot Study of Water Models	43
3.9.1 TIP4P Model Type	44
3.9.2 TIP5P Model Type	50
3.9.3 All-Atom Model Type	55
3.9.4 Summary of the Pilot Study	56
4 Systematic Study of Lennard-Jones Based Molecular Modeling of Mixtures	58
4.1 Combining Rules	59
4.1.1 Lorentz-Berthelot (LB)	59
4.1.2 Kohler (K)	60
4.1.3 Hudson-McCoubrey (HMC)	60
4.1.4 Fender-Halsey (FH)	61

4.1.5	Hiza (H)	61
4.1.6	Sikora (S)	62
4.1.7	Smith-Kong (SK)	62
4.1.8	Halgren (HHG)	63
4.1.9	Waldman-Hagler (WH)	63
4.1.10	Al-Matar-Rockstraw (M1 and M2)	63
4.2	Case Study	64
4.3	Comprehensive Study	74
5	Molecular Simulation of Binary Hydrogen Bonding Mixtures	80
5.1	Adjustment of Unlike Dispersive Interactions	81
5.2	Mixtures with Spherical Non-polar Components	84
5.3	Mixtures with Anisotropic Quadrupolar Components	87
5.4	Mixtures of Anisotropic Dipolar Components	95
6	Structural Properties of Hydrogen Bonding Fluids	98
6.1	Radial Distribution Functions of Methanol	98
6.2	NMR-Spectroscopic Study of Methanol + Carbon Dioxide	98
6.2.1	Experimental NMR Data	101
6.2.2	Hydrogen Bonding Criteria and Types of Hydrogen Bonded Species	105
6.2.3	Hydrogen Bonding Statistics from Molecular Simulation	107
6.2.4	Comparison of Molecular Simulation Results with Experimental NMR Data	110
7	Summary	113
Appendix A	Simulation Details	115
A.1	Vapor-Liquid Equilibria of Pure Hydrogen Bonding Components	115
A.2	Vapor-Liquid Equilibria of Binary Mixtures	115
A.3	Hydrogen Bonding Statistics for Methanol in Carbon Dioxide	116
Appendix B	Simulation Results	118
B.1	Binary Vapor-Liquid Equilibria	118
B.2	Hydrogen Bonding Statistics	126
References		132

List of Symbols

Latin Symbols

a	intramolecular site-site distance
a	parameter in Equation (37)
b	parameter in Equation (37)
c	parameter in Equation (37)
e	electronic charge: $e = 1.6021 \cdot 10^{-19}$ C
f_i	$i = 0, 1, 2$ or 3 hydrogen bonded species fraction
g_{ab}	site a - site b radial distribution function
h	intramolecular site-site distance
Δh_v	molar enthalpy of vaporization
H_i	Henry's law constant of solute i
I	ionization potential
k_{ab}	binary interaction parameter
k_B	Boltzmann's constant: $k_B = 1.3806 \cdot 10^{-23}$ JK ⁻¹
m	mass
N	number of molecules
N_A	Avogadro's constant: $N_A = 6.0221 \cdot 10^{23}$ mol ⁻¹
N_j	nucleus of atom j
n	number of sites in a molecular model
p	pressure
q	point charge
Q_{zz}	linear elongated point quadrupole momentum
r	intermolecular separation distance
R	ideal gas constant: $R = 8.314$ Jmol ⁻¹ K ⁻¹
S_j	site j
T	temperature
t	time
u	pair potential
V	volume
x_i	liquid phase mole fraction of component i
y_i	gas phase mole fraction of component i
z	generalized property

Greek Symbols

α	polarizability
α	angle between sites
β	angle of alignment for a hydrogen bonding group

γ	angle between sites
δ	relative chemical shift between signals of protons in OH and CH ₃ group
δ_i	chemical shift of group i
δ	relative deviation
η	binary size interaction parameter
ϵ	Lennard-Jones energy parameter
ϵ_0	permittivity of vacuum: $\epsilon_0 = 8.8541 \cdot 10^{-12} \text{ C}^2\text{J}^{-1}\text{m}^{-1}$
μ	dipole momentum
μ_i	chemical potential of component i
ξ	binary interaction parameter
ρ	molar density
σ	Lennard-Jones size parameter
ψ_i	potential energy of test particle i

Vector and Tensor Properties

a	point charge separation vector
Q	traceless quadrupole tensor
μ	point dipole vector

Subscripts and Superscripts

A	proton acceptor
a	site index
aa	related to site a – site a interactions
ab	related to site a – site b interactions
b	site index
bb	related to site b – site b interactions
C	carbon atom
c	related to the internal hard-sphere cutoff
c	critical
D	proton donor
exp	experimental data
H	hydrogen atom
i	related to molecule i
M	monomer
MeOH	methanol
O	oxygen atom
OH	hydroxyl group
ref	reference data

sim	molecular simulation data
*	reduced property
'	property of saturated liquid phase
"	property of saturated vapor phase
—	average property
∞	infinite dilution

Abbreviations / Chemical Formulae

1CLJ	spherical and non-polar one-center Lennard-Jones potential
2CLJD	symmetric two-center Lennard-Jones potential with a pointdipole
2CLJQ	symmetric two-center Lennard-Jones potential with a pointquadrupole
A	electronegative atom of a hydrogen bonding group
AH	hydrogen bonding group
Ar	argon
B	electronegative atom of a hydrogen bonding group
C ₂ F ₆	hexafluoroethane
C ₂ H ₂	ethyne
C ₂ H ₄	ethene
C ₂ H ₆	ethane
C ₃ H ₆	propylene
C ₃ H ₆ O	acetone
C ₃ H ₆ O ₂	methyl acetate
C ₃ H ₈	propane
C ₄ H ₈	isobutene
C ₄ H ₁₂	<i>n</i> -butane
C ₆ H ₁₄	<i>n</i> -hexane
CBMC	coupled-decoupled configurational-bias Monte Carlo
CH	methylene group
CH ₂	methylene group
CH ₃	methyl group
CH ₃ Cl	methyl chloride
CH ₄	methane
CHCl ₃	chloroform
CF ₄	tetrafluoromethane
Cl ₂	chlorine
CO	carbon monoxide
CO ₂	carbon dioxide

DIPPR	Design Institute for Physical Property Data
DMA	dimethylamine
FH	Fender-Halsey
GCMC	grand-canonical histogram-reweighting Monte Carlo
GEMC	Gibbs ensemble Monte Carlo
H	hydrogen atom
H	Hiza's combining rule
HHG	Halgren's combining rule
HLC	Henry's law constant
HMC	Hudson-McCoubrey's combining rule
K	Kohler's combining rule
Kr	krypton
LB	Lorentz-Berthelot combining rule
LJ	Lennard-Jones 12-6
M1	Al-Matar-Rockstraw's functional combining rule
M2	Al-Matar-Rockstraw's specific combining rule
MMA	monomethylamine
MTBE	methyl <i>tert</i> -butyl ether
N ₂	nitrogen
Ne	neon
NH	secondary amine group
NH ₂	primary amine group
NMR	nuclear magnetic resonance
<i>NpT</i>	ensemble with constant particle number, pressure and temperature
<i>NVT</i>	ensemble with constant particle number, volume and temperature
O ₂	oxygen
OH	hydroxyl group
R12	dichlorodifluoromethane
R125	pentafluoroethane
R134a	1,1,1,2-tetrafluoroethane
R143a	1,1,1-trifluoroethane
R152a	1,1-difluoroethane
R22	difluorochloromethane
R227ea	1,1,1,2,3,3,3-heptafluoropropane
R23	trifluoromethane
R32	difluoromethane
RGEMC	reaction Gibbs ensemble Monte Carlo
RMS	root mean square
S	Sikora's combining rule
SH	thiol group

SK	Smith-Kong's combining rule
TMS	tetramethylsilane
VLE	vapor-liquid equilibria
WH	Waldman-Hagler's combining rule
Xe	xenon
μVT	ensemble with constant chemical potential, volume and temperature

1 Introduction

Molecular modeling and simulation are applied both in academia and industry due to their suitability to investigate numerous phenomena and their excellent predictive power. The predictive power of molecular methods is based on their sound physical background, i.e., the description of molecular interactions, which are evaluated by molecular simulation. From the simulation results, macroscopic thermophysical as well as structural properties are determined with rigorous methods of statistical thermodynamics.

With classical phenomenological models of thermophysical properties accurate predictions can often be obtained only in ranges of state for which the parameters of those models were adjusted. In contrast to that, an excellent quality of the description of thermophysical properties is often found with molecular modeling and simulation even in ranges of state far away from those for which the parameters were adjusted. This is due to the physical background of molecular simulation.

The description of thermophysical properties for hydrogen bonding systems remains a challenge due to the significantly different behavior of hydrogen bonded and non-hydrogen bonded species. Phenomenological models often fail to describe the interplay between the energetics of hydrogen bonding and its structural effects. Molecular modeling and simulation is much better suited for solving that task.

The quality of a molecular model to explicitly represent the contributions of hydrogen bonding to the energy and the structure of the fluid depends on the level of detail of the employed potential functions. A reasonable balance has to be found between the quality of the molecular model to describe the physico-chemical effects of hydrogen bonding and the requirement of acceptable execution times. A frequently chosen modeling approach for hydrogen bonding was used here to develop new molecular models. This approach is based on the Lennard-Jones potential to account for repulsion and dispersion between the molecules and on point charges for polarity and hydrogen bonding. *It is the central topic of this work to show that with a suitable superposition of the point charges on the Lennard-Jones potential, hydrogen bonding can be well represented.* Apart from computational efficiency, a further benefit of this modeling approach is the compatibility with numerous Lennard-Jones based molecular models from the literature to describe mixtures.

Molecular models for non-hydrogen bonding fluids were adjusted in previous work at the institute of thermodynamics and thermal process engineering to vapor-liquid equilibria [227, 228, 255]. Those models allow an accurate description for several types of thermophysical properties such as transport properties [67, 68], Joule-Thomson inversion [259, 260] and mixture properties [226, 228, 258, 260]. Therefore, new molecular models for the hydrogen bonding fluids methanol, ethanol, monomethylamine, dimethylamine, methanethiol, formic acid and water were developed in the present work and adjusted to experimental vapor-liquid equilibria. These models were investigated regarding thermophysical and structural properties in pure fluids and mixtures.

In mixtures unlike interactions are present and interactions between molecules of different components have to be defined. In contrast to unlike electrostatic interactions, which are fully specified by physical laws, the unlike dispersive interactions are not easily accessible. For the determination of unlike dispersive interactions, i.e., unlike Lennard-Jones parameters, combining rules are frequently applied. Combining rules that use pure component quantities are fully predictive. However, previous investigations showed that such combining rules often yield inaccurate mixture properties [51, 226, 245]. Therefore, the influence of unlike Lennard-Jones parameters on binary vapor-liquid equilibria was examined here in detail and the performance of combining rules was assessed.

Another topic addressed in this work is the capability of the new molecular models for hydrogen bonding fluids to yield structural data. Structural effects due to hydrogen bonding are important in many fields like the description of thermophysical properties or biological applications. Radial distribution functions are the most characteristic structural quantities. Unfortunately, their experimental determination is not straightforward, so that experimental data for this quantity are scarce especially for mixtures. Following this, the comparison of radial distribution functions obtained from molecular simulation was carried out only for liquid methanol.

Other information on structural quantities for pure fluids and mixtures can be obtained from spectroscopic experiments, e.g., NMR, IR, NIR or Raman measurements. To extract structural data from spectroscopic data, phenomenological models are commonly applied. These phenomenological models often require a large number of parameters. The present study shows for the mixture methanol + carbon dioxide that NMR-spectroscopic data can quantitatively be described over wide state ranges by using only three state independent parameters and hydrogen bonding statistics from molecular simulation.

2 Fundamentals

Several good monographs are available on the fundamentals of molecular modeling and simulation. Thus, this chapter only briefly reviews fundamentals of molecular modeling and simulation that are necessary to understand the studies of this work. For more detailed representations, e.g., the monographs by Allen and Tildesley [4] or Frenkel and Smit [73] are recommended.

This chapter includes a discussion of the modeling approach for hydrogen bonding used here. *Since vapor-liquid equilibria of both pure fluids and mixtures are calculated in the present work with molecular simulation, the methods used here are briefly described.* Due to the chosen modeling approach for hydrogen bonding, additional types of electrostatic interactions had to be implemented in a molecular simulation code. Useful details on the implementation of electrostatic interactions are also given.

2.1 Molecular Modeling and Simulation

2.1.1 Reduced Quantities

Physical and thermodynamic properties in molecular simulation programs are commonly expressed in reduced quantities. One benefit of using reduced quantities is to avoid numerical inaccuracies and instabilities which may occur applying unreduced quantities. The conversion of unreduced properties into reduced quantities results from the use of reference quantities, i.e., reference unit length, energy and mass. These reference quantities are labeled in the following with σ^{ref} , ϵ^{ref} and m^{ref} .

The reference unit length σ^{ref} is typically in the order of 10^{-10} meter, the reference unit energy ϵ^{ref} is typically in the order of 10^{-23} Joule and the reference unit mass is typically in the order of 20 to 50 atom units.

A reduced quantity is indicated in the following with *. Table 1 gives the conversion of important properties required in molecular simulations. From these properties, the reduced form of other properties can be easily derived.

2.1.2 Modeling of Hydrogen Bonding Components

The present approach to model hydrogen bonding molecules is based on point charges superimposed on Lennard-Jones 12-6 potentials. The Lennard-Jones 12-6 potential accounts for repulsion and dispersion between pairs of molecules, where 12 indicates the power of the separation distance influence for the description of the repulsion between two molecules and 6 for the dispersion. This potential was introduced by Jones [109, 110] more than eight decades ago. In the following the term 12-6 is omitted. The Lennard-Jones (LJ) potential is used here since it is numerically advantageous in computer simulation as the contribution of the power 12 term can be simply evaluated by multiplying two times the

Table 1: Important properties in reduced quantities.

temperature	$T^* =$	$\frac{Tk_B}{\epsilon^{\text{ref}}}$
density	$\rho^* =$	$\frac{\rho\sigma^{\text{ref}}}{N_A}$
pressure	$p^* =$	$\frac{p(\sigma^{\text{ref}})^3}{\epsilon^{\text{ref}}}$
volume	$V^* =$	$\frac{V}{(\sigma^{\text{ref}})^3}$
potential energy	$u^* =$	$\frac{u}{\epsilon^{\text{ref}}}$
time	$t^* =$	$\frac{t}{\sigma^{\text{ref}}} \sqrt{\frac{\epsilon^{\text{ref}}}{m^{\text{ref}}}}$
point charge	$q^* =$	$\frac{q}{\sqrt{4\pi\epsilon_0\epsilon^{\text{ref}}\sigma^{\text{ref}}}}$
dipole moment	$\mu^* =$	$\frac{\mu}{\sqrt{4\pi\epsilon_0\epsilon^{\text{ref}}(\sigma^{\text{ref}})^3}}$
quadrupole moment	$Q^* =$	$\frac{Q}{\sqrt{4\pi\epsilon_0\epsilon^{\text{ref}}(\sigma^{\text{ref}})^5}}$

power 6 term. Furthermore, this potential requires only two parameters, i.e., the LJ size parameter σ and energy parameter ϵ . Hence, it is also advantageous for parameterization.

Another option for the description of repulsion and dispersion between two molecules is the exponential-6 potential proposed by Buckingham [29] which employs three parameters. The exponential-6 potential is obviously more laborious to be parameterized and to be numerically evaluated due to the exponential function used within this potential. Furthermore, there is generally no benefit in using of the exponential-6 potential as compared to the Lennard-Jones potential for describing thermophysical and transport properties [76]. An additional reason for using LJ based models is the straightforward combination with many molecular models proposed in the literature to simulate mixtures.

In the Lennard-Jones based molecular models for hydrogen bonding components developed in the present work, point charges are used to account for polarity and hydrogen bonding. Hence, the potential energy u between two hydrogen bonding molecules of same type is given by

$$u = \sum_{a=1}^n \sum_{b=1}^n 4\epsilon_{ab} \left[\left(\frac{\sigma_{ab}}{r_{ab}} \right)^{12} - \left(\frac{\sigma_{ab}}{r_{ab}} \right)^6 \right] + \frac{q_a q_b}{4\pi\epsilon_0 r_{ab}}, \quad (1)$$

where n is the number of sites in the molecular model, a and b are the site indices for the regarded molecule. The site-site distances between the two molecules are denoted by r_{ab} , σ_{ab} and ϵ_{ab} are the LJ size and energy parameters, q_a and q_b are the point charges located at the sites a and b . Finally, ϵ_0 is the permittivity of vacuum. The interaction between unlike LJ sites of two identical molecules is defined by the Lorentz-Berthelot combining rules [18, 147]

$$\sigma_{ab} = \frac{\sigma_{aa} + \sigma_{bb}}{2}, \quad (2)$$

$$\epsilon_{ab} = \sqrt{\epsilon_{aa}\epsilon_{bb}}. \quad (3)$$

To avoid nonphysical interactions due to the superposition of point charge and LJ potentials at very small site-site distances, which primarily may occur in Monte Carlo simulations, internal hard-sphere cutoffs at the point charge sites are employed. Such internal hard-sphere cutoffs were also used, e.g., by Lísal et al. [139] for vapor-liquid equilibrium simulations of hydrogen bonding components. However, their internal hard-sphere cutoffs were located at the LJ sites. Thus, the cutoffs chosen by Lísal et al. [139] were considerably larger than the present internal hard-sphere cutoffs, which are located directly at the point charge sites. The approach to shield electrostatic sites directly with an internal hard-sphere cutoff located at the electrostatic site was previously used by Möller and Fischer [165] as well as by Stoll [228]. The diameter of an internal hard-sphere cutoff located at site a is termed σ_{aa}^c in the following. The diameter of the internal hard-sphere cutoff σ_{ab}^c between unlike point charges is set to the arithmetic mean of the diameter for the like internal hard-sphere cutoff σ_{aa}^c and σ_{bb}^c . During a simulation, the pair potential between molecules i and j is set to infinity, if r_{ab} is less than σ_{ab}^c , cf. Figure 1.

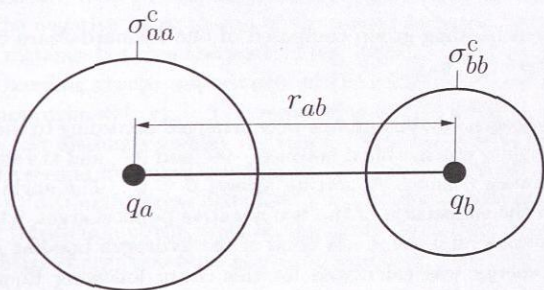


Figure 1: Diameters for the internal hard-sphere cutoff σ_{aa}^c of site a on molecule i and σ_{bb}^c of site b on molecule j directly located at the point charges q_a and q_b , respectively.

Hydrogen bonding occurs typically between a hydrogen atom H, which is bonded to an atom A with high electronegativity, and an atom B of another molecule, which provides

one lone-pair of electrons. A hydrogen bond can be illustrated by $A-H \cdots B$, where A and B are usually of the chemical element type O, N, S or F. However, also weakly electronegative chemical elements like carbon atoms can be bonded to a hydrogen atom which acts as a proton donor, e.g., as can be found in formic acid [106, 199]. A more detailed description of the chemical nature of hydrogen bonds is given, e.g., by Atkins and Paula [12].

In the following, results from a case study carried out in the present work are described which show that hydrogen bonds can reasonably be represented by point charges superimposed on Lennard-Jones sites. Figure 2 depicts the studied hydrogen bonding group. The position of the negative point charge q_- coincides with the Lennard-Jones center ($\epsilon_{AH}, \sigma_{AH}$), i.e. the negative point charge is concentrically arranged. The positive point charge q_+ is positioned excentrically with a distance h to the center of the Lennard-Jones potential, cf. Figure 2.

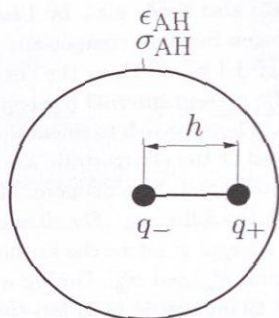


Figure 2: Hydrogen bonding group composed of one Lennard-Jones center ($\epsilon_{AH}, \sigma_{AH}$) and two point charges (q_-, q_+).

Two of those hydrogen bonding groups were arranged according to the geometry shown in Figure 3. The angle γ was modified between -90° and 90° , and the separation distance r_{ab} was altered between 0 and 9 Å, setting always $\beta = 0^\circ$. The angle α represents the alignment between the connection of the two negative point charges, which represent the electronegative atoms A, and the A—H bond of the hydrogen bonding group.

The potential energy was calculated for this setup following Equation (1). Thus, four point charge and one Lennard-Jones interaction were evaluated at each position. Following the argumentation of Section 2.1.1, reduced quantities were used. The reference unit length was chosen to $\sigma^{\text{ref}} = 3 \text{ \AA}$ and the reference unit energy to $\epsilon^{\text{ref}}/k_B = 100 \text{ K}$. Employing the potential parameters of the ethanol hydroxyl group introduced in Section 3.3 for the hydrogen bonding group, the reduced potential energy u^* was determined at the arrangements described above. The results for u^* are given as a three-dimensional

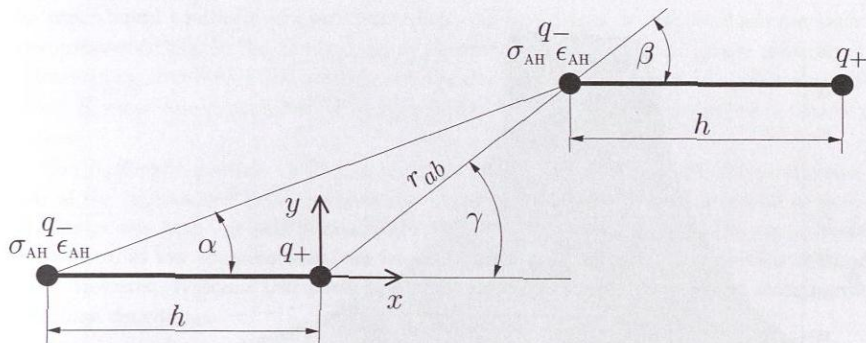


Figure 3: Arrangement of two hydrogen bonding groups modeled by LJ sites, negative and positive point charges which are concentrically and excentrically superimposed on the LJ sites.

plot in Figure 4 in the coordinate system defined by Figure 3. Haughey et al. [89] found that one constraint for hydrogen bonding between hydroxyl groups is that the angle α is smaller than 30° . Therefore, this constraint is indicated as a solid bold line in Figure 4.

For angles α smaller than 30° , a deep energetic well exists, cf. Figure 4. The probability of finding the negative point charge of the second hydrogen bonding group in this well is high. The distance between the positive and negative point charge of the first and second hydrogen bonding group, respectively, at the equilibrium position (deepest point of the well) is at approximately $r_{ab}^* \approx 1$ corresponding to 3 \AA , which is in a physically reasonable range [89]. At distinctly smaller distances, the probability of finding the negative point charge of the second hydrogen bonding group is small since the LJ potential yields strong repulsion. At distinctly larger distances, the potential is predominately determined by the Coulombic interaction of the point charges since the LJ potential diminishes more rapidly than the point charge potential as can be seen from Equation (1).

The plot in Figure 4 shows that describing hydrogen bonds in the simple way chosen here comprises the essential features of hydrogen bonding: strong short range forces at specific orientations. Other approaches for modeling hydrogen bonding such as the Lennard-Jones 12-10 potential, which is employed in CHARMM models [28], were not investigated in this work.

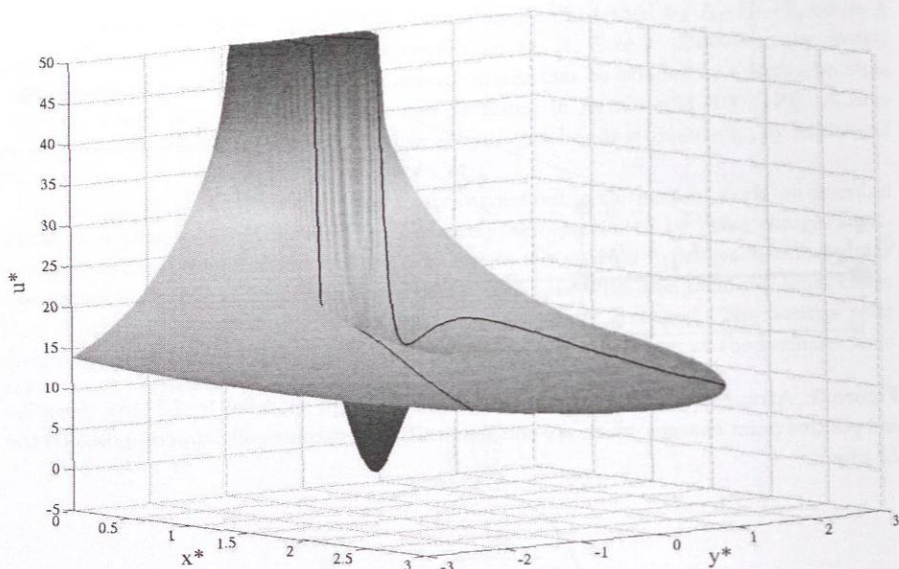


Figure 4: Reduced potential u^* between two hydrogen bonding groups according to Figure 3. The solid black lines on the surface surround the area of $\alpha = \pm 30^\circ$ where typically hydrogen bonding occurs.

2.2 Determination of Vapor-Liquid Equilibria with Molecular Simulation

2.2.1 Vapor-Liquid Coexistence Curves

For the determination of vapor-liquid equilibria with molecular simulation both for pure fluids and mixtures, methods based on Gibbs ensemble Monte Carlo (GEMC) [180] are often applied. GEMC samples the vapor and the liquid phase in two separate simulation volumes simultaneously with molecule transfer between the two phases. The disadvantage of the GEMC method for associating systems is the insertion and deletion of molecules particularly in the liquid phase. To overcome that, combinations of the GEMC method with other methods such as the coupled-decoupled configurational-bias Monte Carlo (CBMC) [215] or reaction Gibbs ensemble Monte Carlo (RGEMC) [137, 138] were proposed. However, these methods require a careful adjustment of simulation parameters to efficiently simulate associating systems. Despite this effort, long simulation times are necessary to obtain reasonable statistics.

The NpT +test particle method [162, 163, 165] is much better suited to determine

the vapor-liquid equilibria of pure fluids since the liquid and the vapor phase are simulated independently. In this method, no molecule transfer between the phases is required. Following this, the NpT -test particle method was used here throughout for the determination of vapor-liquid equilibria of pure hydrogen bonding fluids as described in Chapter 3.

The NpT -test particle method is based on the determination of the chemical potentials of the components in both vapor and liquid phase. The chemical potential of fluids at state points with low and intermediate densities, e.g., vapor close to the vapor-liquid equilibrium at low temperatures, can be determined with Widom's test particle method [269]. However, Widom's test particle method [269] yields poor statistics at state points with high densities.

In order to determine the chemical potential at state points with high density, i.e., liquid or saturated vapor at temperatures close to the critical temperature, the gradual insertion method [172, 213, 257] was applied. The gradual insertion method is based on the gradual deletion and insertion of real molecules in the simulation volume [172, 213, 257]. Simulation details for the determination of the vapor-liquid equilibrium for pure fluids can be found in Appendix A.1.

Critical values of temperature, density and pressure for a molecular model were derived following the procedure proposed by Lotfi et al. [148] using its vapor-liquid equilibrium data.

The Grand Equilibrium method [256], which was used in this work to determine the vapor-liquid equilibrium of binary mixtures, cf. Chapter 4 and 5, is also based on the separate simulation of the vapor and the liquid phase, and hence, the problems with molecule transfer do not occur. With the Grand Equilibrium method, the vapor pressure and dew point composition of mixtures can be determined at specified temperature and bubble point composition.

The first step of the Grand Equilibrium method is the simulation of the liquid phase. Therein, the chemical potential and the partial molar volume of all components are determined at specified bubble point temperature and composition as well as an estimated vapor pressure. For smaller non-associating components, Widom's test particle method [269] can be used to obtain reasonable statistics. For larger or associating components, the gradual insertion method [172, 213, 257] was applied to obtain accurate results.

In the second step of the Grand Equilibrium method, the dew point composition and the vapor pressure related to the specified temperature and bubble point composition are determined in a pseudo grand canonical (pseudo- μVT) ensemble. In this ensemble, the chemical potentials are not constant but continuously updated according to the results for the chemical potential as a function of pressure which is known from the liquid phase simulation. The vapor phase simulation converges quickly to the equilibrium pressure and composition. Only a reasonably large volume has to be chosen as starting point of the vapor simulation. Simulation details on the Grand Equilibrium method can be found in

Appendix A.2.

2.2.2 Henry's Law Constants

The solubility of a solute into a solvent is characterized by Henry's law constant. The solubility of non-hydrogen bonding solutes in hydrogen bonding solvents are discussed in Chapter 5. Several approaches were proposed in the literature [168, 200] to obtain Henry's law constants on the basis of molecular models. The Henry's law constant is related to the residual chemical potential of the solute i at infinite dilution μ_i^∞ [214]

$$H_i = \rho RT \exp \left[\frac{\mu_i^\infty}{k_B T} \right], \quad (4)$$

where k_B is the Boltzmann constant, T the temperature and ρ the molar density of the solvent.

In order to evaluate μ_i^∞ , Molecular Dynamics simulations applying Widom's Test Particle Method [269] are often sufficient. This is due to the fact that the solute molecules are often smaller than the solvent molecules, and hence, acceptable statistics can be achieved. Therefore, test particles representing the solute i were inserted after each time step at random positions into the liquid solvent and the potential energy between the solute test particle of the solvent molecules ψ_i was calculated within the cut-off radius

$$\mu_i^\infty = -k_B T \ln \frac{\left\langle V \exp \left[\frac{-\psi_i}{k_B T} \right] \right\rangle}{\langle V \rangle}, \quad (5)$$

where V is the volume and the brackets represent the NpT ensemble average.

The residual chemical potential at infinite dilution and hence, the Henry's law constant is directly linked to the unlike solvent-solute interaction and indirectly to the solvent-solvent interaction which yields the configurations of the solvent molecules. Into these configurations, solute test particles are inserted. The mole fraction of the solute in the solvent is exactly zero, as required for infinite dilution, since the test particles are instantly removed after the potential energy calculation. Simulations were performed at the specified temperature and the according vapor pressure of the pure solvent.

2.3 Implementation of Electrostatic Interactions

The chosen approach of modeling hydrogen bonding relies on the use of point charges, cf. Equation (1). Point charge interactions were implemented in an existing object oriented FORTRAN 90 molecular simulation program named *ms2* that allows Molecular Dynamics and Monte Carlo simulation. The Molecular Dynamics part in *ms2* is efficiently parallelized with the force decomposition algorithm of Plimpton [184]. *ms2* was developed to efficiently run on parallel platforms, i.e., computer clusters and super computers including vector processors. The simulations of present work were also performed on such platforms.

The parallelization in *ms2* could be used without further programming since the *ms2* code is object oriented.

The following electrostatic interaction types were implemented in *ms2*: point charge - point charge, point charge - point dipole and point charge - linear elongated point quadrupole interactions. Note that all conventions given by Price et al. [189] were followed. The definition of the linear elongated point quadrupole moment in the equations of Price et al. [189] and those of Vrabec et al. [255], which were used in present studies, are consistent with those of Buckingham [30] and Gray and Gubbins [82]. Other authors use different definitions for the quadrupole moment. The linear elongated quadrupole moment as defined by Hirschfelder et al. [95] is two times larger than that of Buckingham [30] and Gray and Gubbins [82].

The new point charge interactions were implemented into *ms2* in such a manner that any electrostatic interaction sites can be located at any position of the molecular model so that they do not necessarily need to be situated in the center of mass. *ms2* is now capable to simulate rigid multi-center LJ, multi-center point charge, multi-center point dipole and multi-center linear elongated point quadrupole molecular models. Those molecular models can be combined to multi-component mixtures consisting of that molecular model type.

The implementation of the point charge interactions includes the equations for internal energy, forces, torques and properties such as pressure or chemical potential. The implementations were tested with approximations of point dipoles and linear elongated point quadrupoles by point charges at small distances for consistency. In the following, these approximations are described.

2.3.1 Approximation of a Point Dipole by Point Charges

Two point charges q of the same magnitude but opposite sign connected by a vector \mathbf{a} form a dipole [146]

$$\boldsymbol{\mu} = q\mathbf{a}. \quad (6)$$

These two charges can be used to approximate a point dipole situated in the middle of the vector \mathbf{a} . Numerical studies for the present work show that reasonable approximations can be obtained by setting $|\mathbf{a}|$ to 0.1 \AA even for small molecules.

2.3.2 Approximation of a Linear Elongated Point Quadrupole by Point Charges

Generally, a quadrupole of a molecule is described by a tensor. The linear elongated point quadrupole is given by a traceless quadrupole tensor \mathbf{Q} . A linear elongated point quadrupole which is aligned along the z-axis writes to

$$Q = \begin{pmatrix} -\frac{1}{2}Q_{zz} & 0 & 0 \\ 0 & -\frac{1}{2}Q_{zz} & 0 \\ 0 & 0 & Q_{zz} \end{pmatrix}, \quad (7)$$

wherein Q_{zz} is the quadrupole moment of the linear elongated point quadrupole. This moment can be approximated by three point charges $q_1, -2q_1, q_1$ at distances a_1 along the z-axis and four point charges $q_2, -q_2, -q_2, q_2$ at distances a_2 , cf. Figure 5, with

$$Q_{zz} = 2q_1 a_1^2 \quad \text{and} \quad Q_{zz} = 4q_2 a_2^2, \quad (8)$$

respectively, whereas good numerical approximations were obtained by setting $a_1 = 0.1 \text{ \AA}$ and $a_2 = 0.05 \text{ \AA}$. The position of the linear elongated point quadrupole approximated by three and four point charges is at $-2q_1$ and at half the distance between the two point charges $-q_2$, respectively, as defined by Figure 5. The sign of the quadrupole moment is positive, i.e., $Q_{zz} > 0$ for positive q_1 and q_2 , thus a point charge arrangement of $+-+.$ Q_{zz} is negative for negative q_1 or q_2 , i.e., a point charge arrangement of $-+.-.$

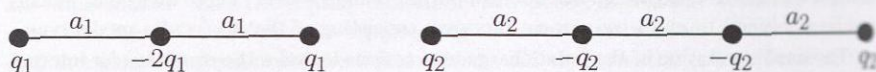


Figure 5: Arrangement of three (left) or four (right) point charges to approximate a linear elongated point quadrupole.

2.3.3 Electrostatic Long-Range Corrections

Two methods are commonly employed in molecular simulation to correct electrostatic long-range contributions of point charges and point dipoles: the Ewald summation [4, 61] and the reaction field method [4, 178]. The Ewald summation method can be employed both for charged or neutral molecules, whereas the reaction field method is only suited for the latter. For neutral molecules, however, both methods yield equivalent corrections [175]. Since the molecular models used in this work are electroneutral, the less time consuming reaction field method was applied for the molecular models used in this work.

For the reaction field method, the point charge distribution is reduced to a point dipole vector μ . For an electroneutral molecular model, it is reduced by

$$\mu = \sum_{b=1}^n (\mathbf{a}_b - \mathbf{a}_0) q_b = \sum_{b=1}^n \mathbf{a}_b q_b - \mathbf{a}_0 \underbrace{\sum_{b=1}^n q_b}_{=0} = \sum_{b=1}^n \mathbf{a}_b q_b, \quad (9)$$

where b is the point charge index of the molecular model, n the number of point charges, \mathbf{a}_b their respective position vector and \mathbf{a}_0 the position vector for an arbitrarily chosen origin of a coordinate system. The origin of the coordinate system is irrelevant for the

determination of the dipole vector as can be seen from Equation (9) since the sum of the point charges within the present molecules yields zero due to electroneutrality.

Although modifications of the plain Ewald summation technique exists as the particle-mesh Ewald method [49], the reaction field method was implemented in the *ms2* code since such modifications are still more time consuming than the reaction field method. Long-range corrections to the internal energy and the torque of a molecule are present for the reaction field method but not for the force. The linear elongated point quadrupole moment does not require long-range correction as it disappears by orientational averaging [225].

3 Development of Molecular Models for Pure Hydrogen Bonding Fluids

New molecular models were developed for the hydrogen bonding fluids methanol, ethanol, monomethylamine, dimethylamine, methanethiol and formic acid. They consist of rigid point charges superimposed on united-atom LJ potentials as described by Equation (1). This modeling approach was also used in a study for water. For all molecular models except for water, a parameterization strategy was found to be suitable which is introduced in the following section. Recently, a quite accurate model for methanol was developed by Stoll [228]. The parameters of this molecular model were improved here, not strictly following the parameterization strategy described below.

The new molecular models for hydrogen bonding fluids were adjusted to correlations of experimental vapor pressure and bubble density. These correlations are part of the DIPPR project [50, 55] and they were fitted to screened experimental data. The correlations are labeled in the following as "experimental". For testing the new molecular models, also the enthalpy of vaporization and the dew density were used. The DIPPR project contains correlations for enthalpy of vaporization, however, not for the dew density. Therefore, "experimental" dew densities were derived from the Clausius-Clapeyron equation using the correlations for bubble density, vapor pressure and enthalpy of vaporization. The dew density determined in that way is also labeled in the following as "experimental". The bubble and dew density, the vapor pressure and the enthalpy of vaporization of the new models are compared to those experimental data. In deviation plots the relative deviation of the property z is shown, this relative deviation is given by

$$\delta z = \frac{z_{\text{sim}} - z_{\text{exp}}}{z_{\text{exp}}} \quad (10)$$

From the results of the vapor-liquid equilibrium simulations, the critical temperature, density and pressure were determined following the procedure proposed by Lotfi et al. [148]. These critical properties are also compared to experimental data [50, 55]. Numerous alternative molecular models for the hydrogen bonding fluids investigated here are available in literature. For the comparison between the models of the present work and those from literature, only the best molecular model from literature regarding the description of vapor-liquid equilibria is used.

3.1 Parameterization Strategy

The new molecular models introduced in this work are rigid. The neglect of internal degrees of freedom decreases the computational effort and the number of model parameters to be determined. Other simplification to lower the computational costs and to determine only a small number of model parameters is the use of united-atom LJ sites [73] for functional groups. The idea of united-atom LJ sites is to reduce the dispersive contribution

of the functional group to one effective interaction site. E.g., the dispersive contribution of the functional methyl group in an alkane molecule can be represented by only one LJ interaction site.

The accuracy on the description of the dispersive contribution of a functional group by one LJ united-atom site was improved by the introduction of the anisotropic united-atom LJ approach by Toxvaerd [241]. The anisotropic united-atom LJ approach accounts for the asymmetrical shape of the functional group which is reduced to the effective interaction site. The position of an anisotropic united-atom site is shifted from the position of the nucleus of the large atom into the direction of the hydrogen nuclei. The position of the anisotropic united-atom site is chosen typically close to the geometric center of the functional group. The offset of the anisotropic united-atom center is an additional parameter to be determined when developing a new molecular model. The quality of molecular models significantly improves with the application of anisotropic united-atom LJ sites [241, 244]. The transferable anisotropic united-atom sites for alkanes proposed by Ungerer et al. [244] were used here for the methyl (CH_3) and the methylene (CH_2) functional groups. New anisotropic united-atom sites for the hydrogen bonding groups of the new molecular models, i.e., for the functional groups OH, NH, NH_2 , SH and CH, were parameterized in the present study.

Nuclei positions of the new hydrogen bonding molecular models except for methanol and for water were determined using the quantum chemistry software package GAMESS (US) [201] with a 6-31G basis set and the Hartree-Fock method. The point charges for a first model can principally be determined by quantum chemical calculations including ESP fits [201]. Such quantum chemical calculations require augmented basis sets, e.g., aug-cc-pVTZ. Reasonable sets of point charges are obtained by arranging the molecule into a cavity with a dielectric constant corresponding to liquid conditions. Subsequently, the Møller-Plesset level 2 method [201] was employed on such a configuration. However, the resulting point charges can serve only as a starting point for the parameterization of molecular models, since those point charges are used to describe the polarity and the hydrogen bonding of the molecule simultaneously. Since the derivation of the electrostatic quantities from such quantum chemical calculations are complex, time consuming and not straightforward, the point charges for a first molecular model were taken from models proposed in the literature in most cases.

The determination of the dispersive parameters of the molecular models by quantum chemistry calculations is not feasible since the computational effort is vast. Augmented basis sets have to be used two interacting molecules which have to be sampled at many distances and orientations. Thus, for a first molecular model the LJ parameters were taken from previous models or models from literature.

For optimizing the new molecular models, the LJ size and energy parameter σ_{ab} and ϵ_{ab} of the hydrogen bonding group, the offset of this anisotropic united-atom LJ site and the point charges of the corresponding model were adjusted to experimental vapor-liquid

equilibrium data [50, 55]. Since all models for the hydrogen bonding molecules developed in this work are electrostatically neutral, the number of point charges to be adjusted reduces by one. The model parameters were adjusted using the optimization procedure introduced by Stoll [228]. The optimization procedure of Stoll [228] is based on a Newton method which uses the experimental bubble densities and vapor pressures of the regarded pure component as target functions. The influence of the molecular model parameters on bubble density and vapor pressure is determined by varying the model parameters and forming the sensitivity of bubble density and pressure on the varied parameters with linear interpolations. Due to the non-linear dependencies of bubble density and vapor pressure on the molecular model parameters, the optimization procedure may require several iterations to find an appropriate molecular model parameter set.

3.2 Methanol

The present molecular model for methanol [206] consists of two united-atom LJ sites accounting for the dispersion and repulsion of the methyl and hydroxyl group. Point charges are located at the LJ sites and at the hydroxyl hydrogen atom, cf. Figure 6 and Table 2. Hence, the molecular model of methanol consists of three interaction sites, i.e., $n = 3$ in Equation (1). The model parameters were obtained using the model of Stoll [228] and optimizing the two point charges of the hydroxyl group. Since the geometry of the present model was not varied during the optimization, the model of Stoll [228] and the present model are identical in shape. Since the methanol model of Stoll [228] is based on the model of van Leeuwen and Smit [248], the geometry of the present methanol model is also identical with the model of van Leeuwen and Smit [248]. The geometry of the methanol model of van Leeuwen and Smit was obtained from gas-phase values of the intramolecular bond lengths and angles [248].

Simulation results for the vapor-liquid equilibrium of the new methanol model together with experimental data [50] are given in Table 3. Figures 7 to 9 depict saturated densities, vapor pressure and enthalpy of vaporization results from present molecular simulations, respectively, including the TraPPE-UA simulation data of Chen et al. [39]. In these figures, the uncertainty of the simulation is indicated by bars. Often the uncertainty is within the symbol size so that the bars are not discernable. For the determination of the TraPPE-UA simulation data, a combination of the GEMC method [180] and the CBMC algorithm [215] was used by Chen et al. [39]. The TraPPE-UA model consists of united-atoms, point charges and internal degrees of freedom.

The simulation results of the present methanol model yield mean unsigned errors compared to experimental data [50] for bubble density, vapor pressure and enthalpy of vaporization of 0.6, 1.1 and 5.5 %, respectively, in the temperature range 280 to 490 K, which is about 55 to 95 % of the critical temperature. The critical temperature, pressure and density of the present model compare favorably to the experimental data of methanol

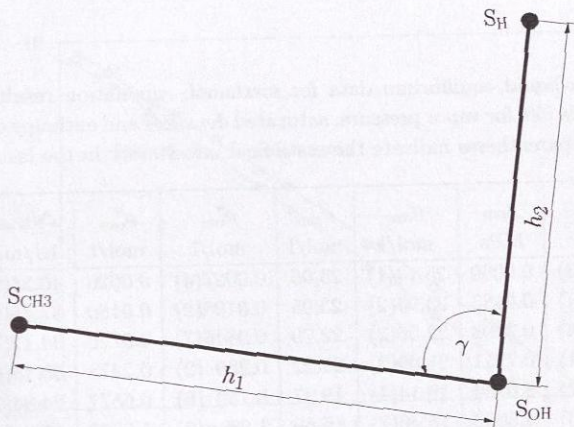


Figure 6: Geometry of the present methanol model: S_i indicates the model interaction site i .

Table 2: LJ, point charge, diameter of the internal hard-sphere cutoff and geometry parameters of the present methanol model, cf. Equation (1) with $n = 3$ and Figure 6.

Site	σ_{aa} Å	ϵ_{aa}/k_B K	q_a e	σ_{aa}^c Å
S _{CH3}	3.7543	120.592	+0.24746	1.5020
S _{OH}	3.0300	87.879	-0.67874	1.2120
S _H	0	0	+0.43128	0.4000

h_1 Å	h_2 Å	γ °
1.42460	0.94510	108.530

[50] (numbers in parentheses): $T_c = 505.87$ (512.58) K, $\rho_c = 8.70$ (8.49) mol/l and $p_c = 6.94$ (8.10) MPa.

The simulation results obtained with the model of Chen et al. [39] yield mean unsigned errors compared to experimental data [50] for bubble density, vapor pressure and enthalpy of vaporization of 2.1, 11.3 and 12.9 %, respectively. The deviations plots given in Figure 10 for bubble density, vapor pressure and enthalpy of vaporization illustrate that the new methanol model yields better agreement over the complete vapor-liquid equilibrium temperature range with experimental data than the model of Chen et al. [39].

Table 3: Vapor-liquid equilibrium data for methanol: simulation results compared to experimental data [50] for vapor pressure, saturated densities and enthalpy of vaporization. The numbers in parentheses indicate the statistical uncertainty in the last digit.

T K	p_{sim} MPa	p_{exp} MPa	ρ'_{sim} mol/l	ρ'_{exp} mol/l	ρ''_{sim} mol/l	ρ''_{exp} mol/l	$\Delta h_{v,\text{sim}}$ kJ/mol	$\Delta h_{v,\text{exp}}$ kJ/mol
280	0.0059(3)	0.0060	25.14(1)	25.06	0.0027(4)	0.0026	40.34(5)	39.75
320	0.049 (1)	0.0483	23.93(2)	23.95	0.0198(2)	0.0180	37.45(5)	38.25
360	0.226 (4)	0.2293	22.59(2)	22.70	0.0846(7)	0.0776	34.12(7)	36.13
400	0.79 (1)	0.7711	21.09(3)	21.22	0.280 (2)	0.2478	30.15(6)	33.23
440	2.02 (2)	2.0464	19.14(4)	19.37	0.769 (6)	0.6577	24.94(7)	29.20
480	4.51 (6)	4.5963	16.46(7)	16.69	1.98 (2)	1.6038	17.9 (1)	23.09

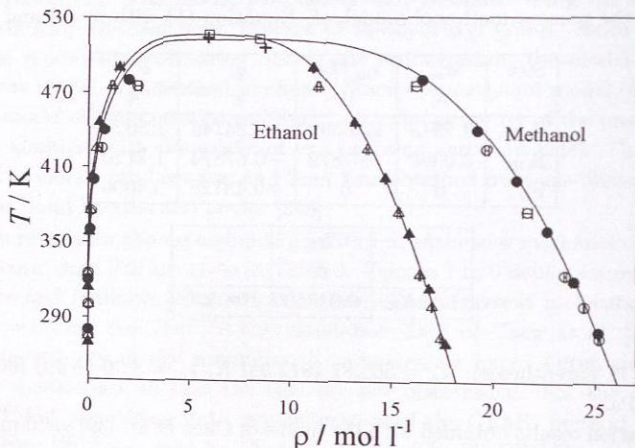


Figure 7: Saturated densities of methanol and ethanol: ● present methanol simulation data; ○ methanol simulation data of Chen et al. [39]; ▲ present ethanol simulation data; △ ethanol simulation data of Chen et al. [39]; + critical point derived from present simulation data; — experimental data [50]; □ experimental critical point [50].

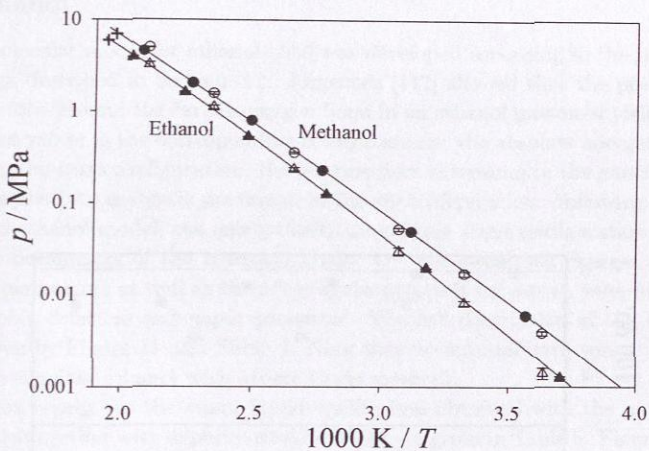


Figure 8: Vapor pressure of methanol and ethanol: ● present methanol simulation data; ○ methanol simulation data of Chen et al. [39]; ▲ present ethanol simulation data; △ ethanol simulation data of Chen et al. [39]; + critical point derived from present simulation data; — experimental data [50].

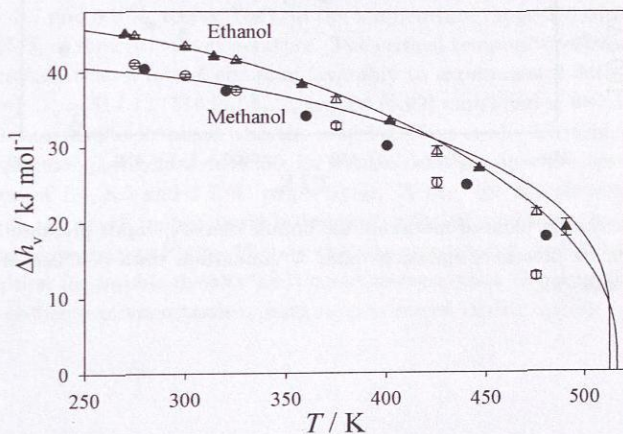


Figure 9: Heat of vaporization of methanol and ethanol: ● present methanol simulation data; ○ methanol simulation data of Chen et al. [39]; ▲ present ethanol simulation data; △ ethanol simulation data of Chen et al. [39]; — experimental data [50].

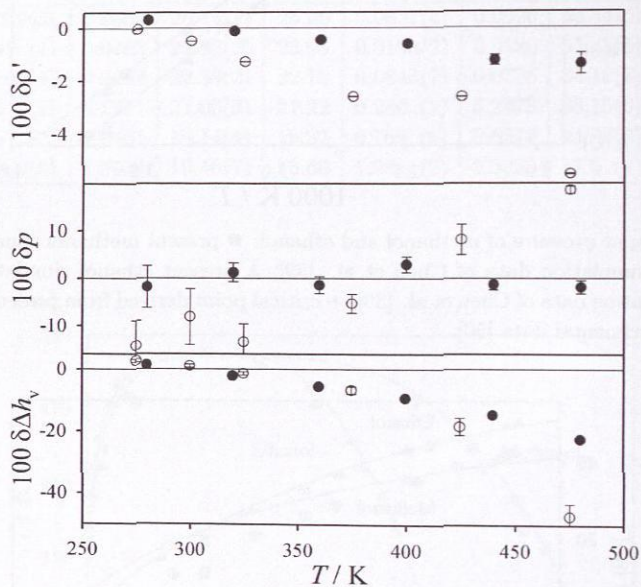


Figure 10: Deviation plots of methanol for bubble density, vapor pressure and enthalpy of vaporization: ● present simulation data; ○ simulation data of Chen et al. [39]; — experimental data [50].

3.3 Ethanol

The new molecular model for ethanol [202] was developed according to the parameterization strategy described in Section 3.1. Jorgensen [111] showed that the potential of the internal rotation around the carbon-oxygen bond in an ethanol monomer yield three energetic extreme values in the corresponding configurations: the absolute energetic minimum is reached in the *trans* configuration, the intermediate extremum in the *gauche* configuration and the absolute energetic maximum in the *cis* configuration. Following this, for the present rigid ethanol model, the energetically most likely *trans* configuration was chosen.

The five parameters of the hydroxyl group, i.e., the two point charges, the LJ size and energy parameters as well as the offset of the hydroxyl LJ center, were fitted to yield optimal bubble densities and vapor pressures. The full description of the new ethanol model is given by Figure 11 and Table 4. Note that no internal hard-sphere cutoffs were necessary to simulate ethanol with Monte Carlo methods.

Simulation results for the vapor-liquid equilibrium obtained with the new optimized ethanol model together with experimental data [50] are given in Table 5. Figures 7 to 9 depict saturated densities, vapor pressure and enthalpy of vaporization results from present molecular simulations including the TraPPE-UA simulation data of Chen et al. [39]. For the determination of the TraPPE-UA simulation data, a combination of the GEMC method [180] and the CBMC algorithm [215] was used by Chen et al. [39].

The simulation results of the present ethanol model yield mean unsigned errors compared to experimental data [50] in bubble density, vapor pressure and enthalpy of vaporization of 0.3, 3.7 and 0.9 %, respectively, in the temperature range 270 to 490 K, which is about 55 to 95 % of the critical temperature. The critical temperature, pressure and density of the present ethanol model compare favorably to experimental data [50] (numbers in parentheses): $T_c = 514.12$ (516.25) K, $\rho_c = 5.94$ (5.99) mol/l and $p_c = 5.89$ (6.38) MPa.

The simulation results obtained with the model of Chen et al. [39] yield mean unsigned errors compared to experimental data [50] for bubble density, vapor pressure and enthalpy of vaporization of 1.4, 8.5 and 1.7 %, respectively. Hence, the transferable TraPPE-UA potential shows an overall more favorable description for ethanol than that for methanol. The deviations plots given in Figure 12 show that the new ethanol model yields a distinctly better description for bubble density and vapor pressure than the model of Chen et al. [39]. For the enthalpy of vaporization, both models are of similar quality.

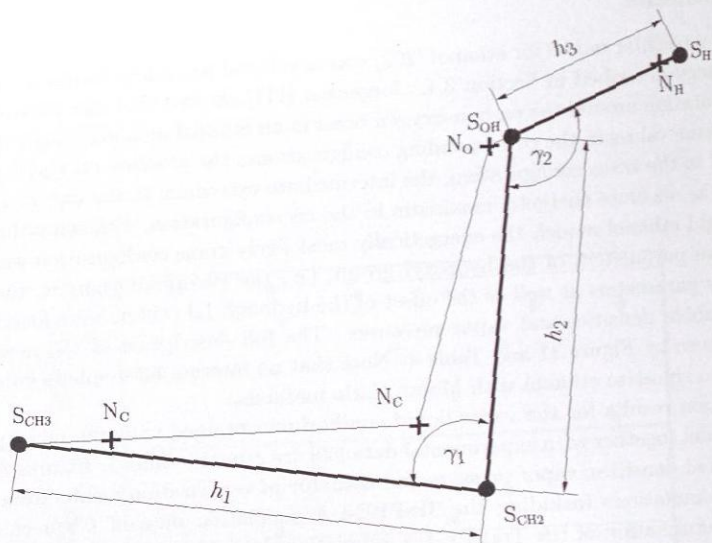


Figure 11: Geometry of the present ethanol model: S_i indicates the model interaction site i and N_j the nucleus position of atom j obtained from quantum chemistry calculations. Note that all sites of the present model are within a plane.

Table 4: LJ, point charge and geometry parameters of the present ethanol model, cf. Equation (1) with $n = 4$ and Figure 11.

Site	σ_{aa} Å	ϵ_{aa}/k_B K	q_a e
S_{CH_3}	3.6072	120.15	0
S_{CH_2}	3.4612	86.291	0.25560
S_{OH}	3.1496	85.053	-0.69711
S_H	0	0	0.44151

h_1 Å	h_2 Å	h_3 Å	γ_1 °	γ_2 °
1.98420	1.71581	0.95053	90.950	106.368

Table 5: Vapor-liquid equilibrium data for ethanol: simulation results compared to experimental data [50] for vapor pressure, saturated densities and enthalpy of vaporization. The numbers in parentheses indicate the statistical uncertainty in the last digit.

T K	p_{sim} MPa	p_{exp} MPa	ρ'_{sim} mol/l	ρ'_{exp} mol/l	ρ''_{sim} mol/l	ρ''_{exp} mol/l	$\Delta h_{v,\text{sim}}$ kJ/mol	$\Delta h_{v,\text{exp}}$ kJ/mol
270	0.00125(4)	0.00129	17.68(1)	17.64	0.0008(4)	0.00056	45.03(4)	44.78
314	0.01951(7)	0.01868	16.83(1)	16.76	0.0077(4)	0.00710	42.03(4)	42.33
358	0.1239 (5)	0.12977	15.84(1)	15.78	0.044 (1)	0.04514	38.32(4)	38.80
402	0.526 (3)	0.55451	14.66(1)	14.65	0.180 (1)	0.18623	33.40(6)	33.99
446	1.60 (3)	1.69564	13.16(2)	13.24	0.56 (1)	0.58896	27.1 (1)	27.48
490	3.88 (8)	4.08339	11.10(4)	11.14	1.5 (2)	1.68190	19.0 (1)	17.96

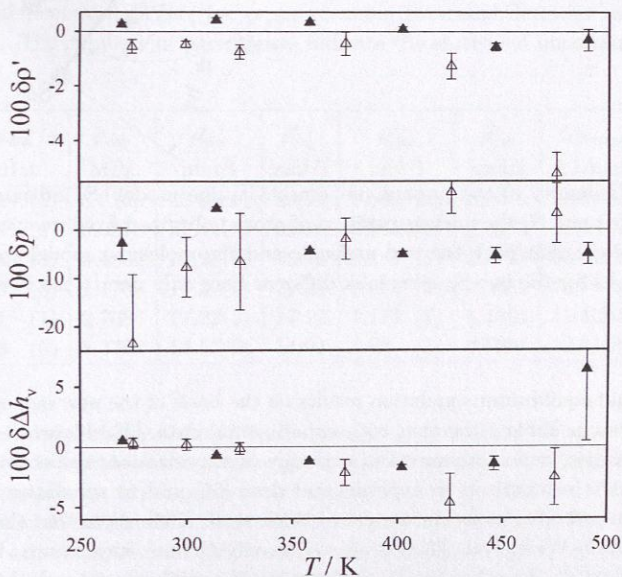


Figure 12: Deviation plots of ethanol for bubble density, vapor pressure and enthalpy of vaporization: \blacktriangle present simulation data; \triangle simulation data of Chen et al. [39]; $—$ experimental data [50].

3.4 Monomethylamine

The present molecular model for the primary amine monomethylamine [207] was developed following the parameterization strategy described in Section 3.1. To describe the intermolecular interactions of monomethylamine, two LJ sites were used, one for the methyl group (CH_3) [244] and one for the primary amine (NH_2) group. For polarity and hydrogen bonding, point charges were located in the core of the LJ spheres as well as on the two hydrogen site positions of the primary amine group. In total, the molecular model consists of two LJ and four point charge sites, i.e., $n = 4$ in Equation (1). The geometry and the potential parameters of the new monomethylamine model are given by Figure 13 and Table 6.

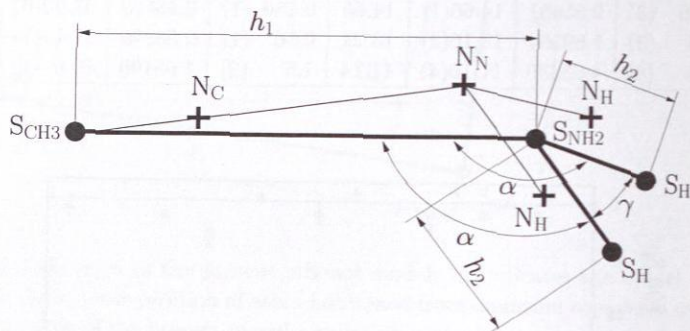


Figure 13: Geometry of the present monomethylamine model: S_i indicates the model interaction site i and N_j the nucleus position of atom j obtained from quantum chemistry calculations. Note that both the real molecule and the molecular model are not planar. Hence, α and h_2 for the two S_H sites look different here only due to the two-dimensional projection.

Vapor-liquid equilibrium simulation results on the basis of the new monomethylamine model are given in Table 7 together with experimental data [50]. Figures 14 to 16 show saturated densities, vapor pressure and enthalpy of vaporization, respectively, from the present model in comparison to experimental data [55] and to simulation data on the basis of the transferable molecular model of Wick et al. [268]. Note that the enthalpy of vaporization from Wick et al. [268] is accessible only at one temperature. However, the model of Wick et al. describes the other vapor-liquid equilibria very well throughout the full temperature range, cf. Figures 14 and 15. It is more complex as it follows the all-atom approach and the internal degrees of freedom are considered. Due to the larger number of sites, it requires a higher computational effort as 41 site-site interactions have to be evaluated per molecule-molecule interaction in simulation instead of 20 for the present

Table 6: LJ, point charge and geometry parameters of the present monomethylamine model, cf. Equation (1) with $n = 4$ and Figure 13.

Site	σ_{aa} Å	ϵ_{aa}/k_B K	q_a e
S _{CH3}	3.6072	120.150	+0.19525
S _{NH2}	3.3151	142.147	-0.88653
S _H	0	0	+0.34564

h_1 Å	h_2 Å	α °	γ °
1.78615	1.01778	111.994	105.920

model.

Table 7: Vapor-liquid equilibrium data for monomethylamine: simulation results compared to experimental data [55] for vapor pressure, saturated densities and enthalpy of vaporization. The numbers in parentheses indicate the statistical uncertainty in the last digit.

T K	p_{sim} MPa	p_{exp} MPa	ρ'_{sim} mol/l	ρ'_{exp} mol/l	ρ''_{sim} mol/l	ρ''_{exp} mol/l	$\Delta h_{v,\text{sim}}$ kJ/mol	$\Delta h_{v,\text{exp}}$ kJ/mol
230	0.0148(4)	0.0138	23.85(1)	23.71	0.0077(2)	0.0072	28.79(2)	28.35
266	0.1057(6)	0.0978	22.44(1)	22.40	0.0470(6)	0.0454	26.44(5)	26.16
302	0.440 (3)	0.4032	20.97(1)	20.93	0.187 (1)	0.1727	23.71(2)	23.67
338	1.230 (5)	1.1735	19.27(1)	19.23	0.503 (2)	0.4861	20.75(3)	20.71
374	2.81 (1)	2.7086	17.22(3)	17.12	1.171 (7)	1.1581	17.12(4)	16.94
410	5.63 (6)	5.3392	14.51(6)	13.99	2.60 (3)	2.7097	12.11(8)	11.17

Compared to experimental data [55], the present monomethylamine model yields mean unsigned errors in bubble density, vapor pressure and enthalpy of vaporization of 0.6, 6.5 and 0.7 %, respectively, in the temperature range from 210 to 410 K, which is about 50 to 95 % of the critical temperature. The critical temperature, density and pressure compare favorably to experimental data [55] (numbers in parentheses): $T_c = 430.29$ (430.05) K, $\rho_c = 8.16$ (6.49) mol/l and $p_c = 7.71$ (7.46) MPa. The experimental critical density of 6.49 mol/l was estimated by the method of Fedors [62] and was "accepted" by DIPPR [55]. Another estimated critical density of 8.00 mol/l [74], which was not accepted by DIPPR, is close to the present result. It should be pointed out that both the present result and that from Frenkel [74] are supported by the rectilinear diameter derived from

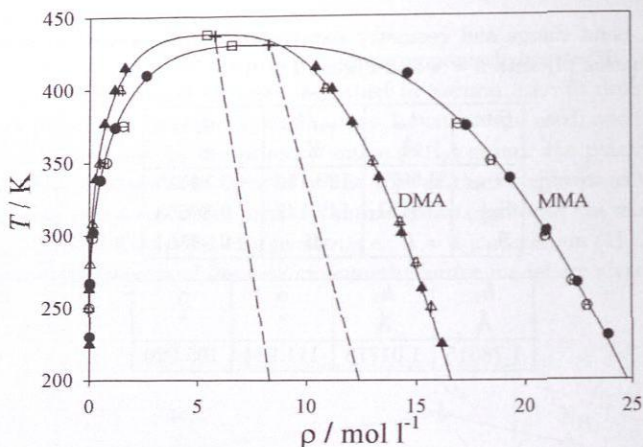


Figure 14: Saturated densities of mono- and dimethylamine (MMA and DMA): ● present MMA simulation data; ○ MMA simulation data of Wick et al. [268]; ▲ present DMA simulation data; △ DMA simulation data of Wick et al. [268]; + critical point derived from present simulation data; □ experimental critical point [55]; — experimental data [55]; - - - rectilinear density derived from experimental data.

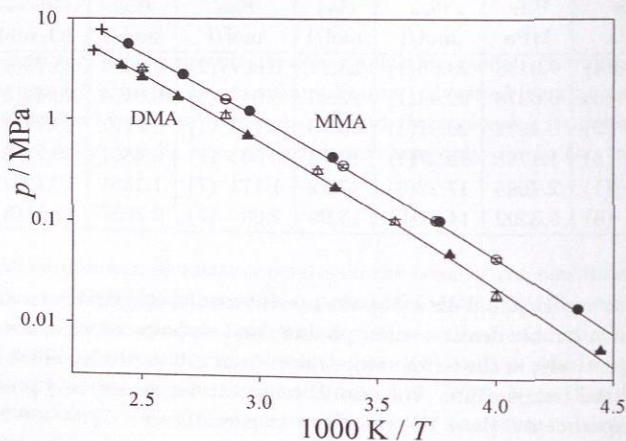


Figure 15: Vapor pressure of mono- and dimethylamine (MMA and DMA): ● present MMA simulation data; ○ MMA simulation data of Wick et al. [268]; ▲ present DMA simulation data; △ DMA simulation data of Wick et al. [268]; + critical point derived from present simulation data; — experimental data [55].

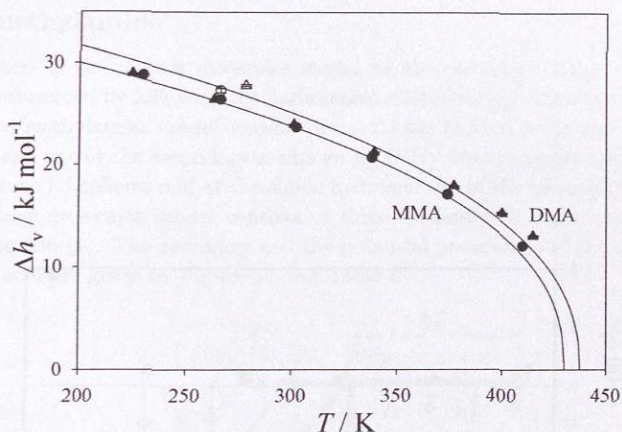


Figure 16: Heat of vaporization of mono- and dimethylamine (MMA and DMA): ● present MMA simulation data; ○ MMA simulation data of Wick et al. [268]; ▲ present DMA simulation data; △ DMA simulation data of Wick et al. [268]; — experimental data [55].

the dew and bubble density correlations from DIPPR itself, cf. Figure 14.

The simulation results obtained with the model of Wick et al. [268] yield mean unsigned errors compared to experimental data [55] for bubble density, vapor pressure and enthalpy of vaporization of 0.9, 2.1 and 4.3 %, respectively. The deviations plots in Figure 17 also show that the transferable model of Wick et al. [268] gives a worse description of the bubble density, a better description of the vapor pressures and a worse description of the enthalpy of vaporization than the present model.

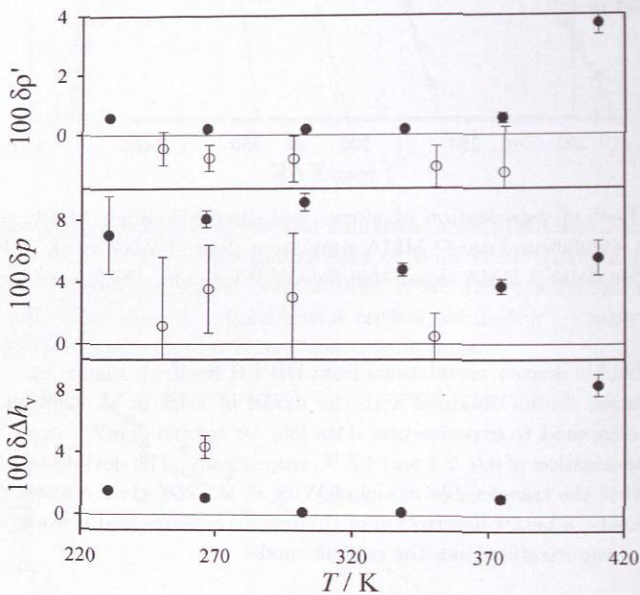


Figure 17: Deviation plots of monomethylamine for bubble density, vapor pressure and enthalpy of vaporization: ● present simulation data; ○ simulation data of Wick et al. [268]; — experimental data [55].

3.5 Dimethylamine

The parameters of the present molecular model for the secondary amine dimethylamine [207] were determined by following the parameterization strategy described in Section 3.1. The present dimethylamine model consists of one LJ site at each of the two methyl groups (CH_3) [244] and one at the secondary amine group (NH). Point charges are located in the core of the three LJ spheres and at the single hydrogen site of the secondary amine group. Hence, the new molecular model consists of three LJ and four point charge sites, i.e., $n = 4$ in Equation (1). The geometry and the potential parameters of the dimethylamine molecular model are given by Figure 18 and Table 8.

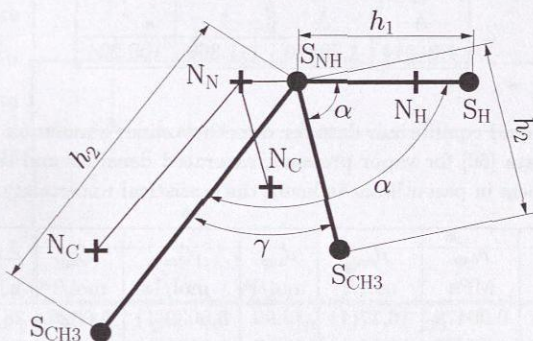


Figure 18: Geometry of the present dimethylamine model: S_i indicates the model interaction site i and N_j the nucleus position of atom j obtained from quantum chemistry calculations. Note that both the real molecule and the model are not planar. Hence, α and h_2 look different here only due to the two-dimensional projection.

Vapor-liquid equilibrium simulation results for the new dimethylamine model are given in Table 9. Figures 14 to 16 show saturated densities, vapor pressure and enthalpy of vaporization in comparison to experimental data [55] and to the results of the transferable potential of Wick et al. [268]. As before for monomethylamine, the enthalpy of vaporization from the model of Wick et al. [268] is accessible only for one temperature and the other vapor-liquid equilibrium properties are described well, cf. Figures 14 and 15. The model of Wick et al. [268] is more complex than the present dimethylamine model as it follows the all-atom approach and it uses internal degrees of freedom. Due to the larger number of sites, it requires a considerably higher computational effort as 97 site-site interactions have to be evaluated per molecule-molecule interaction in simulation instead of 25 for the present model.

The simulation results of the present dimethylamine model yield mean unsigned errors compared to experimental data [55] in bubble density, vapor pressure and enthalpy of

Table 8: LJ, point charge and geometry parameters of the present dimethylamine model, cf. Equation (1) with $n = 4$ and Figure 18.

Site	σ_{aa} Å	ϵ_{aa}/k_B K	q_a e
S _{CH3}	3.6072	120.150	+0.03774
S _{NH}	3.4800	72.856	-0.45959
S _H	0	0	+0.38411

h_1 Å	h_2 Å	α °	γ °
1.01844	1.70196	111.368	108.924

Table 9: Vapor-liquid equilibrium data for dimethylamine: simulation results compared to experimental data [50] for vapor pressure, saturated densities and enthalpy of vaporization. The numbers in parentheses indicate the statistical uncertainty in the last digit.

T K	p_{sim} MPa	p_{exp} MPa	ρ'_{sim} mol/l	ρ'_{exp} mol/l	ρ''_{sim} mol/l	ρ''_{exp} mol/l	$\Delta h_{v,sim}$ kJ/mol	$\Delta h_{v,exp}$ kJ/mol
225	0.00578(7)	0.00479	16.17(1)	16.09	0.0030(1)	0.0026	28.95(2)	30.24
263	0.0497 (3)	0.04607	15.26(1)	15.27	0.0231(1)	0.0214	26.47(1)	27.82
301	0.221 (1)	0.22436	14.30(1)	14.35	0.0936(4)	0.0944	24.02(1)	25.07
339	0.702 (2)	0.71760	13.24(1)	13.29	0.2831(7)	0.2894	21.30(2)	21.84
377	1.667 (5)	1.75403	11.99(1)	11.98	0.682 (3)	0.7300	17.97(3)	17.77
400	2.61 (1)	2.75416	11.07(2)	10.95	1.133 (8)	1.2416	15.35(5)	14.51
415	3.40 (3)	3.59644	10.32(2)	10.06	1.61 (1)	1.7979	13.09(7)	11.70

vaporization of 0.4, 6.2 and 4.9 %, respectively. This holds for the temperature range from 220 to 415 K, which is about 50 to 95 % of the critical temperature. The critical temperature, density and pressure of the present molecular model compare favorably to experimental data [55] (numbers in parentheses): $T_c = 436.73$ (437.65) K, $\rho_c = 5.74$ (5.35) mol/l and $p_c = 4.81$ (5.21) MPa.

The simulation results obtained with the model of Wick et al. [268] yield mean unsigned errors compared to experimental data [55] for bubble density, vapor pressure and enthalpy of vaporization of 0.7, 12.4 and 3.8 %, respectively. The deviation plots in Figure 19 show that the bubble density is described by both models well with slight advantages for the present model. At temperatures higher than about 300 K, the vapor pressure is described by the new model significantly more accurate than that of Wick et al. [268]. At the only

point where a comparison is possible, the enthalpy of vaporization is represented by both models with the same quality, cf. Figure 19.

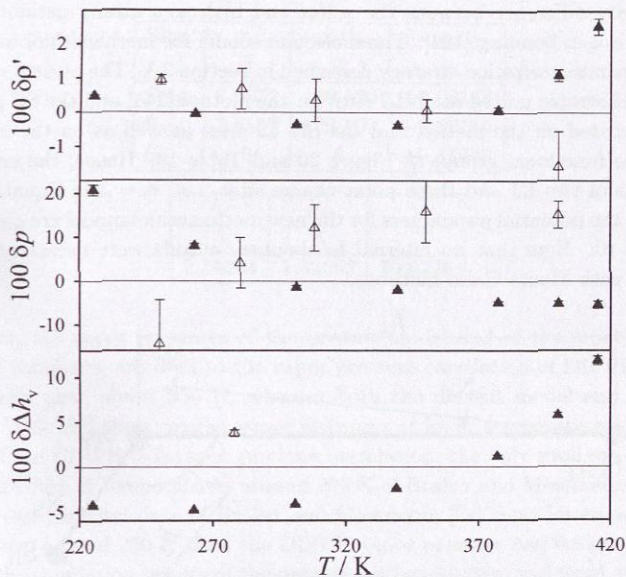


Figure 19: Deviation plots of dimethylamine for bubble density, vapor pressure and enthalpy of vaporization: ● present simulation data; ○ simulation data of Wick et al. [268]; — experimental data [55].

3.6 Methanethiol

Methanethiol is the shortest molecule in the series of alkanethiols. Due to the small electronegativity difference between the sulfur and hydrogen atom, methanethiol shows only weak hydrogen bonding [124]. The molecular model for methanethiol was developed following the parameterization strategy described in Section 3.1. The present methanethiol model uses anisotropic united-atom LJ sites for the methyl [244] and the SH group. Point charges are located on the methyl and the SH LJ sites as well as on the hydrogen site position of the functional group, cf. Figure 20 and Table 10. Hence, the new molecular model consists of two LJ and three point charge sites, i.e., $n = 3$ in Equation (1). The geometry and the potential parameters for the new methanethiol model are given by Figure 20 and Table 10. Note that no internal hard-sphere cutoffs were necessary to simulate methanethiol with Monte Carlo methods.

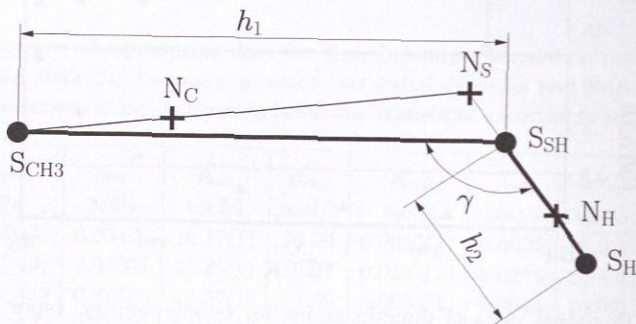


Figure 20: Geometry of the present methanethiol model: S_i indicates the model interaction site i and N_j the nucleus position of atom j obtained from quantum chemistry calculations.

Simulation results for the vapor-liquid equilibrium obtained with the new methanethiol model together with experimental data [55] are given in Table 11. Figures 21 to 23 depict the saturated densities, the vapor pressure and the enthalpy of vaporization of the present methanethiol model together with the experimental data. Figures 21 and 22 include the simulation data of a recently published united-atom transferable potential from Lubna et al. [149, 188]. For the enthalpy of vaporization, no simulation data were given. Lubna et al. [149, 188] employed the grand-canonical histogram-reweighting Monte Carlo method (GCMC) [64, 65, 186]. This more complex but transferable molecular model considers internal degrees of freedom.

The agreement between the present methanethiol model and the experimental saturated densities [55] is excellent, cf. Figure 21. The transferable model of Lubna et al. [149, 188] yields also excellent agreement with the experimental saturated densi-

Table 10: LJ, point charge and geometry parameters of the present methanethiol model, cf. Equation (1) with $n = 3$ and Figure 20.

Site	σ_{aa} Å	ϵ_{aa}/k_B K	q_a e
S _{CH3}	3.6072	120.120	+0.08143
S _{SH}	3.5557	199.100	-0.39186
S _H	0	0	+0.31043

h_1 Å	h_2 Å	γ °
2.14304	1.32662	70.0276

ties. However, the vapor pressures of the present model and of the model of Lubna et al. [149, 188] compares only well to the vapor pressure correlation of DIPPR [55] at temperatures larger than about 250 K, whereas both the present model and the model of Lubna et al. [149, 188] show smaller vapor pressures at lower temperatures, cf. Figure 22. For the fit of the DIPPR [55] vapor pressure correlation, the only available experimental vapor pressure data at temperatures around 200 K of Braker and Mossmann [24] were not used. These experimental data of Braker and Mossmann [24] show lower vapor pressures at temperatures around 200 K than the DIPPR vapor pressure correlation.

Overall, the simulation results of the present methanethiol model yield mean unsigned errors compared to experimental data [50] in bubble density, vapor pressure and enthalpy of vaporization of 0.6, 7.4 and 7.4 %, respectively, in the temperature range from 200 to 450 K, which is about 45 to 95 % of the critical temperature. The critical temperature, density and pressure compare favorably to experimental data (numbers in parentheses): $T_c = 477.29$ (469.95) K, $\rho_c = 6.86$ (6.90) mol/l and $p_c = 8.31$ (7.23) MPa.

The simulation results obtained with the model of Lubna et al. [149, 188] yield mean unsigned errors compared to experimental data [55] for bubble density and vapor pressure of 0.9 and 6.0 %, respectively. The simulation data of Lubna et al. [188] were given without simulation uncertainties and no enthalpies of vaporization were accessible. The deviations plots in Figure 24 show that both models describe the bubble density and the vapor pressure with similar quality.

Table 11: Vapor-liquid equilibrium data for methanethiol: simulation results compared to experimental data [55] for vapor pressure, saturated densities and enthalpy of vaporization. The numbers in parentheses indicate the statistical uncertainty in the last digit.

T K	p_{sim} MPa	p_{exp} MPa	ρ'_{sim} mol/l	ρ'_{exp} mol/l	ρ''_{sim} mol/l	ρ''_{exp} mol/l	$\Delta h_{\text{v,sim}}$ kJ/mol	$\Delta h_{\text{v,exp}}$ kJ/mol
200	0.0006(1)	0.00106	20.556(6)	20.435	0.0007(4)	0.0006	30.49(1)	27.99
250	0.0213(1)	0.02792	19.237(5)	19.214	0.0107(1)	0.0136	28.01(1)	25.93
300	0.1836(6)	0.21389	17.812(7)	17.867	0.0792(3)	0.0890	25.33(1)	23.54
350	0.812 (2)	0.84477	16.173(9)	16.328	0.3206(8)	0.3266	22.09(1)	20.66
400	2.419 (7)	2.31507	14.24 (2)	14.440	0.951 (3)	0.9164	17.86(3)	16.89
450	5.56 (4)	5.29546	11.80 (3)	11.562	2.50 (2)	2.7131	11.76(6)	10.56

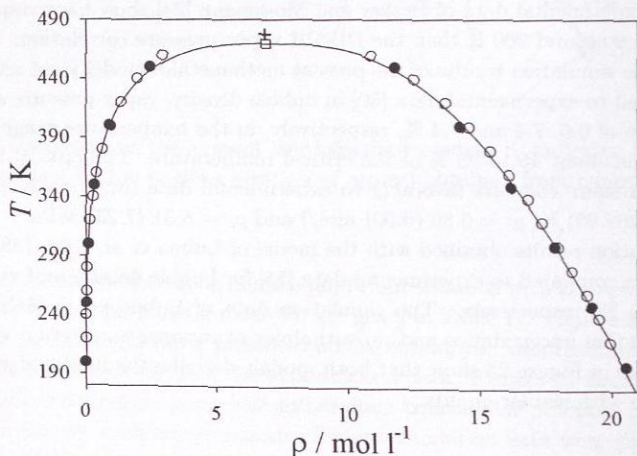


Figure 21: Saturated densities of methanethiol: ● present simulation data; ○ simulation data of Lubna et al. [149, 188]; + critical point derived from present simulation data; — experimental data [55]; □ experimental critical point [55].

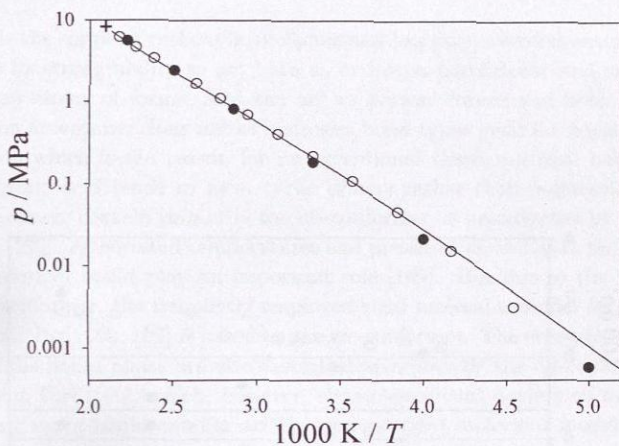


Figure 22: Vapor pressure of methanethiol: ● present simulation data; ○ simulation data of Lubna et al. [149, 188]; + critical point derived from present simulation data; — experimental data [55].

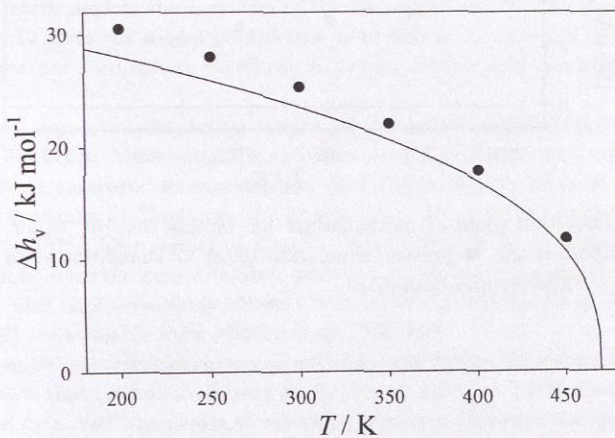


Figure 23: Heat of vaporization of methanethiol: ● present simulation data; — experimental data [55].

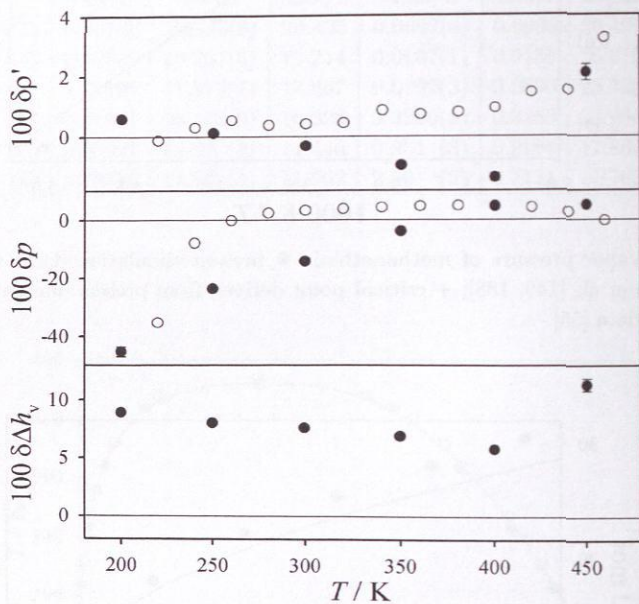


Figure 24: Deviation plots of methanethiol for bubble density, vapor pressure and enthalpy of vaporization: ● present simulation data; ○ simulation data of Lubna et al. [149, 188]; — experimental data [55].

3.7 Formic Acid

Formic acid is the simplest carboxylic molecule and has exceptional thermophysical properties due to its strong ability to act both as hydrogen bond donor and acceptor. Since both hydrogen atoms of formic acid can act as proton donors and both oxygen atoms provide proton acceptance, four unlike hydrogen bond types yield the basis for a complex self-association which is the reason for its exceptional thermophysical behavior. In the gas phase, formic acid tends to form cyclic dimers rather than polymeric chain aggregates. These dimers contain primarily the *cis*-conformer as investigated by Turi [243] and Roszak et al. [199]. At elevated temperatures and pressures as well as in the crystal phase, the *trans*-conformer could play an important role [199]. But due to the lower stability of the *trans*-conformer, the frequently employed rigid molecular model for formic acid of Jedlovsky and Turi [105, 107] is based on the *cis*-conformer. The energetic and structural properties of the liquid phase are also described favorably by the *cis*-conformer model of Jedlovsky and Turi [106], which, however, shows significant deviations to experimental data regarding vapor-liquid equilibria. The present rigid molecular model is introduced to overcome this problem. It also applies the *cis*-geometry. The parameters of the present formic acid model were determined by following the parameterization strategy described in Section 3.1.

Since the formic hydrogen atom also forms weak hydrogen bonds ($C-H \cdots O$), as investigated by Roszak et al. [199] as well as Jedlovsky and Turi [106], the positive formic hydrogen point charge was shifted into the direction of the formic hydrogen nucleus, cf. Figure 25 which depicts the positions of the interaction sites of the present molecular model. Table 12 gives the model parameters according to Equation (1). The diameters for the like internal hard-sphere cutoff of the present formic acid model are included in Table 12.

The present numerical simulation results [204] together with experimental data [55] are given in Table 13. Vapor-liquid equilibrium results of the present molecular model of formic acid are compared to experimental data [55] in Figures 26 to 28. These figures also include the results of Chialvo et al. [40] who used the molecular model of Jedlovsky and Turi [105, 107]. The results of Chialvo et al. [40] had to be extracted from the published graphs since the numerical data were not accessible. For the saturated densities in Figure 26, also Gibbs ensemble Monte Carlo results for the model of Jedlovsky and Turi [105, 107] are available from Mináry et al. [108, 160].

The present bubble densities agree well with the experiment, the mean unsigned error is only 0.8 %. Note that the bubble density of the present model at 290 K shown in Figure 26 was estimated by a NpT simulation at vanishing pressure. However, the agreement of the present dew density simulations to experimental data derived from the Clausius-Clapeyron equation is poor with a mean unsigned error of 29 %. These experimental dew densities are in good agreement with dew densities evaluated with the dimerization constant for formic acid proposed by Büttner and Maurer [33] up to 400 K. Figure 26 indicates that

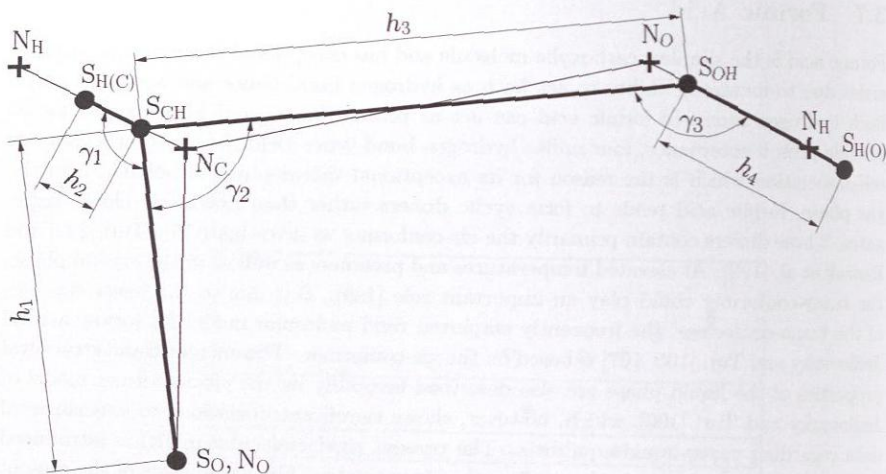


Figure 25: Geometry of the present formic acid model: S_i indicates the model interaction site i and N_j the nucleus position of atom j obtained from quantum chemistry calculations. Note that all sites of the present model are within a plane.

Table 12: LJ, point charge, diameter of the internal hard-sphere cutoff and geometry parameters of the present formic acid model, cf. Equation (1) with $n = 5$ and Figure 25.

Site	σ_{aa} Å	ϵ_{aa}/k_B K	q_a e	σ_{aa}^c Å
S_O	2.9953	96.696	-0.42186	0.2995
S_{CH}	3.2335	59.993	0	0
$S_{H(C)}$	0	0	+0.29364	0.3234
S_{OH}	3.1496	85.053	-0.31574	0.3150
$S_{H(O)}$	0	0	+0.44396	0.3150

h_1 Å	h_2 Å	h_3 Å	h_4 Å
1.21473	0.12650	1.38988	0.98023
γ_1 °	γ_2 °	γ_3 °	
125.545	120.255	110.804	

Table 13: Vapor-liquid equilibrium data for formic acid: simulation results compared to experimental data [55] for vapor pressure, saturated densities and enthalpy of vaporization. The numbers in parentheses indicate the statistical uncertainty in last digit.

T K	p_{sim} MPa	p_{exp} MPa	ρ'_{sim} mol/l	ρ'_{exp} mol/l	ρ''_{sim} mol/l	ρ''_{exp} mol/l	$\Delta h_{v,\text{sim}}$ kJ/mol	$\Delta h_{v,\text{exp}}$ kJ/mol
335	0.030(1)	0.027	25.18(2)	25.36	0.0197(1)	0.0165	18.12(8)	20.97
360	0.067(1)	0.066	24.48(3)	24.64	0.0428(3)	0.0352	17.96(7)	21.68
385	0.145(3)	0.140	23.76(2)	23.87	0.0933(5)	0.0672	17.69(7)	22.36
410	0.267(5)	0.269	22.90(3)	23.06	0.153 (1)	0.1177	17.95(9)	22.93
435	0.513(6)	0.480	22.08(3)	22.19	0.256 (1)	0.1933	18.11(8)	23.31
460	0.766(8)	0.803	21.15(3)	21.25	0.393 (2)	0.3033	18.09(7)	23.37
485	1.36 (2)	1.275	20.23(3)	20.20	0.615 (4)	0.4617	17.98(8)	22.98
510	1.92 (3)	1.937	18.96(5)	19.01	0.914 (6)	0.6933	17.01(8)	21.93
535	3.01 (6)	2.839	17.74(5)	17.58	1.36 (1)	1.0465	15.93(9)	19.99
560	4.4 (1)	4.036	16.17(7)	15.69	2.01 (2)	1.6384	14.2 (1)	16.72

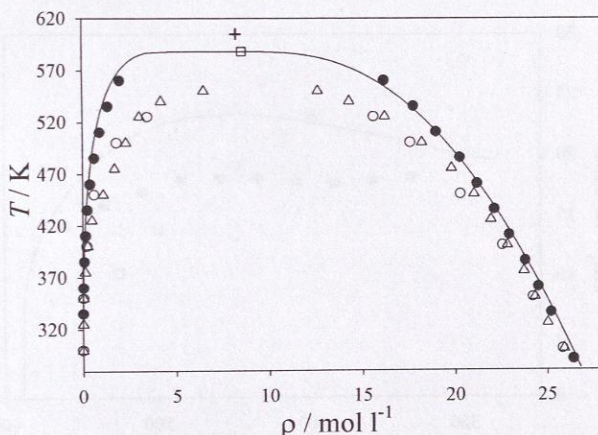


Figure 26: Saturated densities of formic acid: ● present simulation data; ○ simulation data of Chialvo et al. [40]; △ simulation data of Mináry et al. [160, 108]; + critical point derived from present simulation data; — experimental data [55]; □ experimental critical point [55].

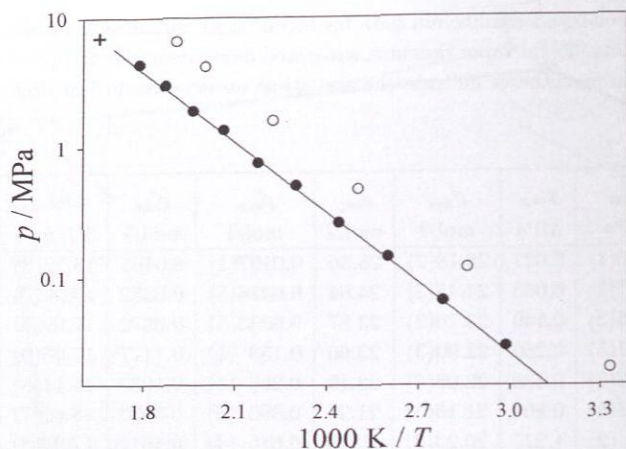


Figure 27: Vapor pressure of formic acid: ● present simulation data; ○ simulation data of Chialvo et al. [40]; + critical point derived from present simulation data; — experimental data [55].

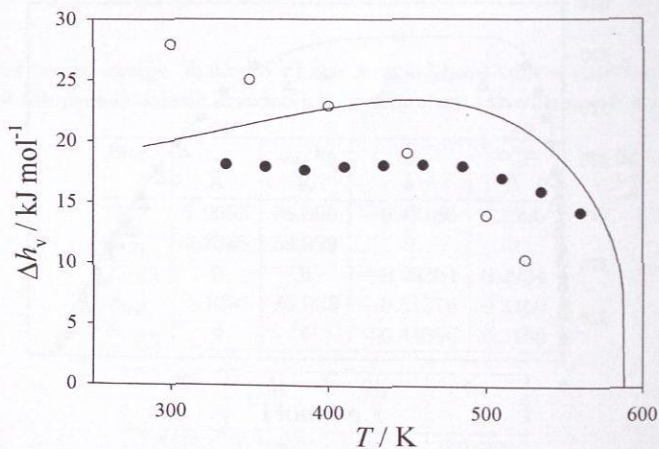


Figure 28: Heat of vaporization of formic acid: ● present simulation data; ○ simulation data of Chialvo et al. [40]; — experimental data [55].

the new molecular model is significantly more precise regarding the saturated densities than the model of Jedlovsky and Turi [105, 107].

The new molecular model is also much more accurate for the vapor pressure and the enthalpy of vaporization, cf. Figures 27 and 28. These two properties are described by the new molecular model with mean unsigned errors of 5.1 and 19.6 %, respectively. The present model predicts the unusual temperature dependence of the enthalpy of vaporization, cf. Figure 28, but the simulation results are systematically too low. It can be speculated that this is due to the inability of the present model to yield accurate vapor configurations. The critical values of temperature, density and pressure were determined (experimental value in parentheses): $T_c = 604.90$ (588.00) K, $\rho_c = 8.21$ (8.00) mol/l and $p_c = 7.02$ (5.81) MPa. The critical temperature is predicted too high predominantly due to the deviations in the dew density.

The simulation results of Chialvo et al. [40] yield mean unsigned errors compared to experimental data [55] for bubble density, vapor pressure and enthalpy of vaporization of approximately 6, 150 and 30 %, respectively. Figure 29, which depicts the deviations for these properties to experimental data [55], demonstrates the significant improvement of vapor-liquid equilibrium description with the new model when compared to the model developed by Jedlovsky and Turi [105, 107].

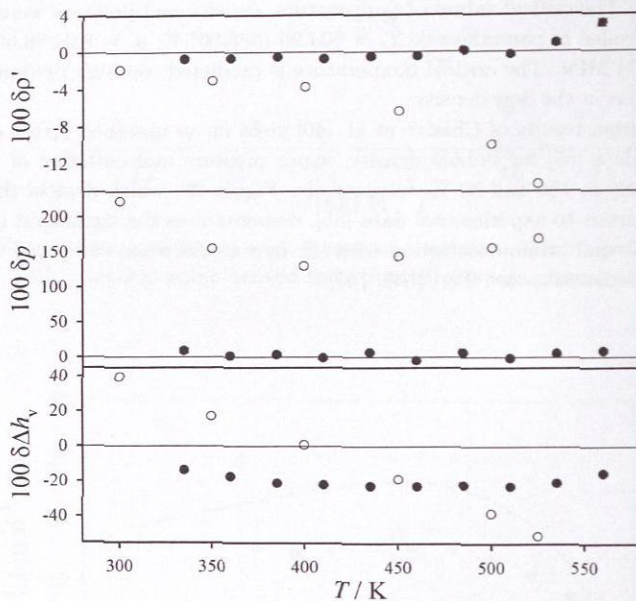


Figure 29: Deviation plots of formic acid for bubble density, vapor pressure and enthalpy of vaporization: ● present simulation data; ○ simulation data of Chialvo et al. [40]; — experimental data [55].

3.8 Summary of Molecular Models for Pure Hydrogen Bonding Fluids

The modeling approach for hydrogen bonding fluids discussed in Section 2.1.2 was used for the development of new models for methanol, ethanol, monomethylamine, dimethylamine, methanethiol and formic acid. For these fluids, the modeling approach turned out to be appropriate describing vapor-liquid equilibria. Table 14 summarizes the mean unsigned errors for bubble density, vapor pressure and enthalpy of vaporization. The mean unsigned errors were evaluated from temperatures close to the triple point to temperatures close to the critical point of the particular component. The respective temperature ranges can be found in the sections in which the new molecular models are introduced.

Table 14: Mean unsigned errors of bubble density, vapor pressure and enthalpy of vaporization of the new molecular models.

Component	$\overline{\delta\rho}$ %	$\overline{\delta p}$ %	$\overline{\delta\Delta h_v}$ %
methanol	0.6	1.1	5.5
ethanol	0.3	3.7	0.9
monomethylamine	0.6	6.5	0.7
dimethylamine	0.4	6.2	4.9
methanethiol	0.6	7.4	7.4
formic acid	0.8	5.1	19.6

The fair description of the enthalpy of vaporization for formic acid leaves room for speculation. The large number of possibilities of formic acid to form complex three-dimensional hydrogen bonded networks might be one reason. Following this, the present modeling approach was tested in a pilot study on the description of vapor-liquid equilibria for water which is the most common fluid that forms complex three-dimensional hydrogen bonded networks.

3.9 Pilot Study of Water Models

Since the early nineteen sixties, a large number of force fields for water were developed and investigated regarding their capability to describe thermophysical and structural properties qualitatively and quantitatively. The number of approaches for the potential functions is vast and the number of water models even more. Due to this, a complete discussion of that topic is not in the scope of this work. Guillot [83] prepared a survey of water models which contain rigid, flexible, dissociable and polarizable interaction sites. Further reviews for water models are given by Brodsky [27], Wallqvist and Mountain [264] and Finney [70].

None of the force fields reviewed by these authors [27, 70, 83, 264] is appropriate for describing the fluid properties of water over the complete fluid state range with high precision. Most of them favorably describe thermophysical properties only at the state points at which they were adjusted, some of them can give additionally fair predictions at state points far away from the adjustment point. Recently, Paricaud et al. [182] proposed a complex force field which predicts water properties from dimer to condensed phases at extreme conditions more accurately. This model describes bubble density, vapor pressure and enthalpy of vaporization for temperatures between 331 and 610 K with mean unsigned errors of 1.4 %, 11.3 % and 3.9 %, respectively.

The model of Paricaud et al. [182] is based on Gaussian charge polarizable interaction sites, i.e., smeared charges to describe electrostatics and hydrogen bonding. Additionally, it uses one Buckingham exponential-6 potential [29] to consider repulsion and dispersion between water molecules. Thus, this water model can not be combined with force fields, which are not based on these complex potential functions, for simulation of mixtures. Furthermore, molecular simulations with those potentials are computationally highly expensive.

To investigate whether a much simpler molecular model can predict thermophysical properties of water with similar quality as the complex molecular model of Paricaud et al. [182], the following modeling approaches were examined. Polarity, hydrogen bonding as well as the dispersion and repulsion are considered by rigid non-polarizable point charges excentrically superimposed on LJ potentials according to Equation (1). Three molecular model types were investigated in the present pilot study to accurately yield vapor-liquid equilibria over the complete temperature range: the TIP4P, the TIP5P and the all-atom model type. These model types are discussed in the following sections.

3.9.1 TIP4P Model Type

The first model type is based on the rigid four-site TIP4P model of Jorgensen et al. [112]. This model type consists of three point charges, excentrically superimposed on one LJ site, cf. Figure 30. The two positive point charges are situated at the hydrogen positions, i.e., S_H sites in Figure 30. The negative point charge is located at a fictive site in the bisection of the hydrogen sites, i.e., S_L site in Figure 30. The LJ site is located at the S_O site and all sites are situated in a plane.

Recently, the TIP4P model was reparameterized by Horn et al. [100] labeled TIP4P-Ew. Two further optimization attempts for the TIP4P model type to describe condensed phases of water were recently suggested by Abascal and Vega [1] labeled TIP4P/2005 and Abascal et al. [2] labeled TIP4P/Ice. For these two water models, no vapor-liquid equilibrium data are available, thus, they are not discussed in the following due to their parameterization aiming of solid state properties. In the present study, two new molecular models of the TIP4P type were developed labeled TIP4P/D and TIP4P/P. The parameters of the TIP4P, TIP4P-Ew, TIP4P/2005 and TIP4P/Ice as well as of the two new models

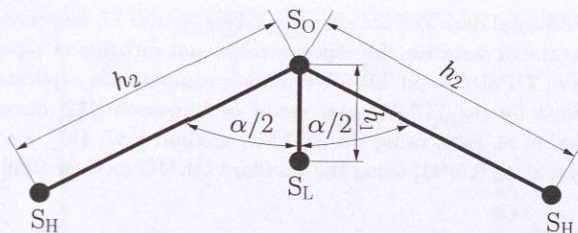


Figure 30: Geometry of the TIP4P model type: S_i indicates the model interaction site i . All sites of the TIP4P models are situated in a plane.

TIP4P/D and TIP4P/P are given in Table 15. The diameters for the internal hard-sphere cutoff of the TIP4P/D and TIP4P/P models at each point charge are 0.3244 and 0.3135 Å, respectively.

Table 15: Geometry, LJ and point charge parameters for molecular models of the TIP4P type, cf. Equation (1) with $n = 4$ and Figure 30.

Model	h_1 Å	h_2 Å	α °	σ_O Å	ϵ_O/k_B K	q_L e	q_H e
TIP4P [112]	0.15000	0.9572	104.52	3.15365	78.020	-1.04000	+0.52000
TIP4P-Ew [100]	0.12500	0.9572	104.52	3.16435	81.921	-1.04844	+0.52422
TIP4P/2005 [1]	0.15460	0.9572	104.52	3.15890	93.200	-1.11280	+0.55640
TIP4P/Ice [2]	0.15770	0.9572	104.52	3.16680	106.100	-1.17940	+0.58970
TIP4P/D	0.17307	0.9757	104.52	3.24443	56.370	-1.12584	+0.56292
TIP4P/P	0.15004	0.9670	104.52	3.13500	95.646	-1.05496	+0.52748

Starting from the TIP4P model of Jorgensen et al. [112], the geometry parameters h_1 and h_2 , the LJ parameters σ_O and ϵ_O as well as the point charge q_H , cf. Figure 30 and Table 15, were optimized to accurately describe bubble densities and vapor pressures of water. However, during the optimization procedure, it turned out to be impossible to improve the description of both the bubble density and vapor pressure simultaneously. Hence, the TIP4P model inherently fails to describe thermophysical properties of water consistently over the complete vapor-liquid equilibria temperature range. Varying the angle α defined in Figure 30 between the two hydrogen sites did also not improve the optimization. Due to that finding, the weighting of the sensitivity to yield experimental bubble densities and vapor pressures was chosen differently during the optimization procedure. The TIP4P/D model was optimized to yield a good bubble density, the TIP4P/P model to yield a good vapor pressure.

The present numerical simulation results of the TIP4P/D and TIP4P/P models to-

gether with experimental data [50] are given in Tables 16 and 17, respectively. Figures 31 to 33 show the saturated densities, the vapor pressure and enthalpy of vaporization for the TIP4P, TIP4P-Ew, TIP4P/D and TIP4P/P models compared to experimental data [50]. The simulation data for the TIP4P water model of Jorgensen [112] discussed here were calculated by Lísal et al. [139] using the RGEMC method [137, 138], for the TIP4P-Ew model by Baranyai et al. [15, 41] using the standard GEMC method [180].

Table 16: Vapor-liquid equilibrium data for water: simulation results of the TIP4P/D model compared to experimental data [50] for vapor pressure, saturated densities and enthalpy of vaporization. The numbers in parentheses indicate the statistical uncertainty in the last digit.

T K	p_{sim} MPa	p_{exp} MPa	ρ'_{sim} mol/l	ρ'_{exp} mol/l	ρ''_{sim} mol/l	ρ''_{exp} mol/l	$\Delta h_{v,\text{sim}}$ kJ/mol	$\Delta h_{v,\text{exp}}$ kJ/mol
310	0.0019(2)	0.0063	54.31(9)	55.69	0.0007(6)	0.0024	54.44(8)	43.46
370	0.0294(5)	0.0905	53.2 (1)	52.93	0.0099(6)	0.0298	49.63(7)	40.82
430	0.241 (1)	0.5692	50.64(9)	49.83	0.0737(2)	0.1674	44.41(6)	37.68
490	1.152 (8)	2.1806	46.50(9)	46.24	0.341 (2)	0.6077	38.43(7)	33.68
550	4.08 (5)	6.1224	41.3 (1)	41.79	1.320 (9)	1.7537	30.1 (1)	28.14
610	9.7 (5)	14.0591	31.8 (3)	35.20	4.8 (1)	4.8534	17.4 (3)	19.20

Table 17: Vapor-liquid equilibrium data for water: simulation results of the TIP4P/P model compared to experimental data [50] for vapor pressure, saturated densities and enthalpy of vaporization. The numbers in parentheses indicate the statistical uncertainty in the last digit.

T K	p_{sim} MPa	p_{exp} MPa	ρ'_{sim} mol/l	ρ'_{exp} mol/l	ρ''_{sim} mol/l	ρ''_{exp} mol/l	$\Delta h_{v,\text{sim}}$ kJ/mol	$\Delta h_{v,\text{exp}}$ kJ/mol
310	0.0035(1)	0.0063	56.0 (1)	55.69	0.0011(1)	0.0024	47.8(1)	43.8
370	0.0647(4)	0.0905	53.65(6)	52.93	0.0189(4)	0.0298	44.2(2)	40.8
430	0.432 (1)	0.5692	50.13(7)	49.83	0.113 (2)	0.1674	40.2(1)	37.7
490	1.796 (7)	2.1806	45.86(7)	46.24	0.442 (5)	0.6077	35.6(1)	33.7
550	5.28 (3)	6.1224	39.4 (1)	41.79	1.39 (1)	1.7537	28.6(1)	28.1
590	11.0 (3)	10.8444	33.5 (2)	37.83	5.12 (9)	3.4119	16.9(2)	22.8

The new TIP4P/D and TIP4P/P models describe the bubble densities with mean unsigned errors of 1.1 % and 2.9 % between 300 and 600 K which is about 46 to 93 %

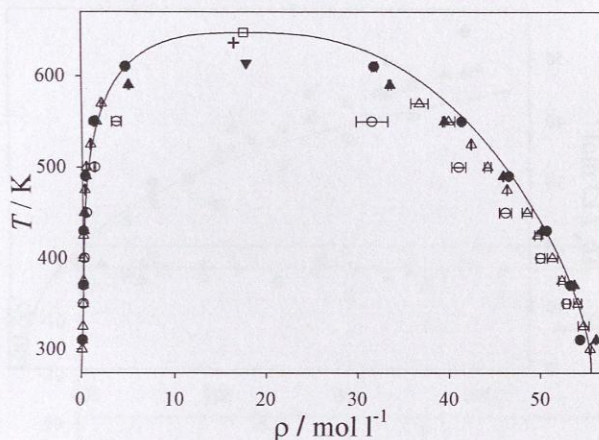


Figure 31: Saturated densities for TIP4P models: ● TIP4P/D simulation data; + critical point derived from TIP4P/D simulation data; ▲ TIP4P/P simulation data; ▼ critical point derived from TIP4P/P simulation data; ○ TIP4P simulation data of Lísal et al. [139]; — experimental data [50]; △ TIP4P-Ew simulation data of Baranyai et al. [15, 41]; □ experimental critical point [50].

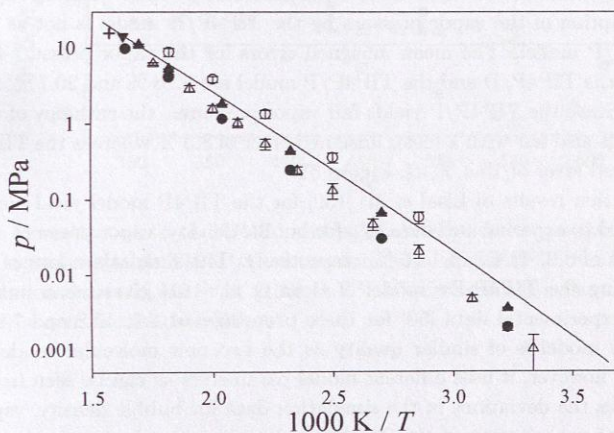


Figure 32: Vapor pressure for TIP4P models: ● TIP4P/D simulation data; + critical point derived from TIP4P/D simulation data; ▲ TIP4P/P simulation data; ▼ critical point derived from TIP4P/P simulation data; ○ TIP4P simulation data of Lísal et al. [139]; △ TIP4P-Ew simulation data of Baranyai et al. [15, 41]; — experimental data [50].

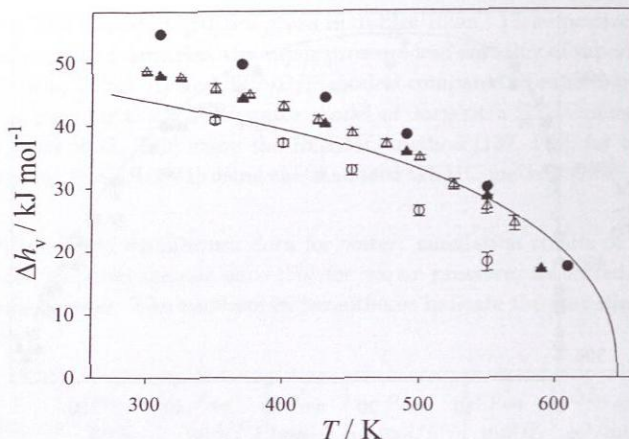


Figure 33: Heat of vaporization for TIP4P models: ● TIP4P/D simulation data; ▲ TIP4P/P simulation data; ○ TIP4P simulation data of Lísal et al. [139]; △ TIP4P-Ew simulation data of Baranyai et al. [15, 41]; — experimental data [50].

of the critical temperature of water. The TIP4P/D model is capable of reproducing the anomalous density behavior of water at low temperatures at least qualitatively, cf. Figure 31. The description of the vapor pressure by the TIP4P/D model is not as favorable as for the TIP4P/P model. The mean unsigned errors for the vapor pressure between 300 and 600 K for the TIP4P/D and the TIP4P/P model are 52.6 % and 20.7 %, respectively, cf. Figure 32. Since the TIP4P/P yields fair vapor pressures, the enthalpy of vaporization for this model is also fair with a mean unsigned error of 8.3 % whereas the TIP4P/D gives a mean unsigned error of 15.4 %, cf. Figure 33.

The simulation results of Lísal et al. [139] for the TIP4P model yield mean unsigned errors compared to experimental data [50] for bubble density, vapor pressure and enthalpy of vaporization of 8.9, 42.4 and 14.6 %, respectively. The simulation data of Baranyai et al. [15, 41] using the TIP4P-Ew model of Horn et al. [101] gives mean unsigned errors compared to experimental data [50] for these properties of 1.7, 47.2 and 7.9 %. Hence, the TIP4P-Ew model is of similar quality as the two new molecular models TIP4P/D and TIP4P/P, however, it uses different model parameters as can be seen from Table 15. Figure 34 shows the deviations of the simulation data for bubble density, vapor pressure and enthalpy of vaporization of the TIP4P models discussed here to experimental data [50].

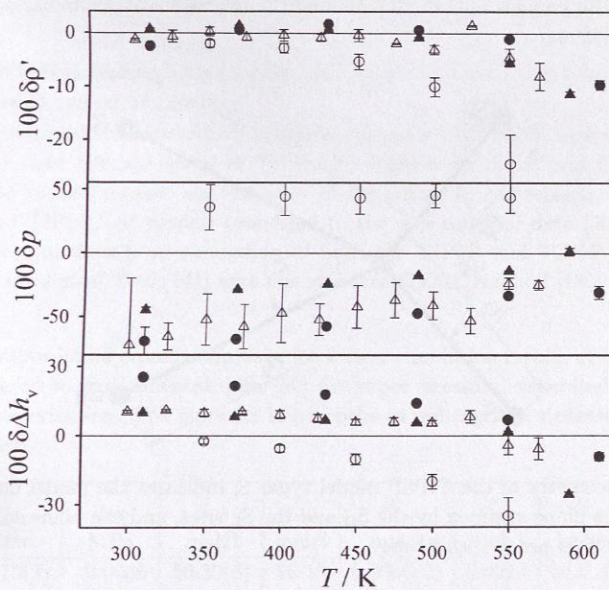


Figure 34: Deviation plots of TIP4P models for bubble density, vapor pressure and enthalpy of vaporization: ● TIP4P/D simulation data; ▲ TIP4P/P simulation data; ○ TIP4P simulation data of Lísal et al. [139]; △ TIP4P-Ew simulation data of Baranyai et al. [15, 41]; — experimental data [50].

3.9.2 TIP5P Model Type

The second model type for water investigated in the present pilot study was proposed by Mahoney and Jorgensen [153] under the name TIP5P. This rigid model type consists of four point charges excentrically superimposed on one LJ site, the point charges are not within a plane. The two negative point charges are located symmetrically along both electron lone-pair directions of the oxygen atom, the two positive point charges are situated each at the hydrogen positions, cf. Figure 35. The two planes which include the two positive point charges plus the LJ site and the two negative point charges plus the LJ site are perpendicular.

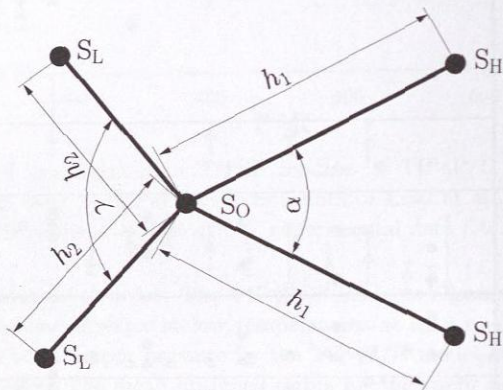


Figure 35: Geometry of the TIP5P model type: S_i indicates the model interaction site i . Note that the plane spanned by the S_O and the S_L sites, and the plane spanned by the S_O and the S_H sites are perpendicular.

The TIP5P model type is based on the reparameterization of the ST2 model of Stillinger and Rahman [223] as well as the BNS model of Ben-Naim and Stillinger [17]. Recently, the TIP5P model of Mahoney and Jorgensen [153] was reparameterized by Rick [195] encoded TIP5P-E model by varying only the LJ parameters of the TIP5P model of Mahoney and Jorgensen [153]. In the present study, the point charges, the positions of the point charges and the LJ parameters of the TIP5P model type were optimized. This new model is labeled TIP5P/DP in the following. The parameters of all discussed models including the present one are given in Table 18. The diameter for the internal hard-sphere cutoff of each TIP5P/DP point charge is 0.3096 Å.

The TIP5P/DP model was obtained by reparameterizing h_1 , h_2 , σ_O , ϵ_O and q_H , cf. Figure 35 and Table 18. Varying the angles α and γ as defined by Figure 35 during the optimization of the present TIP5P model did not improve the description of the vapor-liquid equilibria of water. Similarly to the optimization of the TIP4P model type, the vapor

Table 18: Geometry, LJ and point charge parameters for models of TIP5P type, cf. Equation (1) with $n = 5$ and Figure 35.

Model	h_1 Å	h_2 Å	α °	γ °	σ_O Å	ϵ_O/k_B K	$q_H, -q_L$ e
TIP5P [153]	0.95720	0.70000	104.52	109.47	3.12000	80.570	+0.24100
TIP5P-E [195]	0.95720	0.70000	104.52	109.47	3.09700	89.634	+0.24100
TIP5P/DP	0.80789	0.86146	104.52	109.47	3.09619	120.455	+0.25941

pressure and bubble density cannot simultaneously be accurately described by the TIP5P model type with one parameter set.

The present numerical simulation results for the new TIP5P/DP model together with experimental data [50] are given in Table 19. Figures 36 to 38 depict the saturated densities, the vapor pressure and enthalpy of vaporization, respectively, of the TIP5P, TIP5P-E and TIP5P/DP models compared to the experimental data [50]. The vapor-liquid equilibrium data from simulation of both the TIP5P and TIP5P-E model were obtained by Lísal et al. [140, 141] with the standard GEMC method [180].

Table 19: Vapor-liquid equilibrium data for water: simulation results of the TIP5P/DP model compared to experimental data [50] for vapor pressure, saturated densities and enthalpy of vaporization. The numbers in parentheses indicate the statistical uncertainty in the last digit.

T K	p_{sim} MPa	p_{exp} MPa	ρ'_{sim} mol/l	ρ'_{exp} mol/l	ρ''_{sim} mol/l	ρ''_{exp} mol/l	$\Delta h_{v,sim}$ kJ/mol	$\Delta h_{v,exp}$ kJ/mol
300	0.0015(2)	0.0036	56.30(8)	56.13	0.0006(2)	0.0014	51.9 (1)	43.87
350	0.0183(2)	0.0417	55.35(8)	53.88	0.0059(2)	0.0144	47.9 (1)	41.74
400	0.1136(2)	0.2454	52.88(8)	51.43	0.0435(5)	0.0758	43.27(8)	39.33
450	0.483 (4)	0.9306	49.71(9)	48.70	0.175 (1)	0.2668	38.78(9)	36.47
500	1.563 (9)	2.6369	45.76(9)	45.58	0.543 (3)	0.7334	33.76(8)	32.89
550	3.82 (3)	6.1224	40.6 (1)	41.79	1.40 (1)	1.7537	27.5 (1)	28.14
600	8.6 (2)	12.3716	33.2 (2)	36.60	3.65 (1)	4.0536	19.1 (2)	21.13

The description of saturated densities, vapor pressure and enthalpy of vaporization by the TIP5P/DP model is significantly improved compared to the TIP5P and TIP5P-E models as can be seen in Figures 36 to 38. The mean unsigned errors of the bubble density, vapor pressure and enthalpy of vaporization between 300 and 600 K for the TIP5P/DP model are 2.1, 46.6 and 8.1 %. The TIP5P model type cannot describe the vapor-liquid

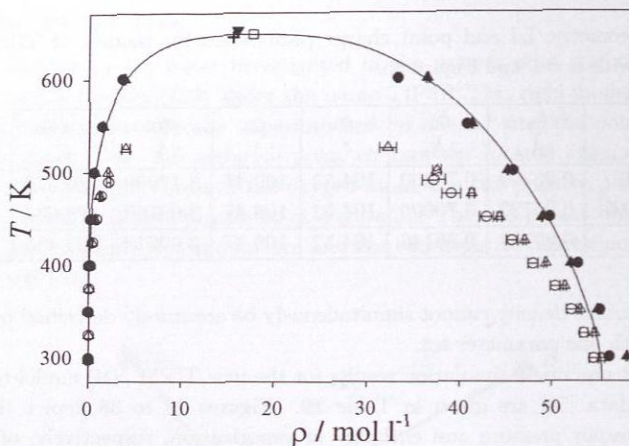


Figure 36: Saturated densities for TIP5P models: ● TIP5P/DP simulation data; + critical point derived from TIP5P/DP simulation data; ○ TIP5P simulation data of Lísal et al. [140]; △ TIP5P-E simulation data of Lísal et al. [141]; ▲ all-atom simulation data; ▼ critical point derived from all-atom simulation data; — experimental data [50]; □ experimental critical point [50].

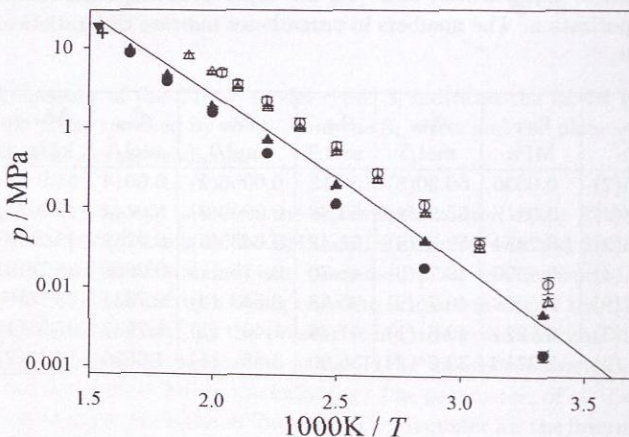


Figure 37: Vapor pressure for TIP5P models: ● TIP5P/DP simulation data; + critical point derived from TIP5P/DP simulation data; ○ TIP5P simulation data of Lísal et al. [140]; △ TIP5P-E simulation data of Lísal et al. [141]; ▲ all-atom simulation data; ▼ critical point derived from all-atom simulation data; — experimental data [50].

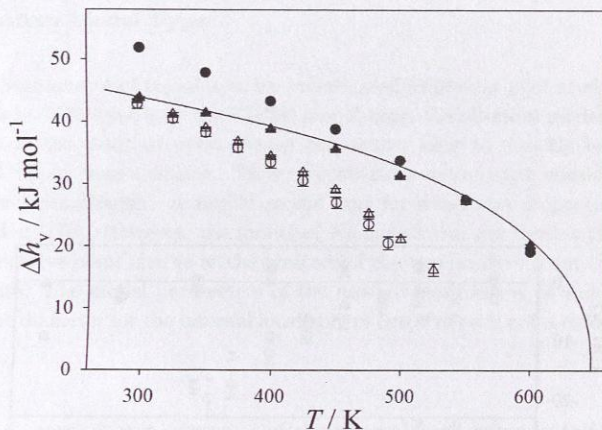


Figure 38: Heat of vaporization for TIP5P models: ● TIP5P/DP simulation data; ○ TIP5P simulation data of Lísal et al. [140]; △ TIP5P-E simulation data of Lísal et al. [141]; ▲ all-atom simulation data; — experimental data [50].

equilibria better than the new models of TIP4P type, although the TIP5P model type consists of a more physical arrangement of the negative point charges than the TIP4P model type.

The simulation results of Lísal et al. [140] for the TIP5P model yield mean unsigned errors compared to experimental data [50] for bubble density, vapor pressure and enthalpy of vaporization of 8.7, 156.9 and 17.8 %, respectively. The TIP5P-E model is only a minor improvement of the TIP5P model since the simulation results of Lísal et al. [141] using this model yield mean unsigned errors compared to experimental data [50] for bubble density, vapor pressure and enthalpy of vaporization of about 8.2, 105.6 and 18.1 %, respectively. Figure 39 shows the deviations of the simulation data for the bubble density, vapor pressure and enthalpy of vaporization of the TIP5P models discussed here to experimental data [50].

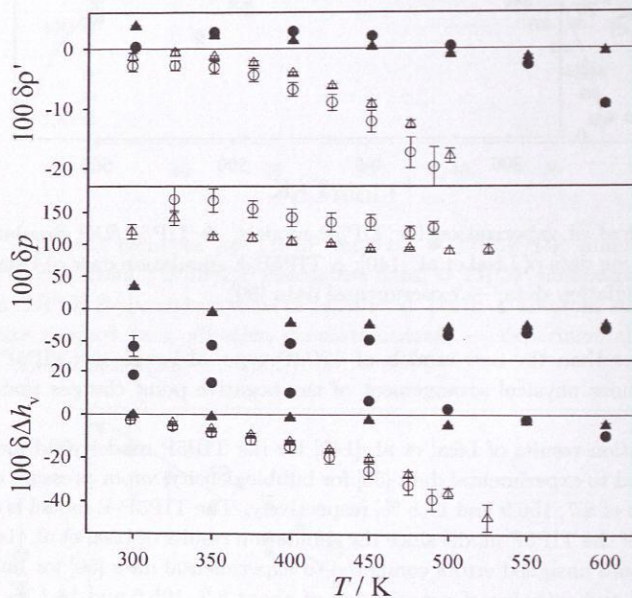


Figure 39: Deviation plots of TIP5P models for bubble density, vapor pressure and enthalpy of vaporization: ● TIP5P/DP simulation data; ○ TIP5P simulation data of Lísal et al. [140]; △ TIP5P-E simulation data of Lísal et al. [141]; ▲ all-atom simulation data; — experimental data [50].

3.9.3 All-Atom Model Type

The third molecular model type for water investigated in present pilot study is a rigid all-atom potential. Additionally to the TIP5P model type, the all-atom model type includes two LJ sites at the positive point charge interaction sites to directly account for the dispersion of the hydrogen atoms. Thus, the all-atom model type consists of three LJ sites and four point charges. A similar model type for water was proposed by Nada and van der Eerden [170]. However, the model of Nada and van der Eerden [170] applies an additional negative point charge at the bisector of the two positive point charges and the oxygen LJ site. The model parameters of the new all-atom model of water are given in Table 20. The diameter for the internal hard-sphere cutoff of each point charge is 0.1589 Å.

Table 20: LJ, point charge, diameter of the internal hard-sphere cutoff and geometry parameters of the present all-atom water model, cf. Equation (1) with $n = 5$ and Figure 35.

Site	σ_{aa} Å	ϵ_{aa}/k_B K	q_a e
S _O	3.17836	99.397	0
S _H	1.84308	37.959	+0.27433
S _L	0	0	-0.27433

h_1 Å	h_2 Å	α °	γ °
0.72870	0.81087	104.52	109.47

Figures 36 to 38 show the simulation data for the saturated densities, vapor pressure and enthalpy of vaporization, respectively, for the present all-atom model. The description of *vapor pressure and enthalpy of vaporization by the new all-atom model* is improved compared to the other new water models, cf. Figures 32 and 33 as well as Figures 37 and 38, respectively. However, the all-atom model gives a poor description of the bubble densities at low temperatures due to the additional attractive contribution of the two LJ sites at the hydrogen positions, cf. Figure 36. The mean unsigned errors for bubble density, vapor pressure and enthalpy of vaporization between 300 and 600 K for the new all-atom model are 1.6, 21.9 and 2.4 %, respectively. The numerical results of the vapor-liquid equilibrium simulations for the all-atom water model together with the experimental data [50] are given in Table 21. Figure 39 includes the deviation plots of the all-atom model for bubble density, vapor pressure and enthalpy of vaporization.

Table 21: Vapor-liquid equilibrium data for water: simulation results of the all-atom model compared to experimental data [50] for vapor pressure, saturated densities and enthalpy of vaporization. The numbers in parentheses indicate the statistical uncertainty in the last digit.

T K	p_{sim} MPa	p_{exp} MPa	ρ'_{sim} mol/l	ρ'_{exp} mol/l	ρ''_{sim} mol/l	ρ''_{exp} mol/l	Δh_{sim} kJ/mol	Δh_{exp} kJ/mol
300	0.0048(1)	0.0036	58.2 (1)	56.13	0.00179(5)	0.00143	43.80(8)	43.87
350	0.0394(6)	0.0417	55.06(5)	53.88	0.0139 (2)	0.01443	41.32(3)	41.74
400	0.192 (1)	0.2454	52.08(5)	51.43	0.0650 (7)	0.07583	38.74(6)	39.33
450	0.701 (3)	0.9306	48.85(5)	48.70	0.2367 (3)	0.26683	35.57(9)	36.47
500	1.86 (1)	2.6369	45.14(8)	45.58	0.684 (8)	0.73344	31.3 (1)	32.89
550	4.51 (3)	6.1224	41.2 (1)	41.79	1.50 (1)	1.75367	27.28(9)	28.14
600	9.3 (2)	12.3716	36.4 (1)	36.60	3.87 (9)	4.05363	20.2 (2)	21.13

3.9.4 Summary of the Pilot Study

Three water model types, i.e., TIP4P, TIP5P and all-atom, were investigated in a pilot study on vapor-liquid equilibria over a wide temperature range. The new models TIP4P/D, TIP4P/P, TIP5P/DP and all-atom model were introduced in Section 3.9.1 to Section 3.9.3. The mean unsigned errors of these models in the temperature range of 300 to 600 K for bubble density, vapor pressure and enthalpy of vaporization are summarized in Table 22.

Table 22: Mean unsigned errors for vapor pressure, bubble density and enthalpy of vaporization of the new water models investigated in the present pilot study.

model	$\bar{\delta p}$ %	$\bar{\delta \rho}$ %	$\bar{\delta \Delta h_v}$ %
TIP4P/D	1.1	52.6	15.4
TIP4P/P	2.9	20.7	8.3
TIP5P/DP	2.1	46.6	8.1
all-atom	1.6	21.9	2.4

None of these models is capable to entirely describe the vapor-liquid equilibria with the similar accuracies over wide temperature ranges as the hydrogen bonding models of pure fluids summarized in Section 3.8. However, the new water models belong to the best LJ plus point charge based molecular models which can be found in the literature for vapor-liquid equilibria over wide state ranges.

The choice to use one of these new models depends on the temperature at which it is intended to be used. E.g., Table 22 indicates that the all-atom gives the overall best description of vapor-liquid equilibria for water better than any other model presently available. However, the all-atom model gives at ambient temperature, at which biological investigations take often place, unfavorable description of liquid densities, cf. Figure 36. For ambient conditions, the TIP4P/P might therefore be a better choice.

4 Systematic Study of Lennard-Jones Based Molecular Modeling of Mixtures

In molecular simulations of a binary mixture $A + B$ with pairwise additive potentials, three different interactions occur: two like interactions between molecules of the same type $A-A$ and $B-B$, which are fully defined by the pure component models, and the unlike interaction between molecules of different type $A-B$. In mixtures consisting of polar molecules, the electrostatic part of the unlike interaction is fully determined by the laws of electrostatics. However, there is no rigorous physical framework that yields reliable unlike repulsion and dispersion parameters like the Lennard-Jones (LJ) parameters studied in the present work. For finding these parameters, combining rules were developed in the past based on physical and mathematical intuition or on empirical approaches. Eleven of these combining rules are investigated in the following. These combining rules rely solely on pure component data, namely, the pure component LJ parameters and, in some cases, additionally the polarizability α or the ionization potential I . Other combining rules, that are not discussed in this work, also employ dispersion force coefficients [35, 52, 234], diamagnetic susceptibility [77, 158] or effective transition energies [53, 54].

Another approach for obtaining unlike LJ parameters is to adjust them directly to experimental binary data, for which a single data point may in principle be sufficient. Kohler et al. [122] fitted both unlike LJ parameters to experimental second virial coefficients of binary mixtures. Following this approach, Möller et al. [164] developed a method for adjusting the unlike LJ size and energy parameters to experimental excess volumes and enthalpies. The findings of Möller et al. [164] are based on the rigorous derivation of the dependence of these properties on the unlike LJ parameters starting from the partition function [71]. Their investigations showed that the unlike LJ size parameter determined from the fits practically does not deviate from the arithmetic mean of the pure component LJ size parameters. This finding is supported by the work of Vrabec and Fischer on $\text{Ar} + \text{CH}_4$ [252] as well as on the three binary mixtures that can be formed of CH_4 , C_2H_6 and CO_2 [253]. Kronome et al. [127] applied a similar approach, specifying the unlike LJ size parameter by the arithmetic mean. They adjusted only the LJ energy parameter to the experimental excess Gibbs enthalpy for the mixture $\text{N}_2 + \text{C}_2\text{H}_6$ and obtained favorable results for vapor-liquid equilibria.

Unlike LJ energy parameters of 44 binary mixtures [226, 228, 258] were fitted to one experimental binary vapor pressure each. These mixtures contain noble gases, homonuclear and heteronuclear diatomics, small hydrocarbons, carbon monoxide, carbon dioxide, carbon disulfide and halogenated hydrocarbons, i.e., refrigerants. Overall 22 components are studied, which are composed of 1 to 9 atoms. These components were modeled by the one-center Lennard-Jones potential (1CLJ) [255], the symmetric two-center Lennard-Jones potential either with a pointdipole (2CLJD) [227] or with a linear elongated pointquadrupole (2CLJQ) [255]. The parameters of the pure component molecular models were adjusted

to experimental pure component bubble density and vapor pressure data [227, 255]. The pure component models are accurate, the mean errors of the bubble density, vapor pressure and enthalpy of vaporization are typically 1, 4 and 3 %, respectively. Vapor-liquid equilibria of the 44 mixtures are described with typical deviations in bubble density, vapor pressure and in dew point composition of below 1 and 5 %, and 0.02 mol/mol, respectively [226, 228, 258].

Ternary mixtures are predicted without further parameterization since the force fields are based on pairwise additive interactions. Results for ternary vapor-liquid equilibria of six mixtures [226, 228, 254, 258] confirm the predictive power of such models.

4.1 Combining Rules

The eleven combining rules which are studied here are summarized in Table 23. In the following sections, these combining rules are discussed in detail [205].

Table 23: Eleven combining rules together with the acronyms used here and corresponding references. In the last column, it is indicated whether the unlike LJ size parameter is given by the arithmetic mean, i.e., the Lorentz rule.

Name	Acronym	Reference	Lorentz
Lorentz-Berthelot	LB	[18, 147]	yes
Kohler	K	[121]	
Hudson-McCourbrey	HMC	[94]	
Fender-Halsey	FH	[63]	
Hiza	H	[91, 92, 93]	no
Sikora	S	[216]	
Smith-Kong	SK	[123, 218]	
Halgren	HHG	[87]	
Waldman-Hagler	WH	[261]	
Al-Matar-Rockstraw-1	M1	[5]	
Al-Matar-Rockstraw-2	M2	[5]	

4.1.1 Lorentz-Berthelot (LB)

The Lorentz-Berthelot combining rule is most widely used to determine the unlike LJ parameters. Lorentz [147] proposed to use the arithmetic mean for the unlike size parameter motivated by collisions of hard spheres

$$\sigma_{ab}^{LB} = \frac{\sigma_{aa} + \sigma_{bb}}{2} \quad (11)$$

Berthelot [18] proposed with little physical argument the geometric mean for the unlike energy parameter

$$\epsilon_{ab}^{\text{LB}} = \sqrt{\epsilon_{aa}\epsilon_{bb}}. \quad (12)$$

The LB combining rule is by far the oldest and most common approach, but due to the fact that it can lead to inaccurate mixture properties [51, 245], numerous other combining rules have been developed.

4.1.2 Kohler (K)

Kohler [121] used the approach of London [144, 145] for the dispersion energy to derive a combining rule for the unlike LJ energy parameter which uses the polarizability α

$$\epsilon_{ab}^{\text{K}} = 2^7 \left[\frac{\sigma_{aa}\sigma_{bb}}{\sigma_{aa} + \sigma_{bb}} \right]^6 \frac{\alpha_{aa}\alpha_{bb}}{\alpha_{bb}^2\sigma_{aa}^6\epsilon_{aa} + \alpha_{aa}^2\sigma_{bb}^6\epsilon_{bb}} \epsilon_{aa}\epsilon_{bb}. \quad (13)$$

The application of the polarizability in combining rules is not straightforward. Generally, the polarizability quantifies the distortion of the overall charge distribution of an atom, group or molecule by an electric field. It is in fact a tensor, which includes the anisotropic contributions of the directionally distorted charge distribution. This tensor is often described by a scalar α which is appropriate to characterize the distortion sensitivity for the whole molecule. Laidig and Bader [129] suggest that atomic or group polarizabilities influenced by the chemical environment additively contribute to the overall molecular polarizability. Hence, the atomic or group polarizabilities required to apply the combining rules to the symmetric two-center LJ potential ascribe 50 % of the molecular polarizability to each of the two LJ sites. For molecules modeled with the one-center LJ potential, e.g., CH₄, the total molecular polarizability was used here. Polarizabilities were taken from [135] except for the refrigerants R125 [272], R134a [272] and R152a [57].

Furthermore, Kohler [121] proposed to use the arithmetic mean for the unlike LJ size parameter (Lorentz rule) as defined by Equation (11).

4.1.3 Hudson-McCoubrey (HMC)

Hudson and McCoubrey [94] reformulated Reed's proposal [193] for the calculation of unlike LJ energy parameters which considers the ionization potential I of the pure components and volume effects of the mixture. They claim that their expression is "suitable to obtain virial coefficients of binary gas mixtures and binary gas-liquid critical temperatures" [94]

$$\epsilon_{ab}^{\text{HMC}} = \frac{2\sqrt{I_{aa}I_{bb}}}{I_{aa} + I_{bb}} \left[\frac{2\sqrt{\sigma_{aa}\sigma_{bb}}}{\sigma_{aa} + \sigma_{bb}} \right]^6 \sqrt{\epsilon_{aa}\epsilon_{bb}}. \quad (14)$$

The ionization potential is defined as the energy which is necessary to remove the outermost electron from an atom or molecule. Since the outermost electron cannot be explicitly assigned to a specific atom or group of a molecule, the full molecular ionization potential is ascribed in the present study to every LJ site of the molecular model. Ionization potentials were taken from [135] except for the refrigerants R125 [66], R134a [66] and R152a [66].

Srivastava and Madan [221] derived the same expression as Equation (14) with an approach similar to that of Kohler [121]. Note that Equation (13) can be transformed to Equation (14) if the following relation between polarizability, ionization potential, LJ size and energy parameters is assumed for both sites a and b

$$4\epsilon_{aa}\sigma_{aa}^6 = \frac{3}{4}\alpha_{aa}^2 I_{aa}. \quad (15)$$

Some authors, e.g., Good and Hope [77] or Reid and Leland [194], suggest that the ratio between the geometric and arithmetic mean of the ionization potentials in Equation (14) can be set to unity. However, in the present work Equation (14) was applied.

For the unlike LJ size parameter in the HMC combining rule the Lorentz rule is applied as defined by Equation (11).

4.1.4 Fender-Halsey (FH)

Fender and Halsey [63] proposed to use the harmonic mean for the unlike LJ energy parameter in their empirical combining rule

$$\epsilon_{ab}^{\text{FH}} = \frac{2\epsilon_{aa}\epsilon_{bb}}{\epsilon_{aa} + \epsilon_{bb}}, \quad (16)$$

which always gives smaller or equal values than the geometric mean. Mixtures of noble gases have mostly smaller unlike LJ energy parameters than those obtained with the geometric mean. Hence, Fender and Halsey [63] achieved with their harmonic mean combining rule more accurate second virial coefficients for the mixture Ar + Kr than with the LB combining rule.

For the unlike LJ size parameter in the FH combining rule the Lorentz rule is applied as defined by Equation (11).

4.1.5 Hiza (H)

Hiza et al. [91, 92, 93] used a semi-empirical approach to correct the LB combining rule. The expressions for the correction factors, dependent on the ionization potentials and empirical factors, were determined by fitting to equilibrium, transport and beam scattering data of noble gases and light hydrocarbons

$$\sigma_{ab}^{\text{H}} = (1 + 0.025k_{ab}) \frac{\sigma_{aa} + \sigma_{bb}}{2}, \quad (17)$$

and

$$\epsilon_{ab}^H = (1 - 0.18k_{ab}) \sqrt{\epsilon_{aa}\epsilon_{bb}}, \quad (18)$$

with

$$k_{ab} = \sqrt{I_{aa} - I_{bb}} \ln \left(\frac{I_{aa}}{I_{bb}} \right), \quad (19)$$

where the component order has to be chosen so that $I_{aa} > I_{bb}$.

Since k_{ab} from Equation (19) is always larger than zero for non-identical ionization potentials, the resulting unlike LJ size parameters are always larger than those from the Lorentz rule. The opposite holds for the unlike LJ energy parameters when compared to the Berthelot rule.

4.1.6 Sikora (S)

In Sikora's combining rule [216] repulsion is considered via deformation energies of the electron clouds and resulting unsymmetrical collision diameters which occur at small distances between overlapping atoms or molecules

$$\epsilon_{ab}^S = 2^{15} \frac{I_{aa} I_{bb}}{(I_{aa} + I_{bb})^2} \frac{\sqrt{\epsilon_{aa} \sigma_{aa}^{12} \epsilon_{bb} \sigma_{bb}^{12}}}{\left[(\epsilon_{aa} \sigma_{aa}^{12})^{\frac{1}{13}} + (\epsilon_{bb} \sigma_{bb}^{12})^{\frac{1}{13}} \right]^{13}} \sqrt{\epsilon_{aa} \epsilon_{bb}}. \quad (20)$$

Applying similar considerations for the unlike LJ size parameter [154], the following equation was proposed

$$\sigma_{ab}^S = 2^{-\frac{13}{12}} \left(\sigma_{aa}^{\frac{12}{13}} + \sigma_{bb}^{\frac{12}{13}} \right)^{\frac{13}{12}}. \quad (21)$$

4.1.7 Smith-Kong (SK)

Smith [218] developed a combining rule considering the repulsive interaction of simple molecules. His combining rule includes the atomic distortion theory for repulsion. Kong [123] used Smith's approach and a geometric mean relationship for the attractive interactions and applied it to the LJ potential leading to

$$\sigma_{ab}^{SK} = \left\{ \frac{\left[(\epsilon_{aa} \sigma_{aa}^{12})^{\frac{1}{13}} + (\epsilon_{bb} \sigma_{bb}^{12})^{\frac{1}{13}} \right]^{13}}{2^{13} \sqrt{\epsilon_{aa} \sigma_{aa}^6 \epsilon_{bb} \sigma_{bb}^6}} \right\}^{\frac{1}{6}}, \quad (22)$$

and

$$\epsilon_{ab}^{SK} = \frac{2^{13} \epsilon_{aa} \sigma_{aa}^6 \epsilon_{bb} \sigma_{bb}^6}{\left[(\epsilon_{aa} \sigma_{aa}^{12})^{\frac{1}{13}} + (\epsilon_{bb} \sigma_{bb}^{12})^{\frac{1}{13}} \right]^{13}}. \quad (23)$$

4.1.8 Halgren (HHG)

From investigations of noble gas mixtures using ab initio and experimental data, Halgren [87] deduced that the experimental pattern of the van der Waals minimum energy distances is well described by the "cubic-mean" combining rule

$$\sigma_{ab}^{\text{HHG}} = \frac{\sigma_{aa}^3 + \sigma_{bb}^3}{\sigma_{aa}^2 + \sigma_{bb}^2}. \quad (24)$$

The van der Waals minimum energy distance is associated with the LJ size parameter. To introduce the experimental unlike noble gas values into the LJ energy parameters, a combination of the geometric and harmonic mean was applied which is claimed to yield good descriptions of the experimental noble gas values

$$\epsilon_{ab}^{\text{HHG}} = \frac{4\epsilon_{aa}\epsilon_{bb}}{(\sqrt{\epsilon_{aa}} + \sqrt{\epsilon_{bb}})^2}. \quad (25)$$

4.1.9 Waldman-Hagler (WH)

Waldman and Hagler [261] derived their combining rule by applying mathematical methods which consider symmetry, uniformed scaling and simplification of a two-parameter to a single-parameter problem to deduce the general functional form of their combining rule. From a "graphical analysis" of noble gas mixture data they obtained

$$\sigma_{ab}^{\text{WH}} = \left[\frac{\sigma_{aa}^6 + \sigma_{bb}^6}{2} \right]^{\frac{1}{6}}, \quad (26)$$

and

$$\epsilon_{ab}^{\text{WH}} = \frac{2\sigma_{aa}^3\sigma_{bb}^3}{\sigma_{aa}^6 + \sigma_{bb}^6} \sqrt{\epsilon_{aa}\epsilon_{bb}}. \quad (27)$$

4.1.10 Al-Matar-Rockstraw (M1 and M2)

Al-Matar and Rockstraw [5] proposed combining rules which are based on similar mathematical considerations as used by Waldman-Hagler, cf. Section 4.1.9. The first of their combining rule, abbreviated in the following with M1, was obtained by functional analysis of experimental noble gas mixture data. They consider the pure component LJ parameters equally weighted. M1 is given by

$$\sigma_{ab}^{\text{M1}} = \frac{1}{3} \sum_{L=0}^2 \left(\frac{0.25(\sigma_{aa}^3 + \sigma_{bb}^3)^2}{\sigma_{aa}^L \sigma_{bb}^L} \right)^{\frac{1}{6-2L}}, \quad (28)$$

and

$$\epsilon_{ab}^{M1} = \frac{3\sigma_{aa}^3\sigma_{bb}^3}{\sum_{L=0}^2 \left(\frac{0.25(\sigma_{aa}^3 + \sigma_{bb}^3)^2}{\sigma_{aa}^L\sigma_{bb}^L} \right)^{\frac{6}{6-2L}}} \sqrt{\epsilon_{aa}\epsilon_{bb}}. \quad (29)$$

The second combining rule, abbreviated in the following with M2, uses weighting matrices which can account for uneven contributions of the pure component LJ parameters to the unlike quantities. The weighting matrices of M2 were obtained by fitting them to noble gas mixture data. The unlike LJ parameters are given by

$$\sigma_{ab}^{M2} = (0.2820\sigma_{aa}^6 + 0.4732\sigma_{aa}^3\sigma_{bb}^3 + 0.2448\sigma_{bb}^6)^{\frac{1}{6}}, \quad (30)$$

and

$$\epsilon_{ab}^{M2} = \frac{0.03995\epsilon_{aa} + 0.9564698845\sqrt{\epsilon_{aa}\epsilon_{bb}} + 0.00355\epsilon_{bb}}{0.2820\sigma_{aa}^6 + 0.4732\sigma_{aa}^3\sigma_{bb}^3 + 0.2448\sigma_{bb}^6} \sigma_{aa}^3\sigma_{bb}^3. \quad (31)$$

In Equation (30), the lower valued pure LJ parameter has to be taken for site index a [5], since unequal weights are used.

4.2 Case Study

Before studying the performance of the different combining rules, it is useful to get a picture of the influence of σ_{ab} and ϵ_{ab} on the vapor-liquid equilibrium of mixtures. For that purpose, in a case study on two vapor-liquid equilibrium data points, the vapor pressure, the bubble density and the dew point composition at specified temperature and bubble point composition were investigated regarding their sensitivity on σ_{ab} and ϵ_{ab} .

Instead of using the absolute values of σ_{ab} and ϵ_{ab} , the unlike LJ parameters are discussed here in terms of the deviations η and ξ from the Lorentz-Berthelot combining rule

$$\sigma_{ab} = \eta \frac{\sigma_{aa} + \sigma_{bb}}{2}, \quad (32)$$

and

$$\epsilon_{ab} = \xi \sqrt{\epsilon_{aa}\epsilon_{bb}}. \quad (33)$$

The influence of η and ξ on the vapor-liquid equilibria of mixtures was investigated for two different binary mixtures: $N_2 + C_3H_6$ and $CO + C_2H_6$, respectively. Three of these components are described by 2CLJQ models, only for CO a 2CLJD model was used.

For $CO + C_2H_6$, the case study was performed at 223 K and $x_{CO} = 0.198$ mol/mol, where experimental vapor pressure and dew point CO mole fraction are 5.614 MPa and 0.8065 mol/mol [242]. To eliminate the influence of experimental scatter, the pressure -

composition data were smoothed [197]. The reference bubble density of 16.499 mol/l was determined using DDMIX [59] which was designed to yield reliable mixture densities.

The experimental data for $N_2 + C_3H_6$ at 290 K and $x_{N_2} = 0.1146$ mol/mol, where the case study was performed, are for the vapor pressure and dew point N_2 mole fraction 6.783 MPa and 0.7497 mol/mol [81]. Again smoothed values were taken here [197]. The bubble density of 12.4094 mol/l was estimated by the Rackett model [192, 220] together with the mixing rule of Chueh and Prausnitz [43].

Vapor-liquid equilibria for $CO + C_2H_6$ were simulated for every combination of $\eta \in [0.96, 0.98, 1, 1.02, 1.04]$ and $\xi \in [0.96, 0.98, 1, 1.02, 1.04]$, i.e., overall 25 combinations. Simulation results for vapor pressure, bubble density and dew point composition can therefore be plotted as functions of η and ξ . Their deviations to the experimental values are illustrated as three-dimensional plots in Figures 40 to 42 where the surfaces were derived from the 25 simulation points. All combinations of η and ξ which yield the experimental value are indicated by a thin solid line in Figures 40 to 42 both on the surface and on the η - ξ plane. For the further discussion experimental and simulation uncertainties are needed. The following estimates were used: 3 % for the vapor pressure, 0.5 % for the bubble density and 4 % (about 0.03 mol/mol) for the dew point composition. These limits are also included in Figures 40 to 42 as solid bold lines.

The vapor pressure significantly depends on both η and ξ , cf. Figure 40. It varies by about 35 % for the studied variations on η (at constant ξ) and 45 % for the studied variations on ξ (at constant η) in the investigated parameter range. Due to that high sensitivity, the range where the simulated and experimental vapor pressures agree within 3 % is rather small.

In contrast, the bubble density is practically independent of the parameter ξ as can be seen from Figure 41, but it varies by about 6 % in the investigated range of η . The experimental value can be obtained by choosing η close to unity in combination with any value of ξ in the studied range.

The dew point CO mole fraction depends both on η and ξ as shown in Figure 42. But in the investigated parameter range it varies only by about 6 % for η (at constant ξ) and 2 % for ξ (at constant η).

Summarizing Figures 40 to 42 in Figure 43, it can be seen that there is one combination of η and ξ where both vapor pressure and bubble density of the molecular mixture model and experiment coincide exactly ($\eta = 0.9972$ and $\xi = 1.0145$). With the uncertainties for the bubble density and the vapor pressure, a target area is defined in which the combination of η and ξ yields an accurate description of both properties, cf. the shaded area in Figure 43. The experimental dew point composition within its (large) uncertainty is also met in this target area.

Figure 43 also allows an easy assessment of the combining rules introduced in Section 4.1. The LB combining rule is the closest to the target area, but outside of it. All combining rules, except SK, describe the bubble density and dew point composition within

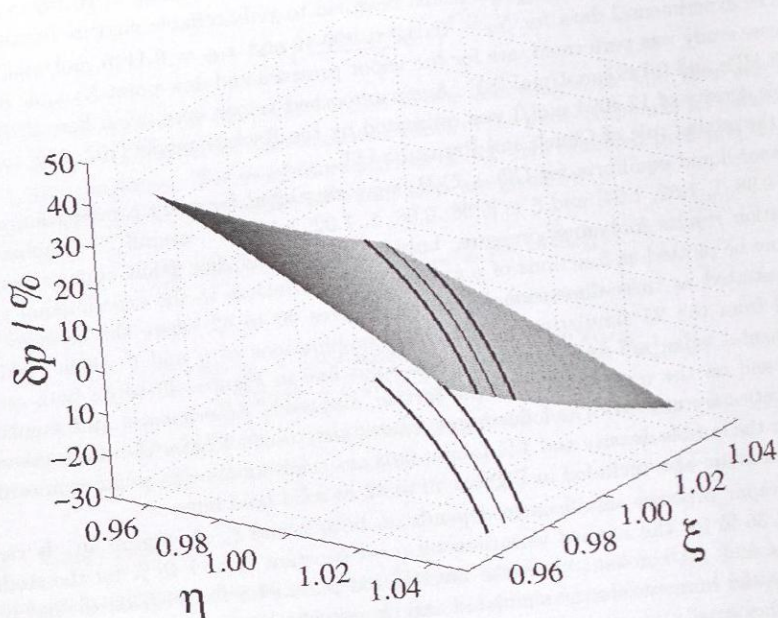


Figure 40: Vapor pressure of CO + C₂H₆ at 223 K and bubble point CO mole fraction of 0.1980 mol/mol: relative deviation of the simulation results to the experimental vapor pressure of 5.614 MPa. The surface is a fit to 25 simulation results with varying η and ξ . Solid slim line: η and ξ combinations yielding the experimental value. Solid bold lines: η and ξ combinations deviating by $\pm 3\%$ from the experiment. Lines in the η - ξ plane: projections of the lines from the surface.

their uncertainty. However, the experimental vapor pressure is predicted by none of them within the experimental uncertainty. The LB combining rule ($\eta = 1$ and $\xi = 1$) yields relative deviations from the experimental vapor pressure, bubble density and dew point CO mole fraction of +5.6 %, -0.3 % and +1.8 %, respectively. The SK combining rule gives the most remote combination ($\eta = 1.0059$ and $\xi = 0.9630$) with relative deviations in vapor pressure of +21.7 %, -0.8 % and +2.3 %, respectively.

An analogous systematic study for N₂ + C₃H₆ includes 30 vapor-liquid equilibrium simulation results for $\eta \in [0.96, 0.98, 1, 1.02, 1.04]$ and $\xi \in [0.94, 0.96, 0.98, 1, 1.02, 1.04]$ at 290 K and $x_{N_2} = 0.1146$ mol/mol. Since the experimental bubble density was estimated

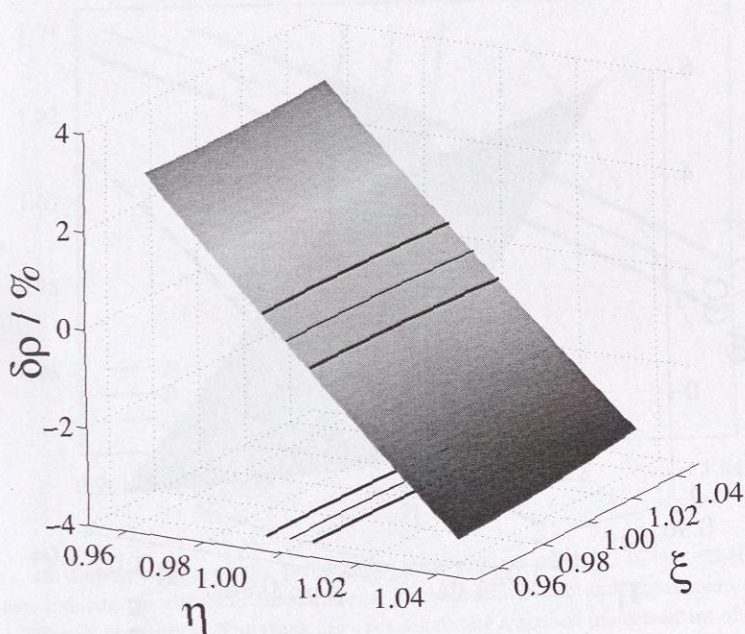


Figure 41: Bubble density of $\text{CO} + \text{C}_2\text{H}_6$ at 223 K and bubble point CO mole fraction of 0.1980 mol/mol: relative deviation of the simulation results to the experimental bubble density of 16.499 mol/l. The surface is a fit to 25 simulation results with varying η and ξ . Solid bold line: η and ξ combinations yielding the experimental value. Solid slim line: η and ξ combinations deviating by $\pm 0.5\%$ from the experiment. Lines in the η - ξ plane: projections of the lines from the surface.

with the Racket model, a higher uncertainty of 1 % was assigned to it. Analogously to the three-dimensional plots for the mixture $\text{CO} + \text{C}_2\text{H}_6$, the relative deviations of the 30 vapor-liquid equilibrium simulations to the experimental values for vapor pressure, bubble density and N_2 dew point mole fraction are illustrated in Figures 44 to 46. The surfaces in these figures were derived from the 30 simulation points.

The influence of the unlike LJ size and energy parameter on vapor pressure, bubble density and dew point composition is in the same order of magnitude as for the mixture $\text{CO} + \text{C}_2\text{H}_6$. However, the influence of the unlike LJ parameters can be different. E.g., the vapor pressure slightly increases with increasing η whereas for the mixture $\text{CO} + \text{C}_2\text{H}_6$

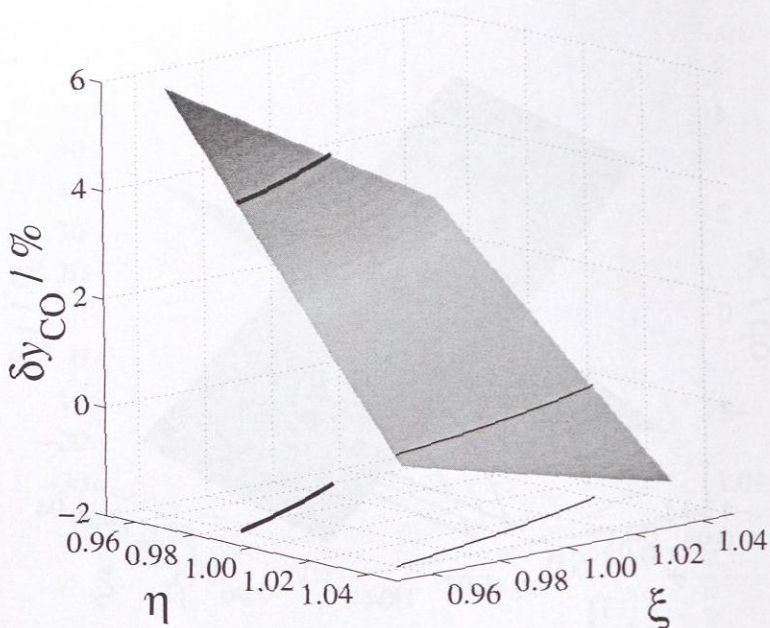


Figure 42: Dew point CO mole fraction of CO + C₂H₆ at 223 K and bubble point CO mole fraction of 0.1980 mol/mol: relative deviation of the simulation results to the experimental dew point CO mole fraction of 0.8065 mol/mol. The surface is a fit to 25 simulation results with varying η and ξ . Solid slim line: η and ξ combinations yielding the experimental value. Solid bold line: η and ξ combinations deviating by +4 % from the experiment. Lines in the η - ξ plane: projections of the lines from the surface.

η shows the contrary influence. The influence of the unlike LJ parameters on the vapor-liquid equilibrium data is summarized in Figure 47. This figure shows the comparison to experimental data where the target area is obtained analogously to the study of CO + C₂H₆.

Also the combining rules can be easily assessed by Figure 47. Only the M2 combining rule is within this area, the HMC is very close to it. For M2 ($\eta = 1.0026$, $\xi = 0.9538$) relative deviations from the experimental vapor pressure, bubble density and dew point N₂ mole fraction of -1.7 %, -0.8 % and +3.0 % were found, respectively. SK ($\eta = 1.0130$, $\xi = 0.9101$) yields again the most remote results with relative deviations of +15.5 %, -1.6

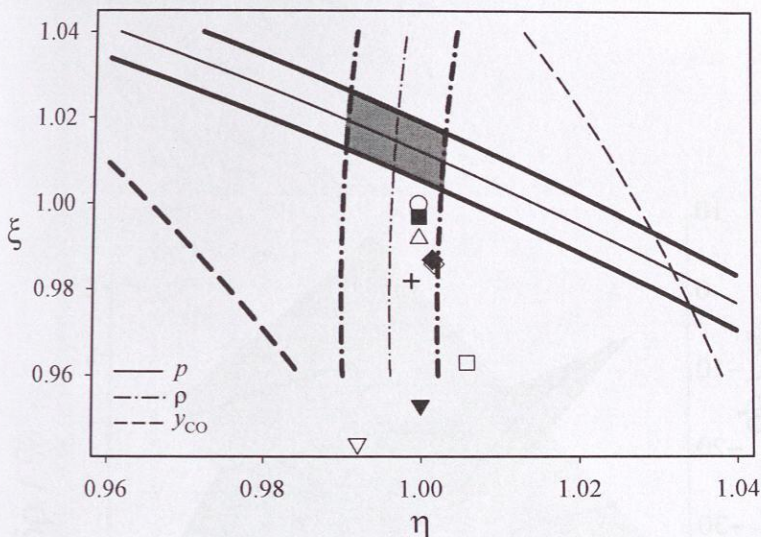


Figure 43: Superposition of the projections from Figures 40 to 42 ($\text{CO} + \text{C}_2\text{H}_6$). The thin lines indicate the combinations of η and ξ where simulation and experiment coincide for the different properties. The thick lines represent the assumed uncertainties of $\delta p = \pm 3\%$, $\delta \rho = \pm 0.5\%$ and $\delta y_{\text{CO}} = +4\%$. The predictions of the combining rules are given by: \circ LB, \blacksquare K, \triangle HMC, ∇ H, \blacktriangledown S, \square SK, \diamond WH, \blacklozenge M1, $+$ M2. The remaining two combining rules are not within the scale. Shaded: target area of η and ξ combinations yielding experimental values within their uncertainties.

% and +4.8 %, respectively.

From both case studies, the conclusion is drawn that the vapor pressure, which significantly depends on both unlike LJ parameters, is the most challenging property to be predicted by combining rules. The bubble density is mainly determined by the unlike LJ size parameter and values close to the arithmetic mean ($\eta = 1$) describe the experimental bubble densities well (see also [252, 253]). This is achieved by most of the combining rules. The dew point composition depends on both η and ξ like the vapor pressure, however, its sensitivity is considerably weaker compared to the vapor pressure. Due to these findings, it can be recommended to use the Lorentz rule for the size parameter since it predicts bubble densities well and to adjust the unlike energy parameter to the vapor pressure.

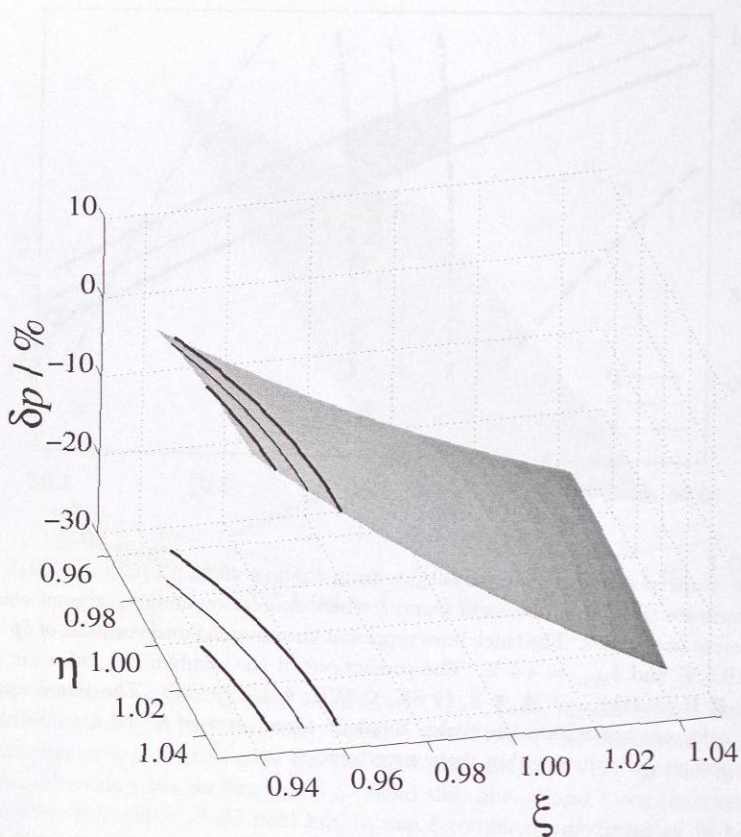


Figure 44: Vapor pressure of $N_2 + C_3H_6$ at 290 K and bubble point N_2 mole fraction of 0.1146 mol/mol: relative deviation of the simulation results to the experimental vapor pressure of 6.783 MPa. The surface is a fit to 30 simulation results with varying η and ξ . Solid slim line: η and ξ combinations yielding the experimental value. Solid bold lines: η and ξ combinations deviating by $\pm 3\%$ from the experiment. Lines in the η - ξ plane: projections of the lines from the surface.

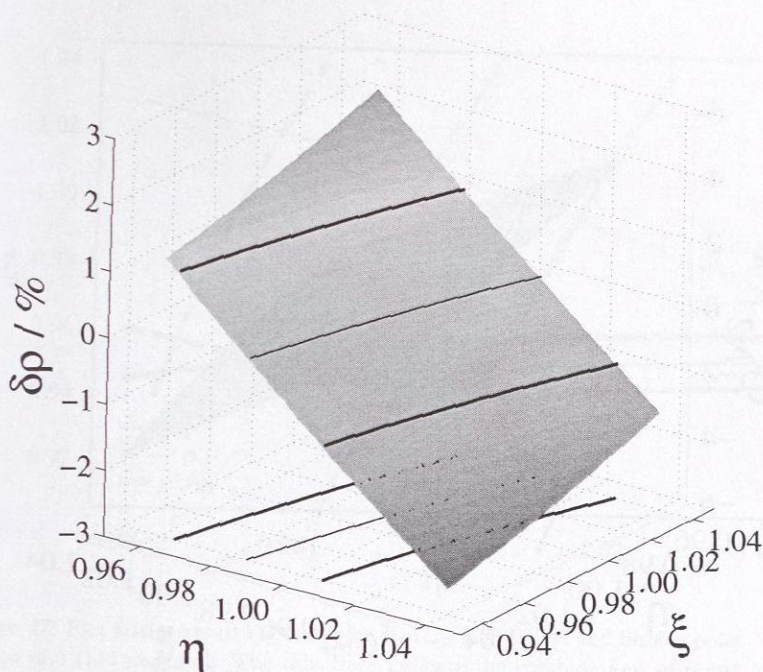


Figure 45: Bubble density of $N_2 + C_3H_6$ at 290 K and bubble point N_2 mole fraction of 0.1146 mol/mol: relative deviation of the simulation results to the experimental bubble density of 12.4094 mol/l. The surface is a fit to 30 simulation results with varying η and ξ . Solid slim line: η and ξ combinations yielding the experimental value. Solid bold lines: η and ξ combinations deviating by $\pm 1\%$ from the experiment. Lines in the η - ξ plane: projections of the lines from the surface.

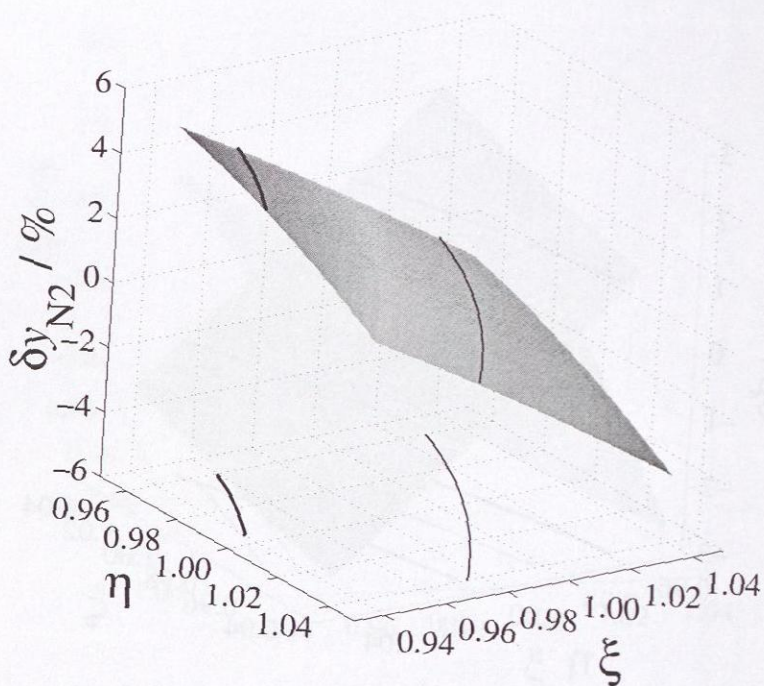


Figure 46: Dew point N_2 mole fraction of $N_2 + C_3H_6$ at 290 K and bubble point N_2 mole fraction of 0.1146 mol/mol: relative deviation of the simulation results to the experimental dew point N_2 mole fraction of 0.7497 mol/mol. The surface is a fit to 30 simulation results with varying η and ξ . Solid slim line: η and ξ combinations yielding the experimental value. Solid bold line: η and ξ combinations deviating by +4 % from the experiment. Lines in the η - ξ plane: projections of the lines from the surface.

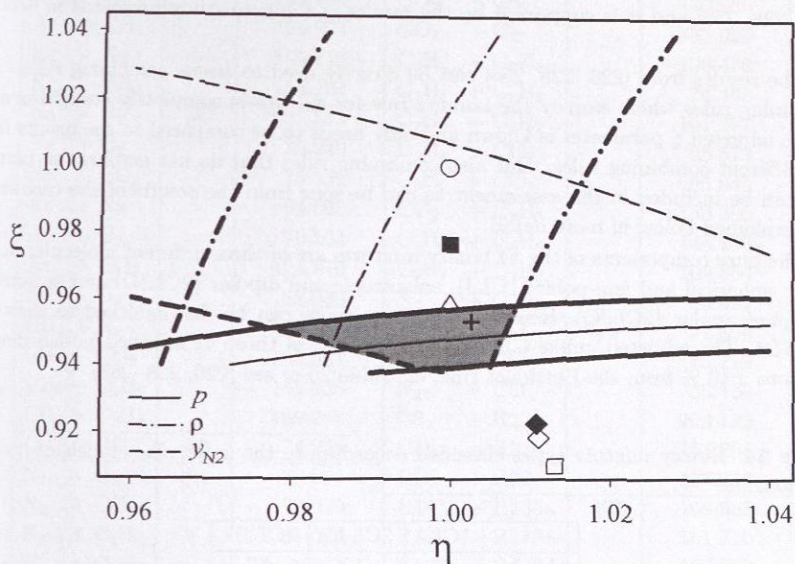


Figure 47: Plot analogous to Figure 43 for $N_2+C_3H_6$ at 290 K and bubble point N_2 mole fraction of 0.1146 mol/mol. The thin lines indicate the combinations of η and ξ where simulation and experiment coincide for the different properties. The thick lines represent the assumed uncertainties of $\delta p = \pm 3\%$, $\delta \rho = \pm 1\%$ and $\delta y_{N_2} = +4\%$. The predictions of the combining rules are given by: \circ LB, \blacksquare K, \triangle HMC, \square SK, \diamond WH, \blacklozenge M1, $+$ M2. The remaining four combining rules are not within the scale. Shaded: target area of η and ξ combinations yielding experimental values within their estimated uncertainties.

4.3 Comprehensive Study

The comprehensive study carried out in the present work for the assessment of combining rules is based on simulation results of 44 binary mixtures [226, 228, 258] from previous work. For describing the mixtures of that work, the Lorentz rule was used for σ_{ab} , while ϵ_{ab} was adjusted via the binary interaction parameter ξ as defined by Equation (33) to one binary experimental vapor pressure data point. That procedure was chosen in [226, 228, 258] and it is supported by the results of the case study presented in Section 4.2.

The results from [226, 228, 258] can be directly used to assess combining rules. For combining rules which employ the Lorentz rule for σ_{ab} this is completely straightforward as the adjusted ξ parameter is known and only needs to be compared to the results from the different combining rules. But also combining rules that do not employ the Lorentz rule can be included in the assessment as can be seen from the results of the case study and explained below in more detail.

The pure components of the 44 binary mixtures are of three different molecular model types: spherical and non-polar (1CLJ), anisotropic and dipolar (2CLJD) and anisotropic and quadrupolar (2CLJQ). Hence, six mixture types can be distinguished as shown in Table 24. The adjusted unlike LJ energy parameters of those 44 mixture models deviate by up to $\pm 10\%$ from the Berthelot rule, cf. Table 25 or see [226, 228, 258].

Table 24: Binary mixture types classified according to the molecular models of the two components.

	1CLJ	2CLJQ	2CLJD
1CLJ	#1	#2	#3
2CLJQ	—	#4	#5
2CLJD	—	—	#6

Seven of the eleven combining rules do not use the Lorentz rule for the unlike LJ size parameter. For an assessment, it has to be investigated by how much they deviate from the Lorentz rule. This was done here with the root mean squares (RMS)

$$\text{RMS}_g^x = \sqrt{\frac{1}{N} \sum_{i=1}^N (\eta_i^x - 1)^2}, \quad (34)$$

where $N = 44$ is the total number of mixture models to which the combining rules ($x = \text{H, S, SK, HHG, WH, M1, M2}$) were applied. In Table 26, RMS_g^x are given distinguishing between the mixture types #1 to #6.

Table 25: Unlike LJ energy parameters of the adjusted mixture models taken from [226, 228, 258], grouped according to the mixture type as defined by Table 24.

Mixture	Type	$[\epsilon_{ab}^{\text{adj}}/k_B] / \text{K}$	Mixture	Type	$[\epsilon_{ab}^{\text{adj}}/k_B] / \text{K}$	
Ne + Ar	#1	53.752	CO ₂ + C ₂ H ₆		128.878	
Ar + Kr		136.280	CO ₂ + CS ₂		170.086	
Ar + CH ₄		126.974	CO ₂ + Cl ₂		137.020	
Kr + Xe		190.225	C ₂ H ₄ + C ₂ H ₆		106.470	
Kr + CH ₄		156.184	C ₂ H ₄ + C ₂ H ₂		76.446	
Ne + N ₂	#2	32.513	C ₂ H ₆ + C ₂ H ₂		101.267	
Ne + O ₂		35.249	C ₂ H ₄ + CO ₂		95.579	
Ne + CO ₂		75.559	C ₂ F ₆ + CO ₂		105.045	
Ar + N ₂		64.065	CO ₂ + C ₃ H ₆		130.390	
Ar + O ₂		70.164	C ₂ H ₆ + C ₃ H ₆		146.450	
Ar + CO ₂		124.610	C ₂ H ₄ + C ₃ H ₆		109.654	
Kr + O ₂		82.030	N ₂ + C ₃ H ₆		69.491	
CH ₄ + N ₂		68.976	C ₂ H ₆ + CO		#5	72.304
CH ₄ + CO ₂		135.331	CO ₂ + CO			75.719
CH ₄ + C ₂ H ₆		142.225	N ₂ + CO			36.134
CH ₄ + C ₂ H ₄	109.268	CS ₂ + R22	203.132			
CH ₄ + CO	#3	74.256	CO ₂ + R22	154.666		
N ₂ + O ₂		#4	39.091	CO ₂ + R23	127.914	
N ₂ + CO ₂	70.979		R143a + R134a	#6	168.985	
N ₂ + C ₂ H ₆	67.344		R125 + R143a		161.770	
N ₂ + C ₂ H ₄	49.851		R125 + R134a		168.663	
O ₂ + CO ₂	74.255		R143a + R152a		177.304	

Table 26 shows that the S combining rule yields practically the same unlike LJ size parameters as the Lorentz rule for all mixture types. Also M2 and SK are very close, deviating by approximately 0.5 % only. The remainder, H, HHG, WH and M1, yield all mean deviations in a narrow band of 1.4 % and below. For mixture type #6, all seven combining rules yield results very close to the arithmetic mean due to fact that all components have very similar parameters.

Figures 43 and 47 give an impression of the influence of a η variation of 1 % on the mixture vapor-liquid equilibria. For the pressure and the dew point composition that variation will typically result in changes that do not exceed the experimental uncertainty. For the bubble density the changes are more significant but still the changes do not exceed 1 % in the bubble density. Thus, it can be concluded that there is only a small influence of

Table 26: Deviations of the unlike LJ size parameters from the arithmetic mean, i.e., the Lorentz rule, for seven combining rules expressed by the root mean square RMS_σ^x as defined by Equation (34) for the different mixture types and for all 44 binary mixture models.

Combining rule	$\text{RMS}_\sigma^x / \%$						
	Mixture type						
	#1	#2	#3	#4	#5	#6	all
S, Eq. (21)	0.0	0.0	0.0	0.0	0.0	0.0	0.0
M2, Eq. (30)	0.3	0.3	0.2	0.7	0.1	0.0	0.5
SK, Eq. (22)	0.7	0.6	1.1	0.5	0.3	0.0	0.6
HHG, Eq. (24)	0.9	1.0	0.7	1.7	0.5	0.0	1.2
H, Eq. (17)	1.0	1.8	0.3	1.2	0.5	0.1	1.3
M1, Eq. (28)	1.0	1.1	0.8	2.0	0.6	0.0	1.4
WH, Eq. (26)	1.0	1.2	0.9	2.0	0.7	0.0	1.4

the combining rules via σ_{ab} on vapor-liquid equilibrium data. Therefore, in the following only results of the combining rules for ξ are discussed.

Unlike LJ energy parameters predicted by the eleven combining rules are compared to the adjusted values in Figures 48 and 49 for each mixture. Figure 48 includes the results for the mixture types #1 to #3, Figure 49 for the mixture types #4 to #6. In these figures, the quality of the combining rules is indicated by the distance from the reference line (unity), which represents the adjusted LJ energy parameter. Generally, too low dispersion energies are predicted, which is particularly visible for mixture types #2 to #5. Note that it is implicitly assumed in Figures 48 and 49 that the adjusted parameter for ϵ_{ab} determined in [226, 228, 258] using the Lorentz rule for σ_{ab} also holds for the combining rules which apply other approaches for determining σ_{ab} . This is justified as discussed above.

To assess the predictive power of the eleven combining rules the deviations of the unlike LJ energy parameters of the particular combining rules from the adjusted values were summarized by the root mean square

$$\text{RMS}_\epsilon^x = \sqrt{\frac{1}{N} \sum_{i=1}^N (\epsilon_i^x - \epsilon_i^{\text{adj}})^2}. \quad (35)$$

The deviations for all eleven combining rules, distinguishing between mixture types, are given in Table 27. For mixture type #1, for which most of the eleven combining rules were tested, they are better than the LB combining rule. Many of them were fitted to noble gas mixture data and they indeed predict good unlike LJ energy parameters for

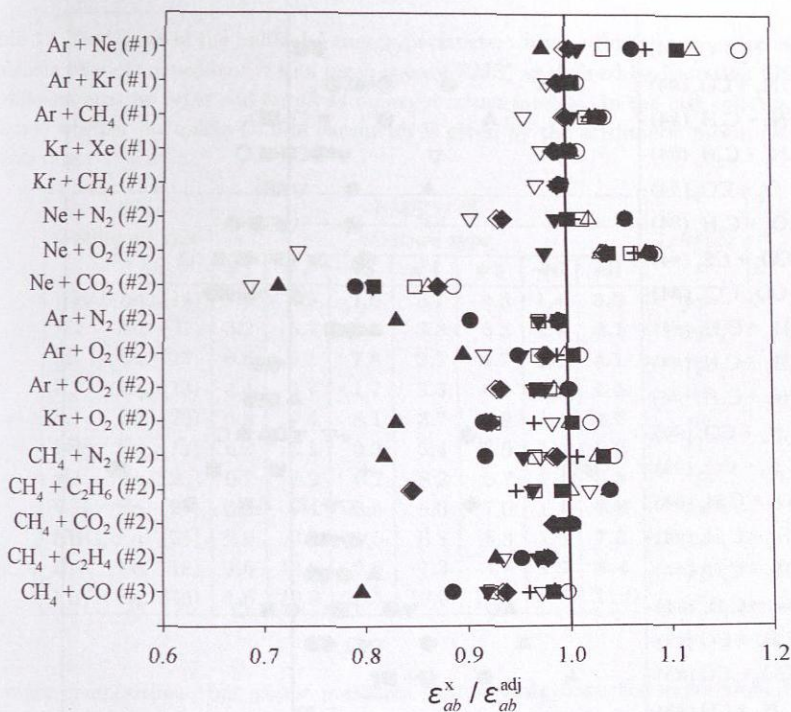


Figure 48: Predicted unlike LJ energy parameters ϵ_{ab}^x from eleven combining rules compared to adjusted values for the mixture types 1CLJ + 1CLJ (#1), 1CLJ + 2CLJQ (#2) and 1CLJ + 2CLJD (#3): \circ LB, \blacksquare K, \triangle HMC, \blacktriangle FH, ∇ H, \blacktriangledown S, \square SK, \bullet HHG, \diamond WH, \blacklozenge M1, $+$ M2.

such mixtures. The reason is that all combining rules, except LB and M2, yield smaller values than the geometric mean. Such a lower unlike dispersion energy is supported by experimental noble gas mixture data [36, 87, 118, 234]. However, for all other mixture types #2 to #5, the combining rules can predict better or worse than the simple LB combining rule. The fact that all combining rules predict similar for mixture type #6 is due to the very similar values of both LJ parameters of the pure components. All in all, the simple LB combining rule has a RMS_e^x of 5 % which is not significantly worse than those of the best rule (HMC) with 3.9 %, where a variation of ξ by 1 % influences the vapor pressure by about 5 %.

Apart from noble gas mixtures, it can be concluded that none of the investigated combining rules has a significant advantage over LB, which yields good bubble densities

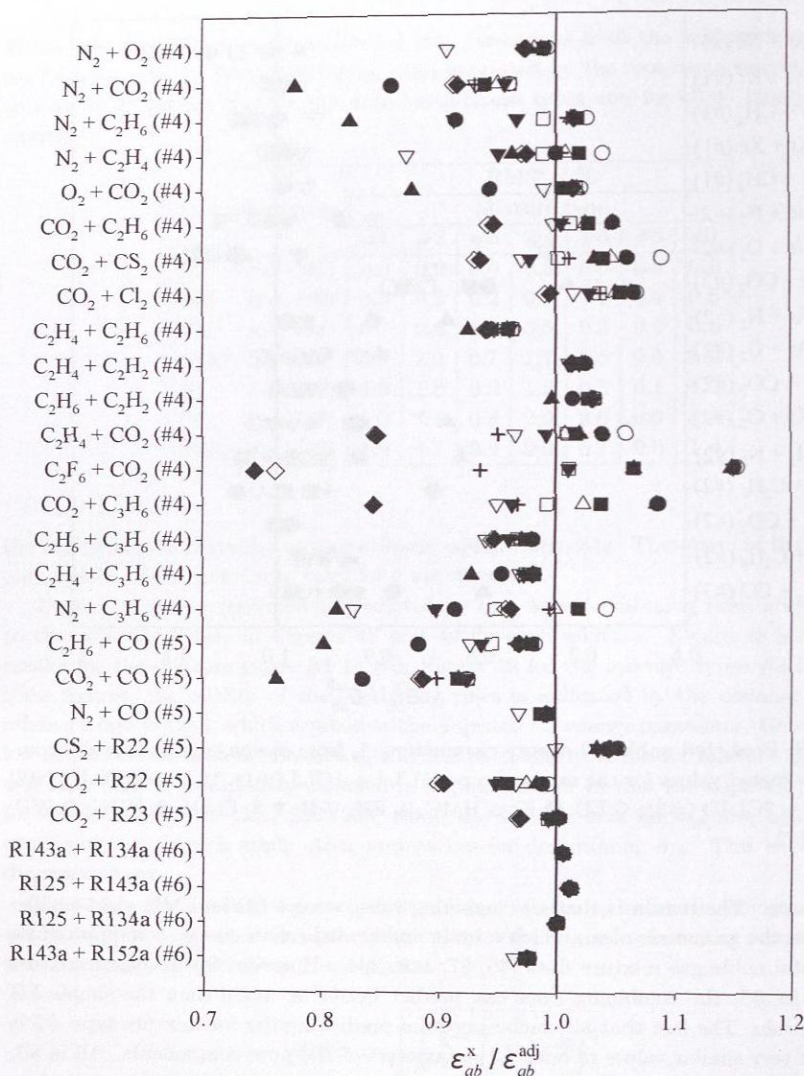


Figure 49: Predicted unlike LJ energy parameters ϵ_{ab}^x from eleven combining rules compared to adjusted values for the mixture types 2CLJQ + 2CLJQ (#4), 2CLJQ + 2CLJD (#5) and 2CLJD + 2CLJD (#6): \circ LB, \blacksquare K, \triangle HMC, \blacktriangle FH, ∇ H, \blacktriangledown S, \square SK, \bullet HHG, \diamond WH, \blacklozenge M1, $+$ M2.

Table 27: Deviations of the unlike LJ energy parameters from adjusted values for eleven combining rules expressed by the root mean square RMS_ϵ^x as defined by Equation (35) for the different mixture types and for all 44 binary mixture models. In the last column, it is indicated whether the unlike LJ size parameter is given by the arithmetic mean, i.e., the Lorentz rule.

Combining rule	$\text{RMS}_\epsilon^x / \%$							Lorentz
	Mixture type							
	#1	#2	#3	#4	#5	#6	all	
HMC, Eq. (14)	4.9	4.9	1.6	3.1	4.3	1.4	3.9	yes
M2, Eq. (31)	3.2	5.2	4.0	3.3	5.3	1.4	4.1	no
SK, Eq. (23)	0.8	6.1	7.8	2.5	4.7	1.3	4.1	no
K, Eq. (13)	4.4	6.7	1.7	3.3	4.6	1.5	4.5	yes
S, Eq. (20)	0.8	7.4	8.1	3.7	4.9	1.4	4.9	no
LB, Eq. (12)	6.8	5.1	0.3	5.4	3.9	1.4	5.0	yes
M1, Eq. (29)	0.7	7.2	6.2	8.2	6.7	1.4	6.8	no
WH, Eq. (27)	0.8	7.4	6.6	8.0	7.0	1.4	6.8	no
HHG, Eq. (25)	2.9	9.1	11.5	6.8	8.8	1.4	7.3	no
H, Eq. (18)	2.6	13.6	2.8	7.3	4.8	1.9	8.4	no
FH, Eq. (16)	1.6	13.9	20.5	10.0	13.3	0.7	11.0	yes

and vapor compositions, but vapor pressures that deviate from the experiment by an estimated 25 % on average. If highly accurate results for the vapor pressure are needed, an adjustment of the unlike LJ energy parameter to at least one experimental binary vapor pressure data point is necessary in most cases.

5 Molecular Simulation of Binary Hydrogen Bonding Mixtures

The prediction but also the description of thermodynamic properties of mixtures that contain both hydrogen bonding and non-hydrogen bonding components is a challenging task which can successfully be addressed by molecular modeling and simulation. Vapor-liquid equilibria are thermodynamic key properties as they are of particular technical interest, e.g., for separation processes, but they are also a good benchmark for evaluating thermodynamic models.

In the following study [203, 207], the molecular models for the pure hydrogen bonding fluids methanol, ethanol, monomethylamine, dimethylamine, methanethiol and formic acid, which are introduced in Chapter 3, are combined with the non-hydrogen bonding components neon, argon, krypton, xenon, methane, oxygen, nitrogen, carbon dioxide, ethyne, ethene, ethane, propylene, carbon monoxide, difluorodichloromethane (R12), tetrafluoromethane (R14), difluorochloromethane (R22), difluoromethane (R32), 1,1,1,2-tetrafluoroethane (R134a) and 1,1-difluoroethane (R152a). These non-hydrogen bonding models are of the model class one-center Lennard-Jones potentials (1CLJ) [255], symmetric two-center Lennard-Jones potentials either with a pointdipole (2CLJD) [227] or with a linear elongated pointquadrupole (2CLJQ) [255] and the model parameters were taken from those works.

The prerequisite to obtain quantitative mixture properties is the use of accurate and physically meaningful pure component models. The non-hydrogen bonding models used here turned out to be accurate in many applications such as in the description of vapor-liquid equilibria [227, 228, 255], of transport properties [67, 68], of Joule-Thomson inversion curves [259, 260] and of mixtures [226, 228, 258]. The performance of the new hydrogen bonding components regarding mixture properties is investigated in the following study on binary vapor-liquid equilibria. This study is also a validation of the physical relevance for the hydrogen bonding modeling approach used here, i.e., point charges superimposed on united-atom Lennard-Jones potentials, cf. Section 2.1.2.

The pure hydrogen bonding and non-hydrogen bonding models, are compatible to be applied in molecular simulations. The unlike electrostatic interactions are straightforwardly obtained according to the laws of electrostatics. The investigation of Chapter 4 on the influence of unlike LJ energy and size parameters on binary vapor-liquid equilibria shows that no combining rule can be presently accepted to accurately describe thermophysical properties of mixtures in general. The conclusion of this study is to use the Lorentz rule [147] for the unlike LJ size parameter and to adjust the state independent binary interaction parameter ξ as defined by Equation (33) to one reliable experimental binary vapor pressure. This modeling approach was investigated previously for mixtures which are composed of pure molecular models with one LJ parameter set.

The mixtures examined in the following are mixtures containing one hydrogen bonding

component and one non-hydrogen bonding component. The mixture model for this type of mixtures consist more than one unlike LJ energy parameter due to the asymmetrically modeled hydrogen bonding molecules. Despite this, only one ξ was adjusted for any pair of components, thus, the same ξ was applied to all unlike Lennard-Jones energy parameters.

A literature survey on binary vapor-liquid equilibria by molecular simulation containing the hydrogen bonding components mentioned above and non-self-associating components is given in Table 28. It shows that only relatively few mixtures of that type have been investigated so far by molecular simulation.

Table 28: Literature survey on molecular simulations of vapor-liquid equilibria (VLE) and Henry's law constants (HLC) by molecular simulation for binary mixtures containing the present hydrogen bonding components and (other) non-hydrogen bonding components.

Mixture (1 + 2)	Property	Ref.
methanol + C ₃ H ₆ O	VLE	[113]
methanol + CO ₂	VLE	[102, 139, 167, 187, 230, 246]
methanol + CO ₂	HLC	[246]
methanol + CHCl ₃	VLE	[113]
methanol + C ₂ H ₆	VLE	[139, 78]
methanol + C ₄ H ₈ , C ₄ H ₁₂ , MTBE	VLE	[137]
methanol + C ₃ H ₆ O ₂	VLE	[114]
methanol + C ₆ H ₁₄	VLE	[39, 187, 229]
methanol + C ₃ H ₈	VLE	[208]
ethanol + CO ₂	VLE	[102, 167]
ethanol + CH ₄ , O ₂ , N ₂ , CO ₂	HLC	[22, 44, 273, 281]
ethanol + C ₂ H ₆	VLE	[79, 80]
ethanol + R227ea	VLE	[58]
ethanol + C ₃ H ₈	VLE	[208]
methanethiol + C ₃ H ₈	VLE	[3]

5.1 Adjustment of Unlike Dispersive Interactions

The systematic study on the influence of unlike Lennard-Jones parameters on binary vapor-liquid equilibria of Chapter 4 showed that the Lorentz rule [147], cf. Equation (11), yields satisfying unlike Lennard-Jones size parameters but that the unlike Lennard-Jones energy parameter should be adjusted to one reliable experimental mixture vapor pressure to achieve a quantitative agreement between simulation and experiment. The unlike Lennard-Jones energy parameter is expressed in the following in terms of a binary interaction parameter ξ that corrects Berthelot's rule [18], cf. Equation (33).

Generally, increasing the binary interaction parameter ξ gives a stronger unlike dispersive attraction that decreases the mixture vapor pressure. In this study, it is investigated whether the same holds for the Henry's law constant: for higher values of ξ , the solubility of the solute is expected to be higher and thus the Henry's law constant lower. Following this, ξ was adjusted to either the binary vapor pressure or the Henry's law constant. It is interesting to validate whether mixture models which were adjusted to the vapor pressure also yield a quantitative correct Henry's law constant and vice versa.

Table 29 lists the binary interaction parameters ξ for 13 binary mixtures which were adjusted to one experimental vapor pressure. Three mixture types can be distinguished (in the order of increasing influence of the polarity): hydrogen bonding + spherical non-polar (mixture type #1), hydrogen bonding + anisotropic quadrupolar (mixture type #2) and hydrogen bonding + anisotropic dipolar (mixture type #3). These types are indicated in Table 29 which also includes the experimental data that were used for the adjustment. Furthermore, simulation results at these state points obtained with the adjusted ξ are given there.

Table 29: Binary interaction parameter ξ adjusted to an experimental vapor pressure (exp) and simulation result (sim), indicating the mixture type. The number in parentheses indicates the statistical uncertainty in the last digit.

Mixture (1+2)	Type	ξ	T K	x_2 mol/mol	p_{sim} MPa	p_{exp} MPa	Ref.
methanol + Ar	#1	1.031	273.15	0.0527	9.9 (4)	10.13	[217]
methanol + CH ₄		1.030	310	0.1227	17.0 (7)	17.24	[99]
ethanol + Ar		1.044	273.35	0.0556	7.5 (3)	7.6	[217]
methanol + CO ₂	#2	1.010	323.15	0.2373	4.80 (4)	4.75	[25]
methanol + C ₂ H ₂		1.090	303.15	0.2350	2.01 (8)	1.96	[120]
methanol + C ₂ H ₄		0.999	313.15	0.2303	6.27 (9)	6.2	[176]
methanol + C ₂ H ₆		1.020	298.15	0.2003	3.2 (1)	3.06	[103]
ethanol + C ₂ H ₆		1.044	298.15	0.3171	3.3 (1)	3.15	[26]
ethanol + C ₃ H ₆		0.955	368	0.2292	2.5 (2)	2.26	[198]
formic acid + CO ₂		0.950	393.15	0.3611	20.2 (5)	20.1	[34]
ethanol + CO	#3	1.081	323	0.0104	1.91 (5)	2	[240]
ethanol + R22		1.010	382.70	0.2998	2.77 (6)	2.364	[276]
methanethiol + CH ₃ Cl		0.986	313.15	0.5012	0.61 (2)	0.613	[60]

For 19 binary mixtures, ξ was adjusted to one experimental Henry's law constant which is given in Table 30 together with the simulation results. Experimental data for adjustment and comparison were obtained from Dortmund Data Bank [56].

In the following three sections, the modeling approach and the adjustment are assessed

Table 30: Binary interaction parameter ξ adjusted to an experimental Henry's law constant and simulation result (sim), indicating mixture type. The number in parentheses indicates the statistical uncertainty in the last digits.

Solvent	Solute	Type	ξ	T K	H_{sim} MPa	H_{exp} MPa	Ref.
ethanol	Ne	#1	0.620	298	935 (8)	926.8	[131]
ethanol	Kr		1.006	298	62 (1)	61.4	[21]
ethanol	Xe		0.988	298	20.3(6)	20.9	[190]
ethanol	CH ₄		1.040	298	79 (1)	78.9	[21]
methanol	CF ₄	#2	0.838	298.15	323 (13)	328.6	[21]
ethanol	O ₂		0.967	298.15	177 (2)	176.7	[21]
ethanol	N ₂		1.018	298.15	283 (4)	283	[21]
ethanol	CO ₂		0.992	298.15	15.9(3)	15.9	[119]
ethanol	C ₂ H ₂		0.967	248.15	2.7(9)	2.5	[166]
ethanol	C ₂ H ₄		1.010	298.15	16.1(9)	17.0	[23]
ethanol	CF ₄		0.831	298	234 (12)	220.1	[21]
monomethylamine	N ₂		0.991	308.15	250 (4)	246.7	[181]
dimethylamine	N ₂		0.940	308.15	135 (2)	132.9	[181]
formic acid	C ₂ H ₂		0.962	273.15	14 (2)	14.6	[179]
methanol	CO	#3	1.050	398	223 (3)	210.2	[48]
ethanol	R12		0.973	313	4.7(6)	4.4	[233]
ethanol	R32		0.889	313	6.4(3)	6.3	[233]
ethanol	R134a		0.974	303	2.5(4)	2.8	[233]
ethanol	R152a		0.963	303	2.6(3)	2.6	[233]

for selected examples of mixtures for all three mixture types. Those systems are selected, for which a broad experimental database is available for comparison. The results are discussed separately for the three mixture types on the basis of phase diagrams or plots of the Henry's law constant as a function of temperature. Graphical data are presented for 14 selected binary mixtures to keep the number of figures in an acceptable range. Numerical vapor-liquid equilibrium and Henry's law constant data are given for all 32 binary mixtures in Appendix B.1, Tables 34 and 35.

5.2 Mixtures with Spherical Non-polar Components

For the mixture methanol + methane, the binary interaction parameter ξ was adjusted to one experimental vapor pressure at 310 K, cf. Table 29. In this case, experimental data for both vapor-liquid equilibrium and Henry's law constant are available and it can be investigated whether these two property types are described consistently. Figure 50 shows a comparison of the vapor-liquid equilibria from the present mixture model to experimental data at 310 and 338.15 K. Simulation and experiment agree well for vapor pressure and dew point composition for both isotherms. It should be pointed out that the dew point composition is a predicted property, as ξ was adjusted to the vapor pressure only. Simulation results for Henry's law constant of methane in methanol are presented in Figure 51. In simulations at low temperatures and high densities, larger statistical uncertainties are encountered due to the calculation of the chemical potential by Widom's test particle method [269], cf. Section 2.2.2. However, Henry's law constant is predicted quite well, taking the experimental scatter into account and keeping in mind that ξ was adjusted to one experimental vapor pressure at 310 K only. Considering the experimental Henry's law constant from Figure 51, which is available up to 310 K only, it could be expected that Henry's law constant continues to increase with increasing temperature. However, the simulation results predict a minimum of solubility, i.e., maximum of the Henry's law constant, at about 350 K.

Also for ethanol + methane, both experimental vapor-liquid equilibrium and Henry's law constant data are available. The binary interaction parameter ξ of this mixture was adjusted to one experimental Henry's law constant at 298 K, cf. Table 30. Simulation results for the vapor-liquid equilibria at 333.4 and 398.15 K are presented in Figure 52 in comparison to experimental data. The two data sets match even slightly better than for methanol + methane. The agreement of the Henry's law constant of methane in ethanol using the same mixture model is favorable over the entire temperature range as shown in Figure 51.

The remaining binary mixtures of hydrogen bonding and spherical non-polar components, cf. Tables 29 and 30, which are not discussed here in detail, are represented with similar quality as the two mixture models discussed above.

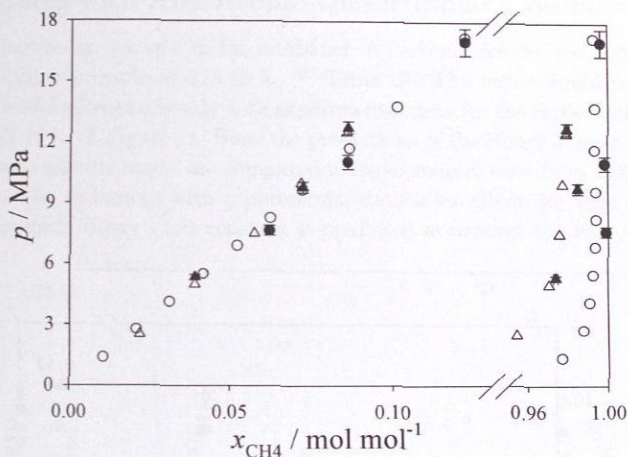


Figure 50: Vapor-liquid equilibria of methanol + methane: ● simulation data and ○ experimental data at 310 K [99]; ▲ simulation data and △ experimental data [279] at 338.15 K.

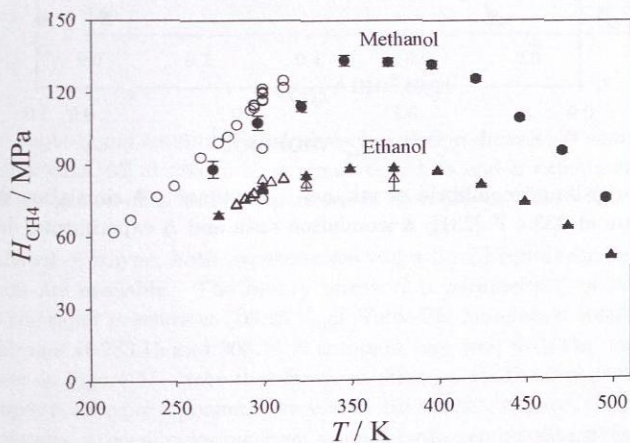


Figure 51: Henry's law constant of methane in methanol and ethanol: ● methanol simulation data; ○ methanol experimental data [21, 23, 19, 132, 134, 157, 159, 212, 236, 239]; ▲ ethanol simulation data; △ ethanol experimental data [21, 23, 75, 132, 239, 274, 275].

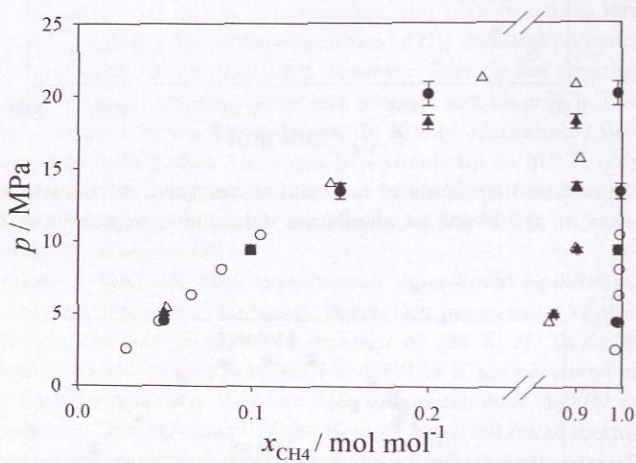


Figure 52: Vapor-liquid equilibria of ethanol + methane: ● simulation data and ○ experimental data at 333.4 K [231]; ▲ simulation data and △ experimental data [231] at 398.15 K.

5.3 Mixtures with Anisotropic Quadrupolar Components

The binary interaction parameter for methanol + carbon dioxide was adjusted to one experimental vapor pressure at 323.15 K, cf. Table 29. The vapor-liquid equilibria from this mixture model agree excellently with experimental data for the three isotherms 298.15, 323.15 and 373.15 K, cf. Figure 53. Here, the predictions of the Henry's law constant on the basis of the same mixture model are compared to experimental data from different sources, cf. Figure 54. The agreement with experimental data is excellent, for high temperatures again a maximum in Henry's law constant is predicted at around 450 K.

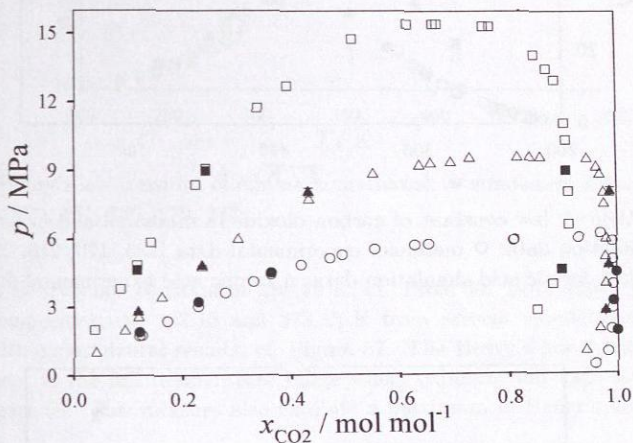


Figure 53: Vapor-liquid equilibria of methanol + carbon dioxide: ● simulation data and ○ experimental data [25] at 298.15 K; ▲ simulation data and △ experimental data [25] at 323.15 K; ■ simulation data and □ experimental data [25] at 373.15 K.

For methanol + ethyne, both experimental vapor-liquid equilibrium and Henry's law constant data are available. The binary interaction parameter ξ of this mixture was adjusted to one vapor pressure at 303.15 K, cf. Table 29. Simulation results for the vapor-liquid equilibrium at 283.15 and 303.15 K compare very well with the experimental data as can be seen in Figure 55. Note that for some state points the dew point mole fraction of the hydrogen bonding component is very low. Taking into account the finite number of sampled molecules, in some cases not even a single hydrogen bonding molecule remains in the simulated vapor phase. In such cases the simulation yields dew point mole fractions of the non-hydrogen bonding component of unity, where no statistical uncertainty is assigned, cf. Table 34. The agreement of the Henry's law constant of ethyne in methanol using the same mixture model is favorable over the entire temperature range as shown in Figure 56.

The binary interaction parameter for ethanol + carbon dioxide was adjusted to one

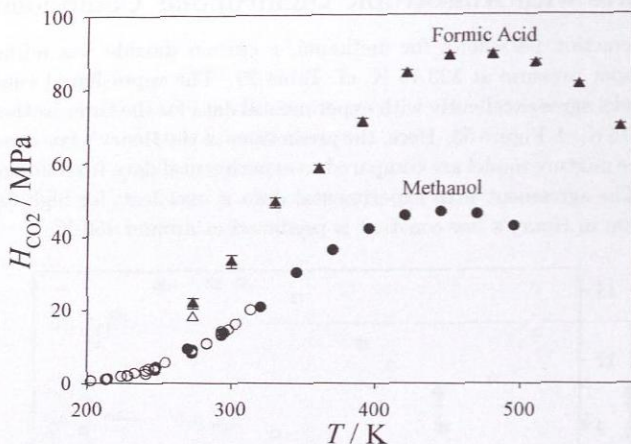


Figure 54: Henry's law constant of carbon dioxide in methanol and in formic acid: ● methanol simulation data; ○ methanol experimental data [125, 179, 210, 211, 222, 238, 250, 265, 266]; ▲ formic acid simulation data; △ formic acid experimental data [179].

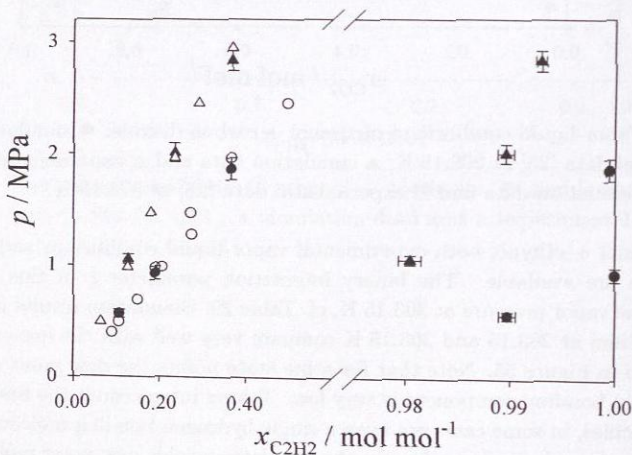


Figure 55: Vapor-liquid equilibria of methanol + ethyne: ● simulation data and ○ experimental data at 283.15 K [120, 196]; ▲ simulation data and △ experimental data [120] at 303.15 K.

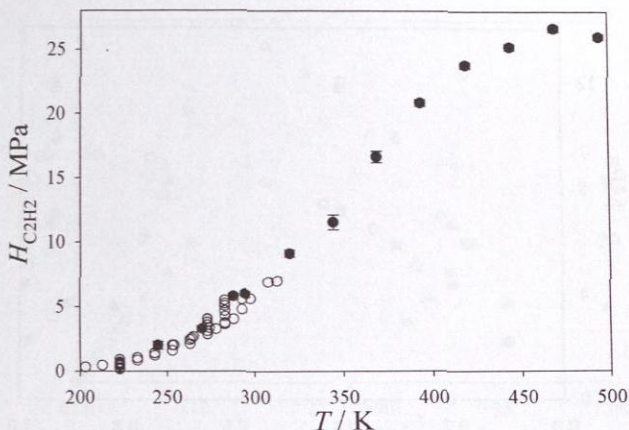


Figure 56: Henry's law constant of ethyne in methanol: ● simulation data and ○ experimental data [120, 161, 166, 179, 247].

experimental Henry's law constant at 298.15 K, cf. Table 30. Both vapor pressures and dew point compositions at 323.15 and 373.15 K from present simulations are in good agreement with experimental results, cf. Figure 57. The Henry's law constant is also in good agreement in the full temperature range where experimental data are available as shown in Figure 58. This mixture also exhibits a maximum in Henry's law constant at about 450 K.

The binary interaction parameter for ethanol + nitrogen was adjusted to one experimental Henry's law constant at 298.15 K, cf. Table 30. The vapor pressures at 298.22 and 398.02 K from present vapor-liquid equilibrium simulations are in good agreement with experimental results, cf. Figure 59. This system shows a lower gradient of the bubble line at 398.02 K compared to 298.22 K. This finding is consistent with the Henry's law constant of nitrogen in ethanol as shown in Figure 58 since the Henry's law constant of nitrogen in ethanol decreases, i.e., increasing solubility of nitrogen in liquid ethanol, with increasing temperature.

Also for ethanol + ethane, both experimental vapor-liquid equilibrium and Henry's law constant data are available and presented here. The binary interaction parameter ξ of this mixture was adjusted to one vapor pressure at 298.15 K, cf. Table 29. Simulation results for the vapor-liquid equilibrium at 298.15, 398.15 and 448.15 K are compared to experimental data in Figure 60. For all three temperatures, the vapor pressures and dew point compositions are predicted very well. The agreement of the Henry's law constant of ethane in ethanol using the same mixture model is favorable over the entire temperature range, almost reaching the critical temperature of the solvent, being within the

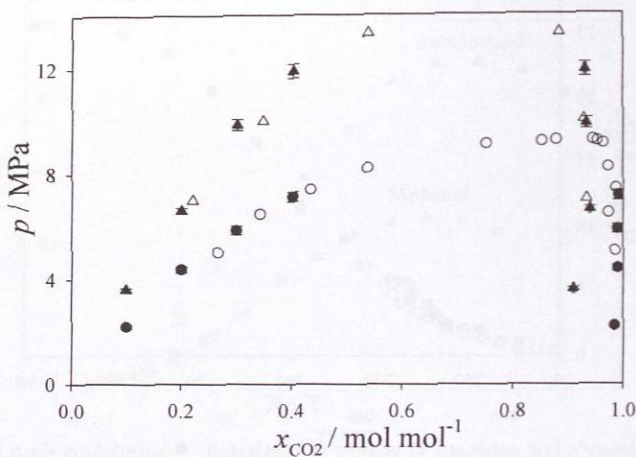


Figure 57: Vapor-liquid equilibria of ethanol + carbon dioxide: ● simulation data and ○ experimental data [136] at 323.15 K; ▲ simulation data and △ experimental data [183] at 373.15 K.

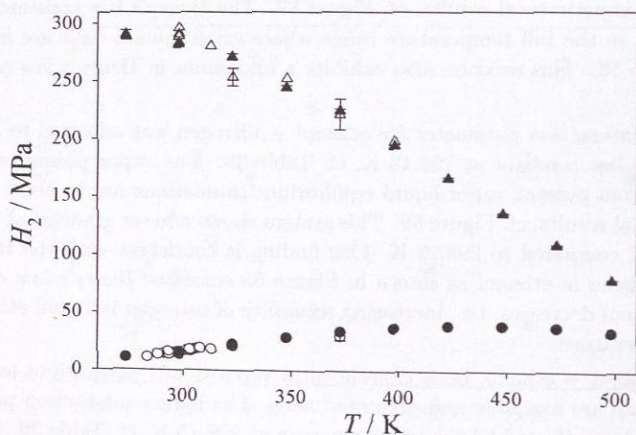


Figure 58: Henry's law constant of carbon dioxide (component 2) and nitrogen (component 2) in ethanol: ● simulation data and ○ experimental data [90, 119, 128, 150, 185, 232, 238, 271] with carbon dioxide; ▲ simulation data and △ experimental data [21, 23, 116, 174, 270] with nitrogen.

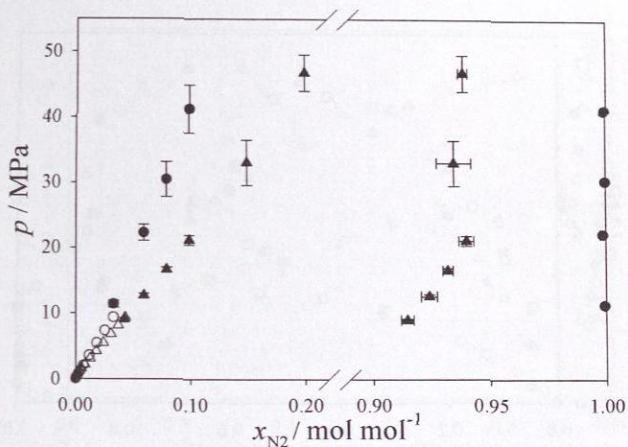


Figure 59: Vapor-liquid equilibria of ethanol + nitrogen: ● simulation data and ○ experimental data [270] at 298.22 K; ▲ simulation data and △ experimental data [270] at 398.02 K.

experimental scatter as shown in Figure 61.

The binary interaction parameter for ethanol + propylene was adjusted to one experimental vapor pressure at 368 K, cf. Table 29. Simulation results for the vapor-liquid equilibrium at 333.1 and 368 K compare well to experimental data for both temperatures, cf. Figure 62. The agreement of the Henry's law constant of propylene in ethanol using the same mixture model is not as good as for ethane at higher temperatures, cf. Figure 61. However, at lower temperatures also a favorable agreement was found being within the experimental scatter.

For formic acid + carbon dioxide, also both experimental vapor-liquid equilibrium and Henry's law constant data are available. The binary interaction parameter of this mixture was adjusted to a vapor pressure at 393.15 K. The vapor pressures and the dew point compositions of formic acid + carbon dioxide at 353.15 and 393.15 K from molecular simulation agree remarkably well with experimental data, cf. Figure 63. Only for the lowest bubble point mole fraction of carbon dioxide at 353.15 K, the vapor pressure is predicted too high. To our knowledge, for this binary system only one experimental Henry's law constant is available at 273.15 K, cf. Figure 54. A slightly lower solubility of carbon dioxide in liquid formic acid is predicted, which is consistent with the too high vapor pressure from simulation at the lowest bubble point mole fraction of carbon dioxide at 353.15 K.

The experimental data base for binary mixtures containing monomethylamine or dimethylamine in combination with the non-hydrogen bonding components from previous

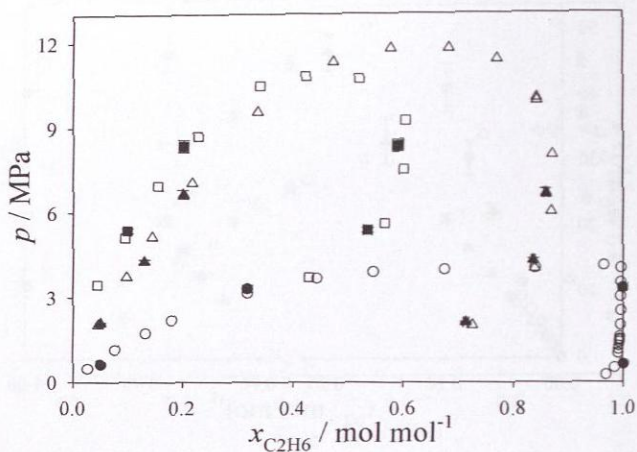


Figure 60: Vapor-liquid equilibria of ethanol + ethane: ● simulation data and ○ experimental data at 298.15 K [26, 85]; ▲ simulation data and △ experimental data [26] at 398.15 K; ■ simulation data and □ experimental data [26] at 448.15 K.

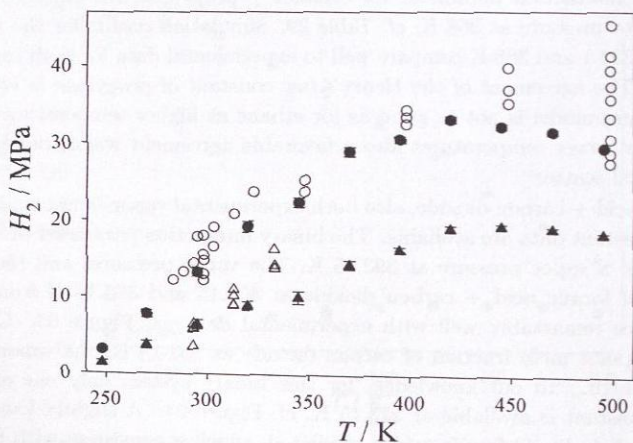


Figure 61: Henry's law constant of ethane (component 2) and propylene (component 2) in ethanol: ● simulation data and ○ experimental data [26, 159, 275] with ethane; ▲ simulation data and △ experimental data [86, 171] with propylene.

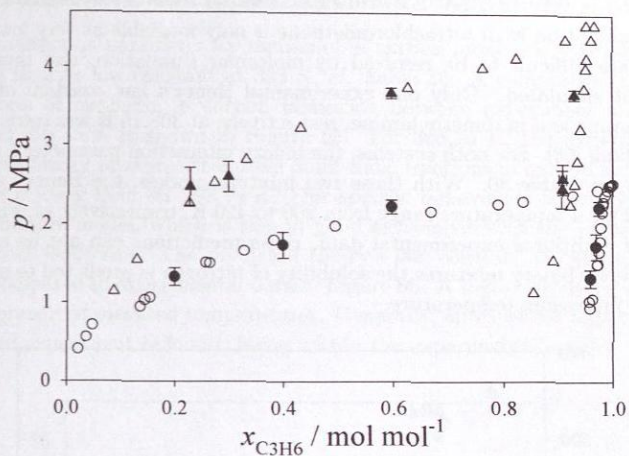


Figure 62: Vapor-liquid equilibria of ethanol + propylene: ● simulation data and ○ experimental data [86, 198] at 333.1 K; ▲ simulation data and △ experimental data [198] at 368 K.

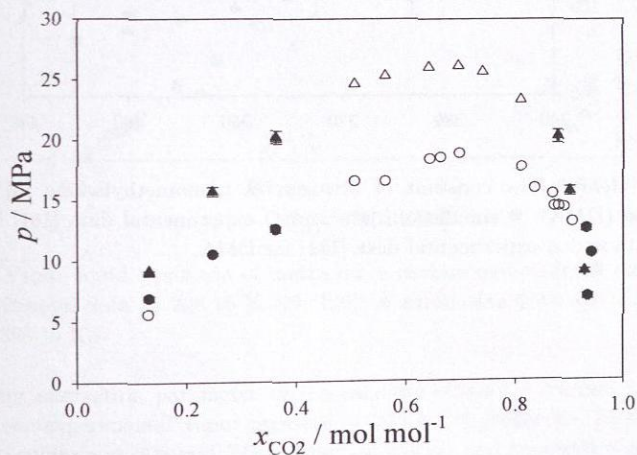


Figure 63: Vapor-liquid equilibria of formic acid + carbon dioxide: ● simulation data and ○ experimental data [34] at 353.15 K; ▲ simulation data and △ experimental data [34] at 393.15 K.

work [255, 227] is very narrow. Experimental data for monomethylamine and dimethylamine in combination with tetrachloromethane is only available at very low vapor pressures which are difficult to be resolved by molecular simulation, and thus, these systems were not simulated. Only one experimental Henry's law constant of nitrogen in monomethylamine and in dimethylamine, respectively, at 308.15 K was retrieved by Dortmund Data Bank [56]. For both systems, the binary interaction parameter ξ was adjusted to these data, cf. Table 30. With these two mixture models, the Henry's law constant was predicted for a temperature range from 260 to 420 K, respectively, cf. Figure 64. Due to the lack of additional experimental data, these predictions can not be assessed here. However, for both binary mixtures the solubility of nitrogen is predicted to monotonously increase with increasing temperature.

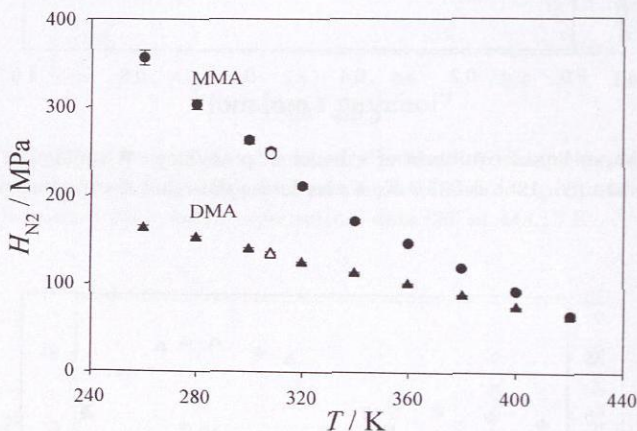


Figure 64: Henry's law constant of nitrogen in monomethylamine (MMA) and in dimethylamine (DMA): ● simulation data and ○ experimental data [181] for MMA; ▲ simulation data and △ experimental data [181] for DMA.

5.4 Mixtures of Anisotropic Dipolar Components

The binary interaction parameter for methanol + carbon monoxide was adjusted to one experimental Henry's law constant at 398 K, cf. Table 30. A comparison for the vapor-liquid equilibria of methanol + carbon monoxide between experiment and simulation at 298.15 and 398.15 K is shown in Figure 65. For 398.15 K, the experimental vapor pressure of this binary mixture for bubble point mole fractions of carbon monoxide above 0.03 mol/mol is lower than for 298.15 K. This specific behavior is correctly predicted by the present mixture model, which is also in good agreement with the experimental data throughout both isotherms. The predicted Henry's law constant of carbon monoxide in methanol is compared to experimental data in Figure 66. A higher solubility of methane in methanol is present at elevated temperatures. Generally, an excellent agreement between simulation and experiment is found, being within the experimental scatter.

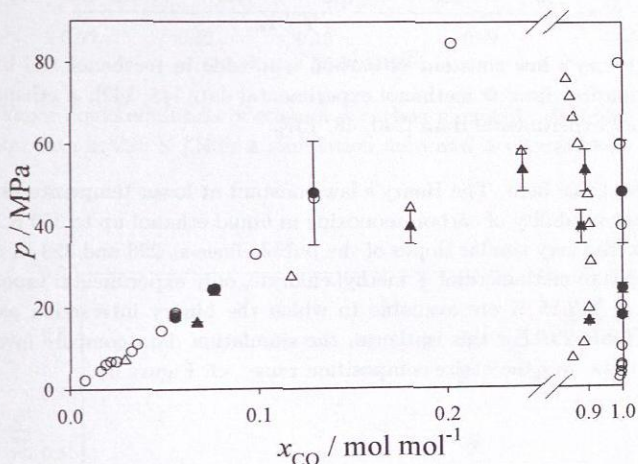


Figure 65: Vapor-liquid equilibria of methanol + carbon monoxide: ● simulation data and ○ experimental data at 298.15 K [25, 126]; ▲ simulation data and △ experimental data [25] at 398.15 K.

The binary interaction parameter of the mixture ethanol + carbon monoxide was adjusted to one experimental vapor pressure at 323 K, cf. Table 29. In Figure 67, the vapor-liquid equilibria at 298 and 323 K from simulation and experiment are compared, respectively, and a reasonable vapor pressure dependence is found. At these two temperatures the vapor pressures for the investigated bubble point mole fractions are very similar. The Henry's law constant prediction for carbon monoxide in ethanol is compared to experimental data in Figure 66. The agreement of the simulation to the experimental

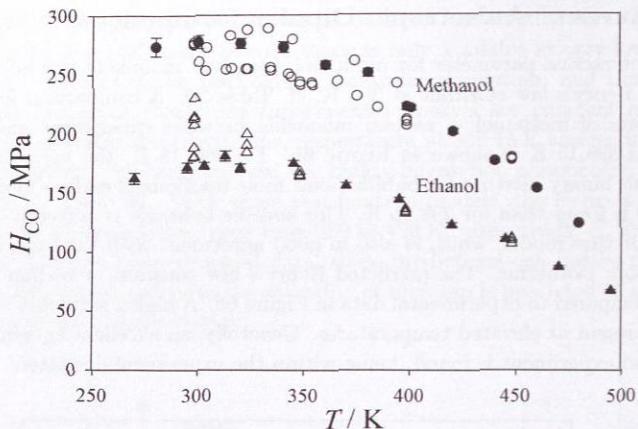


Figure 66: Henry's law constant of carbon monoxide in methanol and in ethanol: ● methanol simulation data; ○ methanol experimental data [48, 142]; ▲ ethanol simulation data; △ ethanol experimental data [240, 48, 157].

data is also favorable here. The Henry's law constant at lower temperatures indicates an almost constant solubility of carbon monoxide in liquid ethanol up to 350 K. This finding corresponds to the very similar slopes of the bubble lines at 298 and 323 K, cf. Figure 67.

For the mixture methanethiol + methyl chloride, only experimental vapor-liquid equilibrium data at 313.15 K are available to which the binary interaction parameter was adjusted, cf. Table 29. For this isotherm, the simulation data compare favorably to the experimental data over the entire composition range, cf. Figure 68.

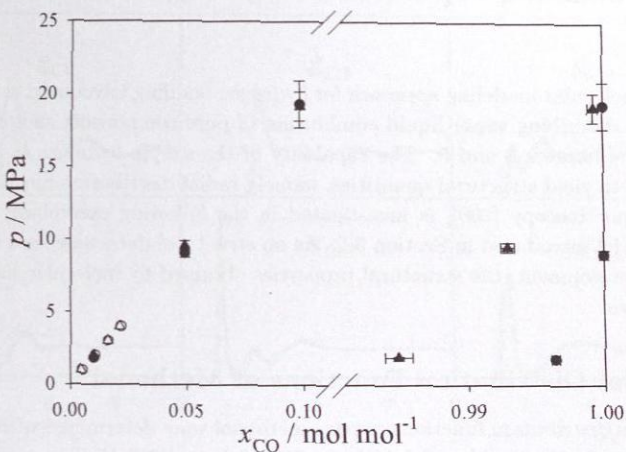


Figure 67: Vapor-liquid equilibria of ethanol + carbon monoxide: ● simulation data and ○ experimental data at 298 K [240]; ▲ simulation data and △ experimental data [240] at 323 K.

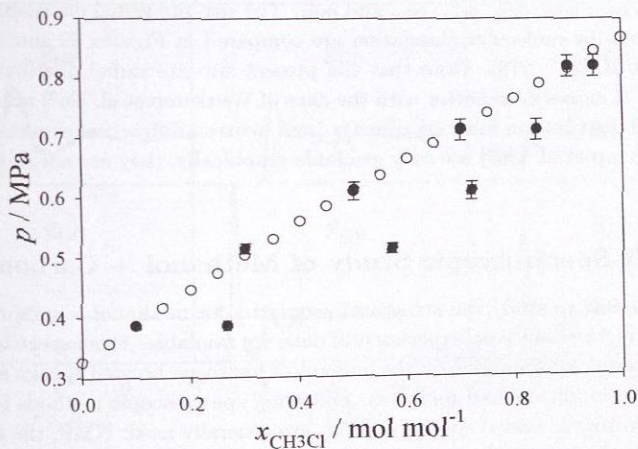


Figure 68: Vapor-liquid equilibria of methanethiol + methyl chloride at 313.15 K: ● simulation data and ○ experimental data [60].

6 Structural Properties of Hydrogen Bonding Fluids

The simple molecular modeling approach for hydrogen bonding introduced in Section 2.1.2 is fruitful for describing vapor-liquid equilibrium of pure components and of mixtures as shown in the Chapters 3 and 5. The capability of the simple hydrogen bonding modeling approach to yield structural quantities, namely radial distribution functions and data from NMR-spectroscopy [206], is investigated in the following exemplarily for the new methanol model introduced in Section 3.2. As no structural data were used in the molecular model development, the structural properties obtained by molecular simulations are fully predictive.

6.1 Radial Distribution Functions of Methanol

Site-site radial distribution functions of pure methanol were determined with NpT molecular simulations in the liquid at 0.1 MPa for 193.15 K and 298.15 K, respectively. These molecular simulation results are compared to site-site radial distribution functions of Yamaguchi et al. [277, 278] who used neutron diffraction experiments and empirical potential structure refinement (EPSR) to determine the entire set of ten site-site radial distribution functions g_{ab} . Since the present methanol model is based on an united-atom approach for the methyl group (C), only six site-site radial distribution functions can be distinguished here, namely, g_{CC} , g_{CO} , g_{CH} , g_{OO} , g_{OH} and g_{HH} . The site-site radial distribution functions determined here by molecular simulation are compared in Figures 69 and 70 to data of Yamaguchi et al. [277, 278]. Note that the present site-site radial distribution function g_{HH} at 298.15 K agrees even better with the data of Weitkamp et al. [267] who derived this site-site radial distribution function directly from neutron diffraction experiments. As the data of Weitkamp et al. [267] are only available graphically, they are not shown in Figure 70.

6.2 NMR-Spectroscopic Study of Methanol + Carbon Dioxide

It was not possible to study the structural properties for methanol in mixtures by radial distribution functions since no experimental data are available. From spectroscopic investigations, however, informations on the amount of hydrogen bonded species are accessible for both pure components and mixtures. Following spectroscopic methods for the determination of hydrogen bonded species in fluids are generally used: NMR, the absorption of electromagnetic infrared (IR) and near-infrared (NIR) radiation as well as the scattering of monochromatic light (Raman).

Data obtained with these spectroscopic methods were modeled using phenomenological self-association models based on physical and chemical theory. A survey on those studies

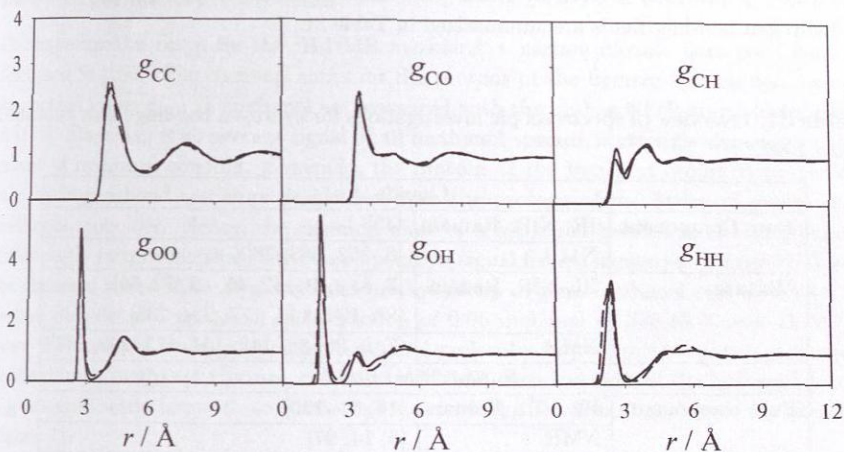


Figure 69: Site-site radial distribution functions g_{ab} over site-site distance r for liquid methanol at 0.1 MPa and 193.15 K: — simulation results; - - - results from neutron diffraction experiments [277, 278].

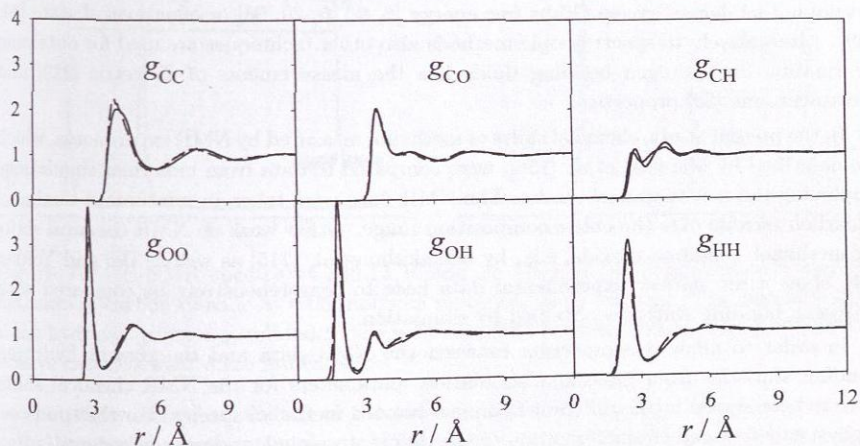


Figure 70: Site-site radial distribution functions g_{ab} over site-site distance r for liquid methanol at 0.1 MPa and 298.15 K: — simulation results; - - - results from neutron diffraction experiments [277, 278].

published before 1995 is given by Hasse [88]. More recent investigations on spectroscopy of hydrogen bonding fluids are summarized in Table 31.

Table 31: Overview of spectroscopic investigations for hydrogen bonding fluids published since 1995.

Liquids		
Pure Component	IR, NIR, Raman	[45]
	NMR	[6, 262, 263, 280]
Mixture	IR, NIR, Raman	[7, 8, 9, 10, 42, 46, 47, 72, 84] [88, 104, 143, 177, 224, 235]
	NMR	[7, 8, 20, 88, 143, 151, 173, 209, 237]
Supercritical Fluids		
Pure component	IR, NIR, Raman	[16, 31, 130]
	NMR	[6, 14, 97]
Mixture	IR, NIR, Raman	[117, 155]
	NMR	[13, 115]

The spectroscopic data given in the publications listed in Table 31 were used for developing models of excess Gibbs free energy [8, 9, 10, 20, 98] or equations of state [84, 169]. Alternatively to spectroscopic methods also other techniques are used for obtaining information on hydrogen bonding fluids like the measurements of dielectric [219] and solvatochromic [32] properties.

In the present study, chemical shifts of methanol measured by NMR experiments, which are described by Maiwald et al. [156], were compared to data from molecular simulations employing the new methanol model. The NMR data were taken in mixtures of methanol + carbon dioxide over the entire composition range. Other work on NMR chemical shifts for methanol + carbon dioxide, e.g., by Kanakubo et al. [115] as well as Bai and Yonker [14], show a too narrow experimental data base to comprehensively be compared with hydrogen bonding statistics obtained by simulation.

In order to allow a comparison between the NMR data and the present hydrogen bonding statistics from molecular simulation, parameters for the NMR chemical shifts have to be assigned to the different hydrogen bonded methanol species. For that purpose, a physically founded characterization of the different species types was introduced.

The NMR data, the criteria used to identify hydrogen bonded species in molecular simulation, the classification of the hydrogen bonded methanol species, the chemical shift assigned to these species and the comparison between the data from experiment and simulation are discussed in the following.

6.2.1 Experimental NMR Data

The experimental setup for the ^1H -NMR methanol + carbon dioxide data used here is discussed in [156]. The chemical shifts for the protons of the hydroxyl group δ_{OH} and of the methyl group δ_{CH_3} in methanol are measured with the on-line NMR setup introduced in [156]. Since δ_{OH} is an average signal of all methanol species, it strongly depends on the extent of hydrogen bonding. Generally, the protons of the hydroxyl group participating in a hydrogen bond are more deshielded than the protons of the hydroxyl group of a methanol monomer. Hence, the chemical shift of a hydrogen bonded hydroxyl group is significantly larger than that of the corresponding signal from a monomer. Figure 71 shows the chemical shifts of the hydroxyl and methyl group of pure methanol and methanol in carbon dioxide at a methanol mole fraction of 0.05 mol/mol at 338.15 K and 25 MPa. Since the extent of hydrogen bonded methanol molecules in pure methanol is higher than in the diluted methanol mixture, the observed NMR chemical shift of the hydroxyl group δ_{OH} is significantly larger than for the mixture with the small methanol mole fraction, cf. Figure 71.

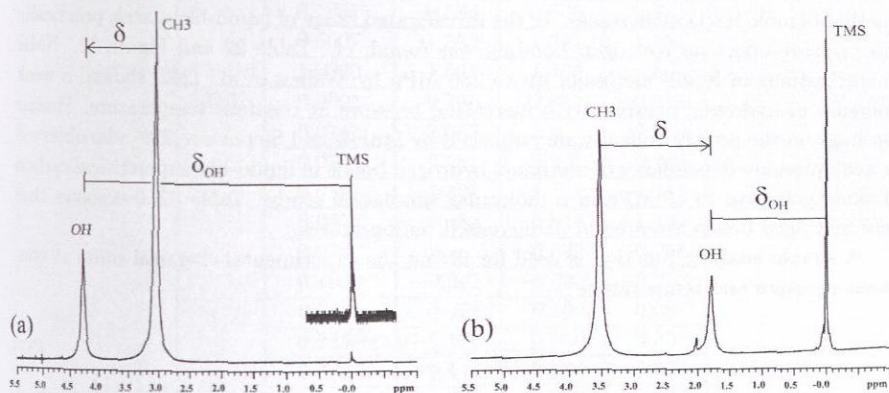


Figure 71: ^1H -NMR spectra at 338.15 K and 25 MPa of (a) pure methanol and (b) methanol + carbon dioxide at 0.05 mol/mol methanol mole fraction. The chemical shift of the hydroxyl group δ_{OH} related to the reference fluid tetramethylsilane (TMS) and the relative chemical shift δ are indicated.

The relative chemical shift δ of the protons in the hydroxyl group to those in the methyl group of the methanol molecule was used here to investigate the extent of hydrogen bonding. The relative chemical shift is also indicated in Figure 71 and it writes to

$$\delta = \delta_{\text{OH}} - \delta_{\text{CH}_3}. \quad (36)$$

This relative quantity is used to eliminate effects from changes in the bulk magnetic

susceptibility [97] and to avoid density effects and other nonspecific contributions to the nuclear shielding of the hydroxyl group [262, 263]. For the relative chemical shift "relative" is omitted in the following. The chemical shift is a weight-average over all methanol species, since the lifetime of a hydrogen bond, being in the order of a few picoseconds [89], is much shorter than the NMR resolution time. E.g., Astley et al. [11] found good agreement between the lifetime of hydrogen bonds obtained by molecular simulations and that from experiment. Following this, Molecular Dynamics simulation is appropriate to yield hydrogen bonding statistics as it can resolve this time scale straightforwardly.

The chemical shifts, to which the hydrogen bonding statistics of methanol in carbon dioxide are compared, were experimentally determined at 293.15, 308.15, 323.15 and 338.15 K, starting from small methanol mole fractions and covering the full composition range up to pure methanol for pressures of 10, 15 and 20 MPa. To obtain isobaric data, the original data were linearly interpolated. The result is given in Table 32. Uncertainties due to this interpolation are well within the experimental scatter. Despite that interpolation, the chemical shifts in Table 32 are called "experimental" in the following.

The data in Table 32 directly show that more hydrogen bonds are present when the methanol mole fraction increases. In the investigated range of liquid-like states, practically no pressure effect on hydrogen bonding was found, cf. Table 32 and Figure 72. NMR investigations of liquid methanol up to 280 MPa by Wallen et al. [262] showed a weak increase of hydrogen bonding with increasing pressure at constant temperature. Similar findings on the pressure effect were published by Stubbs and Siepmann [230] who observed a weak pressure dependence of methanol hydrogen bonds in liquid-like supercritical carbon dioxide going up to 40 MPa in a molecular simulation study. Table 32 also shows that less hydrogen bonds are present at increased temperatures.

A simple analytic function is used for fitting the experimental chemical shifts at constant pressure and temperature

$$\delta = a \frac{1 + b x_{\text{MeOH}}}{1 + c x_{\text{MeOH}}} \quad (37)$$

This function is not based on any chemical or physical consideration. Nevertheless, it is useful for extrapolating the chemical shift data to infinitely diluted methanol, i.e., for finding the monomer chemical shift δ_{M} . Thus, from fitting the parameters a , b and c of Equation (37) to the chemical shifts at constant temperature and pressure from Table 32, monomer chemical shifts in the range of -3.2 to -3.9 ppm were found. The arithmetic mean for all temperatures and pressures yields -3.356 ppm and was used subsequently. The monomer chemical shift δ_{M} found here is in good agreement with the findings of Asahi and Nakamura [6] who obtained $\delta_{\text{M}} = -3.45$ ppm. From methanol gas phase studies, Hoffmann and Conradi [97] found a monomer chemical shift of -3.40 ppm.

Table 32: Relative chemical shifts of methanol in mixtures with carbon dioxide resulting from an interpolation of experimental data [156].

T K	x_{MeOH} mol mol ⁻¹	δ / ppm		
		10 MPa	15 MPa	20 MPa
293.15	0.0052	-2.682	-2.721	-2.644
	0.0091	-2.534	-2.623	-2.510
	0.1152	0.436	0.267	0.408
	0.1857	0.829	0.600	0.827
	0.6607	1.511	n.a.	1.515
	1.0000	1.604	1.565	1.617
308.15	0.0091	-2.623	-2.608	-2.589
	0.0350	-1.547	-1.567	-1.519
	0.1857	0.584	0.546	0.531
	0.6607	1.382	1.381	1.384
	1.0000	1.501	1.505	1.504
323.15	0.0091	-2.730	-2.657	-2.579
	0.0141	-2.567	n.a.	-2.670
	0.0244	-2.181	-2.201	-2.204
	0.0591	-1.121	-1.192	-1.210
	0.0675	-0.484	-0.918	-1.137
	0.0746	n.a.	-0.892	-0.908
	0.1003	-0.391	-0.399	-0.253
	0.1632	0.128	0.104	0.087
	0.2454	0.571	0.550	0.556
	0.4784	0.941	0.964	0.978
	1.0000	1.340	1.343	1.346
338.15	0.0250	-2.255	-2.285	-2.252
	0.0531	-1.558	-1.681	-1.705
	0.0675	-1.315	-1.413	-1.172
	0.0936	-0.911	-0.869	-0.338
	0.1509	-0.273	-0.299	-0.048
	0.2454	0.375	0.359	0.369
	0.4784	0.661	0.844	0.856
	1.0000	1.218	1.222	1.232

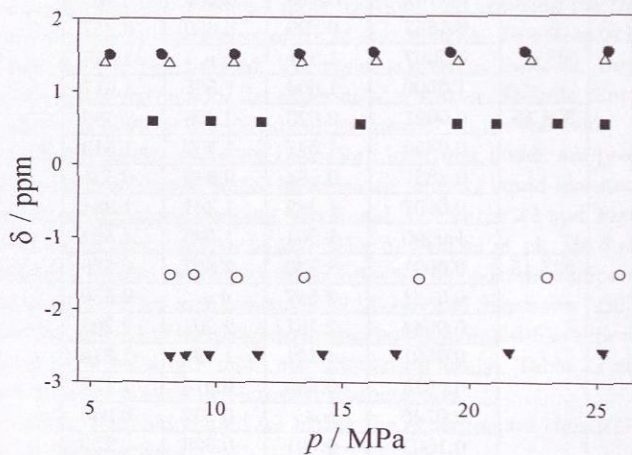


Figure 72: Relative chemical shifts of methanol in carbon dioxide at 308.15 K and different pressures for five methanol mole fractions: ▲ 0.0091 mol/mol; ○ 0.0350 mol/mol; ■ 0.1857 mol/mol; △ 0.6607 mol/mol; ● 1.0000.

6.2.2 Hydrogen Bonding Criteria and Types of Hydrogen Bonded Species

Several geometric or energetic criteria were proposed in the literature to identify hydrogen bonds in molecular simulation studies. Probably the most commonly applied criterion for hydrogen bonding of methanol is the geometric criterion introduced by Haughney et al. [89]. It was also used in the present study. This criterion was developed on the basis of experimental pair distribution functions of pure liquid methanol from X-ray and neutron scattering experiments. According to the geometric criterion of Haughney et al. [89], two methanol molecules in a molecular simulation are regarded as hydrogen bonded if their oxygen site-site separation distance r_{OO} is below 3.5 Å, and the hydrogen site to oxygen site distance r_{OH} is below 2.6 Å, and the angle between oxygen-oxygen alignment and oxygen-hydrogen bond $\theta_{O...OH}$ is below 30°. The molecular dynamics investigation of Chalaris and Samios [37] on hydrogen bonding in supercritical methanol supports the usefulness of this criterion at high pressure conditions.

Other authors suggested modifications of this geometric criterion. E.g., Wallen et al. [262] used the simple assumption that a hydrogen bond is established if r_{OH} is below 2.5 Å, arguing that this distance corresponds to the first minimum of the hydrogen bonding peak in the oxygen-hydroxyl hydrogen atom pair distribution function. In the Monte Carlo simulation study on self-association of methanol in supercritical CO₂ by Stubbs and Siepmann [230], the distance criterion for hydrogen bonds between methanol molecules is the same as the criterion proposed by Haughney et al. [89]. However, Stubbs and Siepmann used other limits for the orientation between hydrogen bonded methanol molecules. A slightly modified geometric criterion for the self-association was applied by Chatzis and Samios [38] in a simulation study of methanol in supercritical CO₂: r_{OO} below 3.6 Å, r_{OH} below 2.5 Å and $\theta_{O...OH}$ below 30°. Note that these two studies [22,23] used other molecular models than those of the present work. Furthermore, Chatzis and Samios [38] additionally investigated hydrogen bonding between methanol and CO₂ which was not done here.

In the present work, Molecular Dynamics simulations of methanol + carbon dioxide at specified temperature, pressure and composition were carried out. Simulation details to these simulations for hydrogen bonding statistics are given in Appendix A.3. The distribution of hydrogen bonded methanol species, with $i = 0, 1, 2,$ and 3 hydrogen bonds per molecule, was determined using the hydrogen bonding criterion of Haughney et al. [89]. The species fraction f_i is the number of methanol molecules with i hydrogen bonds divided by the total number of methanol molecules. In Figure 73, some important configurations of hydrogen bonded methanol molecules are illustrated. The reference molecule for which the hydrogen bond status is classified is labeled by * in Figure 73. The f_0 relates to methanol molecules that are not hydrogen bonded, thus methanol monomers, cf. Figure 73 (a). Molecules being part of dimers, cf. Figure 73 (b) and (c), as well as molecules at the two ends of a hydrogen bonded chain (not shown in Figure 73) contribute to f_1 . Molecules within a chain, e.g., the central molecule of a trimer, contribute to f_2 , cf. Figure

73 (d) and (e). Note that the present statistics does not distinguish whether a chain of hydrogen bonded methanol molecules is linear or cyclic. Molecules that cross-link chains or central molecules in tetramers contribute to f_3 , cf. Figure 73 (f).

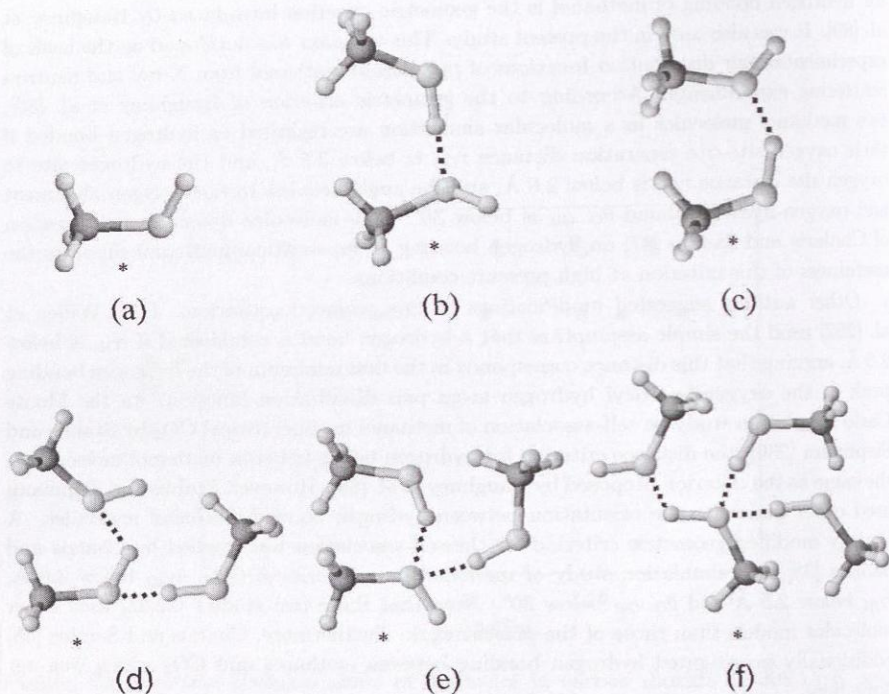


Figure 73: Important hydrogen bonded methanol molecule configurations. The reference molecule is indicated by *. (a) monomer: f_0 ; (b) and (c) dimers: f_1 ; (d) and (e) central molecule of a trimer: f_2 ; (f) cross-linking central molecule of a tetramer: f_3 .

The experimental chemical shift δ is assumed here to be a superposition of the signal for three different methanol species: monomers, methanol molecules which act as proton donors and methanol molecules which act as proton acceptors in a hydrogen bond. The chemical shifts of these three methanol species are labeled as δ_M , δ_D and δ_A , respectively.

The contribution of the monomers to the observed chemical shift is $f_0\delta_M$, cf. Figure 73 (a). Half of the species with one hydrogen bond are donors, the other half acceptors. This holds both for dimers and the two ends of a chain, cf. Figure 73 (b) and (c). Thus, their contributions are $0.5f_1\delta_A + 0.5f_1\delta_D$. The assignment of f_2 is not straightforward. For

molecules acting both as proton donors and acceptors as in Figure 73 (d), it is assumed that the deshielding of the hydroxyl group is primarily determined by the proton donation, and such molecules are assigned to δ_D only. The central molecule in configuration of Figure 73 (e) acts as the proton acceptor twice. It was found in the present molecular simulations that this type of configuration practically does not occur. Hence, it can be assumed that all species in f_2 exhibit the chemical shift δ_D so that the corresponding contribution is $f_2\delta_D$. For the reason given above, i.e., deshielding by proton donation, species with three hydrogen bonds are assigned to δ_D and the last contribution to the observed chemical shift is $f_3\delta_D$. Following all these considerations, the chemical shift is

$$\delta = f_0\delta_M + \frac{f_1}{2}\delta_A + \left(\frac{f_1}{2} + f_2 + f_3\right)\delta_D. \quad (38)$$

6.2.3 Hydrogen Bonding Statistics from Molecular Simulation

Detailed information on the fractions of differently hydrogen bonded species can be obtained from molecular simulation. The quality of these predictions is assessed here by a comparison of calculated and experimental chemical shifts. The distribution of methanol molecules f_i was calculated from NpT ensemble Molecular Dynamics simulations at experimental temperatures, pressures and methanol mole fractions specified in Table 32. Additional simulations were performed at methanol mole fractions of 0.1, 0.2, 0.4, 0.6 and 0.8 mol/mol. Tables 36 to 39 in Appendix B.2 summarize the simulation results for the distribution of differently hydrogen bonded methanol species at these conditions. Figures 74 to 77 show the dependence of f_0 to f_3 on the methanol mole fraction and temperature at the pressure 15 MPa. Due to the weak pressure influence, plots for the other pressures show only very little differences compared to Figures 74 to 77 and are omitted here.

As expected, it can be seen from Figure 74 that the fraction of methanol monomers f_0 increases with increasing temperature and decreasing methanol mole fraction. Also the fraction f_1 , i.e., one hydrogen bond per methanol molecule, increases with increasing temperature, cf. Figure 75. However, the influence of the methanol mole fraction on f_1 is not monotonous and a maximum is observed at methanol mole fractions between about 0.1 and 0.2 mol/mol. Consistently to f_0 and f_1 , the fraction f_2 increases with decreasing temperature and increasing methanol mole fraction, cf. Figure 76. At small methanol mole fractions close to infinite dilution, practically no chains were observed. The fraction f_3 of cross-linking molecules in branched chains or tetramers increases with increasing methanol mole fraction but decreases with temperature, cf. Figure 77. The fraction of this type of species is small compared to the other species types. As for the experimental data in Table 32, the pressure influence can not be resolved in the hydrogen bonding statistics from simulation results, cf. Tables 36 to 39 in Appendix B.2.

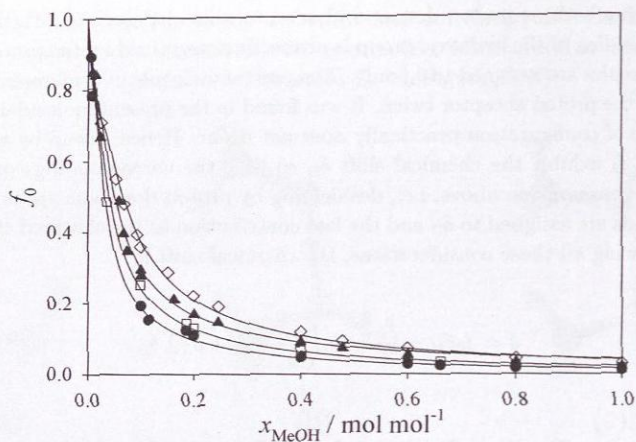


Figure 74: Hydrogen bonding of methanol (MeOH) in carbon dioxide from molecular simulation. Fraction f_0 (unbonded methanol) at 15 MPa: ● 293.15 K, □ 308.15 K, ▲ 323.15 K, ◇ 338.15 K, — guide for the eye. The statistical uncertainties are generally within the symbol size.

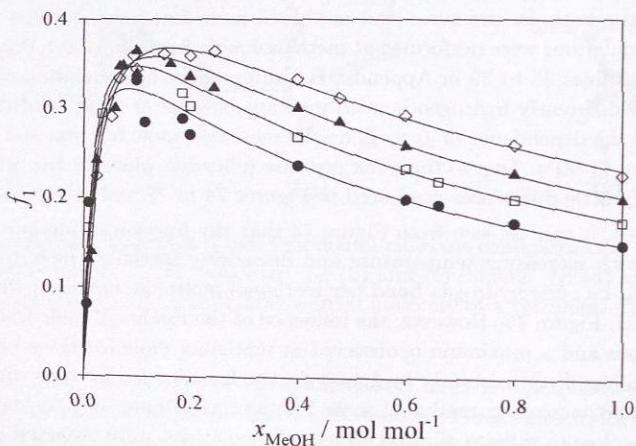


Figure 75: Hydrogen bonding of methanol (MeOH) in carbon dioxide from molecular simulation. Fraction f_1 (one hydrogen bond per methanol molecule) at 15 MPa: ● 293.15 K, □ 308.15 K, ▲ 323.15 K, ◇ 338.15 K, — guide for the eye. The statistical uncertainties are generally within the symbol size.

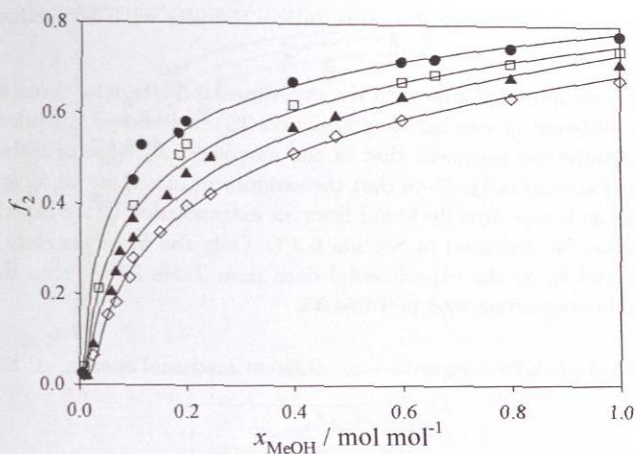


Figure 76: Hydrogen bonding of methanol (MeOH) in carbon dioxide from molecular simulation. Fraction f_2 (two hydrogen bonds per methanol molecule) at 15 MPa: ● 293.15 K, □ 308.15 K, ▲ 323.15 K, ◇ 338.15 K, — guide for the eye. The statistical uncertainties are generally within the symbol size.

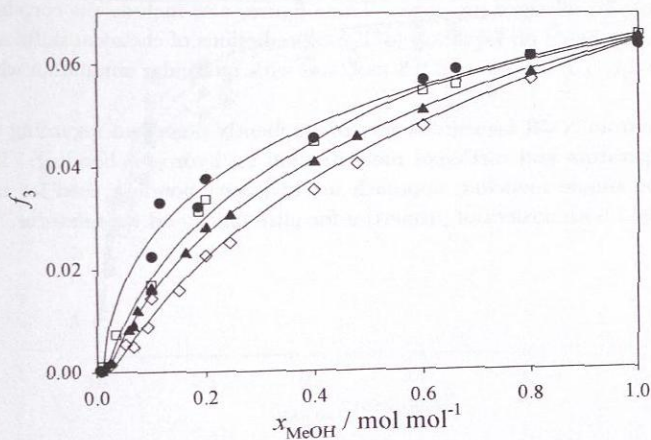


Figure 77: Hydrogen bonding of methanol (MeOH) in carbon dioxide from molecular simulation. Fraction f_3 (three hydrogen bonds per methanol molecule) at 15 MPa: ● 293.15 K, □ 308.15 K, ▲ 323.15 K, ◇ 338.15 K, — guide for the eye. The statistical uncertainties are generally within the symbol size.

6.2.4 Comparison of Molecular Simulation Results with Experimental NMR Data

To compare the simulation results with the experimental NMR data, chemical shifts were assigned to the different species based on Equation (38) as discussed in Section 6.2.2. Only three chemical shifts are assigned, that of the monomers δ_M , that of hydrogen bonded donors δ_D and of acceptors δ_A . Note that the assignment of a value for δ_M is unrelated to simulation data as it was directly found from an extrapolation of the experimental data to infinite dilution as explained in Section 6.2.1. Only the fit of the state independent parameters δ_D and δ_A to the experimental data from Table 32 relies on the simulation data. The results are summarized in Table 33.

Table 33: Chemical shifts assigned to the different methanol species, cf. Equation (38).

δ_M	δ_A	δ_D
ppm	ppm	ppm
-3.356	-1.845	1.876

The predictions of the chemical shifts applying δ_M , δ_D and δ_A from Table 33 together with the hydrogen bonding statistics from the molecular simulation are compared to the experimental data for 10, 15 and 20 MPa in Figures 78 to 80, respectively. The agreement is very favorable for all three pressures. These figures also include the correlation of the experimental data based on Equation (37) and predictions of chemical shifts at methanol mole fractions 0.1, 0.2, 0.4, 0.6 and 0.8 mol/mol with molecular simulation which also fit well.

The results from NMR measurements are excellently described regarding of both the effects of temperature and methanol mole fraction on hydrogen bonding. This finding shows that the simple modeling approach for hydrogen bonding used for methanol is sufficient to yield both structural properties for pure fluids and for mixtures.

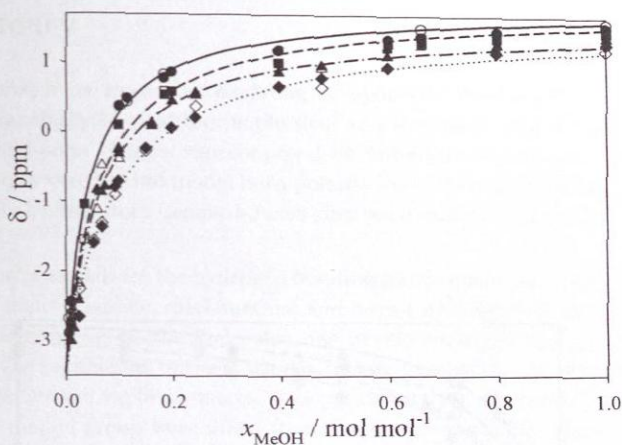


Figure 78: Comparison of chemical shifts from molecular simulation, experiment and fit following Equation (37) at 10 MPa. 293.15 K: ● simulation, ○ experiment, — fit; 308.15 K: ■ simulation, □ experiment, --- fit; 323.15 K: ▲ simulation, △ experiment, ... fit; 338.15 K: ◆ simulation, ◇ experiment, ··· fit.

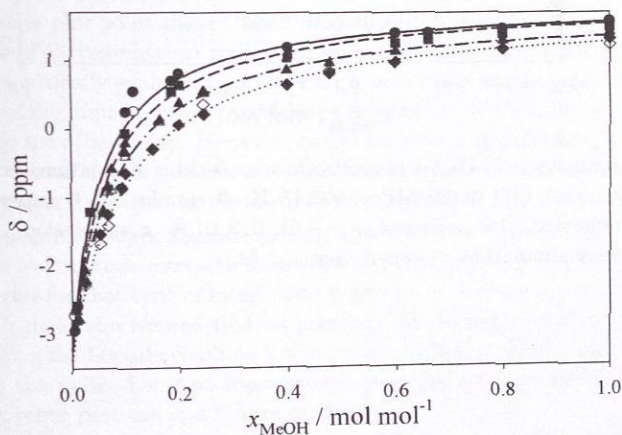


Figure 79: Comparison of chemical shifts from molecular simulation, experiment and fit following Equation (37) at 15 MPa. 293.15 K: ● simulation, ○ experiment, — fit; 308.15 K: ■ simulation, □ experiment, --- fit; 323.15 K: ▲ simulation, △ experiment, ... fit; 338.15 K: ◆ simulation, ◇ experiment, ··· fit.

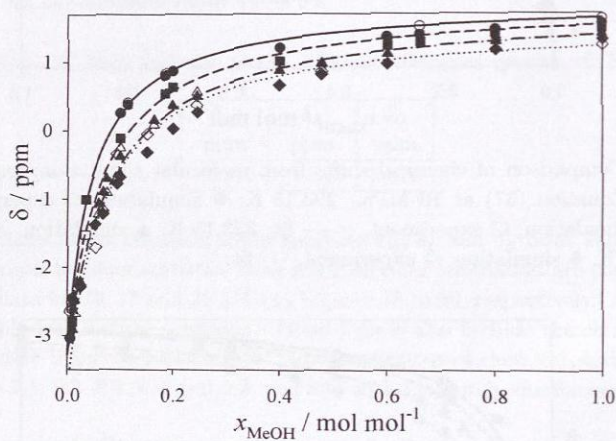


Figure 80: Comparison of chemical shifts from molecular simulation, experiment and fit following Equation (37) at 20 MPa. 293.15 K: ● simulation, ○ experiment, — fit; 308.15 K: ■ simulation, □ experiment, --- fit; 323.15 K: ▲ simulation, △ experiment, -.- fit; 338.15 K: ◆ simulation, ◇ experiment, ··· fit.

7 Summary

A simple approach for molecular modeling of hydrogen bonding fluids is investigated regarding its capability to yield thermophysical and structural properties. This approach is based on rigid point charges superimposed on united-atom Lennard-Jones potentials. The point charges were used to model both polarity and hydrogen bonding of the molecule simultaneously. United-atom Lennard-Jones sites were used to account for dispersion and repulsion.

New molecular models for the hydrogen bonding components methanol, ethanol, monomethylamine, dimethylamine, methanethiol and formic acid were developed based on this approach. The geometry of the molecules was mostly obtained with quantum chemical calculations. The parameters of the hydrogen bonding group were adjusted to experimental bubble densities and vapor pressures. The parameters for the remaining Lennard-Jones centers of the methyl group were taken from Ungerer et al. [244]. These new molecular models for hydrogen bonding fluids describe bubble density, vapor pressure and enthalpy of vaporization with mean unsigned deviations of typically less than 0.6, 6 and 5 %, respectively, compared to experimental correlations. These deviations hold for temperatures close to the triple point up to temperatures close to the critical point. The new models require comparably little computational resources for simulation and they belong to the most accurate models in literature for describing thermophysical properties.

Lennard-Jones plus point charge based models were previously used by many authors for predictions of thermophysical properties of water. Literature models for water from that class were critically evaluated and new improved water models were suggested here. The accuracy of the improved water models for describing vapor-liquid equilibria is not as favorable as for the other fluids. However, one of the new water models, i.e., the all-atom model, shows overall better performance than existing Lennard-Jones plus point charge based water models from literature regarding thermophysical properties.

In mixtures, unlike interactions are present and have to be specified in molecular simulations. Unlike electrostatic interactions are described by physical laws and no adjustment or combining rule for that type of interaction is necessary. Previous investigations of mixtures on simple molecules showed that an excellent description of mixture properties can be obtained using the Lorentz combining rule for the unlike Lennard-Jones size parameter and adjusting the unlike Lennard-Jones energy parameter to one reliable experimental data point for vapor pressure of a binary mixture.

To gain more insight in Lennard-Jones based molecular modeling of mixtures, the influence of unlike Lennard-Jones parameters on bubble density, vapor pressure and dew point composition for mixtures composed of simple molecules was investigated in a systematic study. The simple molecules were modeled by symmetric Lennard-Jones potentials. The systematic study showed that by using the Lorentz combining rule for the unlike Lennard-Jones size parameter favorable bubble densities are obtained regardless

the choice of the unlike Lennard-Jones energy parameter. A further conclusion of the systematic study is that it is necessary to adjust the unlike Lennard-Jones energy parameter to achieve quantitative vapor pressure description. A part of the systematic study was to investigate whether combining rules, which use solely pure component data, can give appropriate unlike Lennard-Jones parameters. With none of 11 examined combining rules unlike Lennard-Jones energy parameters were obtained which allow accurate vapor pressure simulation. Hence, if accurate vapor pressure information is needed, it is desirable to have at least one experimental data point to which the binary unlike Lennard-Jones energy parameter can be adjusted. For cases where no adjustment is possible due to the lack of experimental vapor pressures, it can be recommended to use the Hudson-McCourbrey or Lorentz-Berthelot combining rules.

Following this systematic study, binary interaction parameters were adjusted for 32 binary mixtures containing the new hydrogen bonding components methanol, ethanol, monomethylamine, dimethylamine, methanethiol and formic acid, together with spherical non-polar one-center Lennard-Jones (1CLJ), symmetric anisotropic two-center Lennard-Jones plus dipole (2CLJD) or quadrupole (2CLJQ) models which were taken from previous work. All of the 32 binary mixture models consist of more than one set of unlike Lennard-Jones parameters due to the asymmetric shape of the hydrogen bonding components. Nonetheless, still only one binary interaction parameter was applied for a pair of unlike molecules. The binary unlike Lennard-Jones energy parameter was adjusted to either Henry's law constant data or vapor pressure data. The excellent description of vapor-liquid equilibria over wide temperature and composition ranges showed that only one state independent binary interaction parameter is sufficient also for mixtures with asymmetric molecules. Another finding of this mixture study is that the adjustment of the binary interaction parameter to either a Henry's law constant or vapor pressure is interchangeable.

The investigation of the chosen modeling approach for hydrogen bonding fluids in the present work also includes a study on the prediction of structural data. Due to the lack of experimental data, the prediction of structural data was exemplarily investigated for methanol only. Experimental site-site radial distribution functions for methanol are available from neutron diffraction measurements which are shown here to compare favorably to the results from molecular simulation. For mixtures, the presence of experimental structural data is even more scarce than for pure fluids. Since information on hydrogen bonded species can be derived from spectroscopic data, NMR experiments for methanol + carbon dioxide at elevated pressures were carried out. Only two state independent parameters for chemical shifts of hydrogen bonded methanol species had to be adjusted to the NMR data in order to achieve an excellent agreement for a large chemical shift data set. This shows that the simple molecular models developed here not only describe thermophysical properties of hydrogen bonding fluids excellently but also their structure.

Appendix A Simulation Details

A.1 Vapor-Liquid Equilibria of Pure Hydrogen Bonding Components

For the vapor-liquid equilibrium simulations of the pure hydrogen bonding fluids in Chapter 3, $N = 864$ molecules were used and the NpT +test particle method [162, 163, 165] was employed. The cutoff radius was set to 15 Å in all liquid phase runs. The gradual insertion method [172, 213, 257] was applied to determine the chemical potential in the liquid and the vapor phase. This method inserts and deletes particles in a stepwise manner and is designated for fluids with strongly interacting particles [251]. The liquid runs were equilibrated in the NpT ensemble, typically over 10 000 cycles, and the maximum displacements for translation, rotation and volume were adjusted to yield acceptance rates of 50 %. After that, gradual insertions and deletions were usually performed over 5 000 Monte Carlo cycles with fluctuating molecules to equilibrate the weights of the transition states. The production phase was typically performed over 50 000 Monte Carlo cycles with constant weights of the transition states and constant maximum displacements for translation, rotation and volume.

Due to the formation of hydrogen bonded clusters, particularly in the vapor phase at low temperatures, significantly more cycles for equilibration were carried out than for the liquid phase. The sampling of the chemical potential in the production phase was 60 000 Monte Carlo cycles for the vapor. For the simulation of the vapor phase, the cutoff radius was chosen close to half of the length of the cubic simulation volume to obtain faster equilibration, yielding hydrogen bonded aggregates and a more accurate sampling.

Generally, the Monte Carlo method is superior for vapor simulations at low densities compared to the Molecular Dynamics method as the formation of molecular clusters is sampled much more efficiently.

The Lennard-Jones long range interactions beyond the cut-off radius were corrected employing angle averaging as proposed by Lustig [152]. The Coulombic interactions were corrected using the reaction field method [4] with the conducting boundary condition.

A.2 Vapor-Liquid Equilibria of Binary Mixtures

For the calculation of binary vapor-liquid equilibria in Chapter 4 and 5, the Grand Equilibrium method [256] was employed. The vapor pressure and the dew point composition of a mixture are determined by this method for specified temperature and bubble point composition. The Grand Equilibrium method relies on the chemical potentials of all components in the liquid phase. To determine the chemical potential of the hydrogen bonding component, gradual insertion [257] was applied to obtain good statistics. Widom's test particle method [269] can not be applied for this task as it yields excessively poor statistics for that type of molecules in the liquid state.

The chemical potential of the non-hydrogen bonding component in the liquid phase of the binary mixture was determined using Molecular Dynamics with Widom's test particle method [269]. As for the gradual insertion runs, $N = 864$ molecules were used. The number of test particles was at each time step 3456. After 10 000 NVT and 100 000 NpT equilibration time steps, 150 000 NpT production time steps were sampled with Widom's test particle method. The cutoff radius was again set to 15 Å. For larger non-hydrogen bonding components at lower temperatures and higher densities, the statistics for the liquid chemical potential of the non-hydrogen bonding component were often inappropriate from Widom's test particle method so that the gradual insertion method had to be applied to obtain the chemical potential of the non-hydrogen bonding component with sufficiently high accuracy.

The vapor phase was sampled in the pseudo grand canonical (pseudo- μVT) ensemble which is part of the Grand Equilibrium method [256]. The number of molecules and the composition of the binary mixture change during a pseudo- μVT ensemble run. Hence, the volume V is the extensive variable and it determines the number of molecules in the simulation volume. To avoid too large or too low numbers of molecules, the volume was adjusted in the equilibration phase of the pseudo- μVT runs to yield a desired number of molecules of $N = 864$. With the ideal gas volume as a starting point, between 50 000 and 100 000 Monte Carlo production cycles were carried out. Within one Monte Carlo cycle, N attempts each to translate and rotate, and two attempts to insert or delete molecules were performed. The low percentage of insertion and deletion attempts is sufficient, as the acceptance rate is high due to the relatively low density of the vapor phase.

Henry's law constants are directly related to the residual chemical potential of the solute at infinite dilution [214]. Thus the residual chemical potential at infinite dilution and the Henry's law constant are directly related to the unlike solvent-solute interaction and indirectly to the solvent-solvent interaction which yields the configurations of the solvent molecules. In such configurations, solute test particles were inserted. The mole fraction of the solute in the solvent is exactly zero, as required for infinite dilution, since the test particles are instantly removed after the potential energy calculation. Simulations were performed at specified temperature and the according vapor pressure of the pure solvent. The residual chemical potential was determined with Widom's test particle method [269].

A.3 Hydrogen Bonding Statistics for Methanol in Carbon Dioxide

Molecular Dynamics simulations to obtain the hydrogen bonding statistics for methanol in carbon dioxide of Chapter 6 were carried out using the implicit rotational leapfrog integrator [69] with a time step of 1.5 fs with at least 864 molecules in a cubic simulation box. However, at low methanol mole fractions, the total number of particles was larger, and at least 50 methanol molecules were present in the simulation box to allow a meaningful hy-

drogen bonding statistics. The largest total number of molecules was 10 976 at a methanol mole fraction of 0.0052 mol/mol. Due to the large number of molecules, a combination of Verlet [249] and cell lists [96, 191] were incorporated. Starting from a face-centered cubic lattice, 200 000 time steps for each the equilibration and the production phase were performed. Hence, the sampling time for the equilibration and the production phase was 300 ps, respectively.

Appendix B Simulation Results

B.1 Binary Vapor-Liquid Equilibria

Table 34: Simulation results for the binary vapor-liquid equilibrium of hydrogen bonding and non-hydrogen bonding (component 2) fluids. The number in parentheses indicates the statistical uncertainty in the last digit.

T K	x_2 mol/mol	p MPa	y_2 mol/mol	ρ' mol/l	ρ'' mol/l
methanol (1) + Ar (2): mixture type #1					
273.15	0.0289	5.3 (2)	1	25.40(1)	2.43(9)
273.15	0.0417	7.9 (3)	1	25.46(2)	3.7 (1)
273.15	0.0521	9.9 (4)	1	25.52(1)	4.7 (1)
333.15	0.0301	6.0 (1)	0.9833(4)	23.54(1)	2.24(4)
333.15	0.0405	8.2 (2)	0.9861(9)	23.59(2)	3.0 (7)
333.15	0.0498	10.3 (2)	0.986 (1)	23.65(2)	3.78(7)
methanol (1) + CH ₄ (2): mixture type #1					
310	0.0625	7.6 (2)	0.9989(5)	23.96(2)	3.29(9)
310	0.0868	11.0 (4)	0.9986(7)	23.90(2)	4.9 (2)
310	0.1227	17.0 (7)	0.9965(4)	23.82(3)	7.8 (2)
338.15	0.0394	5.3 (1)	0.974 (1)	23.16(2)	2.01(4)
338.15	0.0729	9.8 (3)	0.985 (1)	23.04(2)	3.8 (1)
338.15	0.0868	12.7 (3)	0.980 (1)	23.07(2)	5.1 (1)
ethanol (1) + Ar (2): mixture type #1					
273.35	0.0104	1.21(3)	1	17.64(1)	0.54(1)
273.35	0.0301	3.7 (1)	1	17.79(1)	1.66(5)
273.35	0.0556	7.5 (3)	1	17.99(1)	3.5 (1)
273.35	0.0694	9.0 (3)	1	18.11(2)	4.2 (1)
323.15	0.0104	1.37(3)	1	16.60(1)	0.51(1)
323.15	0.0498	6.5 (2)	1	16.82(2)	2.44(8)
323.15	0.0995	13.8 (4)	1	17.21(4)	5.3 (1)

Table 34: continued

T K	x_2 mol/mol	P MPa	y_2 mol/mol	ρ' mol/l	ρ'' mol/l
ethanol (1) + CH ₄ (2): mixture type #1					
333.40	0.0498	4.5 (1)	0.9869(9)	16.51(1)	1.70(4)
333.40	0.0995	9.4 (3)	0.9906(5)	16.66(1)	3.7 (1)
333.40	0.1505	13.4 (5)	0.997 (1)	16.78(2)	5.4 (2)
333.40	0.2002	20.1 (8)	0.9918(7)	16.98(2)	8.1 (3)
398.15	0.0498	5.02(9)	0.854 (5)	14.79(1)	1.61(3)
398.15	0.0995	9.4 (2)	0.903 (3)	14.88(3)	3.06(7)
398.15	0.1505	13.7 (3)	0.903 (5)	14.90(4)	4.5 (1)
398.15	0.2002	18.2 (5)	0.902 (3)	14.96(3)	6.0 (2)
methanol (1) + CO ₂ (2): mixture type #2					
298.15	0.1215	1.89(2)	0.9999(1)	24.34(1)	0.84(1)
298.15	0.2292	3.22(4)	0.9932(3)	24.02(2)	1.56(2)
298.15	0.3646	4.50(2)	0.9995(3)	23.56(2)	2.42(1)
323.15	0.1192	2.77(3)	0.9781(9)	23.49(2)	1.16(1)
323.15	0.2373	4.80(4)	0.9853(8)	23.04(2)	2.22(2)
323.15	0.4340	8.0 (2)	0.9877(9)	22.00(5)	4.9 (1)
373.15	0.1181	4.63(3)	0.899 (2)	21.53(2)	1.72(1)
373.15	0.2454	8.98(7)	0.907 (3)	20.81(3)	3.95(3)
methanol (1) + C ₂ H ₂ (2): mixture type #2					
283.15	0.1065	0.57(4)	0.9897(8)	24.47(1)	0.25(2)
283.15	0.1910	0.93(6)	1	24.01(1)	0.42(3)
283.15	0.3657	1.9 (1)	0.9994(3)	23.11(2)	0.91(5)
303.15	0.1273	1.06(4)	0.980 (1)	23.75(1)	0.45(2)
303.15	0.2350	2.01(8)	0.9895(8)	23.14(1)	0.90(4)
303.15	0.3692	2.83(9)	0.9929(5)	22.29(2)	1.35(4)
methanol (1) + C ₂ H ₄ (2): mixture type #2					
298.15	0.0833	2.0 (1)	0.996 (1)	23.64(1)	0.89(4)
298.15	0.2650	5.3 (2)	0.9985(8)	21.58(2)	3.4 (1)
298.15	0.4132	8.3 (2)	1	19.74(2)	5.1 (1)
313.15	0.0914	3.02(3)	0.9857(6)	23.07(1)	1.16(1)
313.15	0.2303	6.27(9)	0.9874(9)	21.47(2)	3.77(5)
313.15	0.3889	8.0 (2)	0.9901(8)	19.53(2)	6.5 (2)

Table 34: continued

T K	x_2 mol/mol	p MPa	y_2 mol/mol	ρ' mol/l	ρ'' mol/l
methanol (1) + C ₂ H ₆ (2): mixture type #2					
298.15	0.0532	1.17(6)	0.986 (1)	23.77(1)	0.52(3)
298.15	0.1134	2.2 (1)	0.9929(7)	22.96(1)	1.07(5)
298.15	0.2003	3.2 (1)	0.9968(6)	21.72(2)	1.80(6)
373.15	0.0289	1.75(4)	0.771 (5)	21.65(2)	0.62(1)
373.15	0.0718	3.66(8)	0.878 (3)	20.98(2)	1.39(3)
373.15	0.0972	4.9 (1)	0.896 (3)	20.63(2)	1.96(4)
ethanol (1) + N ₂ (2): mixture type #2					
298.22	0.0336	11.4 (6)	0.9994(3)	17.40(4)	4.5 (2)
298.22	0.0602	22 (1)	0.999 (1)	17.64(7)	8.3 (4)
298.22	0.0799	30 (3)	0.9999(1)	17.8 (1)	11 (1)
298.22	0.0995	41 (4)	0.9993(3)	18.1 (9)	14 (1)
398.02	0.0428	9.0 (2)	0.915 (3)	14.89(2)	2.71(6)
398.02	0.0602	12.7 (3)	0.924 (3)	14.98(5)	3.71(9)
398.02	0.0799	16.7 (4)	0.932 (2)	15.09(4)	4.8 (1)
398.02	0.0995	21.2 (7)	0.940 (3)	15.3 (1)	6.0 (2)
398.02	0.1505	33 (3)	0.935 (7)	15.6 (5)	8.6 (3)
398.02	0.2002	47 (3)	0.939 (2)	16.0 (2)	11.1 (7)
ethanol (1) + CO ₂ (2): mixture type #2					
323.15	0.0995	2.20(6)	0.984 (1)	16.92(1)	0.90(2)
323.15	0.2002	4.4 (1)	0.9897(9)	17.29(2)	1.99(5)
323.15	0.2998	5.9 (2)	0.9899(6)	17.55(4)	2.9 (1)
323.15	0.4005	7.1 (2)	0.9910(9)	17.77(6)	3.9 (1)
373.15	0.0995	3.62(6)	0.909 (2)	15.62(2)	1.30(2)
373.15	0.2002	6.6 (1)	0.939 (2)	15.75(2)	2.58(4)
373.15	0.2998	9.9 (2)	0.932 (2)	15.90(8)	4.40(9)
373.15	0.4005	11.9 (3)	0.929 (3)	15.8 (1)	5.8 (1)
ethanol (1) + C ₂ H ₄ (2): mixture type #2					
423.15	0.0995	3.45(5)	0.656 (5)	13.52(2)	1.15(2)
423.15	0.1505	4.36(8)	0.721 (6)	13.30(3)	1.47(3)
463.15	0.0694	4.23(5)	0.334 (6)	11.96(6)	1.54(2)
463.15	0.2002	8.5 (1)	0.535 (6)	11.0 (2)	3.42(4)

Table 34: continued

T K	x_2 mol/mol	p MPa	y_2 mol/mol	ρ' mol/l	ρ'' mol/l
493.15	0.0648	6.00(4)	0.185 (4)	9.8 (1)	2.66(2)
493.15	0.0949	6.91(6)	0.226 (4)	9.46(8)	3.24(3)
ethanol (1) + C ₂ H ₆ (2): mixture type #2					
298.15	0.0498	0.63(3)	1	17.00(1)	0.27(1)
298.15	0.3171	3.3 (1)	1	16.30(2)	1.89(6)
398.15	0.0498	2.09(3)	0.713 (5)	14.50(2)	0.71(1)
398.15	0.1296	4.28(7)	0.834 (4)	14.12(2)	1.56(3)
398.15	0.2002	6.6 (2)	0.856 (5)	13.90(2)	2.68(8)
448.15	0.0995	5.37(9)	0.535 (8)	12.5 (2)	1.99(3)
448.15	0.2002	8.4 (2)	0.59 (1)	11.7 (5)	3.59(9)
ethanol (1) + C ₃ H ₆ (2): mixture type #2					
333.1	0.2002	1.3 (1)	0.959 (4)	15.36(1)	0.57(4)
333.1	0.4005	1.7 (2)	0.970 (3)	13.69(1)	0.76(9)
333.1	0.5995	2.23(9)	0.976 (2)	13.13(2)	1.08(4)
368	0.2292	2.5 (2)	0.908 (3)	14.41(1)	1.04(8)
368	0.2998	2.6 (2)	0.909 (7)	13.69(1)	1.6 (1)
368	0.5995	3.68(6)	0.931 (2)	13.13(2)	1.87(3)
ethanol (1) + R22 (2): mixture type #2					
343	0.0995	0.61(3)	0.885 (5)	15.79(1)	0.23(1)
343	0.2998	1.44(6)	0.947 (3)	15.04(1)	0.60(3)
343	0.5000	2.08(6)	0.960 (2)	14.19(2)	0.94(3)
343	0.7998	2.53(4)	0.974 (1)	12.45(3)	1.25(2)
343	0.9005	2.77(4)	0.9811(9)	11.75(6)	1.43(2)
382.7	0.0995	1.31(3)	0.727 (6)	14.77(2)	0.47(1)
382.7	0.2998	2.77(6)	0.850 (5)	13.76(4)	1.15(3)
382.7	0.4005	3.20(6)	0.883 (3)	13.18(4)	1.38(3)
382.7	0.5995	4.36(7)	0.897 (3)	11.94(9)	2.29(4)
382.7	0.7998	5.13(7)	0.873 (4)	10.0 (9)	4.26(6)
formic acid (1) + CO ₂ (2): mixture type #2					
353.15	0.1308	6.9 (2)	0.933 (3)	24.01(2)	3.17(9)
353.15	0.2465	10.5 (1)	0.941 (1)	23.24(2)	5.79(3)
353.15	0.3611	12.6 (2)	0.932 (2)	22.15(3)	8.17(7)

Table 34: continued

T K	x_2 mol/mol	p MPa	y_2 mol/mol	ρ' mol/l	ρ'' mol/l
393.15	0.1308	9.0 (2)	0.928 (2)	22.65(2)	3.50(8)
393.15	0.2465	15.7 (4)	0.901 (3)	21.81(5)	7.48(5)
393.15	0.3611	20.2 (5)	0.879 (2)	20.74(7)	10.5 (1)
methanol (1) + CO (2): mixture type #3					
298.15	0.0556	17.7(7)	0.9981(4)	24.69(2)	6.9 3)
298.15	0.0764	24 (1)	0.9999(1)	24.69(4)	9.0 4)
298.15	0.1296	48 (13)	0.9989(5)	25.1 (4)	14 (4)
398.15	0.0671	16.3 (4)	0.901 (3)	21.08(3)	4.9 (1)
398.15	0.1806	40 (4)	0.878 (8)	20.9 (3)	10.4 (1)
398.15	0.2407	54 (5)	0.891 (5)	21.0 (3)	12.7 (1)
ethanol (1) + CO (2): mixture type #3					
298	0.0104	1.81(6)	0.9964(3)	17.13(1)	0.74(2)
298	0.0498	9.1 (3)	1	17.35(1)	3.7 (1)
298	0.0995	19 (2)	1	17.67(4)	7.4 (8)
323	0.0104	1.91(5)	0.985 (1)	16.64(1)	0.71(2)
323	0.0498	9.6 (3)	0.9930(5)	16.86(3)	3.5 (1)
323	0.0995	19 (1)	0.9993(4)	17.11(4)	6.7 (4)
methanethiol (1)+ methyl chloride (2): mixture type #3					
313.15	0.0995	0.39(1)	0.267(7)	17.39(1)	0.16(1)
313.15	0.3009	0.52(1)	0.572(7)	17.37(1)	0.22(1)
313.15	0.5012	0.61(2)	0.718(7)	17.37(1)	0.26(1)
313.15	0.6991	0.71(2)	0.840(4)	17.39(1)	0.31(1)
313.15	0.8981	0.82(2)	0.947(2)	17.42(1)	0.36(1)

Table 35: Simulation results for Henry's law constants. The number in parentheses indicates the statistical uncertainty in the last digits.

T K	H_2 MPa	T K	H_2 MPa	T K	H_2 MPa	T K	H_2 MPa
methanol (1) + Ar (2): mixture type #1		methanol (1) + CH ₄ (2): mixture type #1		ethanol (1) + Ne (2): mixture type #1		ethanol (1) + Ar (2): mixture type #1	
270	161 (4)	270	88 (4)	270	1213(14)	270	118 (2)
295	180 (4)	295	107 (3)	295	950 (9)	295	129 (2)
320	182 (3)	320	114 (2)	298	935 (8)	298	130 (2)
345	197 (2)	345	133 (2)	320	779 (7)	320	139 (2)
370	189 (2)	370	133 (2)	345	620 (5)	345	131 (2)
395	182 (2)	395	131 (2)	370	488 (5)	370	132 (1)
420	168 (1)	420	125 (1)	395	405 (3)	395	119 (1)
445	143 (1)	445	109 (1)	420	326 (3)	420	111 (1)
470	121 (1)	470	95 (1)	445	243 (2)	445	94.4(9)
495	93 (1)	495	75 (1)	470	181 (2)	470	81.0(7)
				495	129 (1)	495	66.2(6)
ethanol (1) + Kr (2): mixture type #1		ethanol (1) + Xe (2): mixture type #1		ethanol (1) + CH ₄ (2): mixture type #1		methanol (1) + CO ₂ (2): mixture type #2	
270	53 (1)	270	16.0(9)	273	69 (1)	270	9.3(4)
295	66 (1)	295	21.6(7)	298	79 (1)	295	13.7(5)
298	62 (1)	298	20.3(6)	323	84.8(9)	320	20.7(4)
320	74 (1)	320	26.0(7)	348	87.7(8)	345	30.1(4)
345	78 (1)	345	32.9(6)	373	87.8(6)	370	36.2(4)
370	83 (1)	370	35.1(6)	398	86.5(5)	395	42.0(4)
395	79.1(9)	395	38.2(4)	423	80.9(4)	420	45.5(4)
420	76.4(7)	420	40.0(4)	448	73.4(4)	445	46.6(4)
445	70.0(8)	445	38.7(4)	473	63.4(4)	470	45.9(4)
470	60.3(7)	470	36.6(4)	498	50.8(4)	495	42.6(4)

Table 35: continued

T K	H_2 MPa	T K	H_2 MPa	T K	H_2 MPa	T K	H_2 MPa
495	50.6(6)	495	33.1(3)				
methanol (1) + C_2H_2 (2): mixture type #2		methanol (1) + C_2H_4 (2): mixture type #2		ethanol (1) + O_2 (2): mixture type #2		ethanol (1) + N_2 (2): mixture type #2	
270	3.3(2)	270	18 (1)	273	174 (2)	273	290 (4)
295	6.0(2)	295	24.2(9)	298.15	177 (2)	298.15	283 (4)
320	9.1(3)	320	35 (1)	323	180 (1)	323	271 (3)
345	11.6(6)	345	41.0(9)	348	171.0(9)	348	244 (2)
370	16.6(5)	370	46.7(8)	373	164.2(9)	373	225 (2)
395	20.9(3)	395	51.6(8)	398	149.7(8)	398	194 (1)
420	23.8(2)	420	51.4(7)	423	133.2(6)	423	166 (1)
445	25.2(2)	445	51.0(5)	448	114.7(6)	448	137 (7)
470	26.7(2)	470	47.7(5)	473	94.2(6)	473	108.9(8)
495	26.0(2)	495	40.5(7)	498	71.1(6)	498	78.9(7)
ethanol (1) + CO_2 (2): mixture type #2		methanol (1) + C_2H_6 (2): mixture type #2		methanol (1) + CF_4 (2): mixture type #2		ethanol (1) + C_2H_2 (2): mixture type #2	
273	10.6(3)	270	13.7(7)	295	318(14)	248.15	2.7(9)
298.15	15.9(3)	295	23.1(9)	298.15	323(13)	270	10.1(7)
323	22.7(3)	320	34 (1)	320	293 (9)	295	12.8(6)
348	28.6(2)	345	39 (1)	345	299 (8)	298.15	13 (1)
373	34.0(2)	370	50 (1)	370	260 (6)	320	17.0(7)
398	37.2(2)	395	52.6(9)	395	234 (5)	345	21.2(5)
423	39.3(2)	420	57.2(8)	420	200 (3)	370	26.3(4)
448	39.3(2)	445	54.7(7)	445	155 (2)	395	27.6(4)
473	37.9(2)	470	51.9(5)	470	124 (2)	420	29.7(3)
498	33.6(2)	495	45.5(6)	495	89 (2)	445	30.2(3)
						470	29.6(3)
						495	27.7(2)
ethanol (1) + C_2H_4 (2): mixture type #2		ethanol (1) + C_2H_6 (2): mixture type #2		ethanol (1) + C_3H_6 (2): mixture type #2		ethanol (1) + CF_4 (2): mixture type #2	
248.15	5.0(6)	248.15	3.2(3)	248.15	1.3(3)	270	230(12)
270	11.5(8)	270	8.0(5)	270	3.8(5)	295	211(22)
295	15.2(8)	295	13.4(5)	295	4.5(6)	298	234(12)
298.15	16.1(9)	298.15	14.4(6)	298.15	4.2(5)	320	186 (8)

Table 35: continued

T K	H_2 MPa	T K	H_2 MPa	T K	H_2 MPa	T K	H_2 MPa
320	21.7(9)	320	19.3(7)	320	9.0(6)	345	183 (4)
345	26.5(7)	345	22.5(6)	345	10.1(8)	370	175 (4)
370	29.6(7)	370	29.0(6)	370	14.3(6)	395	146 (3)
395	32.9(5)	395	30.6(4)	395	16.3(4)	420	125 (2)
420	34.2(5)	420	33.2(4)	420	19.1(4)	445	103 (2)
445	34.2(4)	445	32.2(4)	445	19.3(3)	470	83 (1)
470	32.3(3)	470	31.5(3)	470	19.0(2)	495	63.3(9)
495	29.4(2)	495	29.4(3)	495	18.3(2)		
MMA (1) + N ₂ (2): mixture type #2		DMA (1) + N ₂ (2): mixture type #2		formic acid (1) + CO ₂ (2): mixture type #2		formic acid (1) + C ₂ H ₂ (2): mixture type #2	
260	356 (8)	260	163 (3)	273.15	22 (1)	273.15	14 (2)
280	303 (5)	280	152 (2)	300	33 (1)	300	23 (2)
300	262 (4)	300	139 (2)	330	49 (1)	330	30 (2)
308.15	250 (4)	308.15	135 (2)	360	58 (1)	360	39 (2)
320	211 (3)	320	124 (1)	390	71 (1)	390	47 (1)
340	171 (2)	340	112 (1)	420	84 (1)	420	53 (1)
360	146 (2)	360	100 (1)	450	88.7(9)	450	54 (2)
380	118 (1)	380	87 (1)	480	89 (1)	480	58.6(8)
400	92 (1)	400	74 (1)	510	86.7(9)	510	58.0(7)
420	65 (1)	420	63 (1)	540	80.8(8)	540	56.0(6)
				570	69.2(9)	570	50.5(6)
methanol (1) + CO (2): mixture type #3		ethanol (1) + CO (2): mixture type #3		ethanol (1) + R12 (2): mixture type #3		ethanol (1) + R22 (2): mixture type #3	
280	274 (8)	270	163 (5)	270	0.8(6)	270	0.7(3)
300	278 (5)	295	172 (4)	295	3.8(5)	295	2.4(2)
320	276 (4)	303	173 (3)	303	3.2(5)	303	2.8(2)
340	273 (5)	313	181 (4)	313	4.7(6)	313	3.8(2)
360	258 (3)	320	171 (4)	320	5.0(5)	320	4.2(2)
380	251 (3)	345	175 (2)	345	7.0(5)	345	5.6(3)
398	223 (3)	370	156 (2)	370	8.5(3)	370	7.8(3)
400	222 (2)	395	144 (2)	395	11.5(3)	395	9.7(2)
420	201 (2)	420	123 (2)	420	13.7(3)	420	11.1(2)
440	176 (2)	445	110 (1)	445	13.5(2)	445	13.1(2)
460	153 (2)	470	87 (9)	470	13.8(2)	470	13.4(1)

Table 35: continued

T K	H_2 MPa	T K	H_2 MPa	T K	H_2 MPa	T K	H_2 MPa
480	124 (1)	495	66.8(9)	495	14.0(1)	495	13.7(1)
ethanol (1) + R32 (2): mixture type #3		ethanol (1) + R134a (2): mixture type #3		ethanol (1) + R152a (2): mixture type #3			
270	3.3(3)	270	0.6(4)	270	0.1(1)		
295	5.3(3)	295	2.6(4)	295	2.5(3)		
303	6.0(4)	303	2.5(4)	303	2.6(3)		
313	6.4(3)	313	3.5(4)	313	3.5(3)		
320	6.6(5)	320	3.6(4)	320	3.7(3)		
345	7.1(8)	345	4.6(3)	345	4.9(3)		
370	10.8(4)	370	6.3(5)	370	7.3(3)		
395	12.9(3)	395	7.3(3)	395	8.5(2)		
420	13.7(4)	420	7.8(6)	420	9.8(3)		
445	14.5(6)	445	8.9(5)	445	10.9(2)		
470	16.2(2)	470	10.0(1)	470	11.8(1)		
495	16.4(1)	495	10.0(2)	495	12.2(1)		

B.2 Hydrogen Bonding Statistics

Table 36: NpT molecular dynamics simulation results for hydrogen bonding statistics and densities of methanol in CO_2 obtained at 293.15 K and 10, 15 and 20 MPa. The number in parentheses indicates the statistical uncertainty in the last digit.

x_{MeOH} mol mol^{-1}	p MPa	f_0	f_1	f_2	f_3	ρ mol l^{-1}
0.0052	10	0.878 (4)	0.094 (3)	0.028(2)	0	19.50(1)
	15	0.893 (5)	0.081 (3)	0.026(3)	0.0003(1)	20.41(1)
	20	0.910 (4)	0.079 (4)	0.010(1)	0	21.07(1)
0.0091	10	0.757 (5)	0.189 (4)	0.054(2)	0.0002(1)	19.54(1)
	15	0.785 (7)	0.194 (6)	0.021(2)	0	20.46(1)
	20	0.757 (7)	0.198 (6)	0.044(3)	0.0007(2)	21.11(1)
0.1000	10	0.168 (4)	0.342 (5)	0.463(7)	0.027 (1)	20.56(3)
	15	0.193 (4)	0.332 (4)	0.453(5)	0.023 (1)	21.22(3)
	20	0.194 (5)	0.325 (6)	0.459(7)	0.022 (1)	21.75(2)

Table 36: continued

x_{MeOH} mol mol ⁻¹	p MPa	f_0	f_1	f_2	f_3	ρ mol l ⁻¹
0.1152	10	0.165 (4)	0.283 (5)	0.525(7)	0.028 (1)	20.68(3)
	15	0.153 (3)	0.285 (3)	0.530(4)	0.033 (1)	21.31(2)
	20	0.179 (3)	0.300 (4)	0.491(4)	0.029 (1)	21.82(2)
0.1857	10	0.112 (2)	0.279 (3)	0.573(3)	0.0368(8)	21.33(3)
	15	0.123 (2)	0.288 (2)	0.557(3)	0.032 (1)	21.90(2)
	20	0.102 (3)	0.294 (4)	0.570(5)	0.0348(8)	22.31(2)
0.2000	10	0.097 (2)	0.274 (3)	0.591(3)	0.0383(8)	21.45(3)
	15	0.109 (2)	0.271 (3)	0.583(4)	0.0377(8)	22.01(2)
	20	0.097 (2)	0.273 (2)	0.594(3)	0.0357(8)	22.37(2)
0.4000	10	0.0486(9)	0.237 (2)	0.666(2)	0.0488(7)	22.89(2)
	15	0.0467(8)	0.237 (2)	0.671(2)	0.0456(6)	23.20(2)
	20	0.0458(8)	0.232 (2)	0.674(2)	0.0487(6)	23.48(2)
0.6000	10	0.0279(5)	0.201 (1)	0.715(2)	0.0560(7)	23.83(1)
	15	0.0265(4)	0.199 (1)	0.718(2)	0.0569(5)	24.05(1)
	20	0.0274(5)	0.200 (1)	0.716(1)	0.0567(5)	24.27(1)
0.6607	10	0.0238(4)	0.193 (1)	0.725(1)	0.0583(6)	24.10(1)
	15	0.0235(4)	0.1931(8)	0.724(1)	0.0591(5)	24.29(1)
	20	0.0238(4)	0.193 (1)	0.723(1)	0.0598(5)	24.44(1)
0.8000	10	0.0165(2)	0.1728(9)	0.750(1)	0.0608(5)	24.52(1)
	15	0.0168(3)	0.1730(8)	0.749(1)	0.0616(4)	24.67(1)
	20	0.0167(3)	0.1726(8)	0.748(1)	0.0623(5)	24.82(1)
1.0000	10	0.0101(1)	0.1485(6)	0.778(1)	0.0634(4)	24.87(1)
	15	0.0099(1)	0.1489(6)	0.777(1)	0.0639(4)	24.98(1)
	20	0.0097(1)	0.1488(7)	0.778(1)	0.0636(4)	25.09(1)

Table 37: NpT molecular dynamics simulation results for hydrogen bonding statistics and densities of methanol in CO₂ obtained at 308.15 K and 10, 15 and 20 MPa. The number in parentheses indicates the statistical uncertainty in the last digit.

x_{MeOH} mol mol ⁻¹	p MPa	f_0	f_1	f_2	f_3	ρ mol l ⁻¹
0.0091	10	0.829 (6)	0.151(5)	0.019(2)	0.0002(1)	16.82 (3)
	15	0.793 (6)	0.166(4)	0.040(3)	0.0012(3)	18.50 (2)
	20	0.838 (4)	0.154(4)	0.008(1)	0	19.51 (1)

Table 37: continued

x_{MeOH} mol mol ⁻¹	p MPa	f_0	f_1	f_2	f_3	ρ mol l ⁻¹
0.0350	10	0.456 (8)	0.287(4)	0.248(6)	0.0091(7)	17.35 (4)
	15	0.485 (6)	0.295(5)	0.213(6)	0.0073(7)	18.83 (3)
	20	0.440 (7)	0.311(5)	0.242(5)	0.0077(6)	19.76 (2)
0.1000	10	0.229 (4)	0.313(5)	0.436(5)	0.0213(8)	18.41 (5)
	15	0.252 (5)	0.334(5)	0.397(7)	0.0170(8)	19.57 (3)
	20	0.255 (5)	0.351(5)	0.377(7)	0.0171(9)	20.36 (3)
0.1857	10	0.149 (2)	0.302(3)	0.518(3)	0.0308(8)	19.73 (3)
	15	0.143 (2)	0.317(4)	0.509(4)	0.0313(8)	20.54 (3)
	20	0.144 (2)	0.314(3)	0.510(4)	0.0325(8)	21.09 (3)
0.2000	10	0.138 (3)	0.309(3)	0.521(3)	0.0320(8)	19.93 (3)
	15	0.130 (3)	0.303(3)	0.534(4)	0.0337(7)	20.62 (3)
	20	0.131 (2)	0.302(3)	0.532(3)	0.0349(8)	21.21 (2)
0.4000	10	0.0686(9)	0.274(2)	0.611(2)	0.0462(7)	21.87 (2)
	15	0.0649(9)	0.269(2)	0.621(2)	0.0450(6)	22.27 (2)
	20	0.068 (1)	0.274(2)	0.614(2)	0.0443(5)	22.63 (2)
0.6000	10	0.0389(6)	0.229(1)	0.679(1)	0.0536(5)	23.10 (2)
	15	0.0379(5)	0.233(1)	0.674(2)	0.0548(4)	23.35 (2)
	20	0.0389(5)	0.236(1)	0.671(1)	0.0548(5)	23.61 (1)
0.6607	10	0.0329(5)	0.223(1)	0.688(1)	0.0562(4)	23.39 (1)
	15	0.0338(4)	0.219(1)	0.691(1)	0.0561(4)	23.63 (1)
	20	0.0334(5)	0.223(1)	0.687(2)	0.0572(5)	23.84 (1)
0.8000	10	0.0234(3)	0.200(1)	0.715(1)	0.0611(5)	23.97 (1)
	15	0.0230(3)	0.199(1)	0.716(1)	0.0617(4)	24.12 (1)
	20	0.0229(2)	0.199(1)	0.716(1)	0.0614(6)	24.27 (1)
1.0000	10	0.0145(1)	0.174(1)	0.746(1)	0.0654(4)	24.448(9)
	15	0.0145(2)	0.174(1)	0.745(1)	0.0659(3)	24.566(9)
	20	0.0146(1)	0.173(1)	0.747(1)	0.0659(4)	24.695(9)

Table 38: NpT molecular dynamics simulation results for hydrogen bonding statistics and densities of methanol in CO_2 obtained at 323.15 K and 10, 15 and 20 MPa. The number in parentheses indicates the statistical uncertainty in the last digit.

x_{MeOH} mol mol ⁻¹	P MPa	f_0	f_1	f_2	f_3	ρ mol l ⁻¹
0.0091	10	0.899 (4)	0.096(4)	0.004(1)	0	8.2 (1)
	15	0.849 (7)	0.131(6)	0.019(2)	0.0001(1)	16.04 (2)
	20	0.870 (5)	0.122(5)	0.008(1)	0	17.71 (2)
0.0141	10	0.853 (9)	0.130(7)	0.017(2)	0	8.52 (3)
	15	0.841 (6)	0.140(5)	0.018(3)	0.0006(2)	16.14 (3)
	20	0.762 (6)	0.192(5)	0.046(3)	0	17.75 (2)
0.0244	10	0.750 (6)	0.201(5)	0.048(3)	0.0007(2)	9.63 (8)
	15	0.67 (1)	0.243(6)	0.089(7)	0.0016(3)	16.35 (4)
	20	0.697 (7)	0.242(6)	0.061(5)	0.0009(2)	17.91 (3)
0.0591	10	0.412 (7)	0.303(6)	0.278(6)	0.0074(7)	13.1 (1)
	15	0.488 (7)	0.300(6)	0.204(6)	0.0079(7)	17.03 (4)
	20	0.451 (8)	0.315(5)	0.226(6)	0.0080(6)	18.33 (4)
0.0675	10	0.411 (6)	0.322(5)	0.258(6)	0.0089(7)	14.1 (1)
	15	0.397 (6)	0.347(5)	0.247(6)	0.0087(7)	17.18 (5)
	20	0.407 (8)	0.345(5)	0.240(7)	0.0073(6)	18.43 (4)
0.0746	10	0.392 (7)	0.333(6)	0.266(6)	0.0093(6)	14.1 (1)
	15	0.347 (7)	0.348(6)	0.293(7)	0.0118(7)	17.26 (5)
	20	0.374 (5)	0.333(4)	0.281(5)	0.0124(8)	18.51 (3)
0.1000	10	0.288 (5)	0.337(4)	0.360(5)	0.0154(7)	15.50 (8)
	15	0.295 (4)	0.365(4)	0.325(6)	0.0159(8)	17.73 (4)
	20	0.350 (5)	0.363(4)	0.274(4)	0.0135(8)	18.87 (4)
0.1003	10	0.294 (4)	0.354(4)	0.337(5)	0.0154(8)	15.49 (7)
	15	0.277 (4)	0.339(4)	0.367(5)	0.0163(7)	17.76 (4)
	20	0.305 (4)	0.353(5)	0.327(6)	0.0151(7)	18.83 (3)
0.1632	10	0.216 (3)	0.353(3)	0.409(4)	0.0223(7)	17.31 (6)
	15	0.210 (3)	0.350(3)	0.417(4)	0.0230(7)	18.67 (4)
	20	0.203 (3)	0.355(3)	0.421(3)	0.0212(6)	19.57 (3)
0.2000	10	0.159 (3)	0.327(3)	0.487(4)	0.0277(7)	18.01 (4)
	15	0.168 (3)	0.336(2)	0.468(4)	0.0280(7)	19.19 (3)
	20	0.170 (3)	0.338(3)	0.464(5)	0.0280(7)	19.90 (3)
0.2454	10	0.139 (2)	0.329(2)	0.499(3)	0.0334(7)	18.68 (4)
	15	0.144 (2)	0.323(3)	0.503(3)	0.0304(6)	19.62 (3)
	20	0.147 (2)	0.328(2)	0.493(3)	0.0319(7)	20.38 (3)

Table 38: continued

x_{MeOH} mol mol ⁻¹	p MPa	f_0	f_1	f_2	f_3	ρ mol l ⁻¹
0.4000	10	0.087 (1)	0.300(2)	0.572(2)	0.0409(6)	20.71 (3)
	15	0.088 (1)	0.301(2)	0.570(3)	0.0408(5)	21.30 (2)
	20	0.087 (1)	0.294(2)	0.576(3)	0.0427(6)	21.63 (2)
0.4784	10	0.072 (1)	0.283(1)	0.598(2)	0.0466(6)	21.45 (2)
	15	0.0723(9)	0.286(1)	0.596(2)	0.0458(5)	21.88 (2)
	20	0.0707(9)	0.289(2)	0.595(2)	0.0452(5)	22.19 (2)
0.6000	10	0.0524(6)	0.263(1)	0.634(2)	0.0505(5)	22.34 (2)
	15	0.0514(7)	0.259(1)	0.639(2)	0.0509(5)	22.62 (2)
	20	0.0530(6)	0.264(1)	0.632(1)	0.0511(5)	22.88 (2)
0.8000	10	0.0321(4)	0.227(1)	0.682(1)	0.0590(4)	23.37 (1)
	15	0.0319(3)	0.228(1)	0.682(1)	0.0582(4)	23.57 (1)
	20	0.0311(3)	0.228(1)	0.682(1)	0.0590(4)	23.74 (1)
1.0000	10	0.0205(2)	0.198(1)	0.717(1)	0.0649(4)	23.99 (1)
	15	0.0202(2)	0.200(1)	0.715(1)	0.0655(4)	24.120(9)
	20	0.0202(2)	0.198(1)	0.716(1)	0.0657(3)	24.265(9)

Table 39: NpT molecular dynamics simulation results for hydrogen bonding statistics and densities of methanol in CO₂ obtained at 338.15 K and 10, 15 and 20 MPa. The number in parentheses indicates the statistical uncertainty in the last digit.

x_{MeOH} mol mol ⁻¹	p MPa	f_0	f_1	f_2	f_3	ρ mol l ⁻¹
0.0250	10	0.809 (7)	0.161(6)	0.029(2)	0.0002(1)	5.91(1)
	15	0.709 (8)	0.225(6)	0.065(4)	0.0015(3)	12.91(5)
	20	0.724 (6)	0.196(5)	0.077(5)	0.0025(4)	15.85(3)
0.0531	10	0.569 (8)	0.267(5)	0.160(6)	0.0038(4)	6.46(3)
	15	0.550 (6)	0.290(5)	0.154(4)	0.0054(4)	13.95(5)
	20	0.509 (7)	0.312(4)	0.175(5)	0.0049(4)	16.27(4)
0.0675	10	0.528 (8)	0.261(6)	0.204(4)	0.0074(6)	6.71(5)
	15	0.480 (6)	0.334(5)	0.182(5)	0.0049(5)	14.51(6)
	20	0.478 (6)	0.317(5)	0.197(4)	0.0084(6)	16.53(4)
0.0936	10	0.403 (5)	0.303(5)	0.282(5)	0.0117(7)	7.69(7)
	15	0.394 (7)	0.360(4)	0.238(7)	0.0088(6)	15.10(6)
	20	0.373 (4)	0.376(4)	0.242(4)	0.0099(7)	16.94(5)

Table 39: continued

x_{MeOH} mol mol ⁻¹	p MPa	f_0	f_1	f_2	f_3	ρ mol l ⁻¹
0.1000	10	0.389 (4)	0.299(4)	0.299(4)	0.0135(6)	7.8 (1)
	15	0.360 (6)	0.344(3)	0.282(6)	0.0144(7)	15.15(6)
	20	0.361 (6)	0.356(4)	0.271(5)	0.0121(6)	17.09(4)
0.1509	10	0.273 (3)	0.366(3)	0.346(4)	0.0145(6)	12.3 (1)
	15	0.286 (3)	0.361(4)	0.338(5)	0.0158(6)	16.45(5)
	20	0.291 (4)	0.359(3)	0.334(3)	0.0159(6)	17.84(4)
0.2000	10	0.223 (3)	0.348(3)	0.405(3)	0.0229(6)	14.95(8)
	15	0.221 (3)	0.359(3)	0.397(3)	0.0227(7)	17.27(5)
	20	0.220 (3)	0.377(3)	0.383(3)	0.0216(6)	18.57(3)
0.2454	10	0.190 (2)	0.354(2)	0.431(3)	0.0250(5)	16.42(7)
	15	0.189 (2)	0.364(2)	0.423(2)	0.0251(6)	18.15(3)
	20	0.181 (2)	0.353(2)	0.437(3)	0.0279(6)	19.07(3)
0.4000	10	0.115 (1)	0.329(2)	0.521(2)	0.0361(5)	19.44(3)
	15	0.117 (1)	0.334(2)	0.514(2)	0.0355(5)	20.16(2)
	20	0.114 (1)	0.331(2)	0.518(2)	0.0364(5)	20.67(2)
0.4784	10	0.093 (1)	0.318(1)	0.547(2)	0.0416(5)	20.43(3)
	15	0.093 (1)	0.313(1)	0.554(2)	0.0406(4)	20.86(2)
	20	0.091 (1)	0.314(2)	0.553(2)	0.0416(4)	21.28(2)
0.6000	10	0.0715(8)	0.293(1)	0.589(2)	0.0465(4)	21.50(2)
	15	0.0697(7)	0.29 (1)	0.590(2)	0.0480(5)	21.84(2)
	20	0.0688(7)	0.294(1)	0.588(2)	0.0484(4)	22.13(2)
0.8000	10	0.0431(4)	0.258(1)	0.643(1)	0.0564(4)	22.78(1)
	15	0.0437(4)	0.260(1)	0.639(1)	0.0570(4)	23.00(1)
	20	0.0430(4)	0.257(1)	0.642(1)	0.0570(4)	23.19(1)
1.0000	10	0.0276(2)	0.226(1)	0.682(1)	0.0640(4)	23.55(1)
	15	0.0284(3)	0.227(1)	0.680(1)	0.0650(3)	23.69(1)
	20	0.0275(2)	0.224(1)	0.684(1)	0.0643(3)	23.84(1)

References

- [1] Abascal, J.L.F. and Vega, C., A general purpose model for the condensed phases of water: TIP4P/2005, *J. Chem. Phys.* **123** (2005) 234505–234516.
- [2] Abascal, J.L.F., Sanz, E., García Fernández, R. and Vega, C., A potential model for the study of ices and amorphous water: TIP4P/Ice, *J. Chem. Phys.* **122** (2005) 234511–234519.
- [3] Agrawal, R. and Wallis, E.P., Molecular simulation of the vapor-liquid equilibrium of methanethiol + propane mixtures, *Fluid Phase Equilib.* **131** (1997) 51–65.
- [4] Allen, M.P. and Tildesley, D.J., *Computer Simulation of Liquids*. Clarendon Press, Oxford, 1987.
- [5] Al-Matar, A.K. and Rockstraw, D.A., A generating equation for mixing rules and two new mixing rules for interatomic potential energy parameters, *J. Comput. Chem.* **25** (2004) 660–668.
- [6] Asahi, N. and Nakamura, Y., Nuclear magnetic resonance and molecular dynamics study of methanol up to supercritical region, *J. Chem. Phys.* **109** (1998) 9879–9887.
- [7] Asprion, N., Anwendung der Spektroskopie in thermodynamischen Untersuchungen assoziierender Lösungen, *PhD Thesis*, Universität Kaiserslautern, 1996.
- [8] Asprion, N., Hasse, H. and Maurer, G., FT-IR spectroscopic investigations of hydrogen bonding in alcohol-hydrocarbon solutions, *Fluid Phase Equilib.* **186** (2001) 1–25.
- [9] Asprion, N., Hasse, H. and Maurer, G., Thermodynamic and IR spectroscopic studies of solutions with simultaneous association and solvation, *Fluid Phase Equilib.* **208** (2003) 23–51.
- [10] Asprion, N., Hasse, H. and Maurer, G., Application of IR-spectroscopy in thermodynamic investigations of associating solutions, *Fluid Phase Equilib.* **205** (2003) 195–214.
- [11] Astley, T., Birch, G.G., Drew, M.G.B. and Rodger, P.M., Lifetime of a hydrogen bond in aqueous solutions of carbohydrates, *J. Phys. Chem. A* **103** (1999) 5080–5090.
- [12] Atkins, P. and de Paula, J., *ATKINS' Physical Chemistry*, Oxford University Press, 2002.
- [13] Bai, S., Taylor, C.M.V., Liu, F., Mayne, C.L., Pugmire, R.J. and Grant, D.M., CO₂ clustering of 1-decanol and methanol in supercritical fluids by ¹³C nuclear spin-lattice relaxation, *J. Phys. Chem. B* **101** (1997) 2923–2928.
- [14] Bai, S. and Yonker, C.R., Pressure and temperature effects on the hydrogen-bond structures of liquid and supercritical fluid methanol, *J. Phys. Chem. A* **102** (1998) 8641–8647.

- [15] Baranyai, A., Bartók, A. and Chialvo, A.A., Testing the adequacy of simple water models at the opposite ends of the phase diagram, *J. Mol. Liq.* **134** (2007) 94–98.
- [16] Barlow, S.J., Bondarenko, G.V., Gorbaty, Y.E., Yamaguchi, T. and Poliakov, M., An IR study of hydrogen bonding in liquid and supercritical alcohols, *J. Phys. Chem. A* **106** (2002) 10452–10460.
- [17] Ben-Naim, A. and Stillinger, F.H., "Aspects of the Statistical-Mechanical Theory of Water," in *Structure and Transport Processes in Water and Aqueous Solutions*, Wiley-Interscience, New York, 1972.
- [18] Berthelot, D., Sur le Mélange des Gaz, *Comptes Rendus de l'Académie des Sciences Paris* **126** (1889) 1703–1706.
- [19] Bezdel, L.S. and Teodorovich, V.P., Solubility of CO₂, H₂S, CH₄, and C₂H₆ in methanol at low temperatures, *Gazovaya Prom.* **8** (1958) 38–43.
- [20] Bich, E., Hensen, U., Michalik, M., Wandschneider, D. and Heintz, A., ¹H NMR spectroscopic and thermodynamic studies of hydrogen bonding in liquid *n*-butanol + cyclohexane, *tert*-butanol + cyclohexane, and *n*-butanol + pyridine mixtures, *Phys. Chem. Chem. Phys.* **4** (2002) 5827–5832.
- [21] Bo, S., Battino, R. and Wilhelm, E., Solubility of gases in liquids. 19. Solubility of He, Ne, Ar, Kr, Xe, N₂, O₂, CH₄, CF₄, and SF₆ in normal 1-alkanols *n*-C₁H_{2l+1}OH (1 ≤ l ≤ 11) at 298.15 K, *J. Chem. Eng. Data* **38** (1993) 611–616.
- [22] Boutard, Y., Ungerer, P., Teuler, J.M., Ahunbay, M.G., Sabater, S.F., Pérez-Pellitero, J., Mackie, A.D., and Bourasseau, E., Extension of the anisotropic united atoms intermolecular potential to amines, amides and alkanols. Application to the problems of the 2004 Fluid Simulation Challenge, *Fluid Phase Equilib.* **236** (2005) 25–41.
- [23] Boyer, F.L. and Bircher, L.J., The Solubility of nitrogen, argon, methane, ethylene and ethane in normal primary alcohols, *J. Phys. Chem.* **4** (1960) 1330–1331.
- [24] Braker, W. and Mossman, A.L., *Matheson Gas Data Book*. Matheson Gas Products, Lyndhurst, New Jersey, 1980.
- [25] Brunner, E., Hültenschmidt, W. and Schlichthärle, G., Fluid mixtures at high pressures. IV. Isothermal phase equilibria in binary mixtures consisting of methanol + hydrogen or nitrogen or methane or carbon monoxide or carbon dioxide, *J. Chem. Thermodynamics* **19** (1987) 273–291.
- [26] Brunner, E. and Hültenschmidt, W., Fluid mixtures at high pressures. VIII. Isothermal phase equilibria in the binary mixtures, *J. Chem. Thermodyn.* **22** (1990) 73–84.
- [27] Brodsky, A., Is there predictive value in water computer simulations?, *Chem. Phys. Lett.* **261** (1996) 563–568.
- [28] Brooks, B.R., Brucocoleri, R.E., Olafson, B.D., States, D.J., Swaminathan, S. and Karplus, M., CHARMM: A program for macromolecular energy, minimization, and dynamics calculations, *J. Comput. Chem.* **4** (1983) 187–217.

- [29] Buckingham, R.A., The classical equation of state of gaseous helium, neon and argon, *Proc. Roy. Soc.* **168A** (1938) 264–283.
- [30] Buckingham, A.D., Direct method of measuring molecular quadrupolar moments, *J. Chem. Phys.* **10** (1959) 1580–1585.
- [31] Bulgarevich, D.S., Otake, K., Sako, T., Sugeta, T., Takebayashi, Y., Kamizawa, C., Shintani, D., Negishi, A. and Tsurumi, C., Hydrogen bonding in supercritical methanol studied by infrared spectroscopy, *J. Chem. Phys.* **116** (2002) 1995–2003.
- [32] Bulgarevich, D.S., Sako, T., Sugeta, T., Otake, K., Takebayashi, Y., Kamizawa, C., Horikawa, Y. and Kato, M., The role of general and hydrogen-bonding interactions in the solvation processes of organic compounds by supercritical CO₂/*n*-alcohol mixtures, *Ind. Eng. Chem. Res.* **41** (2002) 2074–2081.
- [33] Büttner, R. and Maurer, G., Dimerization of some organic acids in the gas phase, *Ber. Bunsenges. Phys. Chem.* **87** (1983) 877–882.
- [34] Byun, H.-S., Kim, K. and McHugh, M.A., Phase behavior and modeling of supercritical carbon dioxide-organic acid mixtures, *Ind. Eng. Chem. Res.* **39** (2000) 4580–4587.
- [35] Bzowski, J., Mason, E.A. and Kestin, J., On combination rules for molecular van der Waals potential-well parameters, *Int. J. Thermophys.* **9** (1988) 131–143.
- [36] Bzowski, J., Kestin, J., Mason, E.A. and Uribe, F.J., Equilibrium and transport properties of gas mixtures at low density: Eleven polyatomic gases and five noble gases, *J. Phys. Chem. Ref. Data* **19** (1990) 1179–1232.
- [37] Chalaris, M. and Samios, J., Hydrogen bonding in supercritical methanol. A molecular dynamics investigation, *J. Phys. Chem. B* **103** (1999) 1161–1166.
- [38] Chatzis, G. and Samios, J., Binary mixtures of supercritical carbon dioxide with methanol. A molecular dynamics simulation study, *Chem. Phys. Lett.* **374** (2003) 187–193.
- [39] Chen, B., Potoff, J.J., and Siepmann, J.I., Monte Carlo calculations for alcohols and their mixtures with alkanes. Transferable potential for phase equilibria. 5. United atom description of primary, secondary, and tertiary alcohols, *J. Phys. Chem. B* **105** (2001) 3093–3104.
- [40] Chialvo, A.A., Kettler, M. and Nezbeda, I., Effect of the range of interactions on the properties of fluids. 2. Structure and phase behavior of acetonitrile, Hydrogen Fluoride, and Formic Acid, *J. Phys. Chem. B* **109** (2005) 9736–9750.
- [41] Chialvo, A.A., *personal communication*, 2007.
- [42] Choi, K. and Tedder, D.W., Molecular interactions in chloroform-diluent mixtures, *AIChE J.* **43** (1997) 196–211.
- [43] Chueh, P.L. and Prausnitz, J.M., Vapor-Liquid equilibria at high pressures: Calculation of partial molar volumes in nonpolar liquid mixtures, *AIChE J.* **13** (1967) 1099–1107.

- [44] Cichowski, E.C., Schmidt, T.R., Errington, J.R., Determination of Henry's law constants through transition matrix Monte Carlo simulation, *Fluid Phase Equilib.* **236** (2005) 58–65.
- [45] Czarniecki, M.A., Maeda, H., Ozaki, Y., Suzuki, M. and Iwahashi, M., Resolution enhancement and band assignments for the first overtone of OH stretching mode of butanols by two-dimensional near-infrared correlation spectroscopy. Part I sec-butanol, *Appl. Spectr.* **52** (1998) 994–1000.
- [46] Czarniecki, M.A., Effect of temperature and concentration on self-association of octan-1-ol studied by two-dimensional Fourier Transform near-infrared correlation spectroscopy, *J. Phys. Chem. A* **104** (2000) 6356–6361.
- [47] Czarniecki, M.A. and Orzechowski, K., Effect of temperature and concentration on self-association of octan-3-ol studied by vibrational spectroscopy and dielectric measurements, *J. Phys. Chem. A* **107** (2003) 1119–1126.
- [48] Dake, S.B. and Chaudhari, R.V., Solubility of carbon monoxide in aqueous mixtures of methanol, acetic acid, ethanol and propionic acid, *J. Chem. Eng. Data* **30** (1985) 400–403.
- [49] Darden, T., York, D. and Pedersen, L., Particle mesh Ewald: $N \log(N)$ method for Ewald sums in large systems, *J. Chem. Phys.* **98** (1993) 10089–10092.
- [50] Daubert, T.E. and Danner, R.P., Physical and Thermodynamic Properties of Pure Chemicals (DIPPR-Project), Hemisphere Publishing Corporation (1989, 1991, 1992).
- [51] Delhommelle, J. and Millié, P., Inadequacy of the Lorentz-Berthelot combining rules for accurate predictions of equilibrium properties by molecular simulation, *Mol. Phys.* **99** (2001) 619–625.
- [52] Diaz Peña, M., Pando, C. and Renuncio, J.A.R., Combination rules for two-body van der Waals coefficients, *J. Chem. Phys.* **72** (1980) 5269–5275.
- [53] Diaz Peña, M., Pando, C. and Renuncio, J.A.R., Combination rules for intermolecular potential parameters. I. Rules based on approximations for the long-range dispersion energy, *J. Chem. Phys.* **76** (1982) 325–332.
- [54] Diaz Peña, M., Pando, C. and Renuncio, J.A.R., Combination rules for intermolecular potential parameters. II. Rules based on approximations for the long-range dispersion energy and an atomic distortion model for the repulsive interactions, *J. Chem. Phys.* **76** (1982) 333–339.
- [55] DIPPR Project 801 - Full Version. *Design Institute for Physical Property Data/AIChE*, 2005.
- [56] Dortmund Data Bank, Version 1.3.0.211, 2004.
- [57] Echt, O., Kreisle, D., Recknagel, E., Saenz, J.J., Casero, R. and Soler, J.M., Dissociation channels of multiply charged van der Waals clusters, *Phys. Rev. A* **38** (1988) 3236–3248.

- [58] Eckl, B., Huang, Y.-L., Vrabec, J. and Hasse, H., Vapor pressure of R227ea + Ethanol at 343.17 K by molecular simulation, *Fluid Phase Equilib.* **260** (2007) 177–182.
- [59] Ely, J.Y., Magee, J.W. and Haynes, W.M., *NBS standard reference database 14, DDMIX, Version 9.06*, NIST, Boulder, Colorado, 1989.
- [60] Eng, W.W.Y., *Vapor-Liquid equilibrium behaviour of thiol binary systems: Studied by the total pressure method*, Master's Thesis, 1977.
- [61] Ewald, P.P., Die Berechnung optischer und elektrostatischer Gitterpotentiale, *Ann. Phys. (Leipzig)* **64** (1921) 253–287.
- [62] Fedors, R.F., A method for estimating both the solubility parameters and molar volumes of liquids, *Polym. Eng. Sci.* **14** (1974) 147–154.
- [63] Fender, B.E.F. and Halsey, G.D., Second virial coefficients of argon, krypton, and argon-krypton mixtures at low temperatures, *J. Chem. Phys.* **36** (1962) 1881–1888.
- [64] Ferrenberg, A.M. and Swendsen, R.H., New Monte Carlo technique for studying phase transitions, *Phys. Rev. Lett.* **61** (1988) 2635–2638.
- [65] Ferrenberg, A.M. and Swendsen, R.H., Optimized Monte Carlo data analysis, *Phys. Rev. Lett.* **63** (1989) 1195–1198.
- [66] Fermeglia, M., Ferrone, M. and Pricl, S., Development of an all-atoms force field from ab initio calculations for alternative refrigerants, *Fluid Phase Equilib.* **210** (2003) 105–116.
- [67] Fernández, G.A., Vrabec, J. and Hasse, H., Self diffusion and binary Maxwell-Stefan diffusion in simple fluids with the Green-Kubo method, *Int. J. Thermophys.* **25** (2004) 175–186.
- [68] Fernández, G.A., Vrabec, J. and Hasse, H., A molecular simulation study of shear and bulk viscosity and thermal conductivity of simple real fluids, *Fluid Phase Equilib.* **221** (2004) 157–163.
- [69] Fincham, D., Leapfrog rotational algorithms, *Mol. Sim.* **8** (1992) 165–178.
- [70] Finney, J.L., The water molecule and its interactions: the interaction between theory, modelling, and experiment, *J. Mol. Liq.* **90** (2001) 303–312.
- [71] Fischer, J., Möller, D., Chialvo, A. and Haile, J.M., The Influence of unlike molecule interaction parameters on liquid mixture excess properties, *Fluid Phase Equilib.* **48** (1989) 161–176.
- [72] Forland, G.M., Liang, Y.Z., Kvalheim, O.M., Hoiland, H. and Chazy, A., Associative behavior of benzyl alcohol in carbon tetrachloride solutions, *J. Phys. Chem. B* **101** (1997) 6960–6969.
- [73] Frenkel, D. and Smit, B., *Understanding Molecular Simulation: from Algorithms to Applications*. Academic Press, London, 2002.

- [74] Frenkel, M., *TRC thermodynamics tables - non-hydrocarbons*. The Texas A & M University System: College Station, Texas, 1985.
- [75] Friend, D.G., Frurip, D.J., Lemmon, E.W., Morrison, R.E., Olson, J.D. and Wilson, L.C., Establishing benchmarks for the Second Industrial Fluids Simulation Challenge, *Fluid Phase Equilib.* **236** (2005) 15-24.
- [76] Galliéro, G., Boned, C., Baylaucq, A. and Montel, F., Molecular dynamics comparative study of Lennard-Jones α -6 and exponential α -6 potentials: Application to real simple fluids (viscosity and pressure), *Phys. Rev. E* **73** (2006) 61201-61209.
- [77] Good, R.J. and Hope, C.J., Test of combining rules for intermolecular distances. Potential function constants from second virial coefficients, *J. Chem. Phys* **55** (1971) 111-116.
- [78] Gotlib, I.Y., Piotrovskaya, E.M. and de Leeuw, S.W., Properties of coexisting fluid phases of a binary system methanol-ethane by computer simulation, *Fluid Phase Equilib.* **129** (1997) 1-13.
- [79] Gotlib, I.Y. and Piotrovskaya, E.M., Numerical simulation of liquid-vapor equilibrium in the ethanol-ethane system, *Russ. Phys. Chem.* **72** (1998) 1562-1566.
- [80] Gotlib, I.Y. and Piotrovskaya, E.M., Properties of coexisting phases for the ethanol-ethane binary system by computer simulation, *J. Phys. Chem. B* **103** (1999) 7681-7686.
- [81] Grausø, L., Fredenslund, A. and Møllerup, J., Vapor-Liquid equilibrium data for the systems $C_2H_6 + N_2$, $C_2H_4 + N_2$, $C_3H_8 + N_2$, and $C_3H_6 + N_2$, *Fluid Phase Equilib.* **1** (1977) 13-26.
- [82] Gray, C.G. and Gubbins, K.E., *Theory of Molecular Fluids*, Volume 1: Fundamentals, Clarendon Press, Oxford, 1984.
- [83] Guillot, B., A reappraisal of what we have learnt during three decades of computer simulations on water, *J. Mol. Liq.* **101** (2002) 219-260.
- [84] Gupta, R.B. and Brinkley, R.L., Hydrogen-bond cooperativity in 1-alkanol + *n*-alkane binary mixtures, *AIChE J.* **44** (1998) 207-213.
- [85] Gupta, S.K., Lesslie, R.D. and King, A.D., Solubility of alcohols in compressed gases. Comparison of vapor-phase interactions of alcohols and homomorphic compounds with various gases. I. Ethanol in compressed helium, hydrogen, argon, methane, ethylene, ethane, carbon dioxide, and nitrous oxide, *J. Phys. Chem.* **77** (1973) 2011-2015.
- [86] Guzechak, O.Y., Sarancha, V.N., Romanyuk, I.M., Yavorskaya, O.M. and Churik, G.P., Solubility of propylene in organic-solvents. *J. Appl. Chem. (U.S.S.R.)* **57** (1985) 1662-1665.
- [87] Halgren, T.A., Representation of van der Waals (vdW) interactions in molecular mechanics force fields: Potential form, combination rules, and vdW parameters, *J. Am. Chem. Soc.* **114** (1992) 7827-7843.

- [88] Hasse, H., Anwendungen der Spektroskopie in thermodynamischen Untersuchungen fluider Mischungen, *Fortschritt-Berichte VDI*, Reihe 3, Nr. 458, VDI-Verlag, Düsseldorf, 1996.
- [89] Haughney, M., Ferrario, M. and McDonald, I.R., Molecular-dynamics simulation of liquid methanol, *J. Phys. Chem.* **91** (1987) 4934–4940.
- [90] Hayduk, W. and Cheng, S.C., Solubilities of ethane and other gases in normal paraffin solvents, *Can. J. Chem. Eng.* **48** (1970) 93–99.
- [91] Hiza, M.J. and Duncan, A.G., Comments on “Intermolecular Forces: Thermal Diffusion and Diffusion in He-Kr and H₂ – Kr”, *Phys. Fluids* **12** (1969) 1531–1532.
- [92] Hiza, M.J. and Duncan, A.G., A Correlation for the Prediction of interaction energy parameters for mixtures of small molecules, *AIChE J.* **16** (1970) 733–738.
- [93] Hiza, M.J. and Robinson, R.L., Comment on “Intermolecular forces in mixtures of helium with the heavier noble gases”, *J. Chem. Phys.* **68** (1978) 4768–4769.
- [94] Hudson, G.H. and McCoubrey, J.C., Intermolecular forces between unlike molecules. A more complete form of the combining rules, *Trans. Faraday Soc.* **56** (1960) 761–766.
- [95] Hirschfelder, J.O., Curtiss, C.F. and Bird, R.B., *Molecular Theory of Gases and Liquids*, J. Wiley & Sons, New York, 1954.
- [96] Hockney, R.W. and Eastwood, J.W., *Computer Simulations Using Particles*, McGraw-Hill, New York, 1981.
- [97] Hoffmann, M.M. and Conradi, M.S., Are there hydrogen bonds in supercritical methanol and ethanol?, *J. Phys. Chem. B* **102** (1998) 263–271.
- [98] Hofman, T. and Casanova, C., Thermodynamics of alkanol-alkane systems - New modifications of the ERAS model, *J. Chem. Soc., Faraday Trans.* **92** (1996) 1175–1185.
- [99] Hong, J.H., Malone, P.V., Jett, M.D. and Kobayashi, R., The measurement and interpretation of the fluid-phase equilibria of a normal fluid in a hydrogen bonding solvent: the methane – methanol system, *Fluid Phase Equilib.* **38** (1987) 83–96.
- [100] Horn, H.W., Swope, W.C., Pitera, J.W., Madura, J.D., Dick, T.J., Hura, G.L. and Head-Gordon, T., Development of an improved four-site water model for biomolecular simulations: TIP4P-Ew, *J. Chem. Phys.* **120** (2004) 9665–9678.
- [101] Horn, H.W., Swope, W.C. and Pitera, J.W., Characterization of the TIP4P-Ew water model: Vapor pressure and boiling point, *J. Chem. Phys.* **123** (2005) 194504–194515.
- [102] Houndonougbo, Y., Jin, H., Rajagopalan, B., Wong, K., Kuczera, K., Subramaniam, B. and Laird, B., Phase equilibria in carbon dioxide expanded solvents: Experiments and molecular simulations, *J. Phys. Chem. B* **110** (2006) 13195–13202.

- [103] Ishihara, K., Tanaka, H. and Kato, M., Phase equilibrium properties of ethane + methanol system at 298.15 K, *Fluid Phase Equilib.* **144** (1998) 131–136.
- [104] Iwahashi, M., Suzuki, M., Katayama, N., Matsuzawa, H., Czarnecki, M.A., Ozaki, Y. and Wakisaka, A., Molecular self-assembling of butan-1-ol, butan-2-ol, and 2-methylpropan-2-ol in carbon tetrachloride solutions as observed by near-infrared spectroscopic measurements, *Appl. Spectr.* **54** (2000) 268–276.
- [105] Jedlovsky, P. and Turi, L., A new five-site pair potential for formic acid in liquid simulations, *J. Phys. Chem. A* **101** (1997) 2662–2665.
- [106] Jedlovsky, P. and Turi, L., Role of the C–H...O hydrogen bonds in liquids: A Monte Carlo simulation study of liquid formic acid using a newly developed pair-potential, *J. Phys. Chem. B* **101** (1997) 5429–5436.
- [107] Jedlovsky, P. and Turi, L., Erratum to “A new five-site pair potential for formic acid in liquid simulations”, *J. Phys. Chem. A* **103** (1999) 3796–3796.
- [108] Jedlovsky, P., *personal communication*, 2006.
- [109] Jones, J.E., On the determination of molecular fields. I. From the variation of the viscosity of a gas with temperature, *Proc. Roy. Soc.* **106A** (1924) 441–462.
- [110] Jones, J.E., On the determination of molecular fields. II. From the equation of state of a gas, *Proc. Roy. Soc.* **106A** (1924) 463–477.
- [111] Jorgensen, W.L., Simulation of liquid ethanol including internal rotation, *J. Am. Chem. Soc.* **103** (1981) 345–350.
- [112] Jorgensen, W.L., Chandrasekhar, J.D., Madura, R.W., Impey, R.W. and Klein, M.L., Comparison of simple potential functions for simulating liquid water, *J. Chem. Phys.* **79** (1983) 926–935.
- [113] Kamath, G., Georgiev, G. and Potoff, J.J., Molecular modeling of phase behavior and microstructure of acetone-chloroform-methanol binary mixtures, *J. Phys. Chem. B* **109** (2005) 19463–19473.
- [114] Kamath, G., Robinson, J. and Potoff, J.J., Application of TraPPE-UA force field for determination of vapor-liquid equilibria of carboxylate esters, *Fluid Phase Equilib.* **240** (2006) 46–55.
- [115] Kanakubo, M., Aizawa, T., Kawakami, T., Sato, Y., Ikushima, O., Hatakeda, K. and Saito, N., Studies on solute-solvent interactions in gaseous and supercritical carbon dioxide by high-pressure ^1H NMR spectroscopy, *J. Phys. Chem. B* **104** (2000) 2749–2758.
- [116] Katayama, T. and Nitta, T., Solubilities of hydrogen and nitrogen in alcohols and n-hexane, *J. Chem. Eng. Data* **21** (1976) 194–196.
- [117] Ke, J., Jin, S., Han, B., Yan, H. and Shen, D., Hydrogen bonding of some organic acids in supercritical CO_2 with polar cosolvents, *J. Supercrit. Fluids* **11** (1997) 53–60.

- [118] Kestin, J., Knierim, K., Mason, E.A., Najafi, B., Ro, S.T., and Waldman, M., Equilibrium and transport properties of the noble gases and their mixtures at low density, *J. Phys. Chem. Ref. Data* **13** (1984) 229–303.
- [119] Kierzkowska-Pawlak, H. and Zarzycki, R., Solubility of carbon dioxide and nitrous oxide in water + methyldiethanolamine and ethanol + methyldiethanolamine solutions, *J. Chem. Eng. Data* **47** (2002) 1506–1509.
- [120] Kiyama, R. and Hiraoka, H., The Solubilities of compressed acetylene gas in liquids, II. The solubility of compressed acetylene gas in methanol, *Rev. Phys. Chem. Japan* **25** (1955) 16–20.
- [121] Kohler, F., Zur Berechnung der Wechselwirkungsenergie zwischen ungleichen Molekülen in binen flüssigen Mischungen, *Monatsh. Chem.* **88** (1957) 857–877.
- [122] Kohler, F., Fischer, J. and Wilhelm, E., Intermolecular force parameters for unlike pairs, *J. Mol. Struct.* **84** (1982) 245–250.
- [123] Kong, C.L., Combining rules for intermolecular potential parameters. II. Rules for the Lennard-Jones (12-6) potential and the Morse potential, *J. Chem. Phys.* **59** (1973) 2464–2467.
- [124] Kosztolányi, T., Bakó, I. and Pálinkás, G., Hydrogen bonding in liquid methanol, methylamine, and methanethiol studied by molecular-dynamics simulations, *J. Chem. Phys.* **118** (2003) 4546–4555.
- [125] Koudelka, L., The solubility of gases in nonelectrolyte mixtures. II. The expression of solubility in binary aqueous solutions by means of a supplement function. *Chemické Zvesti* **18** (1964) 493–501.
- [126] Krichevskii, I., Zhavoronkov, N.M. and Tsiklis, D.S., The solubility of hydrogen, carbon monoxide and their mixtures in methanol under pressure, *J. Phys. Chem. (U.S.S.R.)* **9** (1937) 317–328.
- [127] Kronome, G., Szalai, I., Wendland, M. and Fischer, J., Extension of the NpT + test particle method for the calculation of phase equilibria of nitrogen + ethane, *J. Mol. Liq.* **85** (2000) 237–247.
- [128] Kunerth, W., Solubility of carbon dioxide and nitrous oxide in certain solvents, *Phys. Rev.* **19** (1922) 512–524.
- [129] Laidig, K.E. and Bader, R.F.W., Properties of atoms in molecules: Atomic polarizabilities, *J. Chem. Phys.* **93** (1990) 7213–7224.
- [130] Lalanne, P., Andanson, J.M., Soetens, J.C., Tassaing, T., Danten, Y. and Besnard, M., Hydrogen bonding in supercritical ethanol assessed by infrared and Raman spectroscopies, *J. Phys. Chem. A* **108** (2004) 3902–3909.
- [131] Lannung, A., The Solubilities of helium, neon and argon in water and some organic solvents, *J. Am. Chem. Soc.* **52** (1930) 68–80.

- [132] Lannung, A. and Gjaldback, J.C., The solubility of methane in hydrocarbons, alcohols, water, and other solvents, *Acta Chem. Scand.* **14** (1960) 1124–1128.
- [133] Laso, M., de Pablo, J.J. and Suter, U.W., Simulation of phase equilibria for chain molecules, *J. Chem. Phys.* **97** (1992) 2817–2819.
- [134] Levi, M.G., Assorbimento dei gas in solventi organici ed in soluzioni di solventi organici, *Gazz. Chim. Ital.* **31** (1901) 513–541.
- [135] Lide, R.D., *CRC Handbook of Chemistry and Physics*, CRC Press Inc., 1995–1996.
- [136] Lim, J.S., Lee, Y.Y. and Chun, H.S., Phase equilibria for carbon dioxide-ethanol-water system at elevated pressures, *J. Supercrit. Fluids* **7** (1994) 219–230.
- [137] Lísal, M., Smith, W.R. and Nezbeda, I., Accurate computer simulation of phase equilibrium for complex fluid mixtures. Application to binaries involving isobutene, methanol, methyl *tert*-butyl ether, and *n*-butane, *J. Phys. Chem. B* **103** (1999) 10496–10505.
- [138] Lísal, M., Smith, W.R. and Nezbeda, I., Molecular simulation of multicomponent reaction and phase equilibria in MTBE ternary system, *AIChE J.* **46** (2000) 866–875.
- [139] Lísal, M., Smith, W.R. and Nezbeda, I., Accurate vapour-liquid equilibrium calculations for complex systems using the reaction Gibbs Ensemble Monte Carlo simulation method, *Fluid Phase Equilib.* **181** (2001) 127–146.
- [140] Lísal, M., Kolafa, J. and Nezbeda, I., An examination of the five-site potential (TIP5P) for water, *J. Chem. Phys.* **117** (2001) 8892–8897.
- [141] Lísal, M., Nezbeda, I. and Smith, W.R., Vapor-liquid equilibria in five-site (TIP5P) models of water, *J. Phys. Chem. B* **108** (2004) 7412–7414.
- [142] Liu, Q., Takemura, F. and Yabe, A., Solubility and diffusivity of carbon monoxide in liquid methanol, *J. Chem. Eng. Data* **41** (1996) 589–592.
- [143] Liu, Y.L., Maeda, H., Ozaki, Y., Czarnecki, M.A., Suzuki, M. and Iwahashi, M., FT-near-IR and FT-IR studies of *cis*-9-octadecen-1-ol – Molar absorption-coefficient of a band due to the first overtone of the stretching mode of the terminal OH group and comparison of anharmonicity of an OH stretching mode among the monomeric and associated species, *Appl. Spectr.* **49** (1995) 1661–1668.
- [144] London, F., Über einige Eigenschaften und Anwendungen der Molekularkräfte, *Z. Phys. Chem. (Leipzig, Ger.)* **11** (1930) 222–251.
- [145] London, F., The general theory of molecular forces, *Trans. Faraday Soc.* **33** (1937) 8–26.
- [146] Lorrain, P., Corson, D.R. and Lorrain, F., *Elektromagnetische Felder und Wellen*, Walter de Gruyter, Berlin, 1995.
- [147] Lorentz, H.A., Über die Anwendung des Satzes vom Virial in der kinetischen Theorie der Gase, *Ann. Phys.* **12** (1881) 127–136.

- [148] Lotfi, A., Vrabec, J. and Fischer, J., Vapour liquid equilibria of the Lennard-Jones fluid from the NpT plus test particle method, *Mol. Phys.* **76** (1992) 1319–1333.
- [149] Lubna, N., Kamath, G., Potoff, J.J., Rai, N. and Siepmann, J.I., Transferable potentials for phase equilibria. 8. United-atom description for thiols, sulfides, disulfides, and thiophene, *J. Phys. Chem. B* **109** (2005) 24100–24107.
- [150] Luehring, P. and Schumpe, A., Gas solubilities (hydrogen, helium, nitrogen, carbon monoxide, oxygen, argon, carbon dioxide) in organic liquids at 293.2 K, *J. Chem. Eng. Data* **34** (1989) 250–252.
- [151] Luo, W., Lay, J. and Chen, J., NMR study of hydrogen bonding association of some sterically hindered alcohols in carbon tetrachloride, chloroform and cyclohexane, *Z. Phys. Chem. (München, Ger.)* **216** (2002) 829–843.
- [152] Lustig, R., Angle-average for the powers of the distance between two separated vectors, *Mol. Phys.* **65** (1988) 175–179.
- [153] Mahoney, W.M. and Jorgensen, W.L., A five-site model for liquid water and the reproduction of the density anomaly by rigid, nonpolarizable potential functions, *J. Chem. Phys.* **112** (2000) 8910–8922.
- [154] Maitland, G.C., Intermolecular Forces, *Oxford*, Clarendon Press, 1981.
- [155] Maiwald, M. and Schneider, G.M., Near-infrared spectroscopic investigations on phase behavior and hydrogen-bonding of ω -heptanolactam in supercritical chlorotri-fluoromethane, *J. Supercrit. Fluids* **8** (1995) 25–29.
- [156] Maiwald, M., Li, H., Schnabel, T., Braun, K. and Hasse, H., On-line ^1H NMR spectroscopic investigation of hydrogen bonding in supercritical and near critical CO_2 -methanol up to 35 MPa and 403 K, *J. Supercrit. Fluids* **43** (2007) 267–275.
- [157] Makranczy, J., Rusz, L. and Balog-Megyery, K., Solubility of gases in normal alcohols, *Hung. J. Ind. Chem.* **7** (1979) 41–46.
- [158] Mason, E.A., Islam, M. and Weissmann, S., Thermal diffusion and diffusion in hydrogen-krypton mixtures, *Phys. Fluids* **7** (1964) 1011–1022.
- [159] McDaniel, A.S., The absorption of hydrocarbon gases by non-aqueous liquids, *J. Phys. Chem.* **15** (1911) 587–610.
- [160] Mináry, P., Jedlovsky, P., Mezei, M. and Turi, L., A comprehensive liquid simulation study of neat formic acid, *J. Phys. Chem. B* **104** (2000) 8287–8294.
- [161] Miyano, Y. and Hayduk, W., Solubility of acetylene in several polar and nonpolar solvents and solvent mixtures, *Can. J. Chem. Eng.* **59** (1981) 746–751.
- [162] Möller, D. and Fischer, J., Vapor liquid equilibrium of a pure fluid from test particle method in combination with NpT molecular dynamics simulations, *Mol. Phys.* **69** (1990) 463–473.

- [163] Möller, D. and Fischer, J., Vapor liquid equilibrium of a pure fluid from test particle method in combination with NpT molecular dynamics simulations [Erratum: *Mol. Phys.* **69** (1990) 463–473], *Mol. Phys.* **75** (1992) 1461–1462.
- [164] Möller, D., Óprzynski, J., Müller, A. and Fischer, J., Prediction of thermodynamic properties of fluid mixtures by *Molecular-Dynamics simulations: Methane-ethane*, *Mol. Phys.* **75** (1992) 363–378.
- [165] Möller, D. and Fischer, J., Determination of an effective intermolecular potential for carbon dioxide using vapor-liquid phase equilibria from NpT -test particle simulations, *Fluid Phase Equilib.* **100** (1994) 35–61.
- [166] Mohai, B. and Maleczki, M., Gas-absorption studies. VIII. Absorption of acetylene in ethyl alcohol, methyl alcohol, and diethyl ether at low temperatures, *Veszpremi Vegyipari Egyetem Kozlemenyei* **3** (1959) 211–220.
- [167] Moon, S.D., Monte Carlo simulation for vapor-liquid equilibrium of binary mixtures $\text{CO}_2/\text{CH}_3\text{OH}$, $\text{CO}_2/\text{C}_2\text{H}_5\text{OH}$, and $\text{CO}_2/\text{CH}_3\text{CH}_2\text{CH}_2\text{OH}$, *Bull. Korean Chem. Soc.* **23** (2002) 811–816.
- [168] Murad, S. and Gupta, S., A simple molecular dynamics simulation for calculating Henry's constant and solubility of gases in liquids, *Chem. Phys. Lett.* **319** (2000) 60–64.
- [169] Muthukumaran, P., Brinkley, R.L. and Gupta, R.B., Lattice-fluid equation of state with hydrogen-bond cooperativity, *AIChE J.* **48** (2002) 386–392.
- [170] Nada, H. and van der Eerden, J.P.J.M., An intermolecular potential model for the simulation of ice and water near the melting point: A six-site model of H_2O , *J. Chem. Phys.* **118** (2003) 7401–7413.
- [171] Narasimhan, S., Natarajan, G.S. and Nageshwar, G.D., Solubilities of ethene, propene and 2-methylpropene in normal alcohols, *Indian J. Technol.* **19** (1981) 298–299.
- [172] Nezbeda, I. and Kolafa, J., A new version of the insertion particle method for determining the chemical potential by Monte Carlo simulation, *Mol. Sim.* **5** (1991) 391–403.
- [173] Nikiforov, M.Y., Lukyanchikova, I.A., Grechukhin, M.V., Alper, G.A. and Krestov, G.A., Association of molecules of monobasic aliphatic alcohols according to ^1H NMR spectroscopy data, *Russ. J. Phys. Chem.* **70** (1996) 968–971.
- [174] Nitta, T., Fujio, J. and Katayama, T., Solubilities of nitrogen in binary solutions. Mixtures of ethanol with benzene, ethyl acetate, and diethyl ether, *J. Chem. Eng. Data* **23** (1978) 157–159.
- [175] Nymand, T.M. and Linse, P., Ewald summation and reaction field methods for potentials with atomic charges, dipoles, and polarizabilities, *J. Chem. Phys.* **112** (2000) 6152–6160.

- [176] Ohgaki, K., Nishii, H., Saito, T. and Katayama, T., High-pressure phase equilibria for the methanol-ethylene system at 25°C and 40°C, *J. Chem. Eng. Japan* **16** (1983) 263–267.
- [177] Ohta, A., Murakami, R., Urata, A., Asakawa, T., Miyagishi, S. and Aratono, M., Aggregation behavior of fluoroctanols in hydrocarbon solvents, *J. Phys. Chem. B* **107** (2003) 11502–11509.
- [178] Onsager, L., Electric moments of molecules in liquids, *J. Am. Chem. Soc.* **58** (1936) 1486–1493.
- [179] Otsuka, E. and Takada, M., Studies on purification of acetylene from the burner gas formed by partial oxidation of methan (I) - Study on solubility of acetylene and carbon-dioxide, *J. Fuel Soc. Japan* **42** (1963) 229–237.
- [180] Panagiotopoulos, A.Z., Direct determination of phase coexistence properties of fluids by Monte Carlo simulation in a new ensemble, *Mol. Phys.* **61** (1987) 813–826.
- [181] Pape, D. and Roscher, T., *Solubility of nitrogen in mono-, di-, and trimethylamine*, FIZ Report, 1974.
- [182] Paricaud, P., Předota, M., Chialvo, A.A. and Cummings, P.T., From dimer to condensed phases at extreme conditions: Accurate predictions of the properties of water by Gaussian charge polarizable model, *J. Chem. Phys.* **122** (2005) 244511–244524.
- [183] Pfohl, O., Pagel, A. and Brunner, G., Phase equilibria in systems containing *o*-cresol, *p*-cresol, carbon dioxide, and ethanol at 323.15–473.15 K and 10–35 MPa, *Fluid Phase Equilib.* **157** (1999) 53–79.
- [184] Plimpton, S., Fast parallel algorithms for short-range Molecular Dynamics, *J. Comp. Phys.* **117** (1994) 1–19.
- [185] Postigo, M.A. and Katz, M., Solubility and thermodynamics of carbon dioxide in aqueous ethanol solutions, *J. Solution Chem.* **16** (1987) 1015–1024.
- [186] Potoff, J.J. and Panagiotopoulos, A.Z., Critical point and phase behavior of the pure fluid and a Lennard-Jones mixture, *J. Chem. Phys.* **109** (1998) 10914–10920.
- [187] Potoff, J.J., Errington, J.R. and Panagiotopoulos, A.Z., Molecular simulation of phase equilibria for mixtures of polar and non-polar components, *Mol. Phys.* **97** (1999) 1073–1083.
- [188] Potoff, J.J., *personal communication*, 2007.
- [189] Price, S.L., Stone, A.J. and Alderton, M., Explicit formulae for the electrostatic energy, forces and torques between a pair of molecules of arbitrary symmetry, *Mol. Phys.* **52** (1984) 987–1001.
- [190] Prorokov, V.N., Dolotov, V.V. and Krestov, G.A., Solubility and thermodynamic characteristics for the dissolution of argon, krypton, and xenon in water and in monohydric alcohols, *Russ. J. Phys. Chem.* **58** (1984) 1153–1154.

- [191] Quentrec, B. and Brot, C., New method for searching for neighbors in Molecular Dynamics computations, *Comput. Phys.* **13** (1973) 430–432.
- [192] Rackett, H.G., Equation of state for saturated liquids, *J. Chem. Eng. Data* **15** (1970) 514–517.
- [193] Reed, T.M. III., The theoretical energies of mixing for fluorocarbon-hydrocarbon mixtures, *J. Phys. Chem.* **59** (1955) 425–428.
- [194] Reid, R.C. and Leland, T.W., Pseudocritical constants, *AIChE J.* **11** (1965) 228–237.
- [195] Rick, S.W., A reoptimization of the five-site water potential (TIP5P) for use with Ewald sums, *J. Chem. Phys.* **120** (2004) 6085–6093.
- [196] Ryutani, B., Solubility of acetylene in organic solvents at low temperature under high pressure. II. Solubility of acetylene in hydrocarbons, methanol, and chloroform, *Chem. Soc. Jpn.*, **80** (1959) 1411–1415.
- [197] Robinson, D.B., Peng, D.Y. and Chung, S.Y.K., The development of the Peng-Robinson equation and its application to phase equilibrium in a system containing methanol, *Fluid Phase Equilib.* **24** (1985) 25–41.
- [198] Rojas, A.S., Gros, H.P. and Brignole, E.A., Vapor-liquid equilibrium data for propylene + ethanol, propylene + MEK, and propylene + MTBE, *J. Chem. Eng. Data* **42** (1997) 1238–1240.
- [199] Roszak, S., Gee, R.H., Balasubramanian, K. and Fried, L.E., New theoretical insight into the interactions and properties of formic acid: Development of a quantum-based pair potential for formic acid, *J. Chem. Phys.* **123** (2005) 144702–144711.
- [200] Sadus, R.J., Molecular simulation of Henry's constant at vapor-liquid and liquid-liquid phase boundaries, *J. Phys. Chem. B* **101** (1997) 3834–3838.
- [201] Schmidt, M.W., Baldrige, K.K., Boatz, J.A., Elbert, S.T., Gordon, M.S., Jensen, J.H., Koseki, S., Matsunaga, N., Nguyen, K.A., Shujun, S., Windus, T.L., Dupuis, M. and Montgomery, A.M., General atomic and molecular electronic structure system, *J. Comput. Chem.* **14** (1993) 1347–1363.
- [202] Schnabel, T., Vrabec, J. and Hasse, H., Henry's law constants of methane, nitrogen, oxygen and carbon dioxide in ethanol from 273 to 498 K, *Fluid Phase Equilib.* **233** (2005) 134–143.
- [203] Schnabel, T., Vrabec, J. and Hasse, H., Erratum to Henry's law constants of methane, nitrogen, oxygen and carbon dioxide in ethanol from 273 to 498 K, *Fluid Phase Equilib.* **239** (2006) 125–126.
- [204] Schnabel, T., Cortada, M., Vrabec, J., Lago, S. and Hasse, H., Molecular Model for Formic Acid adjusted to Vapor-Liquid Equilibria, *Chem. Phys. Lett.* **435** (2007) 268–272.

- [205] Schnabel, T., Vrabec, J. and Hasse, H., Unlike Lennard-Jones Parameters for Vapor-Liquid Equilibria, *J. Mol. Liq.* **135** (2007) 170–178.
- [206] Schnabel, T., Srivastava, A., Vrabec, J. and Hasse, H., Hydrogen Bonding of Methanol in Supercritical CO₂: Comparison between ¹H-NMR Spectroscopic Data and Molecular Simulation Results, *J. Phys. Chem. B* **111** (2007) 9871–9878.
- [207] Schnabel, T., Vrabec, J. and Hasse, H., Molecular Simulation Study of Hydrogen Bonding Mixtures and New Molecular Models for Mono- and Dimethylamine, *Fluid Phase Equilib.* **263** (2008) 144–159.
- [208] Šerbanović, S.P., Miljajlović, M.L., Radović, I.R., Djordjević, B.D., Kijevčanin, M.L., Djordjević, E.M. and Tasić, A.Ž., Vapour-liquid equilibria of the OPLS (Optimized Potentials for Liquid Simulations) model for binary systems of alkanes and alkanes + alcohols, *J. Serb. Chem. Soc.* **70** (2005) 527–539.
- [209] Shekaari, H., Modarress, H. and Hadipour, N., Thermodynamic investigation on self-association of alcohols in carbon tetrachloride by FT-NMR spectroscopy, *J. Phys. Chem. A* **107** (2003) 1891–1895.
- [210] Shenderei, E.R., Zelvenskii, Y.D. and Ivanovskii, F.P., The solubility of carbon dioxide in alcohols at low temperature, *Gazovaya Prom.* **12** (1958) 36–42.
- [211] Shenderei, E.R., Zelvenskii, Y.D. and Ivanovskii, F.P., Solubility of carbon dioxide in methanol at low temperature and high pressure, *Khim. Prom., Moskau (U.S.S.R.)* **4** (1959) 50–53.
- [212] Shenderei, E.R., Zelvenskii, Y.D. and Ivanovskii, F.P., The solubility of hydrogen, nitrogen, and methane in methanol under pressure at low temperatures, *Gazovaya Prom.* **6** (1961) 42–45.
- [213] Shevkunov, S.V., Martsinovskii, A.A. and Vorontsov-Velyaminov, P.N., Calculating the critical size and properties of microdrop by the monte-carlo method in a generalized ensemble, *Teplofizika Vysokikh Temperatur* **26** (1988) 246–254.
- [214] Shing, K.S., Gubbins, K.E. and Lucas, K., Henry constants in nonideal fluid mixtures. Computer simulation and theory, *Mol. Phys.* **65** (1988) 1235–1252.
- [215] Siepmann, J.I., A method for the direct calculation of chemical potentials for dense chain systems, *Mol. Phys.* **70** (1990) 1145–1158.
- [216] Sikora, P.T., Combining rules for spherically symmetric intermolecular potentials, *J. Phys. B: Atom. Molec. Phys.* **3** (1970) 1475–1482.
- [217] Sisskind, B. and Kasarnovsky, I., Untersuchungen über die Löslichkeit der Gase. I. Mitteilung. Löslichkeit des Argons unter hohen Drücken, *Z. Anorg. Allg. Chem.* **200** (1931) 279–286.
- [218] Smith, F.T., Atomic distortion and the combining rule for repulsive potentials, *Phys. Rev. A* **5** (1972) 1708–1713.

- [219] Smith, R.L., Saito, C., Suzuki, S., Lee, S.B., Inomata, H. and Arai, K., Temperature dependence of dielectric spectra of carbon dioxide and methanol mixtures at high pressures, *Fluid Phase Equilib.* **194** (2002) 869–877.
- [220] Spencer, C.F. and Danner, R.P., Prediction of bubble-point density of mixtures, *J. Chem. Eng. Data* **18** (1973) 230–234.
- [221] Srivastava, B.N. and Madan, M.P., Thermal diffusion of gas mixtures and forces between unlike molecules, *Proc. Phys. Soc., London, Sect. A* **66** (1953) 278–287.
- [222] Stern, O., Zur kinetischen Theorie des osmotischen Drucks konzentrierter Lösungen und über die Gültigkeit des Henryschen Gesetzes für konzentrierte Lösungen von Kohlendioxid in organischen Lösungsmitteln bei tiefen Temperaturen, *Z. Phys. Chem. (Leipzig)* **81** (1912) 441–476.
- [223] Stillinger, F. H. and Rahman, A., Improved simulation of liquid water by molecular dynamics, *J. Chem. Phys.* **60** (1974) 1545–1557.
- [224] Storange, L., Christy, A.A., Kvalheim, O.M., Shen, H. and Liang, Y., Study of the self-association of alcohols by near-infrared spectroscopy and multivariate 2D techniques, *J. Phys. Chem. A* **106** (2002) 8543–8553.
- [225] Stoll, J., Vrabc, J., Hasse, H. and Fischer, J., Comprehensive study of the vapour-liquid equilibria of the two-centre Lennard-Jones plus point quadrupole fluid, *Fluid Phase Equilib.* **179** (2001) 339–362.
- [226] Stoll, J., Vrabc, J. and Hasse, H., Vapor-liquid equilibria of mixtures containing nitrogen, oxygen, carbon dioxide, and ethane, *AIChE J.* **49** (2003) 2187–2198.
- [227] Stoll, J., Vrabc, J. and Hasse, H., A set of molecular models for carbon monoxide and halogenated hydrocarbons, *J. Chem. Phys.* **119** (2003) 11396–11407.
- [228] Stoll, J., Molecular Models for the Prediction of Thermophysical Properties of Pure Fluids and Mixtures, Fortschritt-Berichte VDI, Reihe 3, 836, VDI Verlag, Düsseldorf, 2005.
- [229] Stubbs, J.M., Chen, B., Potoff, J.J. and Siepmann, J.I., Monte Carlo calculations for the phase equilibria of alkanes, alcohols, water, and their mixtures, *Fluid Phase Equilib.* **183–184** (2001) 301–309.
- [230] Stubbs, J.M. and Siepmann, J.I., Binary phase behavior and aggregation of dilute methanol in supercritical carbon dioxide: A Monte Carlo simulation study, *J. Chem. Phys.* **121** (2004) 1525–1534.
- [231] Suzuki, K., Sue, H., Itou, M., Smith, R.L., Inomata, H., Arai, K. and Saito, S., Isothermal vapor-liquid equilibrium data for binary systems at high pressures: carbon dioxide-methanol, carbon dioxide-ethanol, carbon dioxide-1-propanol, methane-ethanol, methane-1-propanol, ethane-ethanol, and ethane-1-propanol systems, *J. Chem. Eng. Data* **35** (1990) 63–66.

- [232] Takahashi, M., Kobayashi, Y. and Takeuchi, H., Diffusion coefficients and solubilities of carbon dioxide in binary mixed solvents, *J. Chem. Eng. Data* **27** (1982) 328–331.
- [233] Takenouchi, M., Kato, R. and Nishiumi, H., Henry's law constant measurements of CCl_2F_2 , CHClF_2 , CH_2F_2 , C_2ClF_5 , C_2HF_5 , CH_2FCF_3 , and CH_3CHF_2 in methanol, ethanol, and 2-propanol, *J. Chem. Eng. Data* **46** (2001) 746–749.
- [234] Tang, K.T. and Toennies, J.P., New combining rules for well parameters and shapes of the van der Waals potential of mixed rare gas systems, *Z. Phys., D At. Mol. Clust.* **1** (1986) 91–101.
- [235] Thote, A.J. and Gupta, R.B., Hydrogen-bonding effects in liquid crystals for application to LCDs, *Ind. Eng. Chem. Res.* **42** (2003) 1129–1136.
- [236] Tkaczuk, P., *Experimentelle Bestimmung der Gaslöslichkeit von Methan in Ketonen und Vergleich mit vorausgerechneten Ergebnissen*, University of Dortmund, Germany, Report, 1986.
- [237] Tkadlecova, M., Dohnal, V. and Costas, M., ^1H NMR and thermodynamic study of self-association and complex formation equilibria by hydrogen bonding. Methanol with chloroform or halothane, *Phys. Chem. Chem. Phys.* **1** (1999) 1479–1486.
- [238] Tokunaga, J., Nitta, T. and Katayama, T., Solubility of carbon dioxide in aqueous alcohol solutions. Methanol-water, ethanol-water systems, *Chem. Eng. Japan* **33** (1969) 775–779.
- [239] Tokunaga, J. and Kawai, M., Solubilities of methane in methanol-water and ethanol-water solutions, *J. Chem. Eng. Japan* **8** (1975) 326–327.
- [240] Tonner, S.P., Wainwright, M.S. and Trimm, D.L., Solubility of carbon monoxide in alcohols, *J. Chem. Eng. Data* **28** (1983) 59–61.
- [241] Toxvaerd, T., Molecular dynamics calculation of the equation of state of alkanes, *J. Chem. Phys.* **93** (1990) 4290–4295.
- [242] Trust, D.B. and Kurata, F., Vapor-liquid and liquid-liquid vapor phase behavior of the carbon monoxide-propane and the carbon monoxide-ethane systems, *AIChE J.* **17** (1971) 415–419.
- [243] Turi, L., Ab initio molecular orbital analysis of dimers of *cis*-formic acid. Implications for condensed phases, *J. Phys. Chem.* **100** (1996) 11285–11291.
- [244] Ungerer, P., Beauvais, C., Delhommelle, J., Boutin, A., Rousseau, B. and Fuchs, A.H., Optimization of the anisotropic united atoms intermolecular potential for *n*-alkanes, *J. Chem. Phys.* **112** (2000) 5499–5510.
- [245] Ungerer, P., Wender, A., Demoulin, G., Bourasseau, E. and Mougin, P., Application of Gibbs Ensemble and *NpT* Monte Carlo simulation to the development of improved processes for H_2S -rich gases, *Mol. Sim.* **30** (2004) 631–648.
- [246] Urukova, I., Vorholz, J. and Maurer, G., Solubility of carbon dioxide in aqueous solutions of methanol. Predictions by molecular simulation and comparison with experimental data, *J. Phys. Chem. B* **110** (2006) 14943–14949.

- [247] Usyukin, I.P. and Shleinikov, V.M., Solubility of acetylene in selective solvents at low temperatures, *Novosti Neft. i Gaz. Tekhn. Neftepererabotka i Neftekhim* **12** (1961) 33–39.
- [248] van Leeuwen, M.E. and Smit, B., Molecular simulation of the vapor-liquid coexistence curve of methanol, *J. Phys. Chem.* **99** (1995) 1831–1833.
- [249] Verlet, L., Computer “Experiments” on classical fluids. I. Thermodynamical properties of Lennard-Jones molecules, *Phys. Rev.* **159** (1967) 98–103.
- [250] Vitovec, J., Absorption of acetylene and carbon dioxide in water, xylene, and methanol in a packed column. *Collect. Czech. Chem. Commun.* **33** (1968) 1203–1210.
- [251] Vörtler, H.L. and Kettler, M., Efficient simulation of chemical potentials and phase equilibria in associating fluids: monomer/dimer insertion versus gradual particle insertion in primitive water models, *Mol. Phys.* **104** (2006) 233–241.
- [252] Vrabec, J. and Fischer, J., Vapour liquid equilibria of mixtures from the NpT plus Test Particle Method, *Mol. Phys.* **85** (1995) 781–792.
- [253] Vrabec, J. and Fischer, J., Vapor-liquid equilibria of binary mixtures containing methane, ethane, and carbon dioxide from molecular simulation, *Int. J. Thermophys.* **17** (1996) 889–908.
- [254] Vrabec, J. and Fischer, J., Vapor-liquid equilibria of the ternary mixture $\text{CH}_4 + \text{C}_2\text{H}_6 + \text{CO}_2$ from molecular simulation, *AIChE J.* **43** (1997) 212–217.
- [255] Vrabec, J., Stoll, J. and Hasse, H., A set of molecular models for symmetric quadrupolar fluids, *J. Phys. Chem. B* **105** (2001) 12126–12133.
- [256] Vrabec, J. and Hasse, H., Grand Equilibrium: vapour-liquid equilibria by a new molecular simulation method, *Mol. Phys.* **100** (2002) 3375–3383.
- [257] Vrabec, J., Kettler, M. and Hasse, H., Chemical potential of quadrupolar two-centre Lennard-Jones fluids by gradual insertion, *Chem. Phys. Lett.* **356** (2002) 431–436.
- [258] J. Vrabec, J. Stoll and H. Hasse. Molecular models of unlike interactions in mixtures, *Mol. Sim.* **31** (2005) 215–221.
- [259] Vrabec, J., Kedia, G.K. and Hasse, H., Prediction of Joule-Thomson inversion curves for pure fluids and one mixture by molecular simulation, *Cryogenics* **45** (2005) 253–258.
- [260] Vrabec, J., Kumar, A. and Hasse, H., Joule-Thomson inversion curves of mixtures by molecular simulation in comparison to advanced equations of state: Natural gas as an example, *Fluid Phase Equilib.* (2007) in press.
- [261] Waldman, M. and Hagler, A.T., New combining rules for rare gas van der Waals parameters, *J. Comput. Chem.* **14** (1993) 1077–1084.

- [262] Wallen, S.L., Palmer, B.J., Garrett, B.C. and Yonker, C.R., Density and temperature effects on the hydrogen bond structure of liquid methanol, *J. Phys. Chem.* **100** (1996) 3959–3964.
- [263] Wallen, S.L., Palmer, B.J., Garrett, B.C. and Yonker, C.R., Additions and corrections to “Density and temperature effects on the hydrogen bond structure of liquid methanol”, *J. Phys. Chem.* **100** (1996) 20173–20173.
- [264] Wallqvist, A. and Mountain, R.D., Molecular models of water: Derivation and description, *Rev. in Comp. Chem.* **13** (1999) 183–247.
- [265] Weber, W., Zeck, S. and Knapp, H., Gas solubilities in liquid solvents at high pressures: Apparatus and results for binary and ternary systems of N₂, CO₂ and CH₃OH, *Fluid Phase Equilib.* **18** (1984) 253–278.
- [266] Weidlich U., *Experimentelle und theoretische Untersuchung der Löslichkeit von Gasen in Alkanen und Alkoholen*, University of Dortmund, Germany, Master’s Thesis, 1981.
- [267] Weitkamp, T., Neufeind, J., Fischer, H.E. and Zeidler, M.D., Hydrogen bonding in liquid methanol at ambient conditions and at high pressure, *Mol. Phys.* **98** (2000) 125–134.
- [268] Wick, C.D., Stubbs, J.M., Rai, N. and Siepmann, J.I., Transferable potentials for phase equilibria. 7. Primary, Secondary, and Tertiary Amines, Nitroalkanes and Nitrobenzene, Nitriles, Amides, Pyridine, and Pyrimidine, *J. Phys. Chem. B* **109** (2005) 18974–18982.
- [269] Widom, B., Some topics in the theory of fluids, *J. Chem. Phys.* **39** (1963) 2808–2812.
- [270] Wilken, M., Experimentelle Bestimmung und Korrelation von Gaslöslichkeiten und Dampf-Flüssig-Gleichgewichten. *Master Thesis*, Universität Oldenburg, 1999.
- [271] Won, Y.S., Chung, D.K. and Mills, A.F., Density, viscosity, surface tension, and carbon dioxide solubility and diffusivity of methanol, ethanol, aqueous propanol, and aqueous ethylene glycol at 25°C, *J. Chem. Eng. Data* **26** (1981) 140–141.
- [272] Wood, C.D., Senoo, K., Martin, K., Cuellar, J. and Cooper, A.I., Polymer synthesis using hydrofluorocarbon solvents. 1. Synthesis of cross-linked polymers by dispersion polymerization in 1,1,1,2-Tetrafluoroethane, *Macromolecules* **35** (2002) 6743–6746.
- [273] Wu, C., Li, X., Dai, J. and Sun, H., Prediction of Henry’s law constants of small gas molecules in liquid ethylene oxide and ethanol using force field methods, *Fluid Phase Equilib.* **236** (2005) 66–77.
- [274] Yaacobi, M. and Ben-Naim, A., Hydrophobic interaction in water-ethanol mixtures, *J. Solution Chem.* **2** (1973) 425–443.
- [275] Yaacobi, M. and Ben-Naim, A., Solvophobic interaction, *J. Phys. Chem.* **78** (1974) 175–178.

- [276] Xu, N., Yao, J., Wang, Y., Shi, J. and Lu, B.C.-Y., Vapor-liquid equilibria of five binary systems containing R-22, *Fluid Phase Equilib.* **69** (1991) 261–270.
- [277] Yamaguchi, T., Hidaka, K. and Soper, A.K., The structure of liquid methanol revisited: a neutron diffraction experiment at -80°C and $+25^{\circ}\text{C}$, *Mol. Phys.* **96** (1999) 1159–1168.
- [278] Yamaguchi, T., Hidaka, K. and Soper, A.K., Erratum to “The structure of liquid methanol revisited: a neutron diffraction experiment at -80°C and $+25^{\circ}\text{C}$ ”, *Mol. Phys.* **97** (1999) 603–605.
- [279] Yarym-Agaev, N.I., Sinyavskaya, R.P., Koliushko, I.I. and Levinton, L.Y., Phase equilibria in the water methane and methanol-methane binary systems under high pressure, *J. Appl. Chem. (U.S.S.R.)* **58** (1985) 154–157.
- [280] Yonker, C.R., Wallen, S.L., Palmer, B.J. and Garrett, B.C., Effects of pressure and temperature on the dynamics of liquid *tert*-butyl alcohol, *J. Phys. Chem. A* **101** (1997) 9564–9570.
- [281] Zhang, L. and Siepmann, J.I., Direct calculation of Henry’s law constants from Gibbs ensemble Monte Carlo simulations: nitrogen, oxygen, carbon dioxide and methane in ethanol, *Theor. Chem. Acc.* **V115** (2006) 391–397.

Lebenslauf

Geburtsdatum: 26.11.1976
 Geburtsort: Stuttgart
 Familienstand: ledig
 Staatsangehörigkeit: deutsch

Schulbildung

1983 - 1987 Grundschole in Stuttgart
 1988 - 1996 Eberhard-Ludwigs-Gymnasium in Stuttgart

Zivildienst

1996 - 1997 Arbeiter-Samariter-Bund in Stuttgart

Studium

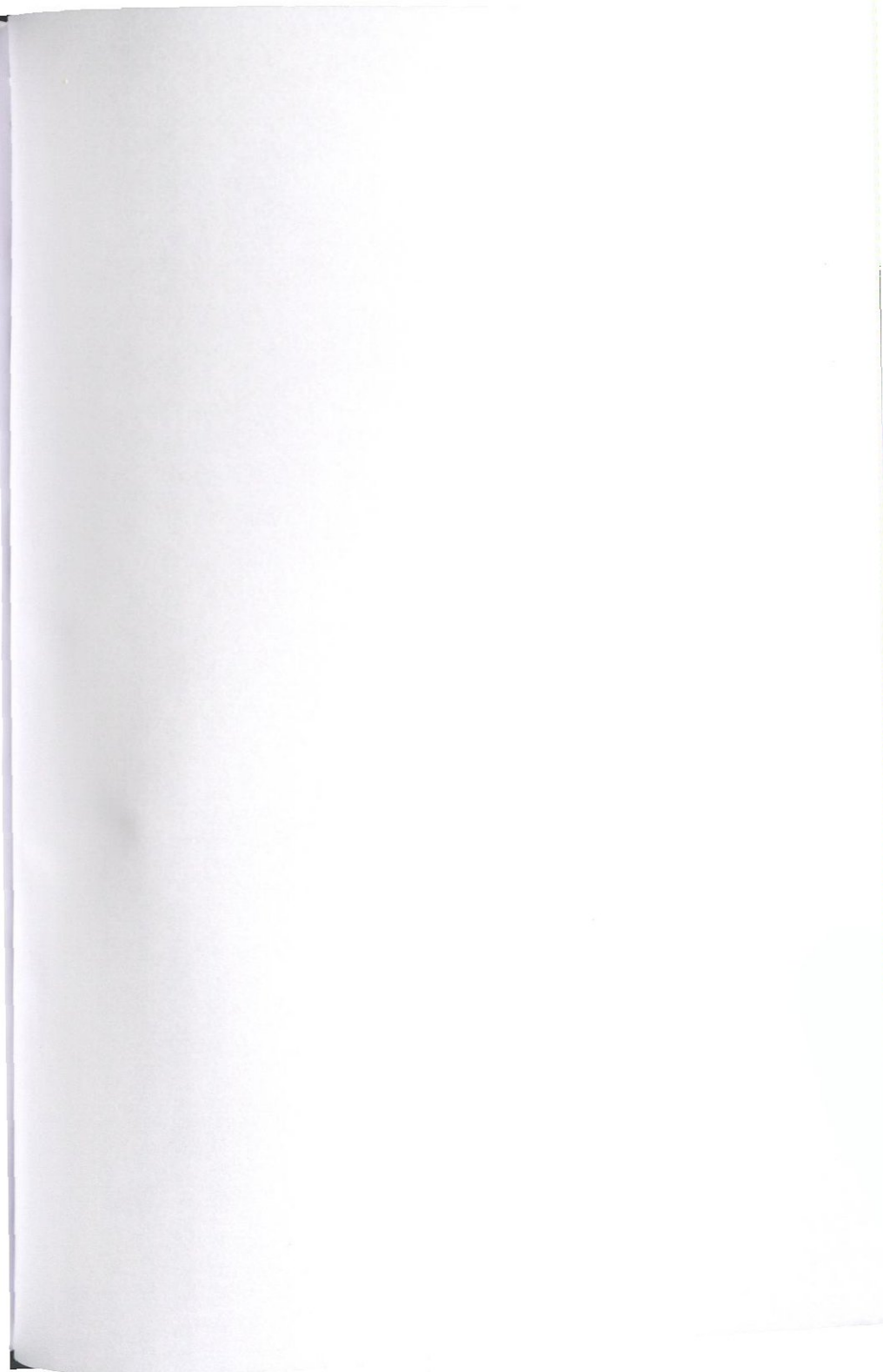
1997 - 2002 Studium an der Universität Stuttgart
 Studiengang: Verfahrenstechnik
 Vertiefungsrichtungen: Apparate- und Anlagenbau,
 Thermische Verfahrenstechnik
 2001 Praktikum in Schweden, Eka Chemicals, Göteborg
 2002 Diplomarbeit in England, University of Manchester
 Institute of Science and Technology (UMIST)
 Abschluss: Dipl.-Ing. (November 2002)

Berufliche Tätigkeit

2003 - 2007 Wissenschaftlicher Mitarbeiter am Institut für
 Technische Thermodynamik und
 Thermische Verfahrenstechnik
 Prof. Dr.-Ing. H. Hasse
 Universität Stuttgart
 Seit 2007 Prozess- und Projektingenieur im VT Engineering
 bei der Lonza AG in Visp, Schweiz

Größte sportliche Erfolge

2000 2. Platz Deutsche Meisterschaften Rudern
 im Zweier ohne Steuermann, Berlin-Grünau,
 Deutschland
 2000 5. Platz Hochschulweltmeisterschaften Rudern
 im Zweier ohne Steuermann, Poznań,
 Polen



Logos Verlag Berlin

ISBN 978-3-8325-1945-2